



Provided by the author(s) and University of Galway in accordance with publisher policies. Please cite the published version when available.

Title	The optical development and calibration of the Galway Astronomical Stokes Polarimeter (GASP) as a multi-detector system for the polarimetric observations of variable optical sources
Author(s)	Kyne, Gillian
Publication Date	2014-06-03
Item record	<a href="http://hdl.handle.net/10379/4572">http://hdl.handle.net/10379/4572</a>

Downloaded 2024-04-23T15:34:02Z

Some rights reserved. For more information, please see the item record link above.



**The optical development and calibration of the  
Galway Astronomical Stokes Polarimeter  
(GASP) as a multi-detector system for the  
polarimetric observations of variable optical  
sources**

Thesis by  
Gillian Kyne

In Partial Fulfillment of the Requirements  
for the Degree of  
Doctor of Philosophy

**Supervisor: Prof. Andrew Shearer**



Centre for Astronomy  
School of Physics  
National University of Ireland, Galway  
Galway, Ireland

**2014**  
(Defended May 12, 2014)



---

# Contents

<b>List of Tables</b>	<b>vi</b>
<b>List of Figures</b>	<b>ix</b>
<b>Abstract</b>	<b>xxvii</b>
<b>Declaration</b>	<b>xxix</b>
<b>Acknowledgements</b>	<b>xxx</b>
<b>Acronyms &amp; Abbreviations</b>	<b>xxxi</b>
<b>1 Introduction: Astronomical Polarisation &amp; Instrumentation</b>	<b>1</b>
1.1 What is Polarisation? . . . . .	3
1.2 Measuring Polarisation . . . . .	8
1.2.1 Stokes Polarimeters . . . . .	10
1.2.1.1 Polaroid-Type Polarimeter . . . . .	10
1.2.1.2 Dual-Beam Polarimeter . . . . .	11
1.2.2 Polarimetry Techniques . . . . .	12
1.2.2.1 Aperture (wavefront) Division . . . . .	13
1.2.2.2 Amplitude Division . . . . .	13
1.3 Current Instrumentation . . . . .	14
1.4 Systematic Errors in Polarimetry . . . . .	21
1.5 Polarimetry Techniques at other Wavelengths . . . . .	24
1.6 Thesis Overview . . . . .	25

---

<b>2 Optical Polarisation Studies of Pulsars</b>	<b>29</b>
2.1 Introduction . . . . .	29
2.2 What is a pulsar? . . . . .	30
2.3 Pulsar Discovery . . . . .	33
2.4 Pulsar Classification . . . . .	37
2.4.1 Rotation-Powered Pulsars . . . . .	37
2.4.2 Binary & Millisecond Pulsars . . . . .	38
2.4.3 Accretion-Powered Pulsars . . . . .	40
2.4.4 Magnetars . . . . .	41
2.5 Pulsar Phenomenology . . . . .	42
2.5.1 Structure . . . . .	42
2.5.2 Magnetic Fields & Pulsar Age . . . . .	43
2.5.3 Pulsar Magnetosphere . . . . .	47
2.5.4 Radio Beam Geometry . . . . .	48
2.5.5 Rotating Vector Model . . . . .	49
2.6 Pulsar Emission Models . . . . .	52
2.6.1 Polar-Cap Model . . . . .	53
2.6.2 Slot-Gap Model . . . . .	55
2.6.3 Outer-Gap Model . . . . .	56
2.6.4 Two-Pole Caustic Model . . . . .	57
2.6.5 The Striped Wind Model . . . . .	58
2.7 Optical Studies of Pulsars . . . . .	60
2.8 Optical Polarisation of the Crab Pulsar . . . . .	64
2.9 Optical Studies of Giant Radio Pulses . . . . .	69
<b>3 The Galway Astronomical Stokes Polarimeter</b>	<b>74</b>
3.1 Science Motivation . . . . .	74
3.2 Instrument Introduction . . . . .	77
3.2.1 The Polarisation State Analyser (PSA) . . . . .	78
3.2.2 The Polarimeter Design . . . . .	81
3.3 Noise Sensitivity of GASP . . . . .	86

---

<b>4 Optical and Hardware redesign of GASP</b>	<b>88</b>
4.1 Imaging using 1-Detector . . . . .	89
4.2 An 8-Detector Polarimeter . . . . .	90
4.3 Imaging using 2-Detectors . . . . .	92
4.3.1 The Field of View Problem . . . . .	93
4.3.2 Choice of Telescope Focus . . . . .	94
4.3.3 FOV and Pupil Conjugation . . . . .	94
4.3.4 The Collimating Optics . . . . .	96
4.4 Final Optical Design for the P200 . . . . .	97
4.4.1 Optical Image Quality . . . . .	100
4.4.1.1 Spot Diagrams . . . . .	100
4.4.1.2 Encircled Energy . . . . .	108
4.5 Pixel Scale and FOV Overlap . . . . .	111
<b>5 Instrument Calibration &amp; Results</b>	<b>114</b>
5.1 Difficulties in Calibrating Astronomical Polarimeters . . . . .	114
5.2 Mueller Polarimetry . . . . .	115
5.3 The Polarisation State Generator . . . . .	118
5.4 The Moore-Penrose Pseudoinverse . . . . .	120
5.4.1 Definition . . . . .	120
5.5 The Eigenvalue Calibration Method . . . . .	121
5.5.1 Mathematical Description . . . . .	122
5.6 Calibrating GASP . . . . .	123
5.7 ECM with Avalanche Photodiodes . . . . .	123
5.7.1 ECM Results . . . . .	124
5.7.2 Polarimetric Results . . . . .	126
5.8 Pixel-by-Pixel ECM using Imaging Detectors . . . . .	133
5.9 ECM Image Registration using Artefacts . . . . .	136
5.9.1 Artefact Residuals . . . . .	146
5.9.2 ECM Analysis & Results of Artefact Registration . . . . .	147
5.9.3 ECM Sample Calibration Artefact Registration . . . . .	151
5.10 ECM Image Registration using Science Data . . . . .	157
5.10.1 Science Residuals . . . . .	164

---

5.10.2	ECM Analysis & Results of Science Data Registration	166
5.10.3	ECM Sample Calibration using Science Data Registration	168
5.11	Stability of the ECM	174
5.11.1	ECM Calibration Verification using Science Data Registration	178
5.12	Concluding Remarks	182
<b>6</b>	<b>Observational Results</b>	<b>187</b>
6.1	Introduction	187
6.2	Polarisation Standards	188
6.2.1	Data Reduction	190
6.2.2	Instrumental Polarisation	201
6.2.3	Conclusions	203
6.3	Zenith Flat-Field Observations	204
6.3.1	Science Data Pixel-by-Pixel Analysis	206
6.3.1.1	Polarimetric Results	209
6.3.2	Science Data Aperture Photometry Analysis	218
6.4	Concluding Remarks	224
<b>7</b>	<b>Observation Results for the Crab Pulsar</b>	<b>227</b>
7.1	Introduction	227
7.2	Polarisation of the Crab Pulsar: Integrated Data	228
7.2.1	Concluding Remarks	232
7.3	Polarisation of the Crab Pulsar: Phase Resolved Data	232
7.3.1	EM Gain & Bias Level	233
7.3.2	Timing Analysis	238
7.3.3	Polarimetric Results	242
7.3.4	Concluding Remarks	247
<b>8</b>	<b>Conclusions &amp; Future Work</b>	<b>249</b>
8.1	Laboratory Instrument Calibration Conclusions	249
8.2	Observational Calibration Conclusions	252
8.3	Science Conclusions: Zenith Flat-Fields	253
8.4	Science Conclusions: Crab Pulsar	254
8.5	Future Instrumentation & Experimentation	255

---

8.5.1	Recommendations . . . . .	256
<b>Appendices</b>		<b>260</b>
<b>A</b>	Polarimetric Expressions	260
<b>B</b>	Pseudo-inverse Calibration Method	262
<b>C</b>	ECM Mathematical Solution	263
<b>D</b>	Avalanche Photodiode Specifications	266
<b>E</b>	iXon Ultra 897 Specifications	269
<b>Bibliography</b>		<b>294</b>

---

# List of Tables

2.1	Pulsar Emission Models Summary. . . . .	59
2.2	High energy polarisation measurements of pulsars and their nebulae (Slowikowska et al., 2009). . . . .	65
3.1	Expected degrees of polarisation fluxes, & minimum exposure time for detecting $\sim 5\%$ polarisation Collins et al. (2013). . . . .	76
3.2	Geometrical and polarimetric properties of the current GASP prism- rhomb Collins et al. (2013). . . . .	82
4.1	RP1 RMS radial spot diagram values for Figure 4.7; values are in microns and pixels. . . . .	100
4.2	RP2 RMS radial spot diagram values for Figure 4.8; values are in microns and pixels. . . . .	101
4.3	TP1 RMS radial spot diagram values for Figure 4.9; values are in microns and pixels. . . . .	102
4.4	TP2 RMS radial spot diagram values for Figure 4.10; values are in microns and pixels. . . . .	102
5.1	Linear polariser laboratory experiment using APD detectors to test the GASP ECM. . . . .	129
5.2	Unpolarised source laboratory experiment using APD detectors to test the GASP ECM. . . . .	132
5.3	Output of the <i>geomap</i> fit for artefact registration. These values refer to the data at the pixel level without any binning. . . . .	142

---

5.4	Output of the <i>geomap</i> fit for the matched TP2 artefact registration. Artefacts were removed in the outer FOV where distortions appeared to grow visually. . . . .	143
5.5	Theoretical and mean values for the normalised Mueller matrix of the AIR ECM sample; registration performed by image artefacts. . .	153
5.6	Theoretical and mean values for the normalised Mueller matrix of the P0 ECM sample; registration performed by image artefacts. . .	153
5.7	Theoretical and mean values for the normalised Mueller matrix of the P90 ECM sample; registration performed by image artefacts. . .	156
5.8	Theoretical and mean values for the normalised Mueller matrix of the R30 ECM sample; registration performed by image artefacts. . .	158
5.9	Output of the <i>geomap</i> fit using science data points in Figure 5.19. . .	160
5.10	Output of each of the <i>geomap</i> fits. The coordinates are given for each channel after registration. . . . .	162
5.11	Output of each of the <i>geomap</i> fits. The RMS values are given for each channel after registration. . . . .	163
5.12	Theoretical and mean values for the normalised Mueller matrix of the AIR ECM sample; registration performed using science data points. .	170
5.13	Theoretical and mean values for the normalised Mueller matrix of the P0 ECM sample; registration performed using science data points.	170
5.14	Theoretical and mean values for the normalised Mueller matrix of the P90 ECM sample; registration performed using science data points. .	172
5.15	Theoretical and mean values for the normalised Mueller matrix of the R30 ECM sample; registration performed using science data points. .	174
5.16	iXon Ultra 897 detector settings for the calibration data presented in this section, and chapter. . . . .	175
6.1	Integrated polarimetric information in the literature for targets ob- served by GASP at the P200 in November 2012. . . . .	189
6.2	Observational logs summary for the polarisation standards observed by GASP on Night 4. . . . .	190

6.3	Polarimetric results for the polarisation standards observed by GASP on Night 4. Sky subtraction has been performed on each set of data. Polarisation angle has been corrected for telescope orientation. The difference in aperture size taken is a result of a changing FWHM for each target in each filter. A radial aperture equal to the radius of the FWHM was used. The expected result for the polarisation standards, including filter if given by there reference, is also stated. . . . .	198
6.4	<i>geomap</i> output for matching RP1 science to RP1 calibration. . . . .	205
6.5	Expected polarisation angle variation over the same 35 minute period of observation by GASP for Zenith flat-field data. The first time is not usable as we are measuring from this value: The $\Delta PA$ values are measured from here. . . . .	209
6.6	Mean polarimetric results for Zenith flat-field data using a pixel-by-pixel analysis for the $3 \times 3$ pixel area in the final image of each polarimetric measurement. The $\Delta PA$ values are also given. . . . .	216
6.7	Mean polarimetric results for Zenith flat-field data using a method of aperture photometry for a 3 pixel radial aperture. . . . .	222
7.1	Observational logs summary for the Crab Pulsar observed by GASP on Night 4. . . . .	227
7.2	Integrated polarimetric information from the literature for the Crab Nebula. The pulsar has a magnitude of 16.5. . . . .	228
7.3	Polarimetric information for each of the targets indicated in Figure 7.1. A radial aperture equal to the FWHM was used, however, any variation caused by seeing/atmosphere must be taken into account when making comparisons to the literature. . . . .	231
E.1	iXon Ultra 897 Key Specifications. . . . .	272

---

# List of Figures

1.1	Huygens's Principle. The image shows the propagation of a wave-front. Two wavefronts with a common centre. Each point indicated on the first spherical wavefront (a, b, c, etc.) emits wavelets such that $a \rightarrow A$ , $b \rightarrow B$ , etc. The image on the RHS shows how the second wavefront forms from the combination of the secondary wavelets. This is known as an envelope of wavelets (Robinson and Clark, 2006).	4
1.2	Image description of linearly polarised light. The vector $\tilde{\mathbf{E}}$ is composed of two vectors $E_x$ and $E_y$ , giving the wave its overall direction (Hecht, 1987). . . . .	5
1.3	Circularly polarised light is a combination of two linearly polarised light waves. If a phase difference of $90^\circ$ is introduced to the system (one wave lags the other by $90^\circ$ ), then elliptically polarised light is generated. If there is a azimuthal difference of $45^\circ$ between the waves, then circularly polarised light is introduced (Hecht, 1987). . . . .	6
1.4	A Dual-beam polarimeter can be used to measure orthogonal polarisation signals simultaneously. A birefringent material, such as a Wollaston prism, may be used to split the incident light. This image shows how the dual-beam polarimeter can be rotated by $180^\circ$ to negate issues such as gain differences, however, a half-wave plate may be used to switch the beams instead (Corbett, 2009). . . . .	11

---

1.5	The optical layout of a DOAP configuration. The main beamsplitter divides the incoming light into r and t, the reflected and transmitted light beams, respectively. The light is then split on each path again by polarising beamsplitters, usually Wollaston prisms indicated by W1 and W2. This is a general design layout compatible with most telescopes and detector systems (Azzam et al., 1988). . . . .	14
1.6	A schematic of the optical layout of the HIPPO polarimeter (Potter et al., 2008). . . . .	16
1.7	Graphical description of the OPTIMA-Burst system. This figure shows the optical path to the polarimeter. For all other apertures, the fibres terminate directly within the slanted mirror in the fieldview unit (Stefanescu et al., 2008). . . . .	18
2.1	A model for a rotating neutron star from the <i>Handbook of Pulsar Astronomy</i> . The figure includes the NS magnetosphere - not drawn to scale - (Lorimer and Kramer, 2004). . . . .	32
2.2	This figure displays the results of the findings of Hewish et al. (1968). The top plot (a) is the time variation of the smoothed pulse amplitude, over 10 pulses. The bottom plot (b) is the daily variation of peak pulse amplitude in units of $\text{W m}^{-2} \text{ Hz}^{-1} \times 10^{26}$ . . . . .	34
2.3	A pulse measured from the Crab pulsar by Cocke et al. (1969) using the Steward Observatory 36 inch f/5 reflecting telescope and a 1P21 photomultiplier. The pulsations were observed on a cathode ray tube, which added successive cycles in phase. The optical pulses were observed to have a geocentric period of 0.033095 seconds, which agreed well with the radio. . . . .	35
2.4	A plot of period vs. period derivative for the currently known rotation-powered pulsars (RPPs), Isolated Neutron Stars (INS), Compact Central Objects (CCO), Rotating Radio Transients (RRATs) and magnetars (Harding, 2013). . . . .	44
2.5	Description of the pulsar beam geometry (Lorimer and Kramer, 2004).	48

---

2.6	A cartoon of the pulsar magnetosphere based on the theories laid out by Goldreich and Julian (1969). A polar-gap is evident here and will be discussed later (Lorimer and Kramer, 2004). . . . .	50
2.7	A phase-averaged spectral energy distribution (SED) plot of Vela, ( $E^2 dN_\gamma/dE$ ). Both statistical (capped) and systematic (uncapped) errors are shown. The authors believe that the latter are conservative; they dominate at all energies below 7 GeV. EGRET data points (Kanbach et al., 1994) are shown for comparison. The curve is the best-fit power law with a simple exponential cut-off (Abdo et al., 2009).	54
2.8	Phase-averaged SED of the Geminga pulsar. The solid line represents the best-fit power law with exponential cut-off (i.e., $b = 1$ ), while the dashed one represents the best-fit power law with exponential cut-off with free exponential index (in this case, the result is $b = 0.81$ ) (Abdo et al., 2010). . . . .	55
2.9	Predicted peak optical luminosity from equation 2 versus observed peak emission. Also shown is the weighted fit described in the text. The weighting was based upon the observational uncertainties in flux and distance (Shearer and Golden, 2001). . . . .	62
2.10	Optical polarisation characteristics of the Crab pulsar compared with the pulsar radio profiles. Radio profiles obtained at radio frequencies of 1400 MHz and 610 MHz are shown as a solid line and dashed line, respectively. Left column is a close in plot of the MP phase, whereas the right column is the IP phase. Points indicate the optical polarisation measurements, while the dotted line shows the optical intensity profile (Słowińska et al., 2009). . . . .	68
2.11	The mean optical ‘giant’ pulse superimposed (including error bars) on the average optical pulse (Shearer et al., 2003). The average pulse is determined from the 40 pulsar periods centred on the GRP, but not including it, from both nights of observation. . . . .	71

---

3.1	The optical layout of the Compain and Drevillon (1998) PSA for an uncoated dielectric prism for the V - NIR (Visible - Near-Infrared). The light beam is separated into two by a prism, then into four by two Wollaston prisms W1 and W2 oriented at 45° with respect to the plane of incidence. Stokes vector S is determined from the four intensities $i_1 - i_4$ . . . . .	78
3.2	The optical layout of GASP. This is a general design used for any telescope and any detector system. The optical prescription (with the exception of the main beam splitting prism) changes depending on the choice of telescope and detector. . . . .	81
3.3	Final Zemax design of the GASP main beamsplitter (Collins et al., 2013). The reflected and transmitted beams can be seen, and the extractor arm, which can be used for guiding. . . . .	84
3.4	Optical layout for GASP as a single-imaging-detector polarimeter (Collins et al., 2013). The instrument used reflecting mirrors orientated to capture all 4 beams on a single chip. . . . .	85
3.5	Monte Carlo Simulation of GASP data using a theoretical calibration matrix (found above) to model both the ingoing light and outgoing polarisation values (degree of linear and degree of circular polarisation). The simulation was modelled for a wavelength of 589 nm (for the prism glass type) (Collins et al., 2013). . . . .	87
4.1	Optical Layout of a non-imaging (8 detectors) version of GASP (Collins et al., 2013). . . . .	90
4.2	A Zemax prescription for the f/9 Cassegrain focus for the Hale 200 inch telescope at Palomar Observatory. Note the extra optics used to convert an f/16 beam to an f/9. This information was found from original drawings of the P200 in the Caltech archives loaned to the group by Paul Gardner, Chief Engineer at Caltech Optical Observatories. The prescription was configured and optimised with the help of Leon Harding. . . . .	95

---

4.3	A Zemax prescription for the f/9 Cassegrain focus for the Hale 200 inch telescope at Palomar Observatory. This is a zoomed in view of the red box in Figure 4.2. These extra lenses provide the means to change the f-number of the Cassegrain focus from f/16 to f/9. . . . .	96
4.4	Zemax description of how the beam will not remain collimated as it moves past the pupil position. This is an optical description for the 200 inch f/9 telescope focus, using a collimator with a focal length equal to 40 mm. . . . .	97
4.5	Field lens solution for the GASP collimator. Two 100 mm focal length lenses of diameter 25 mm were combined to produce a ‘single’ lens with an effective focal length of 50 mm. . . . .	98
4.6	Effective focal length collimator lens of 50 mm using a 30 mm lens to re-image at the detector. The unvignetted FOV was found to be $\sim 21''$ . . . . .	99
4.7	Spot sizes for the RP1 channel. The top left corner is the first field point, and are read left to right. The values are given in microns in Table 4.1 and the scale bar is $1000 \mu\text{m}$ . The Zemax design is optimised based on the optomechanical requirement of the system, but also by giving the best spot size relative to the diffraction limit. The central image refers to the on axis PSF and the outer spot sizes are points on the edge of square FOV of $\sim 18 \times 18''$ . . . . .	103
4.8	Spot sizes for RP2 channel. . . . .	104
4.9	Spot sizes for TP1 channel. . . . .	105
4.10	Spot sizes for TP2 channel. . . . .	106
4.11	Encircled Energy for the RP1 channel. The measured value on the y axis is the fractional percentage. The Zemax design is optimised based on the optomechanical requirement of the system. The plotted lines are colour coded for each position in the FOV, which are indicated by the spot diagrams. . . . .	108
4.12	Encircled Energy for RP2 channel. . . . .	109
4.13	Encircled Energy for TP1 channel. . . . .	110
4.14	Encircled Energy for TP2 channel. . . . .	110

---

4.15	The GASP layout while mounted to the Cass f/9 focus of the P200. The image indicates the GASP Fresnel rhomb beamsplitter and detectors used for science and guiding. Calibration optics and filter wheel can be seen in the top section of the image, and the blue tubing was used for cooling of the iXon Ultra EMCCDs. . . . .	113
5.1	An Intensity Spectrum Curve for a Warm White LED sourced from Thorlabs (Tho, b). . . . .	118
5.2	Transmission and extinction ratio specifications for a linear polariser from Thorlabs for a range 450 - 800 nm (Tho, a). . . . .	119
5.3	Stokes parameters I, Q, U, and V for an experiment passing LED light through a linear polariser to measure the limits of the GASP system using APDs. The Q, U, and V parameters have been normalised to Stokes I to remove any fluctuations in luminosity. A systematic effect is observed on Stokes Q and U, the parameters used to the measurement of the degree of linear polarisation. A different trend is found for V, which suggests an instrumental effect for this laboratory experiment. . . . .	126
5.4	Polarisation angle measurement for an experiment passing LED light through a linear polariser to measure the limits of the GASP system using APDs. The drop, and variation, in Stokes Q and U is observed in this plot. There is a variation of 0.5° from beginning to end, which suggests that the polariser is moving. This is not a random effect and over a prolonged period (2 days) it is possible that there was movement in the laboratory, or in the vicinity of the instrument, that could account for this variation. . . . .	128
5.5	Raw intensity data for each of the 4 channels for an experiment passing LED light through a linear polariser to measure the limits of the GASP system using APDs. A drop in light intensity is evident across all channels indicating that the LED light level dropped during the experiment. This is also found in the plot for Stokes I in Figure 5.3. .	130

---

5.6	Stokes parameters for an experiment passing light from an LED source through GASP to measure the limits of the GASP system for an ‘unpolarised’ using APDs. . . . .	131
5.7	Maximum magnitudes of DOLP and DOCP for a square test image. Solid line is for 360° image wander, dashed line is for 180° image wander. The angle of rotation refer to a retarder that is rotated in the beam and induces image wander. . . . .	134
5.8	All GASP channels for a full frame calibration image. Top LHS: RP1, top RHS: RP2, bottom LHS: TP1 and bottom RHS: TP2. . . . .	137
5.9	All GASP channels for a full frame calibration image. Top LHS: RP1, top RHS: RP2, bottom LHS: TP1 and bottom RHS: TP2. . . . .	138
5.10	All registered GASP channels for a full frame calibration image using the artefacts in Figure 5.9. Top LHS: RP1, top RHS: RP2, bottom LHS: TP1 and bottom RHS: TP2. . . . .	144
5.11	All registered GASP channels for a full frame calibration image using the artefacts in Figure 5.9. The section indicated by the orange box is used in calibration to produce a system matrix using the Eigenvalue Calibration Method. This calibration data set has been binned $4 \times 4$ . Top LHS: RP1, top RHS: RP2, bottom LHS: TP1, and bottom RHS: TP2. . . . .	145
5.12	Calibration residuals from the section of the image indicated above. The top left corner image show the counts on the RP1 channel to which everything is registered. There is a clear systematic variation present across each field. . . . .	146
5.13	The experimental calibration matrix for the image section indicated in Figure 5.11. The calibration images were registered to channel RP1 using artefacts common to all channels. . . . .	148

---

5.14	The normalised calibration matrix for the image section indicated in Figure 5.11. The calibration images were registered to channel RP1 using artefacts common to all channels. Apart from the clear systematic trend in all gain coefficients the mean values for each are in good agreement with the GASP PSA. The only exception is TP2. This is very clearly a result of the pattern in the bottom right corner, which shows a clear contrast in values to the top left. This pattern is a result of image registration and appears on each of the TP2 coefficients. If this area was ignored, the values would better agree with the PSA. Taking a smaller area of the FOV, or shifting would reduce this pattern, however, there is similar compromise on the TP1 image in the top left corner. . . . .	149
5.15	The normalised Mueller matrix for the AIR sample for the image section indicated in Figure 5.11. The calibration images were registered to channel RP1 using artefacts common to all channels. . . . .	152
5.16	The normalised Mueller matrix for the P0 sample for the image section indicated in Figure 5.11. The calibration images were registered to channel RP1 using artefacts common to all channels. . . . .	154
5.17	The normalised Mueller matrix for the P90 sample for the image section indicated in Figure 5.11. The calibration images were registered to channel RP1 using artefacts common to all channels. . . . .	155
5.18	The normalised Mueller matrix for the R30 sample for the image section indicated in Figure 5.11. The calibration images were registered to channel RP1 using artefacts common to all channels. . . . .	157
5.19	This is an image of the Crab Nebula ( $\sim 20''$ ). The points indicated are from a set of data from the first night of observations. This is how they are scattered throughout the field. . . . .	159
5.20	The final registered channels for calibration. The points indicated are from the set of science data used for registration from the first night of observations. This is how they are scattered throughout the field after registration - the points have been passed through the IRAF task <i>geoxytran</i> , which uses the geometric fit to find the new coordinate location. . . . .	161

---

5.21	All registered GASP channels for a full frame calibration image that have been spatially registered using science data points in Figure 5.19. The section indicated by the orange box is used in calibration to produce a system matrix using the Eigenvalue Calibration Method. This calibration data set has been binned $4 \times 4$ . Top LHS: RP1, top RHS: RP2, bottom LHS: TP1 and bottom RHS: TP2. . . . .	164
5.22	Calibration residuals from the section of the image indicated above. All 4 channels have been registered to the calibration image RP1 channel based on science points from Figure 5.19. . . . .	165
5.23	The experimental calibration matrix for the image section indicated in Figure 5.11. The calibration images were registered to channel RP1 using science data. . . . .	167
5.24	The normalised calibration matrix for the image section indicated in Figure 5.11. The calibration images were registered to channel RP1 using science data. . . . .	168
5.25	The normalised Mueller matrix for the AIR sample for the image section indicated in Figure 5.11. The calibration images were registered to channel RP1 using science data. . . . .	169
5.26	The normalised Mueller matrix for the P0 sample for the image section indicated in Figure 5.11. The calibration images were registered to channel RP1 using science data. . . . .	171
5.27	The normalised Mueller matrix for the P90 sample for the image section indicated in Figure 5.11. The calibration images were registered to channel RP1 using science data. . . . .	172
5.28	The normalised Mueller matrix for the R30 sample for the image section indicated in Figure 5.11. The calibration images were registered to channel RP1 using science data. . . . .	173
5.29	A calibration data set recorded using the settings in Table 5.16. This calibration matrix was produced from data recorded at the beginning of observation Night 3 at the Palomar 200 inch telescope. . . . .	175
5.30	A calibration data set recorded using the settings in Table 5.16. This calibration matrix was produced from data recorded $\sim 10$ hours after the data presented in Figure 5.29. . . . .	176

---

5.31	A calibration data set recorded using the settings in Table 5.16. This calibration matrix was produced from data recorded $\sim$ 6 days after the data presented in Figure 5.30. . . . .	177
5.32	Raw intensity plots from a calibration verification test using GASP as an imaging polarimeter for an experiment using a rotating linear polariser. . . . .	179
5.33	Polarimetric results from a calibration verification test using GASP as an imaging polarimeter for an experiment using a rotating linear polariser. . . . .	180
5.34	Raw intensity plots from a calibration verification test using GASP as an imaging polarimeter for an experiment using a rotating linear polariser and a quarter-wave plate. . . . .	181
5.35	Polarimetric results from a calibration verification test using GASP as an imaging polarimeter for an experiment using a rotating linear polariser and a quarter-wave plate. . . . .	182
6.1	Registered images for polarisation standard HD12021 taken in a clear filter. The RP1 images displays the location of the radial aperture (3 pixels), annulus (8 pixels) and dannulus (3 pixels). Sky background subtraction was found to make very little difference to the polarimetric measurements. The data has been binned $4 \times 4$ post-processing. Top LHS: RP1, top RHS: RP2, bottom LHS: TP1 and bottom RHS: TP2. . . . .	191
6.2	A radial profile plot for the RP1 (LHS) and TP1 (RHS) channels of HD12021 for the registered images. These plots are found from the images is Figure 6.1. The size of the radial aperture chosen for photometry is equal to the FWHM of this target, which is almost identical in both channels. It is noted that the FWHM varies from 4 - 6 pixels for the duration of this observation. . . . .	192

---

6.3	Registered images for polarisation standard BD25727 taken in the R Band filter. The RP1 images displays the location of the radial aperture (3 pixels), annulus (10 pixels) and dannulus (3 pixels). Sky background subtraction was also found to have minimal variation on this target's polarimetric measurements. The data has been binned $4 \times 4$ post-processing. Top LHS: RP1, top RHS: RP2, bottom LHS: TP1 and bottom RHS: TP2. . . . .	193
6.4	A radial profile plot for the RP1 (LHS) and TP1 (RHS) channels of BD25727 in the R Band filter for the registered images. These plots are found from the images is Figure 6.3. The size of the radial aperture chosen for photometry is equal to the FWHM of this target, which is almost identical in both channels. . . . .	194
6.5	A plot of Stokes I and the DOLP for the polarisation standard HD12021 in the clear filter. There is a large variation, $\sim 20\%$ of the maximum value, in Stokes I as a function of time (x axis refers to frame number). This variation could indicate movement of clouds, or the target moving in and out of focus. . . . .	195
6.6	The same as Figure 6.5 but using the R Band filter. Less variability is observed but Stokes I is much lower due to the filter. The value in the DOLP jumps higher as Stokes I drops. This could be related to scattering light from transmission through a variable atmosphere. . . . .	196
6.7	A plot of Stokes I and the DOCP for the polarisation standard HD12021 in the clear filter. The x axis refers to frame number. This variation could indicate movement of clouds. There is also the possibility of a change in target focus over time. . . . .	197
6.8	The same plot in Figure 6.7 but using the R Band filter. . . . .	197
6.9	A plot of Stokes I and the DOLP for the polarisation standard BD25727 in the clear filter. There is some variation in Stokes I, which seems to follow a more random pattern of variation with DOLP compared to HD12021. Each measurement is plotted as a function of time (x axis refers to frame number). . . . .	198

---

6.10	A plot of Stokes I and the DOLP for the polarisation standard BD25727 using the R Band filter. Some variability is observed and Stokes I is higher. This could be a result of improved observing conditions. As Stokes I increases the value in the DOLP begins to drop, fluctuating around its mean value. . . . .	199
6.11	A plot of Stokes I and the DOCP for the polarisation standard BD25727 for a clear filter. The x axis refers to frame number. This variation could indicate movement of clouds, or the target moving in and out of focus due to seeing variation. . . . .	200
6.12	The same plot in Figure 6.7 but using the R Band filter. . . . .	200
6.13	All registered GASP channels for a full flat-field frame using science data points and image artefacts. A pixel-by-pixel analysis will be analysed in this chapter on the area indicated by the orange box. Top LHS: RP1, top RHS: RP2, bottom LHS: TP1 and bottom RHS: TP2. . . . .	206
6.14	The experimental calibration matrix for the image section indicated in Figure 6.13. The calibration images were registered to channel RP1 using science data. . . . .	207
6.15	Image residuals for the flat-field section indicated by the orange box for RP1 (top left image) in Figure 6.13: Science data points are used to perform the image registration. The colour bar indicates the percentage intensity remaining when the normalised channel is removed from the normalised reference channel, RP1 calibration channel. . . . .	208
6.16	A plot of the DOLP as a function of scattering angle according to Equation 6.4. The DOLP is observed to change more rapidly after $\sim 20^\circ$ , slowing down from $\sim 80^\circ$ . These angles refer to absolute values, and not $\Delta\gamma$ values. . . . .	210

---

6.17	Degree of linear polarisation found using a registration method by science data points. The mean and $\sigma$ values are given in the title of each flat. The image has been flipped and rotated compared to the images in Figure 6.13 to match the telescope correction. This is the reason for the blue pixels at each corner of the image. The PA vectors are also plotted. The $\sigma$ value refers to the random and systematic error over the FOV of interest in Figure 6.13 for the $3 \times 3$ pixel area indicated by the rectangle on the final image. . . . .	211
6.18	Polarisation angle found using a registration method by science data points. The mean and $\sigma$ values are given in the title of each flat. The image has been flipped and rotated compared to the images in Figure 6.13 to match the telescope correction. This is the reason for the blue pixels at each corner of the image. The $\sigma$ value refers to the random and systematic error over the FOV of interest in Figure 6.13 for the $3 \times 3$ pixel area indicated by the rectangle on the final image.	213
6.19	Degree of circular polarisation found using a registration method by science data points. The mean and $\sigma$ values are given in the title of each flat. The image has been flipped and rotated compared to the images in Figure 6.13 to match the telescope correction. The $\sigma$ value refers to the random and systematic error over the FOV of interest in Figure 6.13 for the $3 \times 3$ pixel area indicated by the rectangle on the final image. . . . .	215
6.20	All registered GASP channels for a full flat-field frame using science data points and image artefacts. The chosen FOV is indicated by the orange box. The blue aperture was selected for aperture photometry analysis as it had a uniform (flat) distribution of flux on each channel. The radial size of the aperture is 3 pixels ( $5''$ ). Top LHS: RP1, top RHS: RP2, bottom LHS: TP1 and bottom RHS: TP2. . . . .	218

---

6.21	The raw intensities, after bias subtraction and registration, for each GASP channel as a function of time. The light level is low (no significant Sunlight) for the first 4 - 5 frames on each channel. The values measured range from 500 to 900 counts, $\sim 2 - 3$ times that of the bias level. These data values are extracted from a set of data that have been averaged in time according to the values in Table 6.5. It is assumed that the intensity value is an average value for that data set and represents the value at the midway point of the recorded data. This plot is produced using the blue aperture in Figure 6.20 and uses a 3 pixel radial aperture, which corresponds to a FOV of $5''$ . . . . .	219
6.22	The raw intensities from Figure 6.21 after each channel is normalised to RP1 channel. This data refers to the blue aperture in Figure 6.20 and uses a 3 pixel radial aperture, which corresponds to a FOV of $5''$ .	220
6.23	Degree of linear and circular polarisation and polarisation angle values found using a registration method by science data points. The x axis is the value for elapsed time according to the image time-stamps. This is a plot of the variation of each of these polarimetric values for each flat-field. It is assumed that the polarimetric value is an average value for that data set and represents the value at the midway point of the recorded data. This data refers to the blue aperture in Figure 6.20 and uses a 3 pixel radial aperture, which corresponds to a FOV of $5''$ . . . . .	221
6.24	Degree of linear polarisation as a function of polarisation angle measured by GASP. The theoretical plot is generated by Equation 6.4 where $\gamma = 90^\circ - \text{GASP PA}$ . . . . .	223
7.1	The location of the apertures used in photometry, for the pulsar and nebula, are shown in red. The polarimetric information of the Crab pulsar and nebula will be analysed at these points. The data has been registered and binned $4 \times 4$ . This data was recorded at the end of the night, before the Zenith flat-fields. The aperture in this plot has a 2 pixel radius. Top LHS: RP1, top RHS: RP2, bottom LHS: TP1 and bottom RHS: TP2. . . . .	229

---

7.2	A radial profile plot for the Crab pulsar (LHS) and Trimble 28 (RHS) for the registered RP1 image. This image is found in Figure 7.1. The wings of the profile appear to lie exactly in the area occupied by the nebula and it is therefore difficult to distinguish between nebula and overlapping targets. It is also true to say that the wings of each target extend into the aperture of the nearby target. . . . .	230
7.3	Each image, on each channel, is summed and averaged for 200,000 images for an exposure time of 0.00074 seconds. Each registered channel contains the Crab pulsar and Trimble 28. A 1.5 pixel radial aperture was used to obtain polarimetric information for the Crab pulsar, and Trimble 28. This data was binned $8 \times 8$ and windowed during acquisition. Top LHS: RP1, top RHS: RP2, bottom LHS: TP1 and bottom RHS: TP2. . . . .	233
7.4	This is a plot of the variation in EM gain over the duration of each data set per GASP path. The RP:TP EM gain is 1.1:1. Each detector was set to an EM gain of 300. . . . .	234
7.5	This is a plot of 10,000 RP science frames used statistically to determine the EM gain using the inverse-slope method. The gain found for these frames was $\sim 600$ and the bias level, which is the peak of the curve on the LHS, is 170 ADU. . . . .	236
7.6	This is a plot of a series of EM gain plots for the TP. Each plot is generated using 10,000 TP science frames from the beginning middle and end of the data cube. The EM gain is calculated using the inverse-slope method. The EM gain value found for these frames was 580, 630, and 620, respectively. The bias level is found from the peak value on the LHS of the gain curve. It was found to vary from beginning to end throughout this data cube. Block 1 has a bias level of 175 ADU, and block 2 and 3 have a bias level of 105 ADU. . . . .	237

---

7.7	This is a plot of 1 million TP1 and TP2 science frames after bias subtraction. The bias was calculated using the inverse-slope method when investigating the level of EM gain that was applied during acquisition. A different bias frame was used for the first 300,000 frames compared to the remaining. This was based on the observations above of a decreasing bias over time. Aperture photometry was performed for a 1.5 pixel radial aperture. . . . .	238
7.8	This is a plot of 1 million RP1 and RP2 science frames after bias subtraction. The bias was calculated using the inverse-slope method when investigating the level of EM gain that was applied during acquisition. There is a difference in RP1 to RP2 in terms of the minimum value of the noise floor. . . . .	239
7.9	This is a plot of 1 million RP1 science frames after bias subtraction. The spikes present in the data are the result of a flashing LED, which was triggered to flash every 60 seconds. The same plot was found for the RP2 channel. . . . .	240
7.10	This is a plot of 1 million TP1 science frames after bias subtraction. The spikes refer to a flashing LED triggered to flash every 60 seconds. The same plot was found for the TP2 channel. . . . .	241
7.11	This is a power spectrum for the first 3 harmonics of the Crab pulsar from the RP1 science frames in Figure 7.9 after bias subtraction. The same plot was found for the RP2 channel. The known frequency of the Crab pulsar is $\sim 29.69$ Hz and it is clear that this is the pulsar. The characteristic increase in power on the $2^{nd}$ harmonic is also evident. Higher harmonics are used data phase folding. . . . .	242
7.12	The same as Figure 7.11 but for the TP1 channel from the bias subtracted data in Figure 7.10. The same plot was found for the RP2 channel. As in the RP1 channel, the frequency of the Crab pulsar was measured to be 29.6969 Hz for the $1^{st}$ harmonic. To achieve more precision higher harmonics are used when phase folding the data. . .	243
7.13	A plot of all phase folded lightcurves for the Crab pulsar from the set of debiased data in Figures 7.8 and 7.7. The data in TP was phase shifted -0.0856. . . . .	244

---

7.14	A plot of the DOLP and Stokes I as a function of phase. The Stokes analysis was performed using the phase folded lightcurves in Figure 7.13. Error bars are plotted. . . . .	245
7.15	A plot of the PA and Stokes I as a function of phase. The expected swing in PA is what is plotted in this figure, however, the range of values is much lower and the mean PA is not what has been produced by the integrated data, or in the literature. Error bars are plotted. . . . .	245
7.16	A plot of the DOCP and Stokes I as a function of phase. The value for this parameter is not known. The measured DOCP by the integrated data is lower than the mean value in this plot, however, it is possible that the DOCP has been measured more accurately as it is not dependent on Q and U, which are used for the DOLP and PA. Error bars are plotted. . . . .	246
7.17	Left column: Stokes parameters Q, U as a vector diagram. Colours refer to the pulse phases as indicated in the input box of upper panel. The scale is such that I = 100 at the maximum light. Phases of the main and inter pulse maxima are indicated with black open squares. Points belonging to the main and inter pulse follow in a counter-clockwise direction on outer and inner ellipses, respectively. Bottom panel shows a zoomed region around the IP phases. The dashed lines indicate the origin of the scaled Q, U coordinates. Any error in background polarisation would correspond to a shift in the origin in this plot. The lower plot shows a zoomed region of the upper panel. Right column: The Crab pulsar position angle as a function of rotational phase. Changes of PA are aligned with the main pulse maximum of the optical light (vertical dot-dashed line), but also with the zero phase, i.e. with the radio phase of the main pulse (vertical solid line). The Crab pulsar polarisation degree as a function of rotational phase (bottom panel). Minimum of p is for the radio phase (vertical solid line), and not for the maximum phase of the optical main pulse (vertical dot-dashed line). The pulse profile (solid line) and DC phase range (dashed region) are indicated also Słowińska et al. (2009). . . . .	248

---

D.1	SPCM-AQR unit used to measure counts from one of the GASP DOAP channels. . . . .	267
D.2	SPCM-AQ4C array unit used to measure counts from one of the GASP DOAP channels. . . . .	268
E.1	iXon Ultra 897 EMCCD detector used to record image data from 2 GASP DOAP channels simultaneously. . . . .	270
E.2	Readout process and EM application for conventional and electron multiplication amplifier. . . . .	271

---

# Abstract

Polarised light from astronomical targets can yield a wealth of information about their source radiation mechanisms, and about the geometry of the scattered light regions. To date, stellar observations have focused, for the most part, on the linearly polarised component of the optical emission. Observations have been restricted due to inadequate instrumentation, and particularly the need for suitable observing conditions and the availability of luminous targets. The motivation in developing the Galway Astronomical Stokes Polarimeter (GASP) makes possible the ability to observe beyond these sources.

GASP is based upon division of amplitude polarimeter (DOAP) (Compain and Drevillon, 1998), which measures the four components of the Stokes vector (I, Q, U and V) simultaneously. This work establishes a suitable optical design that develops GASP as an imaging polarimeter, enabling an acceptable FOV and pixelscale for a 5-m class telescope. It also focuses on two important aspects of using the GASP polarimeter - the calibration of GASP as an imaging polarimeter, and the application of GASP to astronomical targets. The Eigenvalue Calibration Method (ECM) is used to calibrate GASP by reducing systematic errors as a result of calibration optics. It includes all the optical elements of the polarimeter in the output, including the characteristics of the reference ECM samples.

The results of the ECM using GASP as an 8-detector polarimeter give degree of linear polarisation to accuracies of 0.2%, and the polarisation angle is measured to within 0.1°. The ECM was also implemented for GASP using imaging detectors. A number of data analysis methods were explored using image registration techniques; the calibration was performed on a pixel-by-pixel basis. Comparable polarimetric errors, when imaging, were found to those using an 8 detector system, with results of spatial and temporal calibration stability also presented.

---

In November 2012, GASP was allocated observing time on the Hale 200 inch telescope on Palomar Mountain to test the instrument's limitations, and make observations of the Crab pulsar whose linearly polarised emission has been studied extensively. The results of the calibrated data are presented; which were then applied to observational data, performing Stokes reduction and reconstruction of polarimetric information. The results of this observing campaign find the ECM to be a very powerful technique, where GASP was shown to measure observational polarisation accurately, in particular  $\pm 0.1^\circ$  on the PA. The findings of the calibration also show that, when imaging, GASP is sensitive to field position; evidence of this is found in observational results of Zenith flat-field when applying a pixel-by-pixel analysis technique.

Science results of the Crab Pulsar and Nebula are presented. The first set of results produce polarimetric information for the pulsar and Trimble 28 using a set of integrated full frame data. These results are compared to what has been found in the literature. GASP also observed the pulsar at a frame rate  $> 1000$  frames per second in order to perform phase resolved polarimetry. The findings of these results are presented in Chapter 7.

---

# **Declaration**

The work in this thesis is based on research carried out at the Centre for Astronomy, School of Physics, National University of Ireland, Galway. No part of this thesis has been submitted elsewhere for any other degree or qualification and it is all my own work unless referenced to the contrary in the text.

© 2014  
Gillian Kyne  
All Rights Reserved

---

# Acknowledgements

I would like to extend my gratitude to my supervisor Prof. Andy Shearer who gave me this opportunity and provided support throughout my Ph.D. project. I would like to thank Dr. David Lara Saucedo (Cambridge Consultants), Dr. Brendan Sheehan and Dr. Alexander Goncharov for their guidance and patience, and especially to David for his teaching these last 4 years. I would also like especially acknowledge Conor Mc Brierty, Dr. Ollie Ryan, PJ Walsh, and Stuart Harries for all their technical help and expertise in constructing GASP. A special thanks to Tess who was always a source of great help and support. I was fortunate to spend 9 months at the California Institute of Technology last year. I would like to express my gratitude to Prof. Gregg Hallinan who hosted my time there, and all the technical staff who were always willing to lend a hand when needed.

To my fellow students and friends in Physics for the social occasions, tea breaks, and general understanding throughout my time here. There were many difficult times and I would like to extend my appreciation to Ronan, Nav, James, Mike, Susan, Paul, Natalie, and Leon. To the girls, thank you for the many nights out, the trips away, and the fun that kept me going. To Sarah, Sam, Danielle, Mags, Leah, and Sandra.

Finally, I wish to thank my family. To my parents for their constant encouragement that helped me to keep moving forward, and my sisters, Kathryn and Michelle, for being there, and always showing great generosity with their time.

---

# Acronyms & Abbreviations

**AOI**

Angle of Incidence

**APD**

Avalanche Photo-diode

**CCD**

Charge Coupled Device

**DOAP**

Division of Amplitude Polarimeter

**DOCP**

Degree of Circular Polarisation

**DOLP**

Degree of Linear Polarisation

**DOWP**

Division of Wavefront Polarimeter

**ECM**

Eigenvalue Calibration Method

**EMCCD**

Electron Multiplying Charge Coupled Device

**FOV**

Field of View

**FPS**

Frames Per Second

**FWHM**

Full Width at Half Maximum

**GRB**

---

Gamma Ray Burst

**GRP**

Giant Radio Pulse

**HST**

Hubble Space Telescope

**IRAF**

Image Reduction and Analysis Facility

**LED**

Light Emitting Diode

**LP**

Linear Polariser

$M_{\odot}$

Solar Mass

**MM**

Mueller Matrix

**MSP**

Millisecond Pulsar

**PA**

Polarisation (or position) Angle

**PBS**

Polarising Beamsplitter

**PMT**

Photomultiplier Tube

**PSA**

Polarisation State Analyser

**PSF**

Point Spread Function

**PSG**

Polarisation State Generator

**P200**

Palomar (Hale) 200 inch Telescope

**QE**

Quantum Efficiency

---

**QWP**

Quarter-Wave Plate

**RMS**

Root-Mean-Square

**RP**

Reflected Path

**RVM**

Rotating Vector Model

**SNR**

Signal-to-Noise Ratio

**TP**

Transmitted Path

---

# Chapter 1

## Introduction: Astronomical Polarisation & Instrumentation

Optics plays a major role in the engineering of modern astronomy. Every telescope built depends on a precise optical design, and even more so, in the era of extremely large telescopes. There are many areas in which optics is manipulated in astronomy; most astronomical instruments such as photometers, polarimeters or photopolarimeters have been developed using complex optical designs to achieve a desired output.

The word telescope comes from Greek roots meaning ‘far-seeing’. A Dutch spectacle-maker from Middleburg is credited with making the first true refracting telescope in 1608. The use of optics to observe the night sky beyond the human eye happened in 1609 when Galileo constructed a superior version of this telescope to demonstrate the magnifying power of a combination of lenses. Galileo used this optical tool in the discovery of Jupiter’s four major satellites (now known as the ‘Galilean satellites’) demonstrating that bodies other than the Earth might have other objects in orbit around them, supporting the Copernican view of the solar system. Galileo was also able to produce the first maps of the Moon, revealing its rough terrain along the terminator as it passed through different phases. Venus, too, was shown to have phases. Even the Sun was shown to be blemished as spots appeared and moved across its face. Evidence from his drawings suggests that Galileo even saw Neptune in 1613, when it was close to Jupiter, but he failed to observe it for long enough to recognise that it was not a ‘fixed’ star (Murdin, 2001).

Modern reflecting telescopes (reflectors) are the combination of at least two

---

mirrors, one large parabolic primary mirror to gather light, and a hyperbolic secondary mirror which reflects the light back to the detector, or instrument, usually taking care of some of the optical aberrations usually introduced by the primary mirror. There are subcategories of the reflector which include the Gregorian, the Nasmyth, the Newtonian and the Cassegrain telescope. There are many variations within these designs, in terms of choice of focal plane and design mounts, all depending on the science requirement of the telescope and the instruments which will be used.

The primary role of a telescope is to gather light; there are many ways in which this light can be redistributed, and analysed, after the fact. One such tool that provides an abundance of information in astronomy is polarimetry. Far more astrophysical science come from the ability to determine the polarisation state of radiation than intensity alone. At some level, all sources of radiation, whether astronomical or in the laboratory, are polarised. Polarisation is the materialisation of some anisotropy that is identified with the emission mechanism of light or the medium through which it propagates, or both. These range from pulsars (neutron stars), to blazars, which are a class of Active Galactic Nuclei (AGNs), and Quasi-Stellar Objects (QSOs or quasars). Polarisation can be categorised as an intrinsic property, directly from some radiation processes (e.g. cyclotron and synchrotron emission), or extrinsic, from differential absorption of radiation passing through the interstellar medium and most commonly, scattering of radiation. It can also be explained by a simple reflection from a surface, or the Zeeman effect; be it radio waves or gamma rays (Tinbergen, 2003). Another important capability of polarimetry is the measurement of reflected starlight from an exoplanet, and scattered dust clouds or exoplanetary atmospheres. This shows that polarimetry has the capability to be used as a means of detecting extraterrestrial life.

For the most part, astronomical polarimetric observations consist of measuring the linear component of polarisation. Hough (2006) discusses how circular polarisation (CP) can provide many valuable diagnostics. CP is produced when linearly polarised light is scattered; the CP depends not only on the last scatter but also on the previous polarisation state of the radiation. This process usually produces relatively low values of CP (1% or less); but if radiation of any state is scattered from, for example, aligned dust grains, then much higher CP can be produced.

---

Polarimetry has played a very important role in the development of optical astronomy, by furthering our understanding of the nature of the source of emission of light. The polarisation of reflected and emitted optical radiation is highly dependent on material properties and is also influenced by orientation and surface roughness. Measurement of polarisation can therefore be expected to yield additional information about target surface features, shape and configuration without necessarily requiring high spatial resolution, greatly simplifying space optical systems (McMackin et al., 1999). It can also develop our understanding on the nature of radiation sources and on the geometrical and velocity relationship between a radiation source scatterer and observer (Hough, 2005).

Polarimetry, for the most part, uses differential analysis methods and is subject to variations of systematic errors. Polarised signals can be generated by varying atmospheric conditions, optical components, and even detector properties. The advances in observational optical astronomy have been made possible by the use of precision instrumentation. Astronomical polarimetry in instrumentation is an intricate combination of optical design, a suitable choice of detector (depending on the scientific goal), and requires careful instrument design. Many of the points above are taken under consideration in the course of the work of this thesis and will be addressed in greater detail in the design stage chapters. Additional references regarding astronomical polarimetry can be found in Tinbergen (1996a) and Trujillo-Bueno et al. (2002).

## 1.1 What is Polarisation?

The term unpolarised light, or natural light, can sometimes be confusing. It is sometimes understood to mean that there are no polarisation states present; however, natural light is actually comprised of rapidly changing polarisation states. That is to say, all polarisations states are present in unpolarised light. A more technical description is the following: an ordinary light source consists of a very large number of randomly orientated atomic emitters (Hecht, 1987). Each atom radiates a polarised wavetrain for approximately  $10^{-8}$  seconds. All these emissions will combine, as they have the same frequency, and last for  $10^{-8}$  seconds. Therefore, emissions of new wavetrains occur constantly, which results in an overall

unpredictable means of discerning the polarisation of the wave.

Iceland Spar, a variety of calcite, was involved in the official discovery of polarisation in 1669 by Erasmus Bartholinus. He discovered the phenomenon of double refraction when using this material. In 1690 Christiaan Huygens, a Dutch physicist and astronomer, is recognised for the fundamental discovery of polarisation. Huygens's work, entitled '*Traité de la Lumière*', showed that every point on a primary wavefront serves as a source of spherical secondary wavelets. The primary wavefront is therefore an envelope of these wavelets at a later time. He also stated that the secondary wavelets have the same speed and frequency of the primary wave at each point in space. This has since become known as Huygens's Principle.

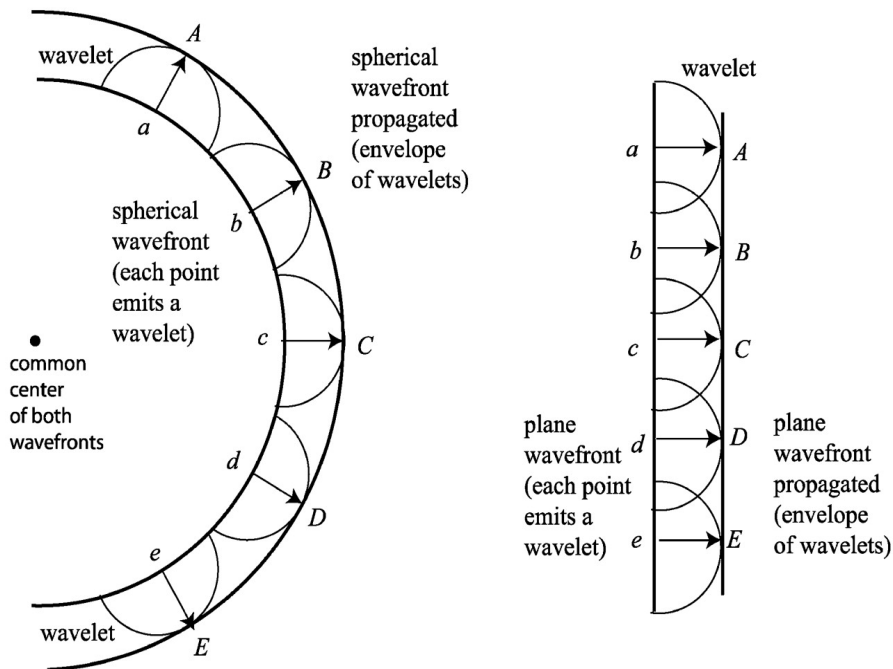


Figure 1.1: Huygens's Principle. The image shows the propagation of a wavefront. Two wavefronts with a common centre. Each point indicated on the first spherical wavefront (*a*, *b*, *c*, etc.) emits wavelets such that  $a \rightarrow A$ ,  $b \rightarrow B$ , etc. The image on the RHS shows how the second wavefront forms from the combination of the secondary wavelets. This is known as an envelope of wavelets (Robinson and Clark, 2006).

Huygens interpreted the double refraction of calcite by applying this principle, that in the crystal, in addition to a primary spherical wave, there is a secondary

ellipsoidal wave. Each of the two rays, arising from refraction by calcite, may be extinguished by passing it through a second crystal of the same material if the latter crystal is rotated about the direction of the ray.

Hecht (1987) describes the term polarisation as the orientation of the vibration of waves under certain conditions. Polarised light simply describes the direction in which light is travelling. Only transverse waves can be polarised as their plane of vibration is perpendicular to the direction in which the wave is travelling.

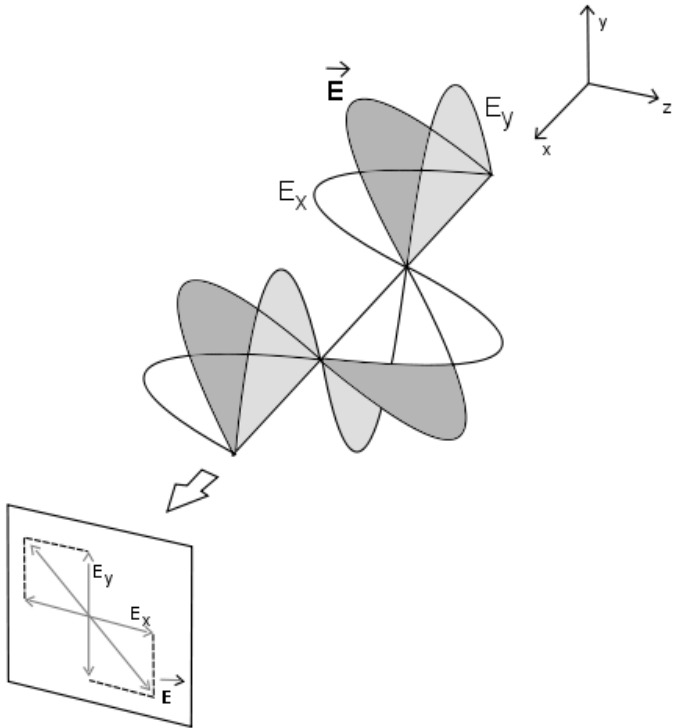


Figure 1.2: Image description of linearly polarised light. The vector  $\tilde{\mathbf{E}}$  is composed of two vectors  $E_x$  and  $E_y$ , giving the wave its overall direction (Hecht, 1987).

Figure 1.2 shows a linearly polarised wave; this describes the shape of vibration of the light as it travels. In general, light is elliptically polarised. Special cases result in linearly polarised light when  $\xi = 0, n\pi$  and circularly polarised light (see Figure 1.3) when  $\xi = \pi/2 \pm n\pi$  and  $E_x = E_y = E_0$ . Namely,  $\xi = -\pi/2$  or any value increased or decreased from  $-\pi/2$  by whole number multiples of  $2\pi$ .

The polarisation state of light can be modified using a device called a quarter-

wave plate (QWP). This is a birefringent, crystalline or polymer material of a specific thickness that changes the state of incoming light, without attenuating, deviating, or displacing the beam. A linearly polarised beam of light, which strikes the plate, will be divided into two rays, called the o-ray (ordinary) and e-ray (extraordinary). These rays are dependent on the two refractive indices of the materials that make up the wave plate. A  $90^\circ$  phase shift is applied to one of the polarised beams, generating elliptically polarised light. Circularly polarised light is generated by adjusting the plane of the incident light so that it makes a  $45^\circ$  angle with the optic axis of the device. Using a wave plate with unpolarised light will not have any impact on its polarisation state and the light will remain unpolarised.

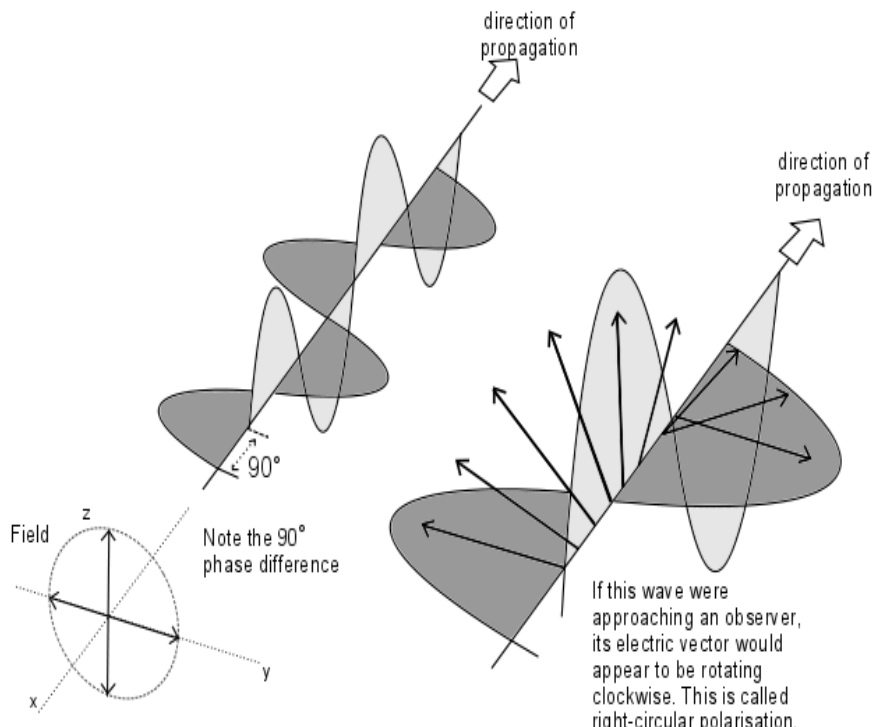


Figure 1.3: Circularly polarised light is a combination of two linearly polarised light waves. If a phase difference of  $90^\circ$  is introduced to the system (one wave lags the other by  $90^\circ$ ), then elliptically polarised light is generated. If there is an azimuthal difference of  $45^\circ$  between the waves, then circularly polarised light is introduced (Hecht, 1987).

---

When the light travelling from the source (i.e. towards the observer) appears to be rotating counter-clockwise, the light is said to be right-circularly polarised. When the light is rotating clockwise then it is called left-circularly polarised light. According to Hecht (1987), the electric field vector makes one complete revolution as the light advances one wavelength away from the source. A linearly polarised wave can be manufactured from two oppositely polarised circular waves (their amplitudes must be equal). It is possible to refer to a lightwave in terms of its specific state of polarisation. Linearly polarised or plane-polarised light is in a P-state, and right- or left-circular light is in the R- or L-state, respectively.

Polarised light can be generated and manipulated by using an optical device known as a polariser. Natural light passes through the device, and depending on the nature of the material, polarised light comes out. The mathematical description of determining whether or not a device can generate polarisation is given by,

$$I(\theta) = I_0 \cos^2 \theta \quad (1.1)$$

where

$$I_0 = \frac{c\epsilon_0}{2} E_0^2 \cos^2 \theta. \quad (1.2)$$

This was first published by Étienne Malus in 1809 and it is known as Malus's Law. Depending on the desired form of the output, there are also circular and elliptical polarisers. Partially reflecting surfaces, such as a window or the surface of a pond, reflect one linearly polarised component of incoming randomly polarised light much more strongly than the others. If a linear polariser is rotated so as to block this reflected linear component, the reflection will be suppressed. This describes one classic use of linear polarisers; to remove reflections.

The mathematical relationship between the polarising angle and the refractive index of the reflective substance was discovered by Sir David Brewster. A special case of this relationship was presented by Brewster where an incoming polarised wave composed of two incoherent orthogonal linearly polarised components, only the component polarised normal to the incident plane and therefore parallel to the surface will be reflected. This angle was known as the polarisation angle or

---

Brewster's angle,  $\theta_p$ . So for a ray moving from a medium of refractive index  $n_i$  to a medium of refractive index  $n_t$  the following is true,

$$\tan \theta_p = \frac{n_t}{n_i}. \quad (1.3)$$

There have been many other contributions to understanding polarisation as it is currently known. Christiaan Huygens and Sir Isaac Newton were both aware of the double refraction phenomenon and later proposed the two-sided nature of light and the effects of polarisation. Later Malus developed his own work in reflection. Augustin Jean Fresnel and Dominique François Jean Arago conducted a series of experiments determining the effect of the interference of light; eventually suggesting that light might be transverse, as a wave on a string. Fresnel's work continued with his famous formulae for the amplitude of reflected and transmitted light.

## 1.2 Measuring Polarisation

Polarised, partially polarised, and unpolarised light can be described by a set of numbers called a Stokes vector. This concept was invented in 1852 by the Irish physicist, and mathematician, G. G. Stokes. It is the simplest method of predicting the result of adding two incoherent beams. It also provides a method of determining the result of how a light beam is affected by the insertion of a polariser or a retarder. The Stokes vector of the emerging beam can be found by multiplying the incident vector by a matrix, known as a Mueller matrix (see Section 5.2), representing the polariser or retarder.

$$\mathbf{S} = \begin{pmatrix} I \\ Q \\ U \\ V \end{pmatrix} \quad (1.4)$$

The operational definition of the Stokes parameters is given by the relationship

$$I = 2I_0 \quad (1.5a)$$

---

$$Q = 2I_1 - 2I_0 \quad (1.5b)$$

$$U = 2I_2 - 2I_0 \quad (1.5c)$$

$$V = 2I_3 - 2I_0 \quad (1.5d)$$

where the values for  $I_0$  -  $I_3$  represent the measured intensities from the polarimeter, depending on the type of polarimeter explained in more detail in Section 1.2.1.

The state of polarisation of light can be produced for experimental need; it can be measured in the laboratory using an instrument called a polarimeter. Most polarimeters contain two basic elements, a modulator and an analyser. The modulator switches Q, U or V at regular intervals leaving I constant. A fixed analyser, or polariser, ensures that the detector measures only intensity (Hough, 2006). An ideal polarimeter should be designed so that it is limited, only, by photon shot noise and should not be sensitive to atmospheric effects and system gain effects.

There exist some various modulators such as photoelastic modulators, Pockels cells and liquid crystals that can be regulated by applying a voltage, and crystal wave plates that are mechanically rotated. Analysers commonly take the form of dual-beam polarising prisms, such as Wollaston prisms, that lead to greater accuracy in measuring polarisation. Simultaneously, analysers image both orthogonal polarisation states on to the detector, providing the most efficient use of the incident light.

Before the charge-coupled device (CCD) detector was brought into use most (single element) optical detectors, used in astronomy, had a very fast frequency response, no readout noise, and the dark current could be made very low by cooling. High frequency response meant there was a use for a large range of modulators. If the modulation rate is higher than 1 kHz atmospheric effects (e.g. scintillation) are mostly eliminated and a simple but efficient polarimeter can be constructed that consists of the modulator, a single beam analyser and a fast detector. It can be noted that a Wollaston prism, i.e. a dual-beam analyser, is not needed to obtain accurate polarimetry; however, including such a device, along with a second detector, provides twice the throughput and the observing time is reduced by a factor of two.

The introduction of the CCD with long integration times (seconds to minutes)

---

was done because of its high quantum efficiency (QE). There are many advantages to using an imaging detector as part of a polarimeter. Depending on the analysis employed, more detail can be observed at a finer resolution than that of a 1D detector system. With the improved technology today, for example EMCCD detectors (electron multiplying), faster readout rates are possible by the detection of weak photon signals that would otherwise be lost within the noise floor of the readout electronics.

### 1.2.1 Stokes Polarimeters

A description of how a Stokes parameter is represented has been described above. A Stokes polarimeter is an instrument which measures light in this form. The information extracted from this light depends on the type of polarimeter, and its limitations. These limitations are due to the polarisation optics used. These optics control the state of polarisation that will be measured, and the modulation rate determine the information that can be deduced from a given state. Polarisation can be measured in a number of ways. Two types of polarimeters that have been in use for some time are the following:

- Polaroid-type polarimeter
- Dual-beam polarimeter

#### 1.2.1.1 Polaroid-Type Polarimeter

A Polaroid-type polarimeter uses a linear polariser, i.e. a polaroid, to measure linear polarisation. The polariser can be used to measure light at  $0^\circ$  to measure Stokes U and  $45^\circ$  to measure Stokes Q. This is a very simple method for measuring polarisation it is, however, not capable of simultaneous measurements, subject to cross-talk and it cuts out half the light entering the system.

To convert a Polaroid polarimeter to a circular polarimeter, a polariser and a quarter-wave plate are used. The same disadvantages are also true for this kind of system.

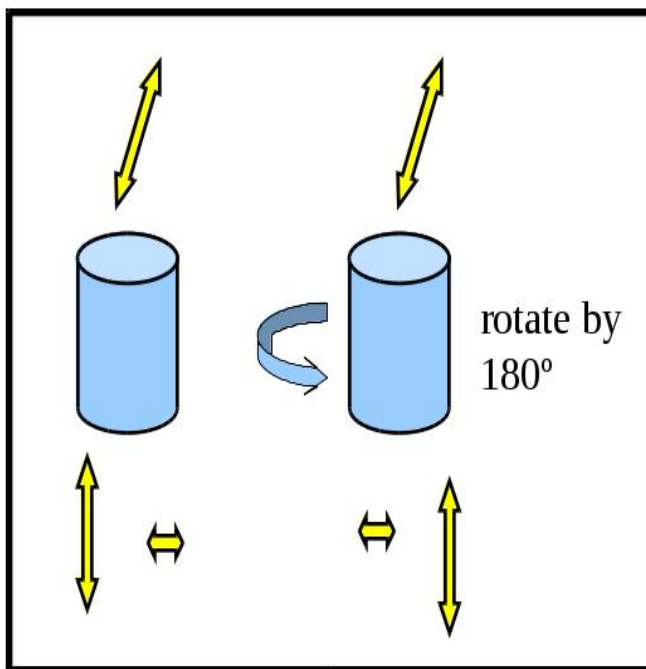


Figure 1.4: A Dual-beam polarimeter can be used to measure orthogonal polarisation signals simultaneously. A birefringent material, such as a Wollaston prism, may be used to split the incident light. This image shows how the dual-beam polarimeter can be rotated by  $180^\circ$  to negate issues such as gain differences, however, a half-wave plate may be used to switch the beams instead (Corbett, 2009).

### 1.2.1.2 Dual-Beam Polarimeter

A dual-beam polarimeter is useful as instead of cutting out one polarisation, and keeping the other, both can be measured simultaneously. This can be achieved by splitting the light with a birefringent material, such as a Wollaston prism. The Wollaston prism then acts as a polarisation analyser. A large enough detector (such as a CCD with a large enough chip) is needed to capture both beams, or 2 detectors, such as PMTs (photon multiplier tubes) or APDs (avalanche photodiodes). Factors such as gain differences become an issue, however, this can be solved by rotating the Wollaston, or adding a half-wave plate (and rotating this instead) to switch the beams and average the polarisation sampling (Corbett, 2009).

Moving on from this design, some polarimeters use crystal wave plates before array detectors were introduced. Slow modulation rates meant that resolving a

---

Stokes parameter ( $Q$ ,  $U$  or  $V$ ) required that each parameter was integrated at two positions of the wave plate. This is because even the slightest atmospheric changes between the two wave plate positions could influence the measured Stokes vector. This problem was overcome easily by using a dual-beam polarising prism so that both orthogonal polarisations were imaged simultaneously by the detector (Tinbergen, 1996b). Since the sum of these two states is the total intensity, any changes in atmospheric transparency can be compensated for in the data reduction. With this method two images are produced on different areas of the detectors that will have very different sensitivities (referred to as gain). These cannot be calibrated better than a few tenths of a per cent, however, by reversing the polarisation states (using a rotated half-wave plate for 1 second exposure) the effects of the different gains can be eliminated, as described above.

### 1.2.2 Polarimetry Techniques

- Division of Time Polarimeter (DOTP) - otherwise known as Time Sequential
  - The most common time of polarimeter
  - Instrument configuration changes between measurements
  - Analogy: filter-wheel camera in spectral imaging
- Amplitude Division
  - Beamsplitter (Wollaston)
- Aperture (wavefront) Division
  - Segmented pupil

The objective of an imaging polarimeter is to retrieve parameters that describe the state of polarisation in every instantaneous field of view (IFOV) of an imaging sensor. Each of the above types can be used as an imaging polarimeter.

An instrument that measures the polarisation state of light:

- A complete polarimeter provides  $I$ ,  $Q$ ,  $U$  and  $V$

- 
- An incomplete polarimeter provides I and Q, and U or less

A complete polarimeter is based on a rotating retarder and a fixed polariser, or a beamsplitter design. In general, polarimeters (for imagers or spectrometers) follow the same basic principle; they are based on a polarisation modulator followed by an analyser, which converts any polarised component into a light intensity that is measured by the detector.

### 1.2.2.1 Aperture (wavefront) Division

A principle has been applied by Collett (1980) to measure all four Stokes parameters simultaneously using a technique called division of wavefront (DOW) of the beam (its cross-section, usually after expansion) into at least four segments, and placing a different stationary analyser in each segment. Photodetectors are placed after these fixed analysers to record signals that determine the four Stokes parameters. The DOW technique is limited by the requirements that the beam be uniformly polarised over its cross-section, that the proportions of the total light flux in different wavefront segments be known, and that the absolute responses of all photodetectors be the same or be calibrated (Azzam, 1982).

### 1.2.2.2 Amplitude Division

In division-of-amplitude photopolarimeter (DOAP), see Figure 1.5, the key element is a beamsplitter divides an incident beam under measurement  $i_{in}$  into reflected (r) and transmitted (t) beams, which are each split again to give  $i_1$ ,  $i_2$ ,  $i_3$ , and  $i_4$ .

Azzam et al. (1988) shows how the intensities are in two orthogonal transverse directions of the reflected and transmitted beams are measured by Wollaston prisms (or any similar polarising elements) WP1 and WP2, which are followed by linear photodetectors whose electrical output signals are measured as  $i_1 - i_4$ .

Compain and Drevillon (1998) explain how DOAP is the most extensively used technique in a large number of applications; it offers a real-time complete measurement of polarisation with neither modulation nor moving parts (Delplancke, 1997). Compain and Drevillon (1998) present a design called the prism DOAP, based on the principle of the DOAP, which can be used in a large spectral range, limited only by the transparency of the materials. The crucial improvement over classical

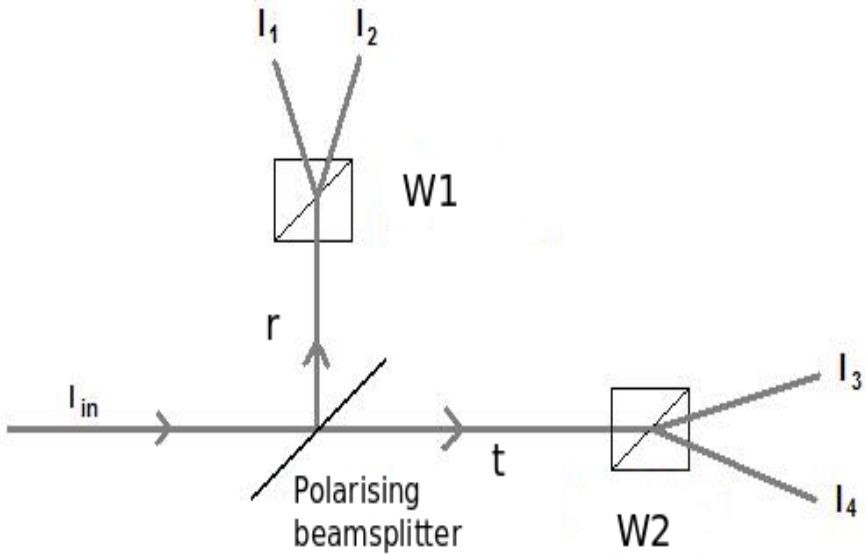


Figure 1.5: The optical layout of a DOAP configuration. The main beamsplitter divides the incoming light into  $r$  and  $t$ , the reflected and transmitted light beams, respectively. The light is then split on each path again by polarising beamsplitters, usually Wollaston prisms indicated by  $W1$  and  $W2$ . This is a general design layout compatible with most telescopes and detector systems (Azzam et al., 1988).

polarimeters, limited to narrower spectroscopic ranges, is obtained by use of only refractive-index contrast effects for splitting the light beam. The demonstrated efficiency of the prism DOAP is characterised by the balance between the intensities of the secondary beams together with close-to-optimal polarimetric properties. This design also pays particular attention to the sensitivity of the polarimeter as a function of the angle of incidence.

### 1.3 Current Instrumentation

Using polarimetric techniques is more widespread now in the fields of solar, stellar and now exoplanetary astronomy. As has been described in previous sections, the polarisation properties of a beam of radiation can be characterised in different ways but rely on four independent quantities, known as a Stokes vector (Landi Degl'Innocenti et al., 2006).

---

Astronomical polarimeters have been developed for many varied science cases, some of which include magnetic field detection, and a measure of magnetic field strength and structure. The sensitivity and time resolution of the polarimeter is dependent on the type of source for which it has been developed. Traditionally, optical polarimetry has focused on objects that exhibit static, or slowly changing polarisation; sources that have well defined periodic behaviour (Collins et al., 2009).

RINGO (optical ring-polarimeter) was developed for the Liverpool Telescope. It was designed for rapid (< 5 minute) follow-up observations of Gamma Ray Bursts (GRBs) to measure early time polarisation (to an accuracy of 0.1%) and its evolution for the first time. The first GRB afterglows were discovered in the X-ray and optical in 1997. According to Steele et al. (2006), measurements of the degree and angle of polarisation in early-time light curves could therefore provide unique information of ejecta geometry and magnetic field strength and structure. Further science with RINGO involves measuring the time evolution of the polarisation properties which would provide the most stringent tests of current jet and internal shock model predictions. RINGO uses a novel ring polarimeter concept, Clarke and Neumayer (2002) based on a principle by Treanor (1968). This rotating Polaroid is used to modulate any polarised flux in the collected radiation. This is followed by co-rotating deviating optics so that each star image is recorded on the CCD chip as a circular pattern. Therefore, the polarisation signal is mapped out around the ring in a  $\sin 2\theta$  pattern (Steele et al., 2010).

The advantages of a device like this include the potential for high-precision measurements using CCDs (flux is spread over many pixels reducing the normal saturation constraints on high-precision photometry). RINGO successfully measured the polarisation of two GRBs. A disadvantage of the RINGO design was overcrowded fields which caused overlap in the rings and issues in data extraction. The speed of the rotation also limited polarimetric accuracy. RINGO2 was developed to improve upon the sensitivity of its predecessor, RINGO, roughly a two order magnitude gain. The following improvements were made:

- Use of an EMCCD detector for rapid readout of the time varying signal no need to convert signal to a spatial ring

- 
- EMCCD provides signal multiplication allowing fast readout with negligible readout noise. Excess sky is removed - improved sensitivity
  - Data can be rebinned on any time scale due to low read noise
  - Trade polarimetric accuracy for time resolution after the event to optimise science data products
  - EMCCD detector fast readout allowed for a faster rotation period of the Polaroid, resulting in improved time resolution

HIPPO is a High-speed Photo-Polarimeter developed by the South African Astronomical Observatory (SAAO) for their 1.9m optical telescope. HIPPO uses rapidly counter-rotating (10 Hz), super achromatic half- and quarter-wave plates, a fixed Glan-Thompson beamsplitter and two photo-multiplier tubes (Potter et al., 2008). The PMTs record the modulated ordinary and extraordinary beams. Each modulated beam gives an independent measurement of the polarisation and therefore simultaneous 2 filter observations. All Stokes parameters are recorded every 0.1 seconds and photometry every 1 millisecond.

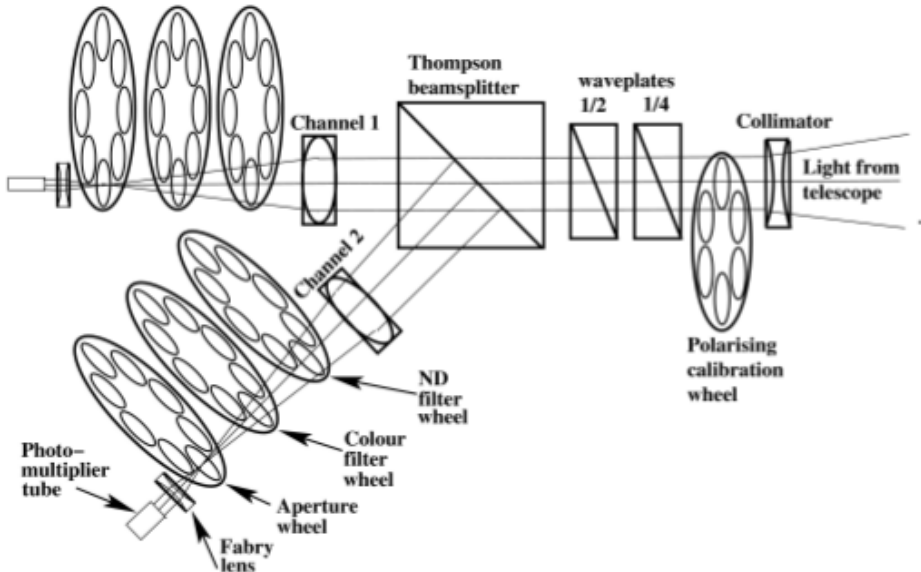


Figure 1.6: A schematic of the optical layout of the HIPPO polarimeter (Potter et al., 2008).

---

HIPPO's purpose is to measure all Stokes parameters (simultaneously), multi-filtered observations of unresolved astronomical sources. It also aims to investigate rapidly varying polarised astronomical sources such as magnetic Cataclysmic Variables (mCVs).

HIPPO is composed of a collimating lens where a polarisation wheel for calibration is placed, followed by half- and quarter-wave plates, see Figure 1.6. The calibration wheel consists of 2 linear polarisers, 1 circular polariser (a linear polariser followed by a quarter-wave plastic retarder), a Lyot depolariser and an open position. HIPPO uses this wheel for calibration and efficiency measurements of the instrument/telescope. A Thompson beamsplitter then produces the ordinary and extraordinary beams. The wave plates are contra-rotated at 10 Hz therefore modulating the extraordinary beams. Modulation is sufficiently rapid that any errors as a result of variable atmospheric conditions or telescope guiding modulations, are reduced. Measurements of all Stokes parameters are made simultaneously from the modulated beams.

The first scientific results from HIPPO shows a dip, once per orbit of one particular mCV. This has been attributed to absorption of emission from the accretion shock by the accretion stream. Stream absorption has been favoured due to photometry and polarimetry not showing very distinct bright and faint phase over orbital cycle. It has also observed the first polarised quasi-periodic oscillation (QPO).

The Optical Pulsar Timing Analyser (OPTIMA), see Figure 1.7 is a high time resolution photopolarimeter (Kanbach et al., 2008). The instrument was primarily designed to study the optical light curves of faint pulsars and other highly variable targets (Słowińska et al., 2009). The instrument consists of 4 main parts: the photon-detectors, the data acquisition unit, the field-view unit and a Twin-Wollaston prism polarimeter. OPTIMA utilises Avalanche Photodiode (APD) modules that are fibre fed to a field-view unit. This unit is used to position the fibres on a target on the sky (Stefanescu et al., 2008). Pointing is achieved through a slanted mirror (where the fibres are mounted) and a CCD detector with a focal reducer.

OPTIMA has different operating modes. These are photometry, polarimetry, and spectrometry. The OPTIMA polarimeter system is an example of a division

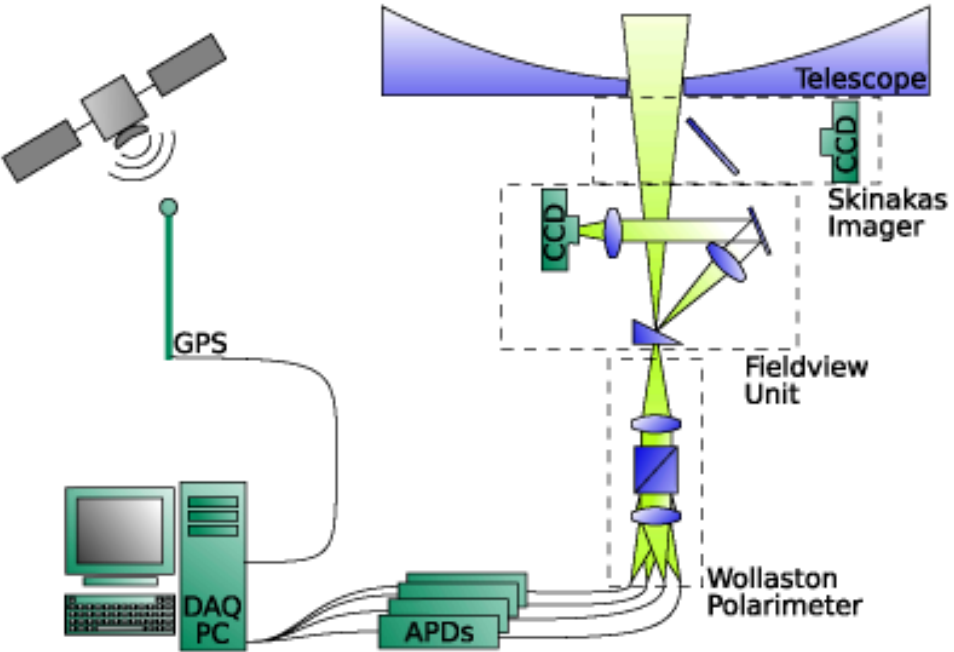


Figure 1.7: Graphical description of the OPTIMA-Burst system. This figure shows the optical path to the polarimeter. For all other apertures, the fibres terminate directly within the slanted mirror in the fieldview unit (Stefanescu et al., 2008).

of time polarimeter (DOTP). For polarimetric observations, OPTIMA is equipped with an aperture-division Twin-Wollaston polarimeter. Collimated light is fed onto the polarimeter by an achromatic lens. Two Wollaston prisms are rotated to one another by  $45^\circ$ . The incident light is split up into the two polarisation projections  $0^\circ$  and  $90^\circ$  by one Wollaston and  $45^\circ$  and  $135^\circ$  by the second. The four beams are re-imaged by four fibres and Stokes I, Q and U are calculated. OPTIMA is also used for very high time resolution observations of the Crab pulsar as a function of pulsar rotational phase.

Solar polarimetry is a growing field and has lead to new insights into a variety of physical phenomena in the solar atmosphere. The Zeeman effect is the splitting of a spectral line into two or more components of slightly different frequency when a light source, or an atom, is placed in a magnetic field. The Zeeman effect has been used in the observation and interpretation of polarisation for a long time. It has also been used as a diagnostic tool for solar magnetism.

---

The technological advances that have been made, regarding imaging detectors in particular, in the last few years have allowed for more detailed analysis of non-magnetic line polarisation caused by scattering in the upper layers of the photosphere and in the chromosphere. This polarisation has a rich spectral structuring due to different physical mechanisms contributing to the linear polarisation that is observed near the solar limb where the observational geometry is favourable to detect the scattered radiation (Gandorfer et al., 2004).

ZIMPOL is the **Zurich Imaging Polarimeter(s)** - ZIMPOL I and II. The ZIMPOL instrument corrects for the two major systematic error sources:

1. Seeing-induced cross talk is avoided by ultrafast polarisation modulation in the tens of kHz range.
2. Noise contributions by the gain table or flat field effects are ruled out by a special CCD sensor that is itself used as part of a synchronous demodulator (Povel, 1995, 2001; Povel et al., 1989, 1994; Gandorfer and Povel, 1997).

The sensitivity of the polarisation analysis is dominated by the shot noise of the collected photoelectrons. Previous versions of the ZIMPOL polarimeter were based on a three phase buried channel silicon CCD, which is front illuminated. This device is sensitive only above 450 nm since the shorter wavelengths are absorbed in the polysilicon electrodes, thus limiting the wavelength region of the second solar spectrum. ZIMPOL takes advantage of the urgent need for a highly sensitive polarimetric system working in this promising part of the solar spectrum.

The problem with CCD imaging at high frame rates (100 Hz range) lies in maintaining a low readout noise at low photon flux and high spatial and/or spectral resolution at the high pixel clock frequency, typically 10 MHz, needed to obtain a high frame rate. Readout noise becomes comparable to the shot noise of the charge accumulated per pixel during one frame period.

ZIMPOL I and, at a later stage, II solves this problem by using masked CCDs. Every second row of the CCD chip of ZIMPOL I is covered by an opaque mask which allows the device to separate the charges generated at two different phases of the modulation. The charges are shifted back and forth vertically, synchronously to the modulation and the frame is read out after integration over many modulation cycles.

---

The advantages of this technique are:

1. Independence of the responsivity of individual pixels - both polarisation states are detected with the same pixel.
2. The combination of fast ( $\geq 1$  kHz) polarisation modulators with CCDs.
3. Integration over many modulation cycles without readout of the frame.
4. Simple and compact set up.

The ZIMPOL I cannot simultaneously detect signals at several frequencies and/or phases, and therefore is sensitive to only one polarisation parameter. The simultaneous measurement of all Stokes parameters has been introduced with ZIMPOL II. The frequency and phase detecting capabilities of the CCD demodulator have been extended by increasing the number of buffer rows. With 3 covered buffer rows and one uncovered row the modulation cycle can be sampled at 4 intervals by vertically shifting the frame synchronously to the modulation. If the modulation pattern is selected appropriately, 4 modulation parameters corresponding to the 4 Stokes parameters can be recorded simultaneously with a single CCD (Stenflo et al., 1992; Gandorfer, 1999a,b).

Seeing induced errors are avoided using a fast polarisation modulation scheme with modulation frequencies in the kHz range. The modulator consists of one photoelastic modulator (PEM) followed by a Glan linear polariser. Circular polarisation is modulated at the mechanical vibration frequency of the modulator. One component of the linear polarisation is modulated and the other component is not. The PEM periodically modulates the incoming polarisation. This polarisation modulation is converted into a periodic intensity modulation via a linear polariser, which acts as an analyser. This configuration does not allow for simultaneous detection of Stokes Q and U, the whole modulator package can be rotated. In this way Stokes I, Q/I and V/I is measured with one setting of the modulator package, while I, U/I and V/I is measured in a second exposure with the modulator package being rotated by  $45^\circ$ . Stokes I and V/I are thus detected in both exposures, while the components of the linear polarisation are detected alternately.

---

Simultaneous detection of the complete Stokes vector in a single CCD exposure is currently not possible in the UV range.

When light is reflected from planetary atmospheres, it is generally polarised. Polarimetry can be used to distinguish the faint signal of the planet from the unpolarised light of the parent star. ZIMPOL has also been used in conjunction with another instrument, a planet finder called SPHERE (Spectro-Polarimetric High contrast Exoplanet REsearch) for measuring these faint signals. The SPHERE/ZIMPOL polarimeter system is another example of how the DOTP technique is used. A fast modulation-demodulation polarimeter has been developed, which combines the high contrast imaging of SPHERE with high-precision polarimetry of ZIMPOL. The SPHERE/ZIMPOL system is optimised for the search of reflected polarised light from old giant planets around nearby stars for wavelengths of 520 - 900 nm. The instrument has many other science capabilities besides exoplanet research. This can be achieved in imaging mode with the diffraction limited resolution of 15 - 20 milliarcseconds provided by the 8.2 m VLT unit telescope and the SPHERE extreme AO system.

## 1.4 Systematic Errors in Polarimetry

Keller (2002) describes astronomical polarimetry as often limited by systematic instrumental errors rather than by statistical errors such as photon and readout noise, in particular in highly sensitive solar observations. The following instrumental errors are commonly encountered in high-precision polarimetry:

- Atmospheric seeing and guiding errors
- Instrumental polarisation due to
  - Telescope and instrument optics
  - Polarised scattered light in telescope and instrument
  - Angle, wavelength and temperature dependence of retarders
  - Crystal aberrations
  - Polarised fringes

- 
- Ghost images
  - Variable sky background
  - Unpolarised scattered light in atmosphere and optics
  - Limited calibration accuracy

Air is not birefringent. This means that seeing does not produce polarisation as such. However, when polarisation measurements are not carried out simultaneously, seeing can introduce spurious polarisation signals because sequentially recorded images will be distorted differently by seeing. The same holds for telescope guiding errors. Therefore, sequential polarisation measurements should be modulated at a frequency that is faster than typical seeing frequencies, which are on the order of a few hundred Hz. According to Keller (2002), to completely avoid this issue, measurements should be carried out simultaneously.

An experiment was carried out by Sen and Kakati to determine instrumental polarisation and depolarisation effects on a 2.3m telescope having beam sizes  $f/3.23$  and  $f/13$  at the prime and Cassegrain foci (Sen and Kakati, 1997). They discovered when polarimetry is conducted for a single point object, the object is normally placed on the telescope's axis (i.e. the field angle for the object is zero). As each unpolarised ray of light falls on the metal coated mirror surface, it is polarised due to oblique incidence. The rays, after being reflected from the primary mirror, also get reflected at the secondary mirror and the polarisation state of the rays gets complicated with a mixture of linear and circular polarisation. However, they also found that if the object is on the axis of the telescope, all the rays are incident on primary parallel to the telescope axis. Thereby, in the case of prime focus or Cassegrain focus, there will be a total circular symmetry for these rays and the net polarisation effect for all the rays considered together will be zero. Thus, the instrumental polarisation will always be zero for an on-axis object point due to the above mechanism.

However, it was also discovered that for an off-axis object point, the field angle will produce some finite value of instrumental polarisation. When the field angle is different from zero the Stokes parameters Q, U and V for the rays for an unpolarised star add up to give a non-zero instrumental polarisation effect.

---

Compared to the other sources of instrumental polarisation, this effect produces polarisation values too small to be detected by any polarimeter. Also, objects are normally not observed off-axis and thereby such effects are normally ignored. As discussed in detail by Serkowski (1974), in polarimetry there are mainly two kinds of errors:

1. The telescope's polarisation uncertainty (or noise) ( $\delta p$ ) in the estimated values of polarisation due to photon count statistics, which is in general  $\sim \delta I/I$  (Sen et al., 1990); where  $\delta I$  is the uncertainty in measured intensity ( $I$ ) and
2. ‘instrumental polarisation’, arising due to the polarimeter optics, is mostly a systematic error. However, such an instrumental polarisation can also arise due to the telescope optics itself.

The ‘instrumental polarisation’ due to the polarimeter can be caused by the chromaticity and incidence angle dependent performance of the optical components (like polarisers, analysers etc.) and also unnecessary reflection from such components (Serkowski, 1974). In addition, errors in polarisation measurements can also be due to the varying sky background.

Sen and Kakati (1997) found that the instrumental polarisation values as calculated at these two focii are 0.000092 and 0.016104% at the field angles 300 and 90 arcseconds, respectively. Furthermore, a 100% polarised star when observed at the above two focii will appear to be 99.9999 and 99.9983% polarised respectively due to depolarisation.

Every piece of glass has some remaining internal stress from the manufacturing process. While these stresses can be minimised by extended annealing periods during the manufacturing there will always be some remaining stress, which introduces birefringence. As a rule of thumb, one should expect about 5 nm of birefringence for every cm of high-quality glass thickness. In the visible, this will lead to a cross-talk of about 1% between V and Q, U for every cm of glass. Apart from these static stresses, there is also temperature-induced stress that leads to a time-dependent birefringence. Temperature gradients in glass lead to stresses due to the varying thermal expansion. The type of glass chosen can often alleviate this problem. For instance, fused silica is 12 times better than BK7 as far as

---

temperature-induced birefringence is concerned. Temperature gradients also introduce optical aberrations because of the temperature dependence of the value for the refractive index. A correlation between birefringence and optical aberrations will lead to different PSFs for different Stokes parameters. This can amount to a few percent for diffraction-limited imaging.

There are various ways to mitigate instrumental polarisation and cross-talk. Keller (2002) discusses some of the more common approaches:

- Avoiding oblique reflections
- Compensating instrumental polarisation and cross-talk with:
  - Retarders
  - Partial polarisers such as tilted glass plates
  - Crossing mirrors at 90°
  - Use two or four mirror arrangements to compensate for a single oblique reflection
- Measure and take into account in data reduction

## 1.5 Polarimetry Techniques at other Wavelengths

According to a paper by McConnell and Ryan (2004), polarimetry is a useful tool for MeV astronomy. The authors describe how it has taken time for this to be accepted due to the fact that it has been experimentally difficult making such measurements and because the levels of polarisation were expected to be quite low. Even at energies (1 - 10 keV), where source fluxes are considerably greater, the astronomical community has been slow to embrace the potential value of polarimetry.

At these energies, there are three physical processes that can be exercised for the sake of measuring linear polarisation. These three processes are: the photoelectric effect, Compton scattering (and its low-energy equivalent, Thomson scattering), and electron-positron pair production. In each case, the by-products of the initial photon interaction have angular distributions that measure as  $\cos^2 \theta$ .

---

A measurement of the angular distribution of these secondaries gives a measure of not only the direction but also the magnitude of the linear polarisation of the incident flux.

McConnell and Ryan (2004) have found that, at energies below approximately 30 keV, either photoelectric or Thomson scattering methods are typically used for polarisation measurements. Polarimeters based on the photoelectric effect have been designed to track the direction of the photo-electron resulting from the absorption of the incident photon. In this case, the photo-electron is most likely emitted parallel to the incident electric field vector.

For energies between roughly 30 keV and several MeV, Compton polarimetry methods are more commonly used. Similar to the case of Thomson scattering, the Compton scattered photons are more likely to scatter at right angles to the incident electric field vector. The magnitude of the modulation of this distribution is maximised for Compton scattering angles near  $90^\circ$ , providing an important constraint for instrument designs.

At higher energies (above approximately 2 MeV), the process of pair production starts to play an increasingly important role in photon interactions. The pair production process is sensitive to the polarisation of the incident photon. For this reason the plane of pair production favours a direction parallel to the incident electric field vector. This aspect of pair production may be utilised for measuring polarisation at higher energies.

## 1.6 Thesis Overview

**Chapter 1** Polarisation is defined with an explanation of terms that will be used in this thesis. The significance of polarisation as a tool in astronomical instrumentation is discussed, including methods and techniques used to measure polarisation. The application of these techniques in current polarimetric instrumentation is discussed in terms of the science objective of the instrument. Polarisation is subject to systematic instrumental errors rather than by statistical errors such as photon and readout noise; a detailed analysis of this is described. Finally, a brief overview of the work of this thesis is presented.

---

**Chapter 2** The first section of this chapter provides an introduction to optical pulsars and their origin, describing how they evolve from supernova explosions. Pulsars are rotating neutron stars and a description of the characteristics of these astronomical sources is reported. This chapter provides a description of the discovery of the pulsar in 1968 in the radio regime, and later in the optical. This leads to the question of how a pulsar works, details of which are better known now in terms of their geometry, magnetic-field strength, magnetosphere properties, and rotation modelling. A classification of pulsars is also described. Observational data and theoretical models provide a basis for pulsar emission mechanisms, spanning across the electromagnetic spectrum. The motivation of this work involves polarisation studies/observations; these are tied in with currently accepted emission models focusing on the high-energy emission. Finally, an overview of optical observations of GRPs is presented, largely the motivation for the construction of GASP.

**Chapter 3** This chapter presents, and develops, the instrumentation involved in the construction of the Galway Astronomical Polarimeter (GASP). It summarises the work of a paper published by Collins et al. (2013) in Experimental Astronomy in 2013 entitled ‘The Galway astronomical Stokes polarimeter: an all Stokes optical polarimeter with ultra-high time resolution’. The GASP Polarisation State Analyser (PSA) was first developed by Collins et al. (2009), however, in order to develop a method of calibration, the PSA was modelled (with some modifications) as a requirement for the work of this thesis. The results of the Monte Carlo noise modelling were produced from the work of this thesis.

**Chapter 4** When work for this thesis began GASP was in the final stages of development as an 8-detector polarimeter using APDs, as a laboratory instrument. An optomechanical description of this is presented, including the obstacles encountered using these detectors. Observation time was awarded to GASP at the Palomar 200 inch telescope (P200), and due to a collaborating group at Caltech, 2 Andor iXon Ultra 897 EMCCDs were loaned to the project. An optical redesign was required in order to use GASP on a 5 m class telescope. This was necessary to correct for a FOV and pixel scale limitation for GASP to operate as an imaging polarimeter. A constraint on project funding meant that it was not

---

possible to obtain new APD detectors, or begin a redesign of the prism rhomb developed by Collins et al. (2009). The final optical design is presented, allowing GASP to continue using the Eigenvalue Calibration Method (ECM) as an imaging instrument.

**Chapter 5** An overview of the difficulties in the calibration of astronomical polarimeters is presented in this chapter. A description of Mueller polarimetry is discussed as this will become the basis in the development of the Eigenvalue Calibration Method for GASP. The implementation of the Polarisation State Generator built for GASP is also discussed. The results section of this chapter are divided into two parts. The first presents a detailed description of how the ECM is applied using Avalanche Photodiodes, where the light is fed to the detectors by optical fibres. This laboratory results demonstrates how well the ECM works and how GASP can be used to measure a polarimetric signal. This result was a bench result and will not be discussed in terms of observational results, but as an analysis of the use of the ECM (described above) for calibrating GASP. The second presents a new technique where the ECM is applied to data using GASP as an imaging polarimeter for data recorded at the 200 inch Hale telescope at Palomar Observatory. Two methods of image registration are discussed, the results of which are described in terms of image residuals. A pixel-by-pixel ECM analysis is performed and the results of each method are compared. A discussion for why the ECM is performed pixel-by-pixel is also presented. The data presented in this chapter provides a calibration result that can be applied to observational results. Finally, conclusions of the calibration results are presented regarding GASP as an 8-detector APD instrument, and a 2-detector imaging instrument.

**Chapter 6** An analysis of a number of polarisation standards are presented in this chapter, including a discussion regarding the instrumental polarisation on this night. This instrumental polarisation will be used to check the polarimetric signal from science targets. A set of data was recorded at twilight with the telescope pointed at the Zenith. These Zenith flat-fields are calibrated (using data in Chapter 5) for the developed analysis methods. One registration method was found to give a reasonable result in calibration, providing a sensible motivation for its application.

---

There are remaining registration errors found in the calibration analysis however, there is a uniform distribution in the polarimetric analysis over the FOV using a pixel-by-pixel analysis method. To reduce any remaining error a method of aperture photometry is also explored.

**Chapter 7** Observational science results of the Crab pulsar are presented in this chapter. A set of integrated data of the Crab Nebula where the pulsar and the nearby star Trimble 28 were imaged. An analysis of the polarimetric signal of each of these targets, and a section of the nebula are explored. A set of phase-resolved polarimetric results are also presented using the Andor iXon Ultra 897 detectors at a frame rate greater than 1000 frames per second. A timing analysis is carried out, including an investigation of the behaviour of the EM gain of these detectors. These polarimetric results are compared to those of the integrated data.

**Chapter 8** Thesis conclusions are presented in this chapter which summarise the work in Chapter 4 and the significance of the optical redesign to the instrument. The concluding remarks of Chapters 5, 6, and 7 are reiterated, summarising the findings of calibration data using 2 different detectors, and the complementary methods of analysis. Comments on observational results are given, showing that if GASP is calibrated it is possible to reproduce polarimetric information. Future instrumentation work and experimentation is presented with a description of improvements to the overall optical design and methods for improving future data analysis.

**Appendices** Analysis methods, polarimetric formulae and mathematical calibration solutions are presented. Specifications are given for the detector types used in obtaining calibration and observational results.

---

# Chapter 2

## Optical Polarisation Studies of Pulsars

### 2.1 Introduction

The first section of this chapter provides an introduction to pulsars and their origin, describing how they evolve from supernova explosions. Following this, a characteristic description of pulsars as rapidly spinning neutron stars whose magnetic-fields produce electromagnetic radiation that sweeps across the surrounding space. Pulsars are primarily observed at radio wavelengths, though some have been found to be radio quiet. Pulsars were discovered in 1968 in the radio regime, and later in the optical. The existence of pulsars had been postulated not long after the discovery of the neutron, and their discovery was made by accident during an unrelated observation project. Leading from this discovery, questions to how they work were theorised. Details of emission and rotation mechanisms are better known now in terms of their geometry, magnetic-field strength, magnetosphere properties, and rotation modelling. A classification of pulsars is also given.

Observational data and theoretical models provide a basis for pulsar emission mechanisms, spanning across the electromagnetic spectrum. A description of the theoretical emission models, that have been developed from observational studies, have given a clearer picture to our general understanding of how a pulsar works, however, a more complete, self-consistent picture of pulsars remains to be established. There has been much work in optical observational studies of pulsars in an

---

effort to further constrain these emission models.

Not long after the discovery of pulsars, the detection of giant radio pulses (GRPs) was reported from the Crab pulsar. It was also reported that these giant pulses are most likely associated with changes in radio emission coherence and that they are superpositions of extremely narrow nanosecond-duration structures. The study of giant radio pulses (GRP), detected from a number of pulsars, offer the possibility to restrict the environment within the radio emission zone and thus inform on the nature of the radio emission and its relationship to the higher energy emission. In contrast ‘normal’ pulsar activity results in regular, repeating periodic lightcurve signals, the giant pulses occur at random intervals and have energies up to many thousands of the mean energy. The motivation of the work of this thesis involves polarisation studies/observations; these are tied in with currently accepted emission models focusing on the high-energy emission. A polarimetric signal from a GRP, comparable to that of the current optical observations, would provide further insight into the geometry pulsars. It is the unique ability of GASP that would allow the study of the polarisation of individual pulses, and with joint radio studies help constrain emission mechanisms, which relate the optical and radio emission.

GRP detections would also enable studies of galactic pulsar populations, and the use of the pulses to probe the interstellar medium (ISM) in those galaxies as well as the intervening intergalactic medium. The Crab pulsar can serve as a prototype of intense, coherent emission from other classes of high-energy objects, which may share a similar physical configuration, namely a collimated flow of relativistic particles. The Crab pulsar could also signify the presence of other source classes in the transient radio universe that could be targets for proposed wide-field telescopes such as the Low-Frequency Array (LOFAR) and the Square Kilometre Array (SKA).

## 2.2 What is a pulsar?

Pulsars are rapidly spinning neutron stars whose strong magnetic-fields produce conal beams of electromagnetic radiation that sweeps out into the surrounding space with each rotation of the star, producing the eponymous pulses that are

---

observed primarily at radio wavelengths. Pulsars are very useful astrophysical probes. A pulsar emits a sharp radio pulse, which is delayed and broadened during its propagation through the dispersive, turbulent interstellar medium, in a way that depends on the frequency and polarisation of the signal as well as the properties of the medium. Multi-frequency studies of pulsar signals can be used to map the distribution and turbulence structure of ionized material in the Galaxy, as well as the average Galactic magnetic-field.

Pulsars are studied because neutron stars are intrinsically interesting astronomical objects, but also because the study of pulsars is deeply intertwined with many different branches of both astronomy and physics. Neutron stars (NS) are small, compact stars with densities comparable to that inside nuclei,  $\rho_0 = 2.8 \times 10^{14} \text{ g cm}^{-3}$ , and radii  $R \simeq 10 - 15 \text{ km}$ . They consist predominantly of neutrons and a few percent of protons and electrons. These huge neutron-rich ‘nuclei’ are bound by gravitation and require a minimum mass of  $\sim 0.1 M_\odot$ . Above a maximum (Chandrasekhar) mass of order  $2 - 3 M_\odot$  neutron stars are unstable towards gravitational collapse to black holes.

Neutron stars are formed from type II or Ib supernova explosions. This is when massive stars ( $M \geq 10 M_\odot$ ) run out of nuclear fuel which was burning for millions of years. When the iron core in the centre of the ageing stars exceeds its Chandrasekhar mass,  $\sim 1.5 M_\odot$ , the star undergoes gravitational collapse in just seconds and suffers violent death. Gravitational and kinetic energy of the order  $\sim 10^{53} \text{ ergs}$  is released mainly by neutrino emission that blows off the outer layers. Only  $\sim 1\%$  of the energy is actually seen in a brilliant burst called a supernova. Supernova explosions occur at a rate of one to three per century in our Galaxy. Historically, the Crab supernova was first recorded by the Chinese in 1054 AD, and was so brilliant, it could be seen in daylight.

The discovery in 1967 of a rotating neutron star (a radio pulsar) in the Crab Nebula supernova remnant confirmed the 1933 hypothesis of Baade and Zwicky, formulated a year after Chadwick discovered the neutron, that neutron stars are formed in supernova explosions. Not long before the discovery of pulsars, Franco Pacini had predicted that rotating, highly magnetised neutron stars were a potential source of electromagnetic radiation. In our Galaxy a large abundance,  $\sim 10^8$ , of neutron stars is expected but they only manifest themselves if powered by

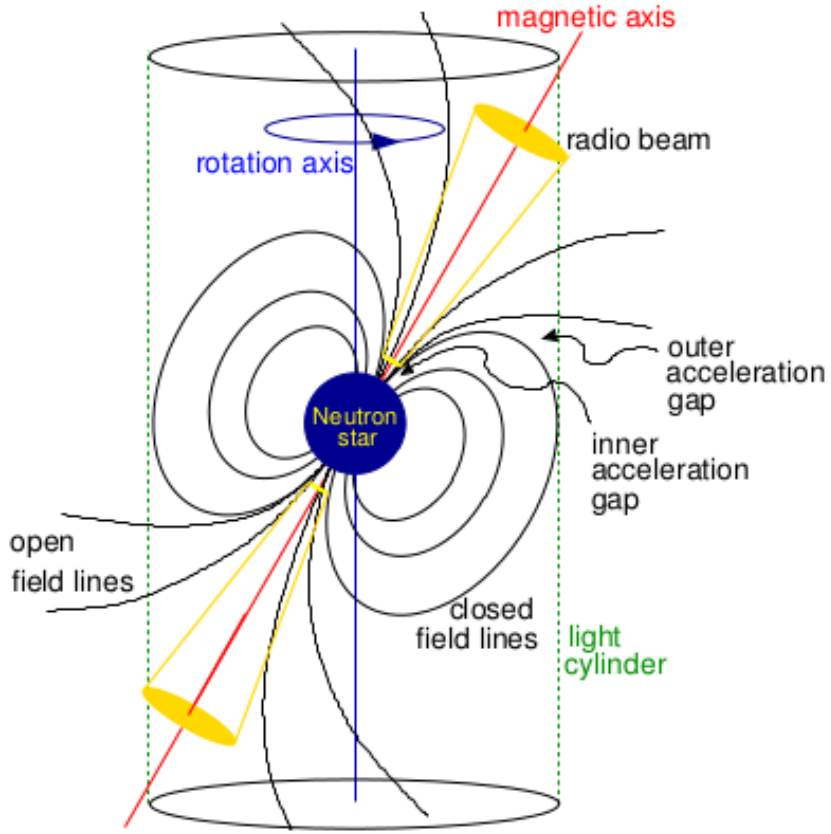


Figure 2.1: A model for a rotating neutron star from the *Handbook of Pulsar Astronomy*. The figure includes the NS magnetosphere - not drawn to scale - (Lorimer and Kramer, 2004).

rotation, accretion, nuclear power or residual heat (Murdin, 2001).

Pulsars are useful astrophysical laboratories, and are enigmatic tools for probing the pulsar emission mechanism. Despite over thirty years of observation, the emission mechanism of pulsars is still a matter of debate. A general consensus exists - the luminosity is rotation powered, the pulsed radio signal is coherent in origin, and it is expected that the optical emission is in the form of synchrotron radiation, whilst in the hard-X and  $\gamma$ -ray it becomes curvature radiation. It is generally accepted that the local electron density is determined to first order by the Goldreich-Julian current that flows from the polar-cap region of the neutron star (where the last open field lines cross the neutron star surface). What is not

---

agreed on is the mechanism that accelerates the electrons to the energy required for synchrotron and curvature radiation, where this acceleration takes place, and what type of coherent mechanism maintains and creates the radio emission.

## 2.3 Pulsar Discovery

The Austrian-born astrophysicist Thomas Gold, described the basic picture and arguments for believing that pulsars are spinning magnetic neutron stars over 40 years ago. He was mostly correct, and since his time many of the details of his picture have been updated. However, a fully self-consistent picture of pulsars remains to be ascertained, in spite of efforts by a substantial number of astronomers. Such a self-consistent and complete picture is very difficult to formulate. In 1934, only two years after the discovery of the neutron, the existence of neutron stars was proposed by astrophysicists, Baade and Zwicky. They proposed that neutron stars form from supernova explosions with a diameter of  $\sim 10$  km. Pacini proposed that the Crab Nebula was powered by such a star, which was highly magnetised, rotating and emitting electromagnetic radiation.

In 1967 a Cambridge University graduate student, Jocelyn Bell Burnell, working under the supervision of her thesis supervisor, Anthony Hewish, discovered the pulsar (Hewish et al., 1968). The discovery came about from a project developed by Hewish, Bell and their collaborators, where they designed and built a new telescope near Cambridge in order to study the rapid scintillation, or twinkling, of radio signals from quasars as they propagated through the solar wind. Bell noticed some unusual ‘scruff’ in the data, from a direction well away from the Sun, that recurred on several nights at a fixed sidereal time. Follow-up observations showed that the signal had the form of a series of short radio pulses, repeated every 1.337 s. The extreme regularity of the pulsations led to many theories. Terrestrial interference was dismissed as a possible source, as was the possibility of an artificial extraterrestrial origin.

Bell’s quick discovery of three more pulsating radio sources demonstrated that they must arise from some natural source. The distance for the source was estimated to be of order 65 pc, which would place the object far beyond the solar system. The rapid variability of the signal required a source that was much

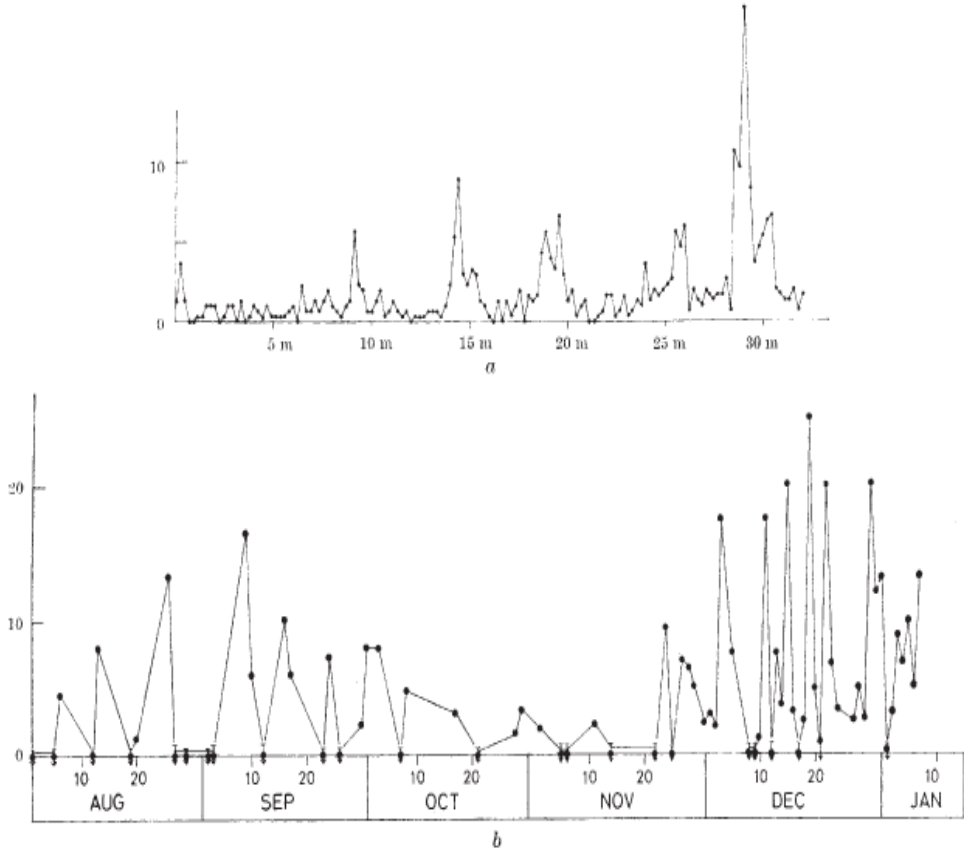


Figure 2.2: This figure displays the results of the findings of Hewish et al. (1968). The top plot (a) is the time variation of the smoothed pulse amplitude, over 10 pulses. The bottom plot (b) is the daily variation of peak pulse amplitude in units of  $\text{W m}^{-2} \text{ Hz}^{-1} \times 10^{26}$ .

smaller than a light-second across: Smaller, that is, than an ordinary star. The group coined the name pulsar - ‘pulsating star’. It preserves the original model put forth by Hewish and his collaborators in which the pulses were produced by radial oscillations of a white dwarf or neutron star. Models involving rotation rather than pulsation were, however, strongly favoured by observations that the pulsation periods were gradually lengthening.

In 1974 Hewish was awarded the Nobel Prize in Physics for his ‘decisive role in the discovery of pulsars’ and his pioneering work in radio astronomy. Bell’s key role in the discovery has also been widely recognised.

---

Optical observations of pulsars began soon after their discovery, with B1919+21 being the first observed in search for its optical counterpart by Ryle and Bailey (1968). Not long after came the identification of the Crab pulsar through the detection of optical pulsations discovered by Cocke et al. (1969). It was found that the time averaged optical flux was the equivalent of a 17.7 magnitude star. They present phase-averaged data showing the main (MP) and inter (IP) pulse in amplitude and position. The short rise and fall times of the main pulse ( $\sim 1.5$  ms), lead the authors to conclude that it implied stringent conditions for a beaming mechanism to explain the pulses.

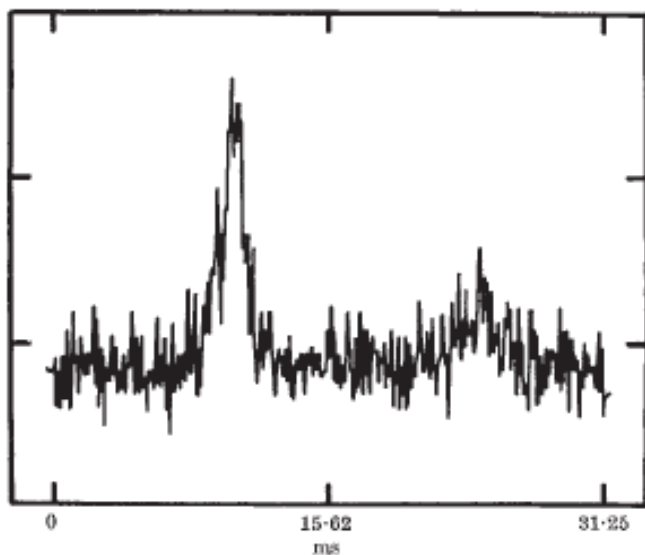


Figure 2.3: A pulse measured from the Crab pulsar by Cocke et al. (1969) using the Steward Observatory 36 inch f/5 reflecting telescope and a 1P21 photomultiplier. The pulsations were observed on a cathode ray tube, which added successive cycles in phase. The optical pulses were observed to have a geocentric period of 0.033095 seconds, which agreed well with the radio.

Since the Crab pulsar optical discovery, Smith et al. (1988) and Kanbach et al. (2005) have presented accurate optical phase-resolved polarisation measurements of this source. These results have shown the phase dependence of the degree of polarisation, with a maximum of  $\sim 50\%$  in the bridge between the main and the inter pulse (Mignani et al., 2007b). Optical polarisation measurements are extremely useful in providing observational constraints to test the different models

---

proposed describing magnetospheric activity of pulsars.

14 other pulsars have been found to pulse optically and, in the interest of this thesis, the optical polarisation signal from 5 of these has been measured. These are far less luminous compared to the Crab pulsar therefore, observations of this nature are not possible due to the currently available technology, and will be discussed in Section 2.8.

Although the application of the general theory of relativity to astronomical problems has a long and venerable history dating back to Einstein himself, it was not until the discovery of pulsars in the 1960s that a great deal of interest was directed toward the impact of the theory on stellar structure. The pioneering theoretical work was done 30 years earlier and can be traced back to Landau in 1932. The fundamental work of Oppenheimer and Volkoff (1939) and Oppenheimer and Snyder (1939), including collaborators, still provides the fundamental basis for most models requiring general relativity for their representation. However, it was the discovery of the existence of neutron stars, and that they were most likely the result of the dynamical collapse of a supernova, that led to the construction of modern models that represent the contemporary view of these objects.

Radio pulsars are born in the supernova explosions that accompany the collapse of massive stars. Pulsars are born rotating at up to about 100 times per second. The pulsar is powered by this stored rotational kinetic energy, so like a spinning top, the pulsar gradually slows reaching spin periods of about a second within a few million years. When the pulsar is, approximately, 100 million years, it is spinning too slowly to maintain its radio emission, and it fades from view. Some old pulsars, with binary companions, can be ‘recycled’, or spun back up to fast rotation periods by mass transfer from their companions. Because the resulting ‘millisecond pulsars’ have relatively low magnetic-field strengths and hence low energy loss rates, they can continue to spin rapidly for times that are long compared with the age of the galaxy (Murdin, 2001).

---

## 2.4 Pulsar Classification

### 2.4.1 Rotation-Powered Pulsars

Neutron stars that are spinning down as a result of torques from magnetic dipole radiation and particle emission are known as rotation-powered pulsars (RPPs) (Harding, 2013). The energy from the spin-down of these sources appears as broadband pulsations from radio to  $\gamma$ -ray wavelengths. This energy also appears as a wind of energetic particles flowing into their surrounding pulsar wind nebulae. More than 2000 radio pulsars are now known, since the discovery of RRP in 1967 (Hewish et al., 1968), with periods ranging from a few ms to several seconds (Manchester et al., 2005). X-ray,  $\gamma$ -ray and optical pulsations were soon discovered in a few of these pulsars by folding the time series obtained at these wavelengths at the radio periods. At present, there are over 100 RPP detected at X-ray energies and over 130  $\gamma$ -ray pulsars (Abdo, 2013); most were discovered using known radio ephemerides, but many were also discovered through their X-ray or  $\gamma$ -ray pulsations and are radio quiet. A term associated with RPPs is spin-down, and is related to the pulsar period by the period derivative. The spin-down of RPPs is typically a smooth process but it has been observed that the pulsar can occasionally undergo sudden changes in spin called ‘glitches’ and then recover to a normal spin-down rate.

There are two main populations of RPPs, normal pulsars with characteristic ages  $\tau = P/2\dot{P} < 100$  Myr, and millisecond pulsars (MSP) with  $\tau \leq 100$  Myr. The periods of the normal pulsars are thought to have increased at a steady rate from their birth periods at the time of supernova core collapse. However, the birth periods of RPPs are not well known, and inferences of the period range from tens of ms to hundreds of seconds (Halpern and Gotthelf, 2010; Kaspi et al., 2006).

MSPs are thought to have originally been members of the normal RPP population, spun down for tens of Myr and then spun up by accretion from a binary companion (Alpar et al., 1982). MSPs make up about 10% of the RPP population and about 80% of them are in binary systems. They are extremely good clocks since they rarely glitch, they have very little of the timing noise seen in young RPPs, and their spin-down is very stable. These characteristics make them po-

---

tentially valuable sources for use in celestial navigation (Coll and Tarantola, 2009) and gravitational wave detection (Hobbs et al., 2010a).

RPPs can be described quite well by the rotating dipole model. It gives estimates of their main electrodynamic properties. The Poynting flux of a rotating dipole in vacuum gives an estimate of the spin-down power. This will be described in more detail later.

Many RPPs (over 100 at present) also show X-ray emission, with pulsations detected in many of these. According to Kaspi et al. (2006), this emission is usually made up of two components: Non-thermal emission that is probably magnetospheric, and 0.05 - 0.1 keV thermal emission from surface cooling or heated polar-caps. Some, like the Crab pulsar, show only non-thermal X-ray emission, but in these cases the thermal components are probably buried under the strong non-thermal emission. The thermal and non-thermal peaks in the pulse profiles are usually not in phase, but the non-thermal peaks are sometimes in phase with one or two  $\gamma$ -ray peaks. In the youngest RPPs, emission from cooling of the NS surface is thought to dominate the thermal radiation.

#### 2.4.2 Binary & Millisecond Pulsars

MSPs make up about 10% of the RPP population and about 80% of them are in binary systems (Harding, 2013). Most of these pulsars are clustered in the lower left of Figure 2.4, with shorter pulse periods, larger characteristic ages, and lower magnetic-fields than the general pulsar population. Only a small number of ordinary pulsars have binary companions. Even though most pulsar progenitors originated in binaries, the majority of these binaries were not bound, gravitationally, by the mass loss associated with supernova explosions, leaving the pulsars isolated (Murdin, 2001).

Millisecond pulsars have, expectedly, shown the behaviour associated with RPPs, however, since these sources are too old to have emission that can be detected from cooling, the thermal components, some of which are multiple black-bodies, must be due to polar-cap heating (this will be explained further in Section 2.6). The non-thermal emission is in most models due to synchrotron radiation from electron-positron pairs, either from the polar-cap or the outer-gap, emitting

---

at high altitude (Harding et al., 2008; Hirotani, 2006). The non-cooling thermal emission could come from polar-caps heated by high-energy particles flowing toward the NS from the polar-cap (Harding and Muslimov, 2001) or outer-gap (Halpern and Ruderman, 1993) accelerators.

## Recycling

Usually, the more massive component of a binary star system will evolve most rapidly. If the star is above  $\sim 8 M_{\odot}$  this will result in a supernova explosion. However, if the binary remains bound, the system may appear as a young pulsar with a main sequence companion. The second star will finish core hydrogen burning and move off the main sequence, gradually swelling. If the binary is sufficiently wide, the companion will continue its evolution as if it were an isolated star. In the case where the binary is sufficiently compact, the surface of the companion will eventually come into contact with its Roche surface and begin transferring mass (and angular momentum) to the neutron star, spinning it up to shorter rotation periods. During this stage, the system will be visible as a luminous X-ray binary. The fate of the system depends on the mass of the companion.

A massive companion evolves quickly, and will explode as a supernova after a relatively short mass transfer period (as a high-mass X-ray binary). The result will be a pulsar with a spin period of 30 - 50 ms, with a neutron star companion or no companion at all if the system becomes unbound. A light companion will evolve slowly, with a long mass transfer period (as a low-mass X-ray binary), leaving a pulsar with period 1 - 10 ms and a light, helium white dwarf companion. An intermediate mass companion will leave a pulsar with intermediate spin period and a massive, carbon-oxygen white dwarf companion.

The magnetic-fields of these ‘recycled’ pulsars have been observed to be smaller than those of young pulsars. The resulting torques are also, very small. Therefore, recycled pulsars can spin down much more slowly than ordinary pulsars and remain active for billions or even tens of billions of years (Murdin, 2001).

---

### 2.4.3 Accretion-Powered Pulsars

Accretion-powered pulsars account for most, but not all, X-ray pulsars where the gravitational potential energy of accreted matter is the power source (producing X-rays that are observable from the Earth). Harding (2013) explains how a neutron star in a binary system can pull matter from a companion star creating an accretion disk and an associated jet. This can be achieved through stellar winds or from an accretion disk that forms if the companion star overflows its Roche Lobe. The gravitational energy as a result of the infalling matter provides part of the energy for the observed radiation. The torques created due to the accretion also dominate the spin evolution. Accreting neutron stars display a wide variety of behaviours, depending on the NS magnetic-field strength, mass of the companion and properties of the accretion. The following is a description of types of accreting systems:

Low-Mass X-ray Binaries (LMXBs) is a type of binary system in which one member is a NS (or black hole) and the other, companion star, is a low-mass main sequence star, white dwarf or red giant that fills its Roche Lobe, transferring matter onto the compact object (Abdo, 2013) through an accretion disk. Most of the radiation is emitted as X-rays with  $\sim 1\%$  in the optical spectrum. NSs in LMXBs are thought to be old, have weak magnetic-fields ( $\sim 10^8$  G) and are spun up by torques from the accretion disk. One explanation for their very weak fields is that the accretion has reduced or submerged the magnetic flux (Cumming et al., 2001; Romani, 1993; Ruderman, 2005).

The NS and companion will reach an equilibrium where the pressure of the NS magnetic-field balances the pressure of the accretion flow. This end point will depend on the accretion rate  $\dot{M}$ , however, after 1 Myr the NS period will have reached an equilibrium period  $P_{eq}$ . The value of  $P_{eq}$  depends on the NS field and  $\dot{M}$ .

Binary systems containing a neutron star or black hole and high-mass O or B star ( $M \geq 5 M_\odot$ ) are known as High-Mass X-Ray Binaries (HMXB). In HMXB, in general, the NS orbits a Be star in a very eccentric orbit. Accretion occurs occasionally in outbursts when the NS crosses a disk of material surrounding the Be star. An example of a Be X-ray binary is A0535+26. A donor star with an

---

intermediate-mass star ( $1.0 \text{ M}_\odot \leq M \leq 5 \text{ M}_\odot$ ), will result in an intermediate-mass X-ray binary (IMXB) (Podsiadlowski et al., 2002), an example of this being Her X-1.

In HMXBs, the compact object accretes material from the wind of the companion star or from a Be star disk, while in IMXBs the NS accretes from a disk as in LMXBs. Both of these classes, numbering about several hundred, are bright X-ray sources, and a large number show either persistent or transient X-ray pulsations (in the case of Be star binaries) (Harding, 2013).

#### 2.4.4 Magnetars

Magnetars were first known as Anomalous X-Ray Pulsars (AXPs) before this became a magnetar subclass along with Soft Gamma-Ray Repeaters (SGRs). A magnetar, or ‘magnetic star’, is a neutron star where the greatest source of energy generated is that of the magnetic-field, including rotation. This implies a magnetic field strength of  $10^{14} - 10^{16}$  G, making magnetars the objects with the most intense magnetic-fields known (Murdin, 2001). Their locations and possible associations with supernova remnants suggest that they are neutron stars. There are three known to be in our Galaxy and a fourth in the Large Magellanic Cloud (LMC).

AXPs and SGRs were thought for many years to be separate and unrelated objects. SGRs were first detected around 1979 as  $\gamma$ -ray transients and were thought to be a type of classical  $\gamma$ -ray burst. They undergo repeated bursts with several tenths of second duration and average energy  $10^{40} - 10^{41}$  erg, and their bursting often occurs in episodes spaced years apart.

SGRs and AXPs are both neutron stars possessing magnetic-fields of exceptional strength, that show both steady X-ray pulsations as well as soft  $\gamma$ -ray bursts. A power source much greater than magnetic dipole spin-down, which powers RPPs, is required for these objects. This is due to an inferred steady X-ray luminosity, which is about 100 times higher than their spin-down luminosity.

The magnetar model postulates that the energy source for all of these outbursts is an intense magnetic-field, which stresses the neutron star crust and causes it to crack, exciting Alfén waves and energising electrons in the neutron star magnetosphere. There is experimental evidence for the existence for these excessive

---

magnetic-fields from observations of the spin-down of the SGRs, deduced from the low-energy X-rays (Kouveliotou et al., 1998). The interpretation of these observations is that, similar to the radio pulsars, the neutron star is losing energy by dipole radiation from its magnetic-field. Small cracks explain the frequent, less intense bursts, while global cracking and magnetic-field reconnection are responsible for the giant bursts. New high-energy components discovered in the spectra of a number of AXPs and SGRs require non-thermal particle acceleration and look very similar to high-energy spectral components of young rotation-powered pulsars (den Hartog et al., 2008). The periods are in the range 5 - 8 s and, in the magnetar model, are explained by the presence of hot spots on the neutron star surface, with magnetic-field dissipation and neutron star crustal stress as the heating source.

## 2.5 Pulsar Phenomenology

As the neutron star spins, charged particles are accelerated from the surface of the star along magnetic-field lines in the magnetosphere. This acceleration causes the particles to emit electromagnetic radiation, which is more readily detected at radio frequencies as a sequence of observed pulses produced as the magnetic axis, and hence the radiation beam, crosses the observer's line of sight for every rotation. Pacini (1968) and Gold (1968) correctly predicted that the pulse period of a neutron star should gradually increase as the outgoing radiation carries away the rotational kinetic energy. Gold also showed that a rotating neutron star with a large magnetic-field is the dominant energy supply from studies of the pulsar in the Crab nebula (Lorimer, 1998).

### 2.5.1 Structure

The average mass density of a neutron star is  $6.7 \times 10^{14} \text{ g cm}^{-3}$ , which is even larger than the density of nuclear matter which is  $\sim 2.7 \times 10^{14} \text{ g cm}^{-3}$ . Near the surface the solid crystalline crust consists of mainly iron nuclei and a sea of degenerate electrons,  $\rho \simeq 10^6 \text{ g cm}^{-3}$ . When going further inward, the density increases to a point at which protons and electrons combine to form neutrons, creating the neutron-rich nuclei of the inner crust. Passing the *neutron drip point*

---

at  $\rho \simeq 10^{11}$  g cm $^{-3}$ , several hundred metres below the surface, the number of neutrons released from the nuclei will increase rapidly. After the crust dissolves fully at  $\rho \simeq 2 \times 10^{14}$  g cm $^{-3}$ , the largest fraction of the neutron star is made up of a ‘sea’ of free, superfluid neutrons, mixed with about 5% superconducting electrons and protons.

A neutron star is not a uniform sphere. Glitches in the rotation of young pulsars have been observed and these indicate a solid crust. These glitches (and their recovery) strongly indicate the existence of a fluid component inside the solid outer crust of the neutron star. Glitches can be explained as a result of star quakes where abrupt changes in the oblateness of the neutron star crust cause a change in the moment of inertia and hence the spin frequency as angular momentum is conserved. This has been observed for the Crab pulsar (Lyne, 1992). Observational studies have shown that these glitches are related to timing irregularities in residuals of pulsar timing models. This will be discussed further in Section 2.7.

### 2.5.2 Magnetic Fields & Pulsar Age

Observational estimates of magnetic-fields of neutron stars fall into the range  $10^{10-12}$  G, and come from the detection of cyclotron radiation features in spectra of X-ray binaries. A useful method of demonstrating the distinctions between ages and magnetic-field strengths of sub-classes of pulsars is the  $P - \dot{P}$  diagram, see Figure 2.4.

Figure 2.4 is a logarithmic scatter plot of non-accreting NS for their observed pulse period versus their period derivative. The majority of the objects in the top right corner of the diagram show normal pulsars, while the lower left section of the diagram is mainly occupied by millisecond pulsars (explained in Section 2.4.2). The radio pulsars occupy the largest region with their population extending from the very short period, low  $\dot{P}$  to the high  $\dot{P}$ , high magnetic-field pulsars that border the magnetar range. The characteristic age of a radio pulsar is given by Equation 2.1 for a braking index  $n = 3$ . This is an approximate measure for the pulsar’s true age and the corrected formula is found in Equation 2.2 which takes into account the braking index,  $n$ , of the pulsar.

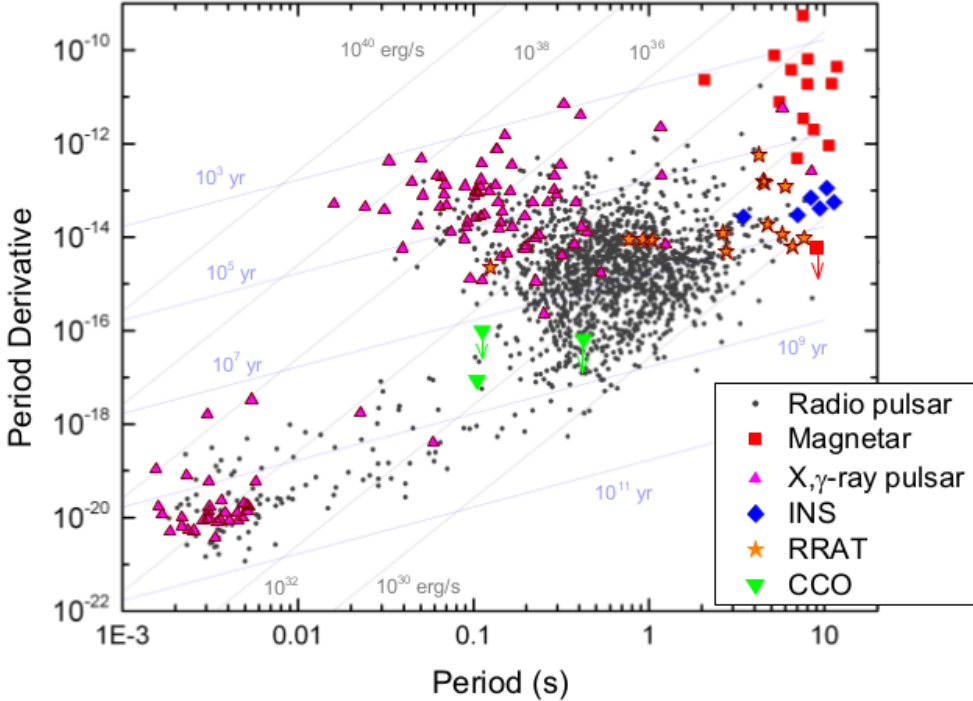


Figure 2.4: A plot of period vs. period derivative for the currently known rotation-powered pulsars (RPPs), Isolated Neutron Stars (INS), Compact Central Objects (CCO), Rotating Radio Transients (RRATs) and magnetars (Harding, 2013).

$$\tau = \frac{P}{2\dot{P}} \quad (2.1)$$

$$\tau = \frac{P}{(n-1)\dot{P}} - \frac{P_0}{(n-1)\dot{P}_0}, \quad (2.2)$$

where  $P_0$  and  $\dot{P}_0$  are the initial spin period and derivative, respectively.

In the determination of characteristic pulsar age, timing observations pulsars have been less accurate than estimated ages of the remnant e.g. PSR 1509-58 (van den Bergh and Kamper, 1984) where the timing age is found to be  $\sim 1500$  yr and the estimated age is  $10^4$ . A possible explanation for this discrepancy is that the magnetic-field grew from a small value within the last  $10^3$  years. If pulsars were rotating dipoles, the slow-down rate would be proportional to the cube of the rotational frequency. This is called the braking index and it has a theoretical

---

value of 3, which disagrees with most pulsars. In the case of the Crab pulsar, and PSR 1509-58, Blandford and Romani (1988) discusses how the two deceleration parameters, with a braking index of 2.5, was consistent with the spin-down law. The authors conclude that the measured deceleration parameters suggest that either the magnetic dipole model is inadequate or the dipole moment is changing.

In a paper by Alpar et al. (2001), the possibility that neutron stars are surrounded by fall-back disks from supernova core-collapse is discussed. In the case where the disk circumscribes the light cylinder, the neutron star will be an active radio pulsar spinning down under the propeller spin-down torque applied by the disk as well as the usual magnetic dipole radiation torque. When the spin-down is dominated by the propeller torque, evolution across the  $P - \dot{P}$  diagram is rapid; explained by pulsar distribution in the diagram. The authors have modelled pulsar spin-down under these combined torques that predicts braking indices for 2/3 of all pulsars to be  $< 2$  at  $P > P_0$ , and half of these are expected to have negative breaking indices,  $-1 < n < 0$ . The model also predicted small numbers of the oldest pulsars, with long periods and large  $\dot{P}$  values. These pulsars would give magnetic-fields  $B_{\perp} \sim 10^{12} - 10^{13}$ , with the combined model, yet for these pulsars the pure dipole spin-down model would yield higher magnetic-fields, extending into the magnetar range, and young ages. It was concluded that kinematic age measurements were capable of distinguishing between these methods of spin-down.

Magnetars have the highest  $\dot{P}$  and some of the longest periods in terms of neutron stars. Some magnetars have a period of 11 s, where the longest period of a radio pulsar is about 8 s. Isolated Neutron Stars have periods very similar to those of magnetars, achieving periods of up to 11 s, but with  $\dot{P}$  and magnetic-fields a factor of ten lower than those of the lower magnetic-field magnetars. Compact Central Objects (CCOs) have very low  $\dot{P}$ , almost as low as Millisecond Pulsars (MSPs). Their spin periods are similar to those of RPPs.

Pulsar pulse periods are observed to increase with time. The rate of increase of  $\dot{P} = dP/dt$  can be related to the loss of rotational kinetic energy

$$\dot{E} \equiv \frac{dE_{rot}}{dt} = \frac{d(I\Omega^2/2)}{dt} = -I\Omega\dot{\Omega} = 4\pi^2 I \dot{P} P^{-3}, \quad (2.3)$$

where  $\Omega = 2\pi/P$  and is the rotational angular frequency and  $I$  is the moment of

---

inertia.  $\dot{E}$  is called the spin-down luminosity and represents the total power output of the neutron star. Therefore, differences seen in  $P$  and  $\dot{P}$  indicate differences in ages and surface magnetic-field strengths. If the pulsar is treated as a rotating magnetic dipole, the change in rotational energy can be used to estimate  $P_{rad}$ ,

$$P_{\text{rad}} = \frac{dE_{\text{rot}}}{dt}$$

and since the inclination angle,  $\alpha$ , is not generally known,

$$\begin{aligned} \frac{2}{3c^3} (\mathbf{B}R^3 \sin \alpha)^2 \left( \frac{4\pi^2}{P^2} \right)^2 &= \frac{4\pi^2 I \dot{P}}{P^3} \\ \mathbf{B}^2 &= \frac{3c^3 I P \dot{P}}{2 \cdot 4\pi^2 R^6 \sin^2 \alpha} \\ \mathbf{B}^2 &> \left( \frac{3c^3 I}{8\pi^2 R^6} \right)^{\frac{1}{2}} (P \dot{P})^{\frac{1}{2}} \end{aligned}$$

and hence,

$$\mathbf{B} \propto \sqrt{P \dot{P}} \quad (2.4)$$

where  $B$  is the surface magnetic-field strength. On evaluation of constants for the canonical pulsar in cgs units,

$$\left[ \frac{3 \cdot (3 \times 10^{10} \text{ cms}^{-1})^3 \cdot 10^{45} \text{ g cm}^2}{8\pi^2 (10^6 \text{ cm})^6} \right] \approx 3.2 \times 10^{19}, \quad (2.5)$$

so the minimum magnetic-field strength at the pulsar surface is

$$\left( \frac{\mathbf{B}}{\text{Gauss}} \right) > 3.2 \times 10^{19} \left( \frac{P}{\dot{P}} \right)^{\frac{1}{2}}. \quad (2.6)$$

Lines of constant characteristic age,  $P = 2/\dot{P}$ , and dipole spin-down luminosity,  $E_d$ , are superimposed in Figure 2.4. From these, magnetic-fields and ages of  $10^{12}$  G and  $10^7$  years for normal pulsars and  $10^8$  G and  $10^9$  years for millisecond pulsars Lorimer and Kramer (2004).

---

### 2.5.3 Pulsar Magnetosphere

The pulsar magnetosphere is a plasma-filled surrounding dominated by the pulsar's magnetic-field. This was shown by Goldreich and Julian (1969), based on the work of Deutsch (1955). They presented the case for a neutron star with aligned rotation and magnetic axes, which resulted in external electric fields, and ultimately, the extraction of plasma from the neutron star surface. The Goldreich-Julian model does not describe a realistic case, and this is beyond the scope of this work, however it can illustrate some basic principles necessary to understand the observations of pulsars. At any point in a rotating magnetised sphere there will be an induced electric field,

$$(\Omega \times \mathbf{r}) \times \mathbf{B}, \quad (2.7)$$

due to the presence of a magnetic-field  $\mathbf{B}$ . If the sphere is perfectly conducting it will be balanced by a distribution of charge giving an electric field,  $\mathbf{E}$ , so that at any point  $\mathbf{r}$  inside the sphere a force-free state is obtained,

$$\mathbf{E} + \frac{1}{c}(\Omega \times \mathbf{r}) \times \mathbf{B} = 0, \quad (2.8)$$

satisfying Ohm's Law.

Goldreich and Julian estimated the charge density of the pulsar magnetosphere, which represents a maximum value unless other processes exist. The magnetosphere co-rotates with the star inside this radius. This is because the plasma experiences the same  $\mathbf{E} \times \mathbf{B}$  field as the neutron star interior. This process generates the Goldreich-Julian density  $\rho_{GJ}$  (Goldreich and Julian, 1969). The characteristic size of the magnetosphere is given by the light cylinder radius,

$$R_{LC} = \frac{c}{\Omega} = \frac{cP}{2\pi} \simeq 4.77 \times 10^4 \text{ km} \left( \frac{P}{\text{s}} \right). \quad (2.9)$$

The light cylinder is the cylinder centred on the pulsar and aligned with the rotation axis at whose radius the co-rotating speed equals the speed of light. It can also be defined for where the co-rotation is maintained up to this (maximum) distance where the plasma reaches the speed of light.

## 2.5.4 Radio Beam Geometry

It has been established that the magnetic-field lines are divided into two groups. The open field line region provides a narrow and confined site for a stable radio beam. The generally accepted model of a cone-shaped beam centred on the magnetic axis can account for many of the pulse profile properties.

The general picture is, plasma flows from the surface along the open field lines, emitting photons in a direction that is tangential to the open field lines at the point of emission. This creates an opening angle from the resulting conical envelope, which depends on the width of the open field line region at the emission height. Conal beams emitted at a lower height are expected to be narrower than those emitted at a higher altitude. However, the pulse width depends on geometrical factors - where the observers line of sight cuts the emission cones.

The midpoint of the observed pulse profile is expected to coincide with the plane that contains the rotation and magnetic axes and the vector pointing from the pulsar to the observer. This geometrically defined *fiducial plane* represents the proper reference point for timing measurements and the rotation phase is usually defined as  $\phi = 0$  for this *fiducial point*.

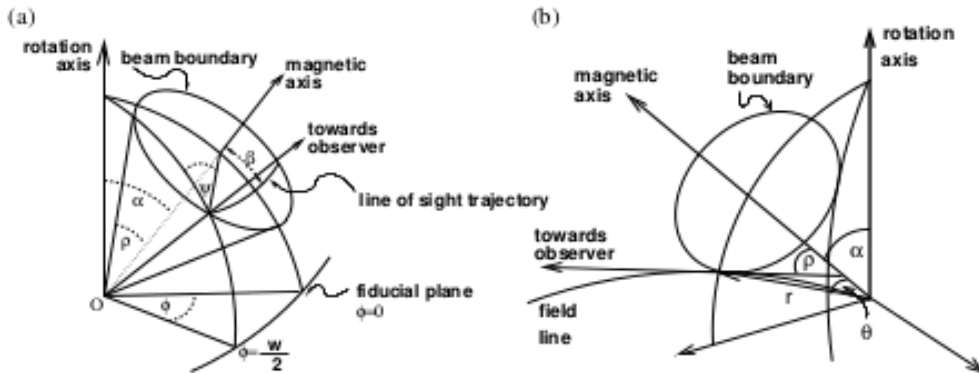


Figure 2.5: Description of the pulsar beam geometry (Lorimer and Kramer, 2004).

There are a number of important features found in Figure 2.5:

- The rotation and magnetic axes are inclined by an angle  $\theta$
- The emission cone with an opening angle  $\rho$  is cut by the observer's line of sight measured at the fiducial plane

- 
- The impact parameter  $\beta$  is the angle cut by the trajectory of the observer's line of sight on the conical beam with the magnetic axis
  - The position angle of the linearly polarised emission,  $\Psi$ , is measured with respect to the projected direction of the magnetic axis

If the emission cone is confined by the last open magnetic-field lines, then a relationship can be found between the opening angle of the cone,  $\rho$ , and the polar coordinates  $(r, \theta)$ . This relationship is given by Gangadhara and Gupta (2001).

$$\tan \theta = -\frac{3}{2 \tan \rho} \pm \sqrt{2 + \left(\frac{3}{2 \tan \rho}\right)^2}, \quad (2.10)$$

which can be seen in Figure 2.5.

### 2.5.5 Rotating Vector Model

Most pulsars were discovered in the radio regime (presently about two thousand objects are listed in the Australia Telescope National Facility Pulsar Catalogue1, Manchester et al. 2005) and for a large fraction, polarisation studies were performed (Gould and Lyne, 1998; Karastergiou and Johnston, 2006). Most radio pulsars were found to show strong linear polarisation, including often a characteristic swing of the polarisation (position) angle (PA) in an S-like shape near the pulse centre. This swing is interpreted in the ‘rotating vector model’ proposed by Radhakrishnan and Cooke (1969) as a projection of the magnetic-field line at the point of emission onto a plane perpendicular to the observer’s sight-line. The point of emission is usually assumed to be in the polar-cap region of the pulsar where a regular dipolar field line points with a small angle (beam width) towards the observer. The free parameters of this simple geometrical model are the inclination angle between the axes of rotation and magnetic dipole, and the viewing angle between the line of sight and the rotation axis.

The open magnetic-field lines and the particles that flow along them become the pulsar wind, which carries the bulk of the Poynting flux beyond the light cylinder radius,  $R_{LC}$ . The pulsed radiation of RPPs (Rotation Powered Pulsars) carries less than about 10% of the total spin-down power,  $\dot{E}_d$ . Most of the power

in pulsed emission is in  $\gamma$ -rays around a GeV for all but a few RPPs, notably the Crab pulsar whose pulsed emission power peaks in hard X-rays. The radio pulsations make up typically only  $10^{-4}$  or less of the spin-down power, but are easier to detect since the photon flux is much higher. Since the  $\gamma$ -ray pulsations typically carry the highest percentage of  $\dot{E}_d$ , they can reveal the most information about the particle acceleration in pulsar magnetospheres.

The plasma outside the neutron star experiences the same magnetic-field as the neutron star interior forcing it to co-rotate with the star. However, co-rotation can only be maintained up to a maximum distance where the plasma reaches the speed of light (Lorimer and Kramer, 2004).

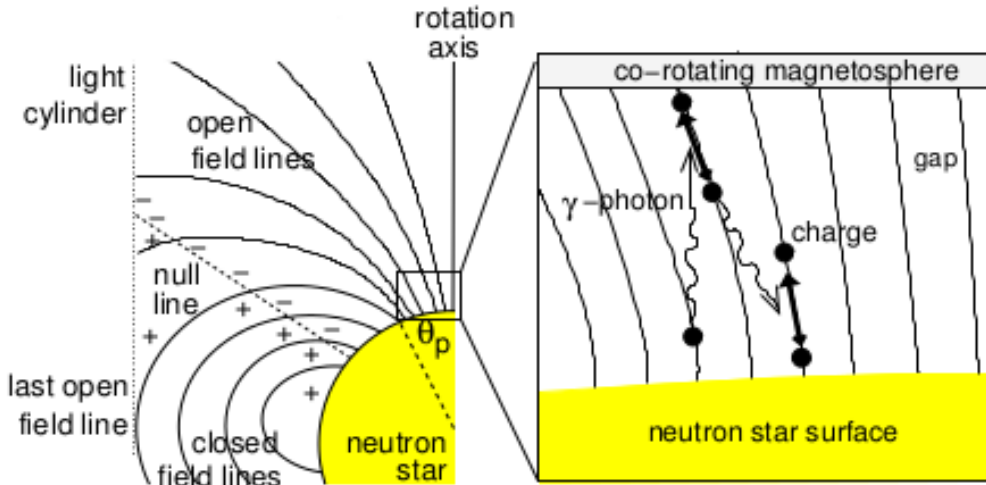


Figure 2.6: A cartoon of the pulsar magnetosphere based on the theories laid out by Goldreich and Julian (1969). A polar-gap is evident here and will be discussed later (Lorimer and Kramer, 2004).

This maximum distance where co-rotation is maintained is called the light cylinder. The magnetic-field strength at the light cylinder radius (see Section 2.5.3 for this equation) is

$$B_{LC} = B_s \left( \frac{\Omega R^3}{c} \right) \simeq 9.2G \left( \frac{P}{s} \right)^{-\frac{5}{2}} \left( \frac{\dot{P}}{10^{-15}} \right)^{\frac{1}{2}}. \quad (2.11)$$

It is shown in Figure 2.6 that the existence of the light cylinder divides the dipolar magnetic-field lines into two groups:

- 
1. Field lines that close within the light cylinder (closed field lines)
  2. Field lines that do not close (open field lines).

The open field line region defines the *polar-cap* on the neutron star surface, centred on the magnetic pole. Its boundary, given by  $(R, \theta_p)$ , is defined by the last ‘open field line’, which is tangential to the light cylinder. For a given dipolar field line, the expression  $\sin^2 \theta/r$  is a constant. For the last open field line

$$\frac{\sin^2 \theta}{r} = \frac{1}{R_{LC}} = \frac{2\pi}{cP} = \frac{\sin^2 \theta_p}{R}. \quad (2.12)$$

If the radius of the polar-cap measured on the surface,  $R_p$ , is not too large, Equation 2.11 can be used and computed as

$$R_p \simeq R \sin \theta_p = \sqrt{\frac{2\pi R^3}{cP}} = 150m \left(\frac{P}{s}\right)^{(-\frac{1}{2})} \quad (2.13)$$

for  $R = 10$  km. The polar-cap parameters can be used to estimate the potential drop between the magnetic pole and the edge of the polar-cap (Lorimer and Kramer, 2004).

The overall magnetic-field is expected to be dipolar. Observations of several bright pulsars by Eilek and Hankins (2000) show position angle sweeps that are not consistent with a simple dipole field in the radio emission region. Polarisation is the only measure of the geometry of the magnetic-field, where the linear polarisation direction is uniquely tied to **B** (perpendicular or parallel depending on the emission model). If this is the case, a dipolar field has a unique signature in the polarisation angle (PA) sweep (Radhakrishnan and Cooke, 1969). Deviations from this signature are then signs of a non-dipolar field in the emission region. The standard pulsar model assumes all radio emission comes from the open field line region above the polar cap, predicting a clear relation of the emission and the PA behaviour with pulse phase. Deviations here are also important: They are either signs of a non-dipolar field, or signs of problems with the standard emission model. The authors show several stars that indicate such deviations.

Close to the pulsar surface, high-order multipole moments of the magnetic-field may be important. Although the strength of the multipoles is small compared to

---

a dipolar field further away from the surface, multipoles above the polar-caps may be relevant for the creation of additional plasma that is eventually responsible for the observed radio emission (Jones, 1980).

## 2.6 Pulsar Emission Models

When considering pulsars models involving rotation, rather than pulsation, were favoured strongly by observations that the pulsation periods were gradually lengthening. To give a better understanding, an example of a spinning top can be used. As the top loses energy, it slows down mostly due to frictional forces acting on the top. The identification of pulsars with neutron stars rather than white dwarfs came with the discovery in 1968 of pulsars in the Vela and Crab supernova remnants. Not only were neutron stars thought to be born in supernovae, but the Crab pulsar had a period of only 33 ms, much faster than allowed by any white dwarf model.

The existence of gaps is proposed for the outer magnetosphere near the location of the *null line*  $\Omega \cdot \mathbf{B} = 0$  which separates the space charges of different sign. Depending on the radiation mechanism large magnetospheric plasma densities, exceeding the Goldreich-Julian density by many orders of magnitude, are required. Many models predict such plasma multiplication due to the existence of magnetospheric *gap* regions. In these gaps the Goldreich-Julian condition of a co-rotating magnetosphere breaks down, the force-free state inside the gaps cannot be maintained and a residual electric field  $E_{||}$  must exist. Therefore, gaps are expected in regions where plasma is depleted in the magnetosphere. Two such regions have been identified:

1. In the open field lines above the magnetic polar-cap ('polar-gap')
2. Between the outer and inner field lines close to the light cylinder ('outer-gap')

These can be found in Figure 2.1. The following section will address the currently proposed emission models, in terms of high-energy emission models, though radio will also be considered. These models will also address emission in terms of their relationship with polarisation, which are expected to correlate with the

---

observational data in this thesis, particularly that of the optical emission of the Crab pulsar.

### 2.6.1 Polar-Cap Model

The nature of radio emission is still unknown. The process for this emission must be able to explain the coherency and high degree of polarisation of the emission, and it must work over nearly 4 orders of magnitude in rotation period and 6 orders of magnitude in magnetic-field. Considering how broad a range the radio regime has, this must also be accounted for by the emission mechanism.

The significance of optical polarimetric observations (discussed in Section 2.8) provide huge insights into high-energy emission from pulsars: This section will provide some detail on a radio emission mechanism developed by Ruderman and Sutherland (1975) who proposed that a polar-gap is attributed to the strong binding of nuclei to the stellar surface, preventing ions from being ripped off the surface. Melrose (1995) describes polar-cap models as such that, the gap occurs immediately above the stellar surface in the polar-cap.

A polar-gap provides a dense electron-positron pair plasma which is required for most radio emission models. The plasma is assumed to originate in a *pair cascade* in the gap (Sturrock, 1971). It has been proposed that charged particles are pulled from the surface and are accelerated by a large residual electric field, reaching relativistic energies ( $\gamma \lesssim 10^7$ ). Moving along the magnetic-field lines, these particles produce  $\gamma$ -ray photons either by curvature emission or inverse Compton scattering on lower-energy photons. Due to the presence of the strong magnetic-field, the  $\gamma$ -ray photons can split, resulting in magnetic one-photon electron-positron pair creation if the photon energy exceeds twice the rest mass of the electron, i.e.  $E_\gamma \geq 2m_ec^2$ . *Secondary pair plasma* is believed to produce the observed radio emission at some distance from the pulsar surface. This plasma is a result of new generation particles producing more photons and particles.

The situation changes when going to higher energies, i.e. optical, X- and  $\gamma$ -ray regimes. Daugherty and Harding (1996) shows that in the polar-cap model, a sharp turnover is expected in the few to 10 GeV energy range due to attenuation of the  $\gamma$ -ray flux in the magnetic-field. However, Abdo et al. (2009) show that the

---

spectral change at  $\sim 2.9$  GeV does not appear to fit this model. It was concluded that low-altitude radiation subject to  $\gamma$ -B pair production cannot account for the bulk of the Vela  $\gamma$ -ray emission. The observed cut-off can be used to estimate a minimum emission height as  $r \approx (\epsilon_{\text{max}} B_{12}) / 1.76 \text{ GeV}^{\frac{2}{7}} P^{-\frac{1}{7}} R_*$ , where max is the unabsorbed photon energy, P is the spin period, and the surface field is  $10^{12} B_{12}$  G (Baring, 2004). Abdo et al. (2009) present their Fermi observational results for Vela in Figure 2.7.

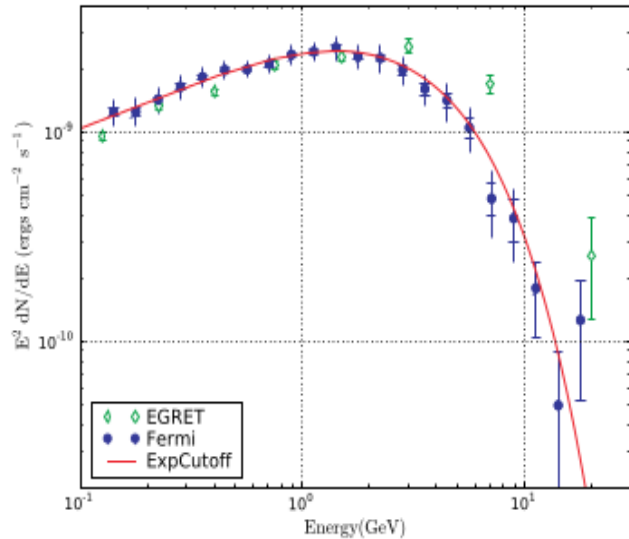


Figure 2.7: A phase-averaged spectral energy distribution (SED) plot of Vela, ( $E^2 dN_\gamma/dE$ ). Both statistical (capped) and systematic (uncapped) errors are shown. The authors believe that the latter are conservative; they dominate at all energies below 7 GeV. EGRET data points (Kanbach et al., 1994) are shown for comparison. The curve is the best-fit power law with a simple exponential cut-off (Abdo et al., 2009).

Fermi-LAT observational results reported by Abdo et al. (2010) have also shown that even in the absence of radio emission characterising the Geminga pulsar (radio quiet) clearly favours models where the high-energy emission occurs in the outer magnetosphere of the pulsar. Polar-cap models, where the high-energy emission is located near the neutron star surface, are unlikely to explain the Geminga pulsar, since the line-of-sight is necessarily close to the magnetic axis for such models where one expects to see radio emission.

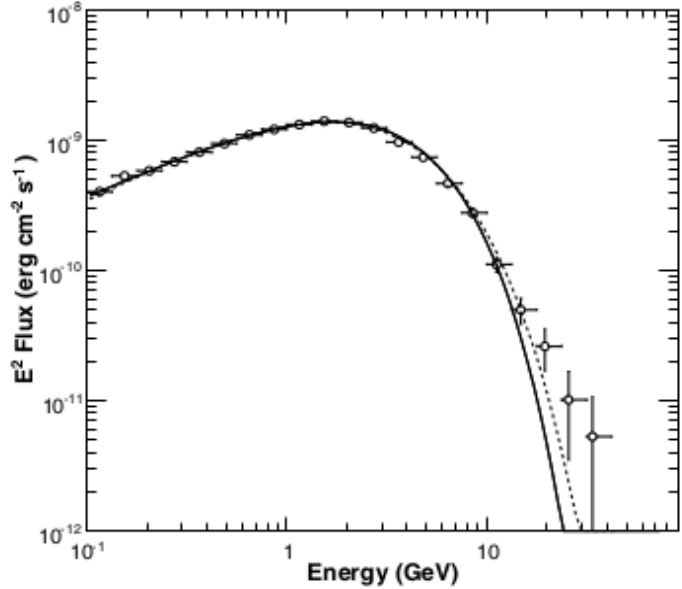


Figure 2.8: Phase-averaged SED of the Geminga pulsar. The solid line represents the best-fit power law with exponential cut-off (i.e.,  $b = 1$ ), while the dashed one represents the best-fit power law with exponential cut-off with free exponential index (in this case, the result is  $b = 0.81$ ) (Abdo et al., 2010).

### 2.6.2 Slot-Gap Model

The slot-gap, a narrow region bordering the last open magnetic-field line where particles cannot accelerate rapidly enough to produce pairs before the field drops, is an unavoidable feature of polar-cap space-charge limited flow (SCLF) models by Arons and Scharlemann (1979) and Arons (1983). SCLF models assume that charges are freely emitted from the NS polar-cap surface and flow out along open field lines. Since this charge flow is not sufficient to supply the Goldreich-Julian charge above the surface, an  $\mathbf{E}_{\parallel}$  exists and the charges are accelerated. Radiation from these charges forms electron-positron pairs in the strong magnetic-field, which can screen the  $\mathbf{E}_{\parallel}$  above a pair formation front (PFF) in a distance small compared to the acceleration distance, which is typically less than a stellar radius (Harding et al., 2008).

The pair formation front across the polar-cap thus forms a bowl shape as pairs are produced at higher and higher altitudes, approaching the last open field line. Although the existence of a slot-gap has been known for some time, its potential

---

as a high-energy emission site has only recently been explored. Muslimov and Harding (2003) derived the electric potential and field in the slot-gap, and modelled the acceleration and pair cascades at altitudes from the neutron star surface up to several stellar radii. They found that cascades develop over a range of 3 - 4 stellar radii along the slot-gap inner boundary. These cascades have higher pair multiplicity (number of pairs per primary electron) than cascades nearer the magnetic axis because the primary electrons accelerate and produce pairs over a larger distance. The radiation from the slot-gap cascades naturally produces a wider hollow cone of emission than the cascades near the surface.

Muslimov and Harding (2004) extended the electric field solution in the slot-gap to high altitudes and modelled only the curvature radiation of the primary particles. They found that such emission formed caustic patterns, like those of the ‘two-pole caustic’ model proposed by Dyks and Rudak (2003) to naturally explain the double-peaked profiles of  $\gamma$ -ray pulsars. However, the spectrum of curvature radiation from radiation reaction limited particles alone is too difficult to match that of observed  $\gamma$ -ray pulsars.

### 2.6.3 Outer-Gap Model

Another model, known as the outer-gap, has been developed by Cheng et al. (1986); Romani and Yadigaroglu (1995); Romani (1996), and it involves particle acceleration, high-energy emission and pair production. The parameters for the outer-gaps close to the light cylinder differ to those of the inner polar-gap. The local magnetic-field is weaker, such that the magnetic-field strength at the light cylinder is a more important factor than that at the surface. Radhakrishnan and Cooke (1969), and later Blaskiewicz et al. (1991), have provided information regarding geometric frameworks for this model with lowest order special relativity effects. However, the non-coherent high-energy emission has a different spatial origin and requires a separate study.

Romani (1996) describes the outer-gap model for  $\gamma$ -ray pulsars based on curvature radiation-reaction-limited charges in the outer magnetosphere. The authors show how pair production on thermal surface flux can limit the acceleration zones; estimates for the efficiency of GeV photon production  $\eta_\gamma$  and the  $\gamma$ -ray beam-

---

ing fraction are also derived by this model, including their dependence on pulsar parameters. In general,  $\eta_\gamma$  increases with pulsar age but is decreased for low magnetic-fields for small magnetic inclinations. It has been shown that this model produces GeV pulse profiles, curvature spectra, and detection statistics consistent with the observations. Romani (1996) also describes the optical and X-ray pulsar synchrotron spectrum and the spectral variations with the pulsar phase. Vela-like parameters have been shown to give GeV spectra consistent with those observed by EGRET.

Outer-gaps are not expected to be associated with radio emission as this high-energy emission comes from a wide variety of altitudes, contrary to radio, although exceptions may exist. Outer-gaps are expected to explain high-energy emission of pulsars such as curvature and synchrotron emission. However, according to Dyks and Rudak (2003), the model is unable (without additional postulates) to account for the presence of outer wings in the double-peak light curves. More importantly, the model in its present form (Zhang and Cheng, 1997) is unable to account for a substantial level of the off-pulse emission in the Crab pulsar.

#### 2.6.4 Two-Pole Caustic Model

The two-pole caustic model (Dyks et al., 2004a,b) proposes another picture to explain the origin of high-energy radiation within the pulsar magnetospheres in regions confined to the surface of last open magnetic-field lines (similar to thin outer-gap accelerators) but extending between the polar-cap and the light cylinder. According to Dyks and Rudak (2003), the polar-cap and outer-gap model both suffer from serious problems in terms of high-energy emission.

The two-pole caustic model predicts fast swings of the position angle and minima in the polarisation degree from the caustic nature of the peaks: Superposition of emission from different altitudes (e.g. with different PAs), which produces the peaks. This is similar to what has been observed, see Section 2.6, and was also expected of the outer-gap model. The polar-cap model (see Section 2.6.1) and the outer-gap model have not been able to reproduce the observational polarisation characteristics of the Crab pulsar.

The key component of the model is the gap region (i.e. the region where particle

---

acceleration is taking place and high-energy photons originate) that satisfies the following assumptions:

1. The gap region extends from each polar-cap to the light cylinder.
2. The gap is thin and confined to the surface of last open magnetic-field lines.
3. Photon emissivity is uniform within the gap region.

The model is well suited for four  $\gamma$ -ray pulsars - Crab, Vela, Geminga, and B1951+32 - with double-peak light curves exhibiting the peak separation of 0.4 to 0.5 in phase. Dyks and Rudak (2003) goes on to say that, unlike other pulsar models with caustic effects, the double peaks arise from crossing two caustics, each of which is associated with a different magnetic pole. The generic features of the light curves are consistent with the observed characteristics of pulsar light curves:

1. The most natural (in terms of probability) shape consists of two peaks (separated by 0.4 to 0.5 in phase for large viewing angles).
2. The peaks possess well-developed wings.
3. There is a bridge (inter-peak) between each emission component.
4. There is a non-vanishing off-pulse emission level.
5. The radio pulse occurs before the leading high-energy peak.

### 2.6.5 The Striped Wind Model

A model has been proposed by Pétri and Kirk (2005) which places the origin of the pulsed optical emission from the Crab in a striped pulsar wind zone. This model develops the original work introduced by Coroniti (1990) and Michel (1994) and elaborated by Lyubarsky and Kirk (2001) and Kirk and Skjæraasen (2003), which also features polarisation characteristics that bear a certain resemblance to the observations made by the authors. This model provides a theoretical explanation for observed polarisation high-energy emission, which has been investigated by Kirk et al. (2002).

Table 2.1: Pulsar Emission Models Summary.

Model	Emission Type	Emission Cause	Location	Polarisation	Observed
Polar-Cap	Coherent radio	Electron-positron plasma (pair cascade)	Polar cap surface	Radio	Disagree with Fermi observations (Vela & Geminga)
Slot-Cap	Radio & High-energy	Electron-positron (pair cascade)	Polar cap surface	-	Wider hollow cone than near stellar surface
Outer-Gap	Curvature & Synchrotron	Pair production	Variety of altitudes	-	Cannot account for wings in double-peak, or off-pulse emission in Crab pulsar DOLP of MP & IP are similar; Large swing in PA in both peaks
Two-Pole Caustic	High-energy	Pair production	Last open field line between polar cap and LC <sup>1</sup>	Predicts swings in PA; minima DOLP by the peaks - superimposed altitudes	Light curves consistent with observed (Crab pulsar)
Striped Wind	Optical	Magnetic reconnection	Outside LC	Pulsed optical	Observed synchrotron emission in Crab pulsar DOLP of MP & IP are similar; Large swing in PA in both peaks

It is assumed that magnetic energy is released by reconnection in the thin regions where the toroidal field reverses its polarity, producing a non-thermal electron/positron population. But, unlike in Lyubarsky's model, emission from the striped wind originates outside the light cylinder, and relativistic beaming effects are responsible for the phase coherence of the synchrotron radiation. A strength of this model is that the geometry of the magnetic-field, which is the key property determining the polarisation properties of the emission, is relatively well known. Synchrotron emission from the striped wind applies successfully to the pulsed optical polarisation properties of the Crab pulsar.

Table 2.1 summarises the main points of each of these emission models:

---

## 2.7 Optical Studies of Pulsars

There is still much disagreement on the emission mechanism of pulsars (some of these emission models have been discussed). However, what has been agreed upon is, the luminosity is powered by the rotation of the pulsar, the pulsed radio signal comes from a coherent process, and the optical emission up to X-ray, is incoherent synchrotron radiation; where low end  $\gamma$ -ray emission is curvature radiation and higher energies is inverse Compton (Shearer et al., 2003). Optical emission observed from a survey of radio pulsars (Caraveo, 2000) had a thermal nature, which was found to be connected to the hot neutron star surface or to the polar cap when it is bombarded by the secondary electrons (or positrons) and heated by them. However, it was also found that there was a significant non-thermal component to the optical emission. There is still debate on the mechanism that accelerates the electrons to the energy required for synchrotron and curvature radiation, where this acceleration takes place, how coherency is maintained, and the stability of the electron-positron plasma outflow from the neutron star surface (Malov and Machabeli, 2001).

Taking the example of the Crab pulsar, there are two primary features of radio and optical profile: A main pulse and an inter pulse. Figures for these can be found in Section 2.3. At lower energies a radio precursor can be seen, and at higher energies in the optical, X-ray, and  $\gamma$ -ray regions, a bridge is observed between the two pulses. A suggestion for why the precursor is present is that it represents emission from the pulsar polar cap region near the neutron star surface, like radio emission for most pulsars, and that the other features come from higher in the magnetosphere (Harding and Daugherty, 1998).

At present the number of optical pulsars observed at optical wavelengths stands at 14, see Mignani et al. (2005). The first five optical pulsars detected are the only ones from which confirmed optical pulsations have been observed; these are the Crab (PSR B0531+21; Cocke et al. (1969)), Vela (PSR B0833-45; Wallace et al. (1977)), PSR B0656+14 (Shearer et al., 1997; Kern et al., 2003), and Geminga (PSR B0633+17; Shearer et al. (1998); Kargaltsev et al. (2005)). Pulsed high-energy emission (optical to  $\gamma$ -ray) from pulsars is accepted as being due to complex

---

<sup>1</sup>Light cylinder.

---

physical processes occurring within the pulsar magnetosphere (O'Connor et al., 2005). O'Connor et al. (2005) considered the lack of agreement that exists within the area of high-energy emission from pulsars. The authors also describe a more phenomenological approach to the area of non-thermal emission from optical pulsars.

Goldoni et al. (1995) carried out a phenomenology of the population of (pulsed and non-pulsed) optical pulsars. The conclusion of this work showed that  $\dot{P}$  may act as a distinguishing parameter in describing the multi-frequency emission of isolated neutron stars (INS). Therefore, the high-energy emission mechanism of INSs is dominated by the magnetic-field both as a photon generator and absorber. Shearer and Golden (2001) used a larger sample of pulsars and focused on the 5 known to pulsate. It must be noted that the results of this sample were limited due to its size. Their work revealed an empirical scaling of optical (and  $\gamma$ -ray) flux with the magnetic-field strength at the light cylinder ( $B_{LC}$ ). The results of the Shearer and Golden (2001) study gave further validation to the predictive model of optical emission, the Pacini model of magnetospheric synchrotron emission located at the constant fraction of the light cylinder (Pacini, 1971; Pacini and Salvati, 1983, 1987). Figure 2.9 shows the predicted peak luminosity against the peak luminosity observed by the authors, accounting for the differing observed energy spectrum exponent at 4500 Å. Shearer and Golden (2001) also considered the expected flux from the anomalous X-ray, a class of magnetar. It was found that if the observed  $P$  and  $\dot{P}$  relationship can be interpreted in the same way as for normal pulsars to derive a canonical surface field then it can be estimated what the expected luminosity of these objects would be. The derived luminosity was very low - a reflection of the weak light cylinder field.

In the discussion of synchrotron emission from pulsars, Malov and Machabeli (2001) addresses the cyclotron instability, which causes an appearance of transverse momenta of relativistic particles in the outer parts of the magnetospheres. This transverse momentum loss, via synchrotron, occurs during a very short period of  $\leq 10^{-20}$  seconds. The authors formulate an equation that describes how such processes are controlled and find its solution. A distribution of pitch angles for particles via synchrotron emission were determined and they also show that this radiation is emitted near the light cylinder showing a correlation with Shearer and

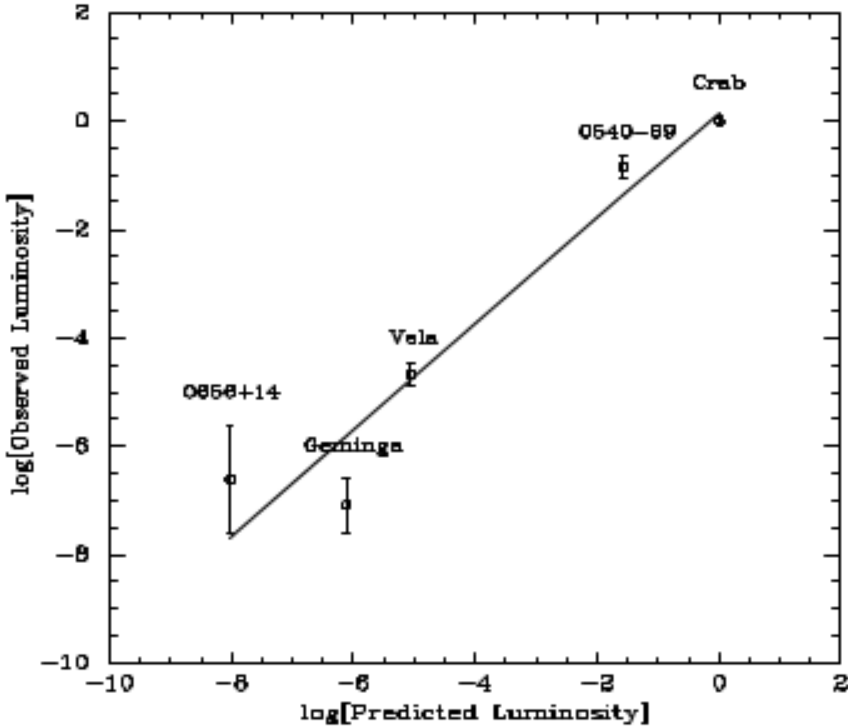


Figure 2.9: Predicted peak optical luminosity from equation 2 versus observed peak emission. Also shown is the weighted fit described in the text. The weighting was based upon the observational uncertainties in flux and distance (Shearer and Golden, 2001).

Golden (2001). It was also shown that optical emission will be observed in pulsars with small angles between the rotation and magnetic axes.

Another predictive model for optical emission was proposed by Malov (2001). They derive the luminosity of radio pulsars due to synchrotron radiation by the primary beam at the magnetosphere periphery. Their model shows a strong correlation between the observed optical luminosities of radio pulsars and the parameter  $\dot{P}/P^4$ : It predicts appreciable optical emission from several dozen pulsars, particularly those with a  $P < 0.1$  seconds. They found that when  $\gamma_p = 2 - 13$ , agreement is found in the predicted and observed optical luminosities. It was found that the magnetic-field structure near the neutron star surface must deviate strongly from a dipolar field in order to produce secondary plasma from Lorentz factors such as these, as was proposed by Ruderman and Sutherland (1975). It is concluded that

---

the shorter the period of a pulsar, the harder the energy at which the peak of its synchrotron radiation is observed.

O'Connor et al. (2005) investigated and proposed a synchrotron self-absorption (SSA) scaling model for optical pulsar emission based on the Pacini model. The SSA model allows the possibility of two alternative scaling laws, the difference arising from different assumptions about how the underlying particle population is generated - specifically, whether one is dealing with a single magnetic  $\gamma B$  generation event, or a cascade process. One method of this model predicts cut-off frequencies not inconsistent with observations. It predicted magnitudes for younger pulsars, but underestimated luminosities of the two older optical pulsars (Geminga and PSR B0656+14). An age-dependent variation in optical emissivity could account for this part of the design. The models proposed by Pacini and Salvati (1987) and Shearer and Golden (2001) remain the most accurate (to first order) in predicting the luminosity of optical pulsars, both of which use light cylinder magnetic-field scaling as an assumption that emission is at a constant fraction of the light cylinder distance. This suggests that it's possible that light cylinder scaling shows light cylinder fields are intrinsically related to the high-energy emission from pulsars in some way.

The pulsar timing method (Lorimer and Kramer, 2004; Lyne and Graham-Smith, 2006; Manchester and Taylor, 1977) compares observed pulse times with those modelled based on the pulsar's astrometric, orbital, and rotational parameters. Any features in the residuals of this model may include calibration errors, orbital companions, or spin-down irregularities. There exist two main types of irregularity; ‘glitches’, which are sudden increases in rotation rate followed by a period of relaxation, and ‘timing noise’, which consists of low-frequency structures. Understanding the cause of these irregularities may allow us to relate these phenomena and provide insight into the interior structure of neutron stars. Hobbs et al. (2010b) carried out a large-scale analysis of pulsar timing noise over time scales  $> 10$  years, for multiple observing frequencies and for a large sample of normal and recycled pulsars. The authors found that the pulsars with the smallest characteristic ages were shown to be dominated by the recovery from glitch events, whereas, for older pulsars, timing irregularities were quasi-periodic. It is concluded that previous models that explained timing residuals as a low-frequency

---

noise process are not consistent with these observations, which were of significance due to the length of the observation period.

## 2.8 Optical Polarisation of the Crab Pulsar

The most optically bright pulsar that has been observed to date is the Crab pulsar, including its pulsar wind nebula (PWN). This pulsar, as has been discussed, is the remnant of a supernova first observed in 1054 AD. It is the pulsar itself which powers the Crab Nebula, and polarimetric observations over the last 60 years have revealed interesting activity and geometry about the pulsar and its surrounding nebula. It is with this information that it will be possible to limit the number of emission models (i.e. location of particle acceleration) and gain a better understand for how the pulsar itself works.

The number of optical pulsars is growing (14 are known), however, there are only 5 where the polarisation signal has been measured; the Crab (Wampler et al., 1969; Smith et al., 1988; Kristian et al., 1970; Słowińska et al., 2009; Moran et al., 2013), Vela (Wagner and Seifert, 2000; Mignani et al., 2007a), PSR B0540-69 (Middleditch et al., 1987; Chanan and Helfand, 1990; Wagner and Seifert, 2000; Mignani et al., 2010) PSR B0656+14 (Kern et al., 2003), and PSR B1509-58 (Wagner and Seifert, 2000). In particular, the Crab pulsar has been studied extensively owing to having the largest optical magnitude  $V \sim 16.8$  (Nasuti et al., 1996); both phase-averaged and phase-resolved studies of its optical polarisation have been undertaken. Table 2.2 is a summary of the polarisation measurements of optical pulsars from Słowińska et al. (2009), where the polarisation degree is given as a percentage, and position angle in degrees (North,  $0^\circ$  to East,  $90^\circ$ ).

Table 2.2: High energy polarisation measurements of pulsars and their nebulae (Słowińska et al., 2009).

Band	Pulsar/Polarisation	Nebula (near PSR)	Ref
Optical (V $\sim$ 16.6)	<b>Crab</b> phase-resolved phase-averaged $9.8\% \pm 0.1\%$ and $109.5^\circ \pm 0.2^\circ$ phase-averaged $5.2\% \pm 0.3\%$ and $105.1^\circ \pm 1.6^\circ$	$9.7\% \pm 0.1\%$ ; $139.8^\circ \pm 0.2^\circ$ ( $< 5''$ from PSR) ( $< 5''$ from PSR)	[1],[2] [3] [14]
UV	phased-resolved, similar to optical -		[4]
X-ray	P.D. and P.A. (MP and IP) X-ray only upper limits	$19.2\% \pm 0.9\%$ ; $155.8^\circ \pm 1.4^\circ$	[5],[6]
Hard X-ray/soft $\gamma$ -ray	off-pulse (phase: 0.52 - 0.88) $> 72\%$ ; $120.6^\circ \pm 8.5^\circ$ phase-averaged $47\%^{+19\%}_{-13\%}$ ; $100^\circ \pm 11^\circ$		[7] [7]
$\gamma$ -ray	off-pulse (phase: 0.5 - 0.8) $46\% \pm 10\%$ ; $123^\circ \pm 11^\circ$		[8]
<b>B0540-69</b>			
Optical (V $\sim$ 22.5)	phase-averaged: $\sim 5\%$ , no error quoted; phase-resolved: $< 15\%$	$5.6\% \pm 1.0\%$ ; $79^\circ \pm 5^\circ$	[9],[10],[11]
<b>Vela</b>			
Optical (V $\sim$ 23.6)	phase averaged: $9.4\% \pm 4\%$ , $146^\circ \pm 11^\circ$		[9],[12]
<b>B0656+14</b>			
Optical (V $\sim$ 25)	double peak light curve; P.D. bridge $\sim 100\%$ , peaks $\sim 0\%$ P.A. sweeps in agreement with RVM		[13]
<b>B1509+58</b>			
Optical (V $\sim$ 25.7)	phase-averaged: $\sim 10.4\%$ (very uncertain, no error quoted)		[9]

References: [1] Smith et al. (1988), [2] Słowińska et al. (2008), [3] Słowińska et al. (2009), [4] Graham-Smith et al. (1996), [5] Silver et al. (1978), [6] Weisskopf et al. (1978), [7] Forot et al. (2008), [8] Dean et al. (2008), [9] Wagner and Seifert (2000), [10] Middleditch et al. (1987), [11] Chanan and Helfand (1990), [12] Mignani et al. (2007a), [13] Kern et al. (2003), [14] Moran et al. (2013).

---

The characteristics of the beamed radiation from the Crab pulsar can be measured in greatest detail at optical wavelengths. The suggestion of variation in polarisation and rotation of polarisation angle (PA) was first reported by Warner et al. (1969). Results for the phase-resolved linear polarisation of the optical emission was first published by Wampler et al. (1969); Kristian et al. (1970); Cocke et al. (1970), and early observations assumed that the emission between the pulses was negligible. It was shown that the polarisation angle sweeps through the peak and the polarisation degree decreases and then increases within each pulse, reaching the minimum shortly after the pulse peak. It was also found that the polarisation behaviour of the sub-pulse is similar to that of the main pulse and the intensities are asymmetric in the opposite sense. These observations were limited to the main pulse (MP) and inter pulse (IP) phase region only. It was later shown by Peterson et al. (1978); Jones et al. (1981); Percival et al. (1993); Golden et al. (2000) that the emission persisted throughout the pulsar's cycle.

Smith presented an accurate method of removing the background polarised signal, following from Jones, from the Nebula, to find the pulsar's intrinsic polarisation. These results confirmed previous observations, and were the first studies to reveal the degree of polarisation profile of the pulsar during the bridge and off-pulse phase regions. They also found that the off-pulse region is highly polarised. The degree of polarisation was measured at a level of 70% and  $47 \pm 10\%$  by Jones et al. (1981); Smith et al. (1988), respectively. The polarisation angle was also measured by both authors, at a value of  $\sim 108^\circ$  and  $\sim 130^\circ$ , respectively. Smith et al. (1988) shows a similarity between the polarisation behaviour of the 2 pulse components; both the main and inter pulse occur at the same position angle and at the same point in the loop traced by the polarisation vector. A polarisation measurement of the background at the pulsar of 8% was made, with a polarisation angle of  $152^\circ$ . This was in reasonable agreement with work carried out by McLean et al. (1983). Smith et al. (1988) proposed that the two pulse components represent radiation, which is beamed by a combination of relativistic beaming and an intrinsic directivity in the source. It is indicated that this may be due to curvature radiation along the direction of magnetic-field lines.

Słowińska et al. (2009) report the most detailed phase-resolved observations of the optical linear polarisation of the Crab pulsar. Their results are consis-

---

tent with previous observations, however, with better definition and statistics. Słowińska et al. (2009) recorded a phase averaged degree of polarisation value to be  $9.8 \pm 0.1\%$  with a polarisation angle of  $109.5 \pm 0.2^\circ$ . The values measured after DC subtraction (removing the signal contribution by the Knot, or the off-pulse region) are  $5.4 \pm 0.1\%$  and  $96.4 \pm 0.2^\circ$ , respectively. Figure 2.10 gives a detailed description of the findings by Słowińska et al. (2009) and the phase location of the DOLP and PA with respect to the radio phase. The authors also report changes in the PA, which are aligned with the MP maximum of the optical light, and with the zero phase, i.e. with the radio phase of the MP. Figures and a more detailed analysis can be found in the published work. The authors have completely resolved the polarisation characteristics of both peaks of the Crab pulsar, MP and IP, in the optical pass bands. They have also characterised the polarised emission between the peaks, i.e. the bridge as well as the DC ('off-pulse') region. The authors have also better characterised the polarised emission between the peaks, i.e. the bridge as well as the DC ('off-pulse') region, and they report that the MP of the Crab pulsar arrives  $231 \pm 68 \mu\text{s}$  before the peak of the radio pulse.

Another striking correlation between the radio pulse profile and the degree of optical polarisation can be seen in Figure 2.10. The radio precursor seems to be well aligned with the bump in the degree of optical polarisation. During this phase of the leading wing of the optical main pulse, the position angle change is also characterised by a nearly linear swing. It is premature to speculate, with current models of emission from the pulsar magnetosphere, how the coherent and incoherent emissions interact.

Further observations in the polarimetric characteristics of the Crab pulsar have been carried out by Moran et al. (2013). The authors have studied the phase-averaged polarisation properties of the Crab pulsar and its nearby synchrotron knot marking the first high-spatial resolution multi-epoch study of the polarisation of the inner nebula and pulsar. An apparent alignment between the polarisation position angle of the pulsar and the pulsar's proper motion vector was found, and confirmation that the inner Knot is responsible for the highly polarised off-pulse emission seen in observations in the optical. It was also the first reporting of the variability in the inner Knot's position and brightness over these observations, and

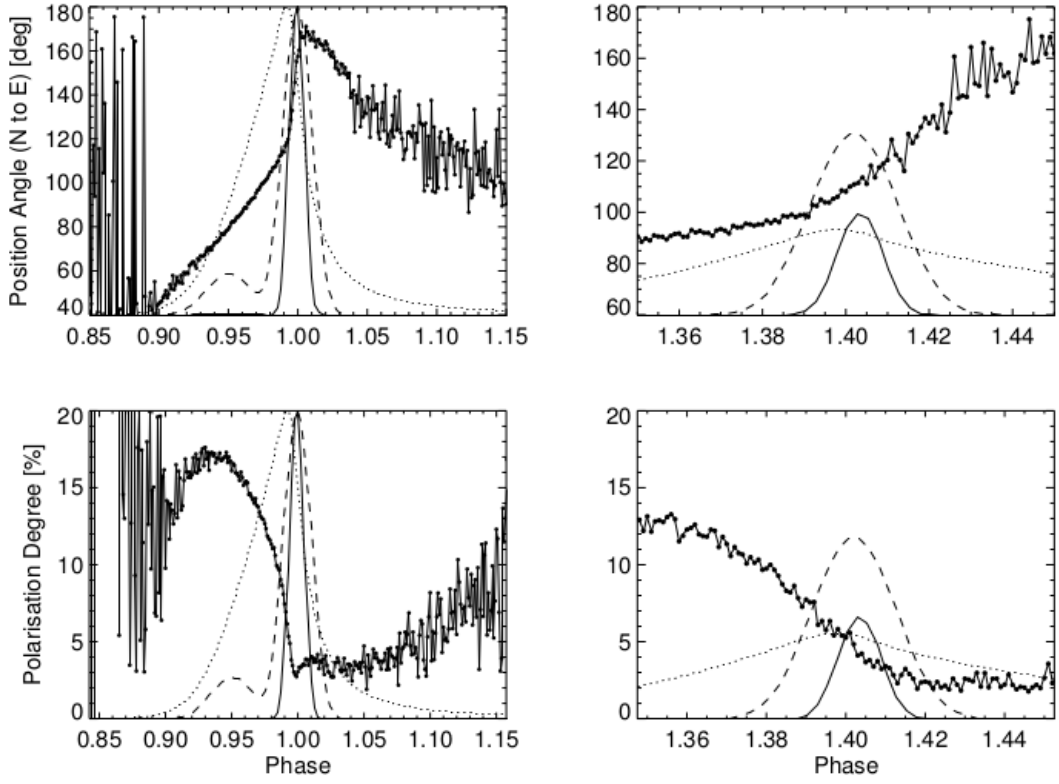


Figure 2.10: Optical polarisation characteristics of the Crab pulsar compared with the pulsar radio profiles. Radio profiles obtained at radio frequencies of 1400 MHz and 610 MHz are shown as a solid line and dashed line, respectively. Left column is a close in plot of the MP phase, whereas the right column is the IP phase. Points indicate the optical polarisation measurements, while the dotted line shows the optical intensity profile (Słowińska et al., 2009).

the linear polarisation signal. The findings of this work show that the pulsar is  $5.2 \pm 0.3\%$  and  $105.1 \pm 1.6^\circ$ , and the synchrotron Knot measured  $59.0 \pm 1.9\%$  and  $124.7 \pm 1.0^\circ$  for degree of linear polarisation and polarisation angle, respectively. The polarisation of the wisps and inner nebula have also been measured with no significant variation in a 3 month period.

It is expected that these, and further, polarisation measurements will help provide essential data to constrain theoretical models, such as those mentioned above and also McDonald et al. (2011) who have developed an inverse mapping approach for determining the emission height of the optical photons from pulsars.

---

In the case of the Crab pulsar, the model uses the optical Stokes parameters to determine the most likely geometry for emission, including: Magnetic field inclination angle ( $\alpha$ ), the observers line of sight angle ( $\chi$ ), and emission height. The findings of this model show that the most likely emission altitude is at 20% of the light cylinder radius above the stellar surface, in the open field region; also showing agreement with the Pacini model and Shearer and Golden (2001) - the emission occurs at a constant fraction of the light cylinder radius. The authors also present a general treatment of the expected polarisation from a synchrotron source with a truncated power law spectrum of particles.

## 2.9 Optical Studies of Giant Radio Pulses

Not after the discovery of pulsars, Staelin and Reifenstein (1968) and Heiles and Campbell (1970) reported the detection of giant radio pulses (GRPs) from the Crab pulsar. These were discovered during a search for dispersed periodic signals after the discovery by Hewish et al. (1968). The term giant-pulses was coined for individual radio pulses that are 10 - 20 times stronger than the mean pulse energy (Slowikowska et al., 2007). Finding a correlation, or lack of one, between the lowest (radio) and highest ( $\gamma$ -ray) energy emissions would have profound implications for models of the nature of pulsar emission. Lundgren et al. (1995) reported that giant-pulse fluctuations are most likely associated with changes in the coherence of the radio emission. It is reported that, after accounting for scintillation effects resulting in propagation of the signal through the interstellar medium, the giant pulses remain. This suggests that they are caused by a change in the emission mechanism at the pulsar. The authors show that the correlation analysis between  $\gamma$ -ray and radio observations reveal that the  $\gamma$ -ray emission does not vary more than 2.5 times the average level at the giant radio-burst times. Lack of correlation implies that giant radio-bursts are primarily caused by enhanced coherence, not variable pair-creation rates. Sallmen et al. (1999) showed that the giant pulse emission from the Crab pulsar is broadband where 70% of the pulses were observed at 1.4/0.6 - GHz. This was concluded to be intrinsic to the pulsar emission process and not the result of multiple imaging in the intervening plasma. Further work in radio emission resulted in a discovery by Hankins et al. (2003) where the authors

---

show that these giant pulses are superpositions of extremely narrow nanosecond-duration structures.

The radio emission is chaotic (pulse-by-pulse), however, an averaged pulse profile is steady. This is made more complex by the existence of GRPs. The study of giant radio pulses detected from a number of pulsars, can begin to restrict the environment within the radio emission zone and thus inform on the nature of the radio emission and its relationship to the higher energy emission. On the other hand ‘normal’ pulsar activity results in regular, repeating periodic lightcurve signals, the giant pulses occur at random intervals and have energies up to many thousands of the mean energy.

Jessner et al. (2005) showed that GRPs are located in all phases of ordinary radio emission, and not restricted to only two of the pulse components (main and inter), which was originally proposed by Cordes et al. (2004) observations of the Crab pulsar. These components are the same as those detected at optical, X-ray and  $\gamma$ -ray energies, suggesting that the mechanism for giant pulse emission occurs high in the magnetosphere, where these emissions are expected to originate, also discussed by Harding and Daugherty (1998). The occurrence of giant pulses is strongly frequency dependent. Cordes et al. (2004) found that giant pulses ‘follow’ the inter pulse in pulse phase as it shifts to earlier phases above  $\sim 4$  GHz; they conclude that the same physical region produces both the low-frequency and the shifted, high-frequency inter pulse.

GRPs are believed to be associated with non-thermal high energy emission, the Crab pulsar being the best known example. Confirmation of this idea came from observations by Romani and Johnston (2001) of millisecond pulsar PSR B1821-24. The authors detect individual pulses from the high  $\dot{E}$  of this MSP with energies exceeding 50 times the mean pulse energy. These giant pulses are concentrated in a narrow phase window coincident with the power-law non-thermal pulse seen in hard X-rays. The idea that large  $B$  fields in the outer magnetosphere are critical to the formation of such pulses is supported by the phenomenon of GRPs.

A correlation was detected between optical and giant radio pulse emission from the Crab pulsar by Shearer et al. (2003) which showed that the giant radio pulses were on average 3% brighter than those coincident with normal radio pulses, see Figure 2.11. It was observed that only the optical pulse, which is coincident with

---

a GRP, shows enhanced intensity ( $7.8\sigma$  brighter than the mean profile); this suggests that the GRPs and increased optical emission produced in the Crab pulsar's magnetosphere are linked to an increase in the electron-positron plasma density. Whatever triggers the GRP, it releases energy uniformly throughout most of the electromagnetic spectrum, as implied by similar energies of radio and enhanced optical pulses. Therefore, it is proposed that changes in the pair production rate at the level of a few percent could explain the optical variations, and would be expected at higher energies (not contradicted by existing limits to enhanced  $\gamma$ -ray emission). Further information is required to account for the radio GRPs mechanism.

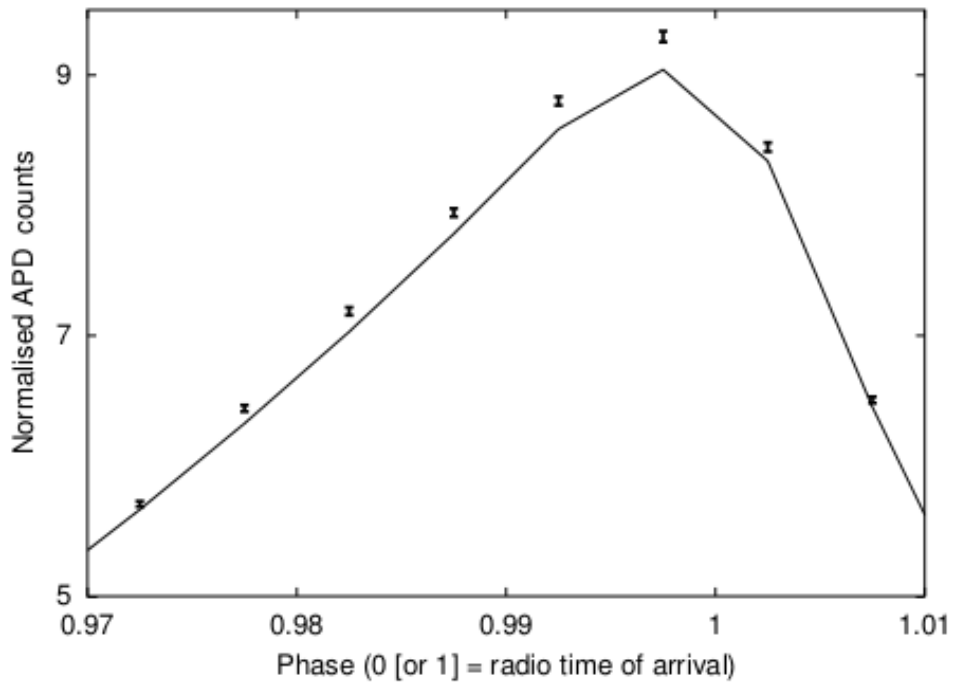


Figure 2.11: The mean optical ‘giant’ pulse superimposed (including error bars) on the average optical pulse (Shearer et al., 2003). The average pulse is determined from the 40 pulsar periods centred on the GRP, but not including it, from both nights of observation.

Knight et al. (2006) detected giant pulses from the pulsar PSR J1824-2452A. The pulses were found to occur in two narrow regions, which correlate in phase with the X-ray emission and trail the peaks of the integrated radio pulse-components.

---

The authors show that X-ray emission occurs over a wider phase range than the giant pulses, and (again) conclude that the two emission phenomena likely originate from similar regions in the magnetosphere, but not necessarily from the same physical mechanism. Furthermore, Lommen et al. (2007) reports correlations between the Vela pulsar’s X-ray emission and radio arrival times on a pulse-by-pulse basis. A significantly higher flux density was found in Vela’s main X-ray peak during radio pulses that arrived early. The excess flux was found to shift to the ‘trough’ following the second X-ray peak during radio pulses that arrived later. This further strengthens the case where it is believed that the mechanism producing the radio pulses is connected to that producing the X-rays.

Słowińska et al. (2009) show that there exists a subtle connection between the presumed non-coherent (optical) and coherent (radio) emissions. This supports findings by Shearer et al. (2003). Słowińska found that the minimum degree of optical polarisation occurs at the phase of 0.999, which is very close to the radio pulsar phase. It was found that the behaviour of  $\theta$  as a function of phase observed for the Crab pulsar at optical wavelengths differs from those observed at radio wavelengths (e.g. Moffett and Hankins (1996); Karastergiou et al. (2004), and Słowińska 2005). Two possible factors that could account for this difference are: Different propagation effects, and different intrinsic emission mechanisms. The former, in particular, has a role in explaining high-energy emission models such as the outer-gap or the two-pole caustic model. These have been discussed in Section 2.6.

Strader et al. (2013) observed a link in the Crab pulsar between enhancement of an optical pulse and the timing of the corresponding GRP. This was observed using the ARray Camera for Optical to Near-IR Spectrophotometry (ARCONS) (a unique superconducting energy-resolving photon-counting array); radio observations were taken at the Green Bank Telescope. An  $11.3 \pm 2.5\%$  increase in peak optical flux for pulses that have an accompanying GRP arriving near the peak of the main optical pulse, in contrast to  $3.2 \pm 0.5\%$  increase when an accompanying GRP arrives soon after the optical peak. In the case of the inter pulse, for the same analysis, there is a  $2.8 \pm 0.8\%$  optical enhancement. This strengthens the link in the origin of optical and radio emission; no significant, statistical differences were found in spectral data suggesting the same mechanism is responsible for all

---

optical emission.

Further studies of the linear polarimetric characteristics in the high-energy regime is a powerful tool which would further our understanding of the pulsar emission mechanism. Polarimetric information of GRP emission could be an indication that these pulses have the same polarisation as the optical emission and hence, the same geometry. From an optical observational standpoint, GRPs are significantly more difficult than normal pulsars to observe - random arrival of pulses albeit in phase with normal emission, and at a rate significantly less than the normal pulsar rate. For this reason, polarisation studies of these types of event restrict the type of polarimeter, which can be used in the GRP studies; this makes simultaneous measurements of all Stokes parameters important (Shearer, 2008). Observing the optical polarimetric signal during GRP events is one of the main motivations in developing the GASP instrument for high-time resolution astrophysics. Studies involving joint radio observations with GASP offer the opportunity to constrain current emission models.

---

# Chapter 3

## The Galway Astronomical Stokes Polarimeter

This chapter summarises the work of a paper published by Collins et al. (2013) in Experimental Astronomy in 2013 entitled ‘The Galway astronomical Stokes polarimeter: an all Stokes optical polarimeter with ultra-high time resolution’. More detail of the prism-rhomb design and development may be found in Collins (2012). The Monte Carlo noise modelling for the *GASP flux* found in Table 3.1, and the results in Section 3.3 were produced from the work of this thesis.

### 3.1 Science Motivation

There are many astronomical objects that emit polarised light. Quite a lot of information can be gathered by taking polarimetric measurements, both about their source mechanisms, and about (scattering) geometry in their source regions. To date, stellar observations have focused, for the most part, on the linearly polarised component of the emission. Largely, the motivation in developing the Galway Astronomical Stokes Polarimeter (GASP) has been to enable the ability to make observations on these very sources.

Observations have been restricted due to inadequate instrumentation, and particularly the need for suitable observing conditions and the availability of luminous targets. This leaves a whole range of interesting objects beyond the range of observation at present.

---

Polarisation can be considered to be either intrinsic, that is coming from the object's source function, or extrinsic, in that the radiation is modified after emission primarily through scattering (Collins et al., 2013). Optical observations of astronomical objects, which benefit from polarimetric observations include active galactic nuclei (Angel and Stockman, 1980; Laor et al., 1990; Goosmann et al., 2007; Agol and Blaes, 1996), compact binaries (Patterson, 1994; Cropper, 1990; Stockman et al., 1992; Wickramasinghe and Meggitt, 1986; West, 1989; Katajainen et al., 2007), and pulsars (Słowińska et al., 2009). In all these cases, the emission comes from non-thermal sources - most likely the interaction of relativistic plasma with a strong magnetic field. Stellar scale binary systems normally show distinct stochastic and periodic variability; consequently, time resolved polarimetric observations are important. GASP is ideally designed to observe targets such as isolated neutron stars, either pulsars or magnetars, and compact binary systems. Shearer et al. (2010) give a review of the current state of optical polarimetric observations of these systems. Table 3.1 gives a summary of fluxes and exposure times for detecting targets with a degree of polarisation of  $\sim 5\%$  against normal sky background and  $1''$  seeing/aperture.

---

<sup>1</sup>Four main groups of targets have been identified. The first two groups, pulsars and magnetars, the time scale given is the rotation period. Gamma-Ray bursts, a one second integration period has been used. For the binary systems, the orbital period of the secondary has been specified. We note that the rotation period of the primary is likely to be significantly less than this.

<sup>2</sup>The GASP flux is based upon the measured throughput of GASP and assuming 70% detector quantum efficiency and 95% total reflectivity of the telescope mirrors.

<sup>3</sup>counts/second/channel

<sup>4</sup>The given polarisation is either for the pulsed signal (P) or the time-averaged signal (A). In terms of understanding the physics of the objects it is usually the pulsed signal, which is of primary interest.

<sup>5</sup>The figure given here shows the actual sensitivity required for the science case and the actual polarisation assuming an unpolarised sky background. A V-band sky background of 21.5 magnitudes/ $''^2$  has been assumed.

<sup>6</sup>Periodic

<sup>7</sup>Aperiodic

<sup>8</sup>E 1841-045 and GRB exposure times have been based upon I and R band sensitivity and sky background, respectively.

Table 3.1: Expected degrees of polarisation fluxes, & minimum exposure time for detecting  $\sim 5\%$  polarisation Collins et al. (2013).

Target <sup>1</sup>	Time Scale (s)	Magnitude (V)	GASP Flux <sup>2</sup> c/s/c <sup>3</sup>		Object Polarisation (%)	Polarisation sensitivity requirement <sup>5</sup> (%)		Exposure Time - 5% polarisation (s)	Ref
<b>Pulsar</b>			4m	10m		Object	Total	4m 10m	
Crab	0.033	13.8	2800	17100	16 (P) <sup>6</sup>	0.1	0.1	6000 1000	Slowikowska et al. (2009); Smith et al. (1988)
Vela	0.089	24	3.7	22.5	9.4 $\pm$ 4 (A) <sup>7</sup>	1	0.03	> 12 13800 hours	Wagner and Seifert (2000); Mignani et al. (2007b)
B0540-60	0.050	23	9.3	56.6	< 15 (P) 5 (A)	1	0.07	10000 1700	Wagner and Seifert (2000); Middleitch et al. (1987); Chanan and Helfand (1990)
B0656+14	0.385	25	1.5	9.0	0 - 100	2	0.03	> 12 15000 hours	Kern et al. (2003)
<b>Magnetars</b>									
4U 0142+61	8.69	25 - 26	0.8	5.1	Not known	5	0.03	> 12 15000 hours	Hulleman et al. (2000)
1E 1841-045	11.78	25.3 (I)	1.5	9.4	Not known	10	0.05	> 12 28000 <sup>8</sup> hours	Dhillon et al. (2009)
<b>Gamme Ray Bursts</b>									
GRB 090102	1	13 (R)	92000	56400	1%	1	1	55 9	McConnell et al. (2009)
<b>Close Binary System</b>									
RX J0649.8-0737 (polar)	15811	17.2	1940	11800	Not known	0.1	0.09	6200 1030	Motch et al. (1998)
RXJ1914.4+2456 (intermediate polar)	569	19.7	194	1180	Not known	0.1	0.06	14000 2300	Strohmayer (2004)

---

## 3.2 Instrument Introduction

The Stokes polarimeter (see Section 1.2.1) is a design that has been used experimentally for a wide variety of science objectives. Azzam et al. (1988) has developed a technique that is employed by this project called Division of Amplitude Polarimeter (DOAP). It has been described in Section 1.2.2.2 and the GASP PSA has been developed around this work and that of Compain et al. (1999), which will be discussed in more detail later. Figure 1.5 gives the general layout for a division of amplitude polarimeter.

The basis of this work comes from a design implemented in the laboratory by Compain and Drevillon (1998). It has been shown that (see Section 1.2.2.2) division of amplitude polarimeter (DOAP) involves the splitting of an incident beam of light into reflected and transmitted beams. The design of GASP is based on this DOAP design using partial reflection from the uncoated end surfaces of a rhomb-type prism, similar to a Fresnel rhomb. Two total internal reflections (TIR) within the main beamsplitting prism introduce a relative phase delay between the p and s waves of the transmitted light; this is dependent upon the refractive index of the glass and the angle of TIR. For glasses of typical refractive index (1.4 - 1.6) and suitable total internal reflection angles the relative phase delay can be  $45^\circ$  at each reflection, producing an effective quarter wave retardation overall. Hence, the rhomb can be used to convert linear to circular polarisation and vice versa.

A requirement of GASP is that the quarter wave phase retardation of the Polarisation State Analyser (PSA) is fully achromatic (explained in more detail in Section 3.2.1). The principle of the GASP design makes use of additional polarisation-dependent transmission/reflection introduced when the beam enters and exits the prism at steep angles. This was first reported by Compain and Drevillon (1998) in their paper ‘Broadband division of amplitude polarimeter based on uncoated prisms’. The main objective for GASP is to make use of the results reported by Compain and Drevillon (1998) and optimise their design for astronomical observations.

### 3.2.1 The Polarisation State Analyser (PSA)

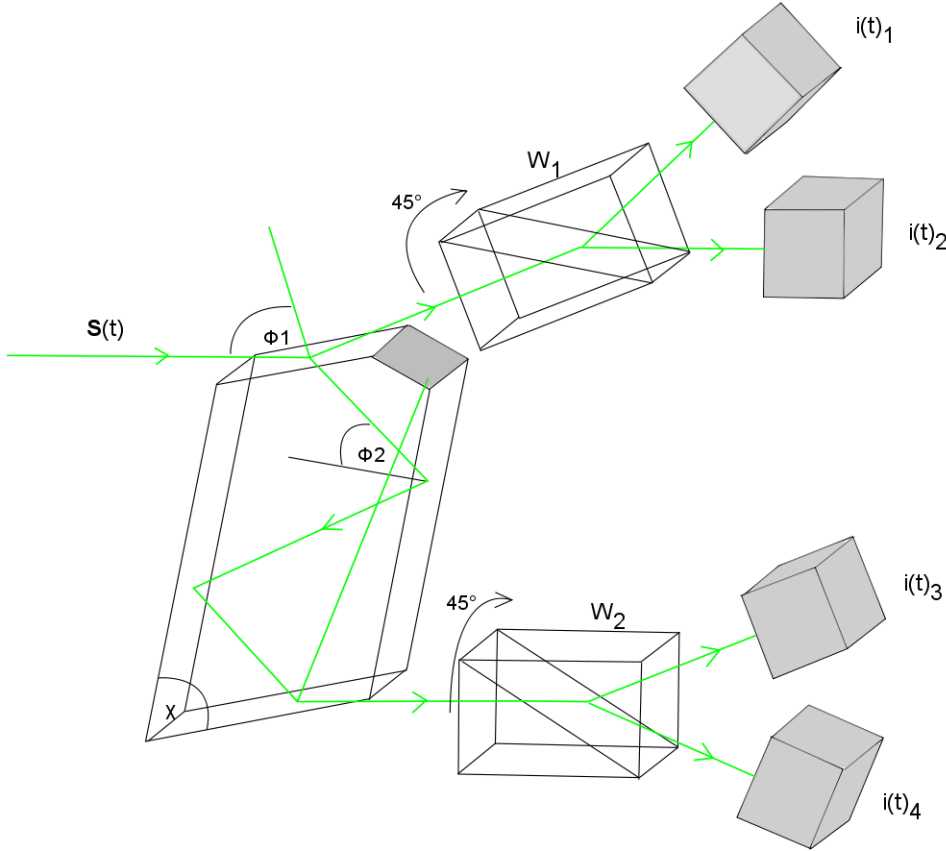


Figure 3.1: The optical layout of the Compain and Drevillon (1998) PSA for an uncoated dielectric prism for the V - NIR (Visible - Near-Infrared). The light beam is separated into two by a prism, then into four by two Wollaston prisms  $W_1$  and  $W_2$  oriented at  $45^\circ$  with respect to the plane of incidence. Stokes vector  $S$  is determined from the four intensities  $i_1 - i_4$ .

The usefulness of using the Stokes vector to measure the polarisation of light mathematically has already been described in Section 1.2. A DOAP is a polarimetric tool where an incident light beam is separated into four beams in order to measure the incoming Stokes parameters from the four detected intensities. This is done using a Polarisation State Analyser, known as the PSA from here on. The PSA is the combination of the main beamsplitting Fresnel rhomb and two polar-

---

ising beamsplitters such as Wollaston or Foster prisms. The orientation of the Wollaston prisms is not critical in a relative sense, as long as they are aligned to some integer multiple of  $45^\circ$ . An orientation at  $0$  or  $90^\circ$  would result in a non-invertible matrix  $A$ . A  $45^\circ$  angle produces an invertible matrix and splits the beam 50:50; once the system has been aligned experimentally, it must be calibrated based on this alignment.

The PSA has a characteristic matrix that fully describes the instrument, polarimetrically, by linking the four measured intensities to their corresponding Stokes vector, i.e., it contains all the information for how well the instrument is calibrated, experimentally. Figure 3.1 describes a typical layout for the DOAP configuration. The orthogonal prism, with its base in the plane of incidence, acts as a first-stage beamsplitter and provides the essential polarimetric properties. These properties are displayed, as usual, by the reflection and transmission Fresnel coefficients of the prism (Azzam and Bashara, 1988),

$$T^2 = \frac{1}{2} (t_p^2 + t_s^2) \quad (3.1a)$$

$$R^2 = \frac{1}{2} (r_p^2 + r_s^2), \quad (3.1b)$$

where p refers to the plane of incidence and s to the orthogonal direction. Transmission coefficient T must often be corrected to take into account the absorption, which is not negligible when high-refractive-index glasses are used. The absorption depends on the optical path L inside the prism and on absorption coefficient  $\alpha$ . The intensity of the transmitted beam is then multiplied by

$$\exp(-\alpha L). \quad (3.2)$$

The ellipsometric angles  $\Psi$  and  $\Delta$  describe the polarimetric properties of the prism. They are defined by

$$\tan(\Psi_r) \exp(i\Delta_r) = \frac{r_p}{r_s}. \quad (3.3a)$$

$$\tan(\Psi_t) \exp(i\Delta_t) = \frac{t_p}{t_s} \quad (3.3b)$$

---

The  $4 \times 4$  real matrix  $\mathbf{A}$  is the characteristic matrix of the polarimeter. It can be derived from the ellipsometric angles of the prism given by Equations 3.3a and 3.3b

$$\mathbf{A} = \mathbf{D} \begin{bmatrix} 1 & -\cos 2\Psi_r & \sin 2\Psi_r \cos \Delta_r & \sin 2\Psi_r \sin \Delta_r \\ 1 & -\cos 2\Psi_r & -\sin 2\Psi_r \cos \Delta_r & -\sin 2\Psi_r \sin \Delta_r \\ 1 & -\cos 2\Psi_t & \sin 2\Psi_t \cos \Delta_t & \sin 2\Psi_t \sin \Delta_t \\ 1 & -\cos 2\Psi_t & -\sin 2\Psi_t \cos \Delta_t & -\sin 2\Psi_t \sin \Delta_t \end{bmatrix}, \quad (3.4)$$

where  $\mathbf{D}$  is defined by

$$\mathbf{D} = \frac{1}{2} \begin{bmatrix} G_1 R & 0 & 0 & 0 \\ 0 & G_2 R & 0 & 0 \\ 0 & 0 & G_3 T & 0 \\ 0 & 0 & 0 & G_4 T \end{bmatrix}, \quad (3.5)$$

where the values for  $G_i$  refer to the gain coefficients of each detector. The system matrix that is calculated experimentally contains all this information including detector gain. The optimization of the PSA for this work will not be discussed in this thesis, but can be found in Collins (2012).

The matrix is divided into 4 rows. The first 2 rows represent both RP channels, and the second 2 rows are each of the TP channels. Of course, the order of these channels within each path depend on the experimental optical alignment. The first column of the system matrix (and the PSA) represents the gain of the 4 channels of the DOAP, which also includes the gain of each detector. The last 3 columns represent the physical meaning of the ellipsometric angles of the rhomb-prism. The second column of the GASP PSA is the  $-\cos$  of the relative amplitude change of the s- and p- components of the light ( $\Psi$ ). The last 2 columns use  $\Psi$  and  $\Delta$ , the phase difference between the p- and s-direction of the complex Fresnel reflection and Transmission coefficients. These values are dependent on the AOI, and hence the TIR angle. These are essentially the properties of the entire PSA and an experimental matrix is calculated by probing the PSA with many polarisation states of light (this is discussed in Section 5.3). This is discussed in greater detail by references such as Compain and Drevillon (1998); Azzam et al. (1988); Azzam and Bashara (1988), which is beyond the scope of this work.

---

### 3.2.2 The Polarimeter Design

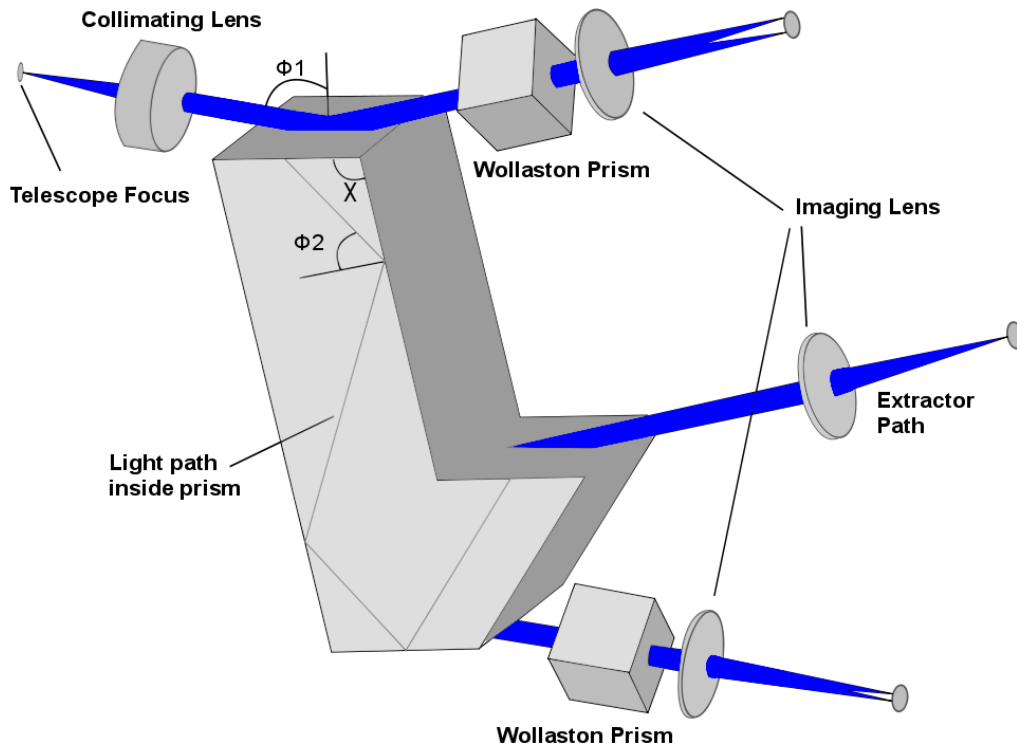


Figure 3.2: The optical layout of GASP. This is a general design used for any telescope and any detector system. The optical prescription (with the exception of the main beam splitting prism) changes depending on the choice of telescope and detector.

The initial GASP design was presented by Collins et al. (2009); where it describes how GASP measures the four components of the Stokes vector simultaneously with a retardance error  $\ll 1\%$  over a spectral range of 400 - 800 nm. The optical design of GASP contains no moving or modulating components. Therefore, it is possible to achieve high time resolution (of order microseconds), and temporal stability based on the choice of detector.

The beam at telescope focus is collimated to a suitable pupil size (see Section 4.3.3), producing  $S(t)$  and is separated into two beams:  $R(t)$  - reflected, and  $T(t)$  - transmitted. The expected intensities of  $T(t)$  and  $R(t)$  are arranged to be approximately equal when fully unpolarised light is incident on the prism.

---

This is dependent on the chosen angle of incidence (AOI) of the prism, and the orientation of the subsequent polarising beamslitters. There is a range of values for the AOI for which the prism rhomb can achieve a suitable TIR producing a quarter wave retardance. Therefore, this configuration can vary for reasons that will be explained in Chapter 4. The AOI is denoted by  $\phi_1$ , on the uncoated face of the prism, and the internal angle that defines the shape of the parallel sided prism, is denoted by  $\chi$ . Both  $R(t)$  and  $T(t)$  are, subsequently, divided into two by two polarising prisms (Wollaston prisms, W1 and W2, in this case) oriented at  $45^\circ$  to the plane of incidence on the prism. The internally transmitted beam  $T(t)$  undergoes a quarter wave uniaxial phase delay created by two total internal reflections at angle  $\phi_2$  (determined by the geometry and the refractive index of the glass) inside the prism, and is then partially transmitted and partially reflected at the bottom face of the prism. The values in Table 3.2 are the properties corresponding to the current GASP rhomb and configuration for the instrument. All measurements, theoretical and experimental, use these values.

Table 3.2: Geometrical and polarimetric properties of the current GASP prism-rhomb Collins et al. (2013).

Prism Geometry	Glass Properties	Polarimetric Properties	
		Reflection	Transmission
$\phi_1 = 78.50^\circ$	$\lambda = 589\text{nm}$	$R = 0.3533$	$T = 0.4352$
$\phi_2 = 58.48^\circ$	$n = 1.589$	$\Delta_r = 180^\circ$	$\Delta_t = 90^\circ$
$\chi = 96.62^\circ$	$\alpha = 0.2002$	$\Psi_r = 30.48^\circ$	$\Psi_t = 59.85^\circ$

GASP works by splitting the beam into two components, and then using each of the Wollaston prism in each of the two beams producing intensities  $i_1-i_4$ . The ratios of intensities  $i_1$  and  $i_2$  carry information about Stokes parameters Q and U when related to the instrument calibration. An achromatic quarter wave phase retardation (turning circular into linear polarisation) and additional diattenuation

---

is introduced into one of the beams, which the second polarising beamsplitter (PBS) can then examine - the ratios of  $i_3$  and  $i_4$  therefore carry information about the Stokes parameters  $Q$  and  $V$ , as above. Information about  $I$  is carried by the linear combination of  $i_1 + i_2 + i_3 + i_4$ , again through calibration.

The Stokes vector is determined from the intensities  $i_1$ ,  $i_2$ ,  $i_3$  and  $i_4$ . In Figure 3.2 (modified version from Collins (2012) and Collins et al. (2013)), it can be seen that in the original Compain and Drevillon (1998) design there was an inevitable  $\sim 20\%$  of the light reflected from the second face of the main beamsplitting prism. In their design, one vertex of the prism was removed and the resulting surface roughened and blackened in an attempt to absorb this waste light, which might otherwise result in stray reflections. In the design stage of GASP, an additional ‘extractor’ prism, was designed to produce transmission of  $\sim 80\%$  of the stray light into an external beam parallel to  $R(t)$  to be used for finding, guiding, and/or photometry; however, it would not be possible to produce any components of the original Stokes vector from this extractor arm. The final  $\sim 4\%$  waste light is also absorbed by a blackened ground surface.

Various optical designs of GASP have been explored, in which the four beams  $i_1 - i_4$  have been detected in various ways. These include a single imaging detector design, a double imaging detector design, and a multiple non-imaging detector design (using an array of photon counting avalanche photodiodes). These various solutions are appropriate to different astronomical targets; the imaging solutions offer high efficiency and the ability to perform polarimetry on point or extended sources in complex field regions, under varying atmospheric seeing conditions, however, they have limited time resolution. For the highest time resolution, photon counting detectors are required. Whilst these considerations are peripheral to the optical design and performance of GASP, detector limitations (noise and stability) ultimately limit its performance.

The initial design for GASP utilised a single-imaging-detector, see Figure 3.4. The collimated light beam  $S(t)$  is split into two beams  $R(t)$  and  $T(t)$  by the retarding beamsplitter. The resulting four beams are refocused upon one imaging detector using a 2-mirror solution to capture both beams. A third beam ( $\sim 16\%$  of the total intensity) can be extracted and refocused on a further imaging detector. This can be used for guiding during observations for a non-imaging system.

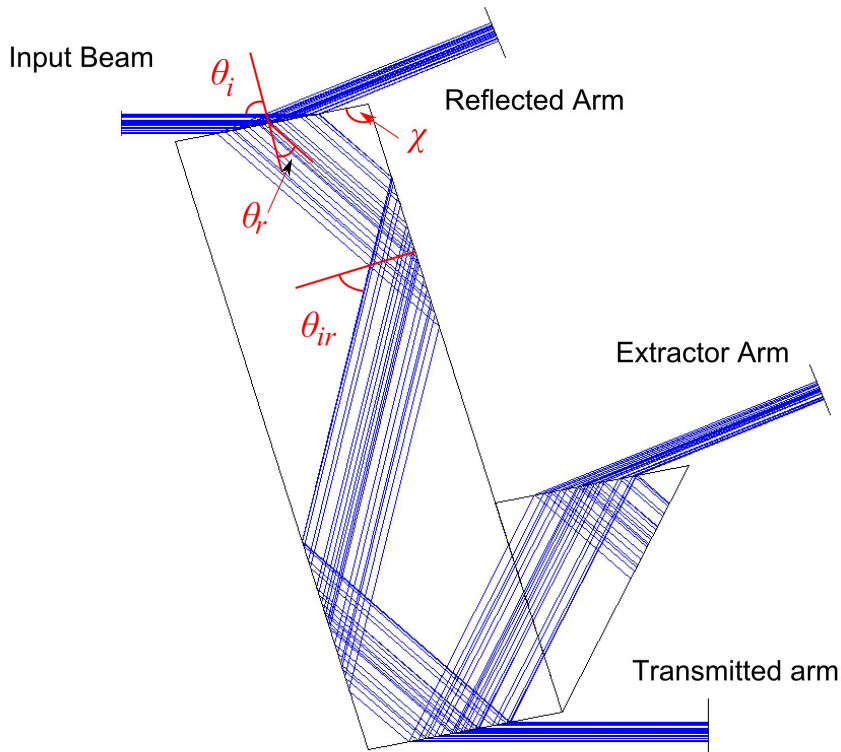


Figure 3.3: Final Zemax design of the GASP main beamsplitter (Collins et al., 2013). The reflected and transmitted beams can be seen, and the extractor arm, which can be used for guiding.

This design had considerable difficulties in alignment and resulted in reduced light throughput due to the extra optical reflections. A double-imaging-detector and 8-detector system will be explored in Chapter 4.

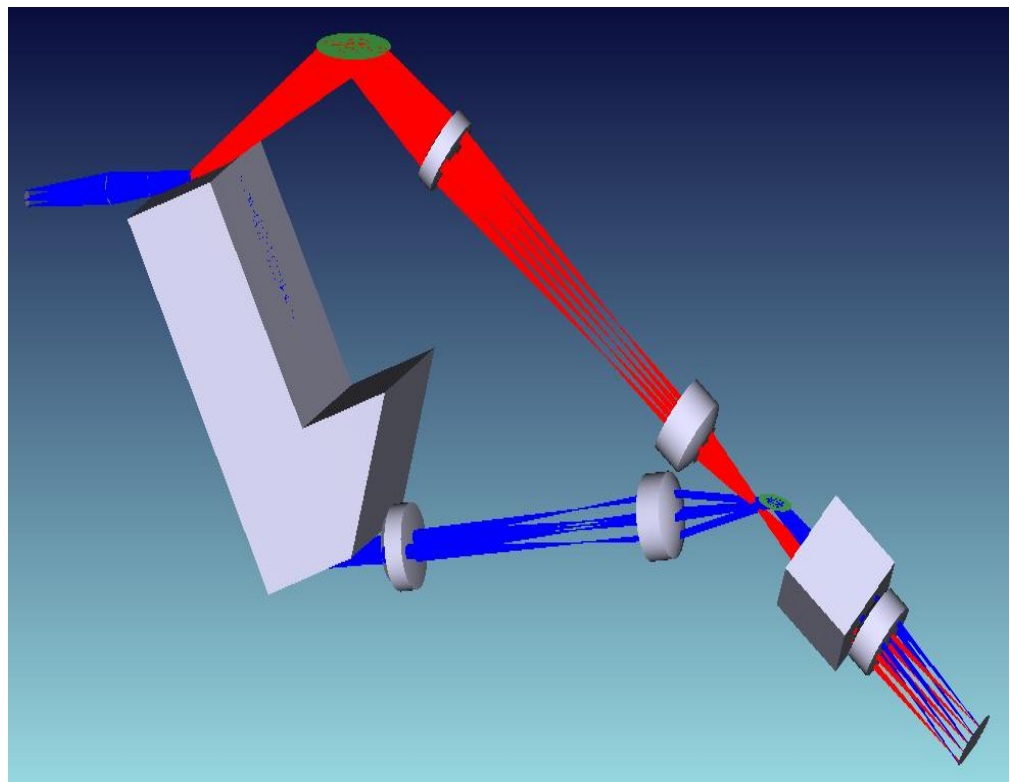


Figure 3.4: Optical layout for GASP as a single-imaging-detector polarimeter (Collins et al., 2013). The instrument used reflecting mirrors orientated to capture all 4 beams on a single chip.

---

### 3.3 Noise Sensitivity of GASP

A photon counting polarimeter like GASP - which relies upon comparing the intensities of four light beams - is inherently subject to Poisson noise at various stages in its calibration and use. The effect of noise in calibration is to produce (fixed) errors in the calibration matrix (**A**) which lead to small systematic errors in the measurement of the components of the Stokes vector of the incoming light, but it does not introduce random noise. These systematic effects during calibration can be minimised by combining very large numbers of counts at each calibration angle, and the use of a calibration method, which achieves this through averaging effects or a set of algebraic conditions (further discussion in Section 5.5).

Part of the work of this thesis was a theoretical investigation into the Poisson noise contribution to the GASP PSA during calibration, and use as a full Stokes polarimeter. The results of this analysis can be found in Figure 3.5 where the degree of linear and circular polarisation (DOLP and DOCP respectively) are examined.

The effect of noise in actual target measurements is more complex, affecting different Stokes vectors differently. This is because certain extreme values - for example nearly 100% polarised light, either linear or circular, at particular orientations - could lead to one of the output intensities  $i_1$ ,  $i_2$ ,  $i_3$  or  $i_4$  becoming very small. Then small statistical fluctuations in one of these numbers become exaggerated in the mathematics of the matrix inversion used to generate the input Stokes vector from the output intensity vector. In the case of astronomical targets, however, these extreme situations essentially never occur and for the purposes of investigating the Poisson-noise sensitivity of GASP, polarised light with 20% linear and 0% circular polarisation, and a total count rate of  $3 \times 10^6$  counts per second subject to Poisson fluctuations, has been simulated and then analysed. An investigation of these errors using simulated GASP data has been carried out, and the results of one such simulation run are given in Figure 3.5.

A simulation, illustrated in Figure 9, shows that in the situation where the counts are approximately equally distributed between the four output channels, output noise in the measurement of the degree of linear polarisation (DOLP) has a noise corresponding to Poisson fluctuations in 50% of the total count, and in the

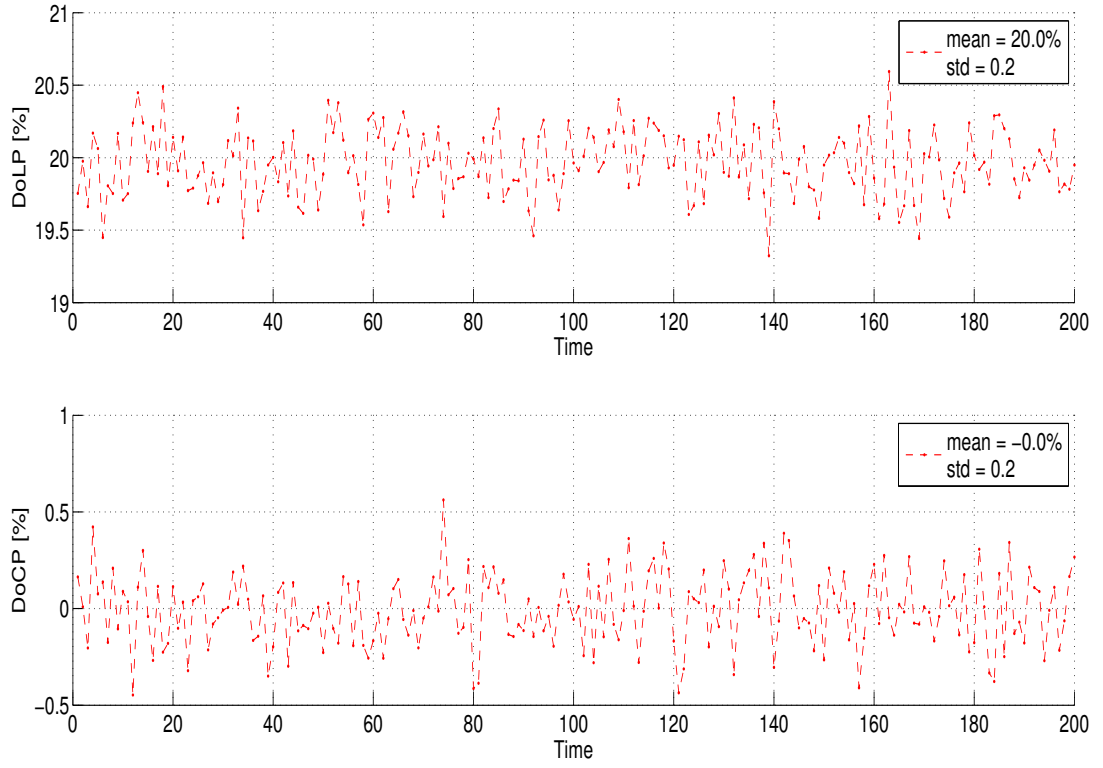


Figure 3.5: Monte Carlo Simulation of GASP data using a theoretical calibration matrix (found above) to model both the ingoing light and outgoing polarisation values (degree of linear and degree of circular polarisation). The simulation was modelled for a wavelength of 589 nm (for the prism glass type) (Collins et al., 2013).

degree of circular polarisation (DOCP) to 100% of the total count. This enables us to compute the sensitivity of GASP as a function of bandwidth for targets of different magnitudes, observed on various sized telescopes. Figure 3.5 plots the absolute value for DOCP. DOCP can be both positive and negative, which simply implies a different direction. The subject of these simulations was investigated for the purpose of publication by Collins et al. (2013); however, detailed investigations of the noise sensitivity of GASP will be the subject of a later paper.

---

## Chapter 4

# Optical and Hardware redesign of GASP

The optical skeleton of GASP as a working polarimeter was near to completion when this thesis work began. The Polarisation State Analyser was developed by Collins et al. (2009). The choice of polarimeter was Division of Amplitude Polarimeter, which has been discussed in Section 1.2.2.2 and 3.2.1.

When work for this thesis began GASP was in the final stages of development as an 8-detector polarimeter using APDs, the specifications for which can be found in Appendix D. These detectors were used for laboratory purposes; they were brought to Loiano observatory in Bologna Italy but due to inadequate weather conditions testing the polarimeter's calibration on astronomical targets was not possible.

It was discovered that a number of APD modules were beginning to fail prior to moving GASP to the California Institute of Technology (Caltech). There were also issues regarding the noise level of the APD array modules, which showed that for the purpose of observation, these would not be sufficient for observing fainter targets. It was not possible to replace these APDs due to funding limitations.

Observation time was awarded to GASP at the Palomar 200 inch telescope (P200), and due to a collaborating group at Caltech, 2 Andor iXon Ultra 897 EMCCDs were loaned to the project. An optical redesign was required: This was due to mechanical modifications made to the polarimeter to establish a suitable method of calibration. The objective of this redesign was to produce an acceptable FOV and pixel scale for GASP to use it as an imaging polarimeter. The solution

---

will be presented in Section 4.3.4.

Another approach to solving the FOV problem when imaging is a redesign of the prism-rhomb. Details of the design constraints can be found in Collins (2012); the main objective of the prism-rhomb design was to produce a quarter wave retardation that was as achromatic as possible. This was carried out using a low dispersion glass with a refractive index of  $\sim 1.59$ ; it was optimised thusly. To redesign this prism-rhomb, for a criterion such as a larger FOV, would require further funding to the project, which was not available at the time, however, it is an important consideration for future imaging polarimeter systems based on the GASP design.

## 4.1 Imaging using 1-Detector

GASP is a versatile instrument regarding the choice of detector; the detector choice is dependent on the main science motivation for this instrument. The initial design concept for the polarimeter was a 1-detector imaging system (see Collins (2012) for further reading on the implementation of this design). The 1-detector design used the GASP PSA with some modifications in order to capture the 4 intensity beams on a single detector chip. This created a number of issues in terms of alignment and light loss for the overall system. Optomechanical restrictions along with the number of detectors available meant that GASP was required to image 4 beams on one chip. The reflected and transmitted beams are each reflected using 2 plain mirrors. It is important that they be parallel to each other before entering the Wollaston prism, and the final imaging lens, to prevent any vignetting of the FOV or beam elongation. There were both advantages and disadvantages associated with this type of optical system. In terms of alignment in the laboratory, it made for a simpler optical design to incorporate a 2-detector imaging system, or an 8-detector photon counting system, for GASP. This removed the need for making any alterations to the direction of the light beam after the prism-rhomb, keeping as close as possible to the PSA design by Compain and Drevillon (1998).

---

## 4.2 An 8-Detector Polarimeter

In addition to measuring polarisation, it is possible for GASP to work as a high-time resolution polarimeter - at microsecond time scales. It has been explained in Section 3.1 that valuable information can be uncovered when measuring phase folded polarisation for light curves of sources with millisecond periods. This is difficult to achieve with imaging detectors due to high readout noise and limited frame rate capability. This problem has been overcome by other high-time resolution instruments such as OPTIMA (Stefanescu et al., 2008), where these groups have used non-imaging photon counting avalanche photodiodes to achieve the necessary time resolution.

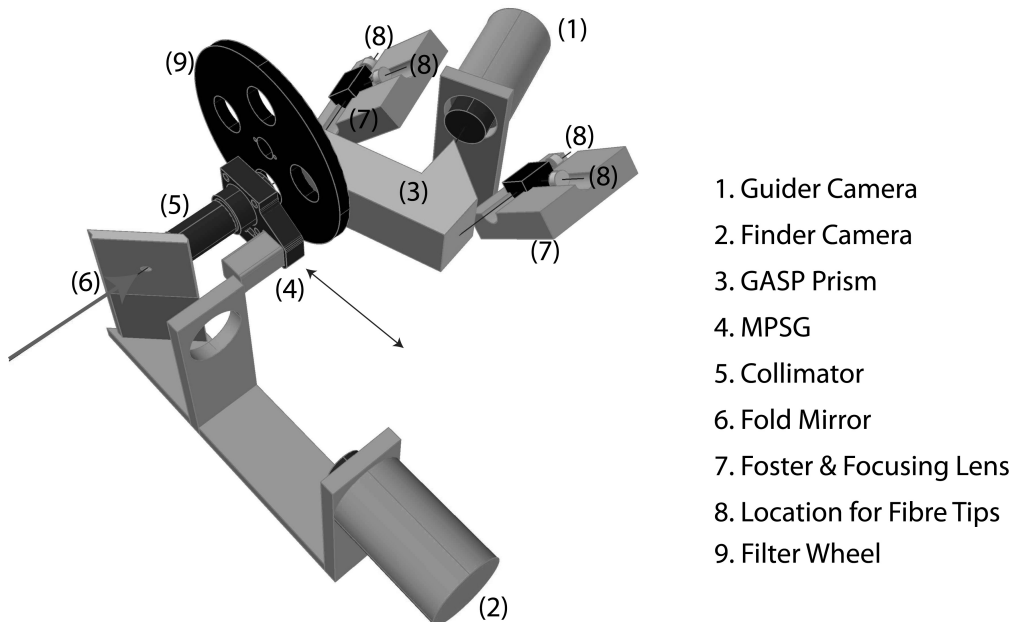


Figure 4.1: Optical Layout of a non-imaging (8 detectors) version of GASP (Collins et al., 2013).

Figure 4.1 describes how GASP uses an array of eight fibre-fed single photon counting avalanche photodiodes (APDs). The type of APDs that have been used by GASP are described in Appendix D. These are arranged as four pairs in four bundles with fibre tips separated by 250 microns, one pair for each of 4 PSA outputs. Supplementary optical components, needed for calibration of the

---

instrument, are common to imaging and non-imaging versions of GASP. GASP uses Foster prisms, instead of Wollaston, to achieve the second division of light. These are used for mechanical reasons, however, they provide less dispersion of the beam as the collimated beam is incident on the Foster prism-rhomb at  $90^\circ$ . This ensures all the collimated light retains its shape as it is passed to the fibre. Any elongation of the beam would not be accounted for if it extended past the physical size of the entrance aperture of the fibre head.

When using Foster prisms, it is important that the mounts are made to mechanically suit the experimental alignment that is required of a system such as this. All alignment is carried out by measuring counts from a detector such as a photon multiplier-tube (PMT) or an APD. When focusing the fibre optics, a well focused beam is found by obtaining a maximum count value. The mechanical structure, which holds the Foster prism must be adjusted rotationally to ensure that the beam is split 50:50. This is difficult to achieve, but it is a requirement to ensure no loss of light, and that the final calibrated system produces an invertible matrix.

Re-imaging is carried out using 4 aspheric lenses, one per fibre, which are used to eliminate spherical aberration. The lenses used in this design were 9 mm in diameter with a focal length of 12 mm. When combined with a collimating lens focal length equal to 40 mm, this produced a large enough demagnification to project a target of  $\sim 3 - 4''$  onto the fibre. The important aspect of this design is to gather all the light from a single target only. Corruption of the signal could occur if the demagnification was not large enough; this could occur if a signal from a nearby star was also acquired. As will be examined in Section 4.3.1 onwards, this is not a concern for an 8-detector system such as this. Assuming adequate seeing conditions, a field of view no larger than 6 or 7'' is sufficient, which is the case for the optical design used by GASP. All the light in this FOV is gathered by the fibre through each of the 4 lenses. 8 extra fibres are positioned either side of the target fibre (all fibres in one row) and these measure the background light. The project had access to 8 APD units and so 1 background fibre was used per target.

In order to locate astronomical sources after pointing, a finder camera is used and, using a fold-mirror, is located off axis. The finder camera and polarimeter

---

detectors are aligned so that optical axes of their respective fields match. This can be done using the prism-rhomb extractor arm which shares the same beam as the reflected and transmitted paths. The choice of design layout, and other considerations of a non-imaging version, will be described here.

In order to introduce all the necessary calibration components to the system, some minor mechanical changes were made to the front end of the polarimeter. In the early design stages, GASP used a pseudo-inverse calibration method. This required a rotating linear polariser and quarter waveplate to generate an over-determined system and was placed in collimated space. It has been discussed in Section 5.5 that this method can not eliminate errors introduced by the optical and polarimetric elements themselves as it bases all intensity measurements on an assumed alignment of the polarisation state generator.

During the design stage for an APD version of GASP, it was apparent that in order to create enough space for the calibration optics the position of the GASP PSA would need to be adjusted. This alteration to the polarimeter would mean that the pupil generated by the collimating optics would not be formed on the footprint of the prism-rhomb. This extra space allowed for a filter wheel, the Polarisation State Generator (PSG), and the main beamsplitting prism-rhomb.

For an 8-detector system, the location of the pupil was not of great concern. The further the PSA is from the pupil (ideally the pupil should form on the prism-rhomb footprint) the less collimated the beam will be as it passes through the prism-rhomb. This can result in vignetting and clipping of the FOV. However, the size of the field is completely limited by the size of the detector, and is usually chosen based on this factor. It is important that the field chosen is covered by the size of the detector head (commonly  $150\ \mu\text{m}$ ), and the optics determine the magnification required to image the target onto the APD fibre. Some initial calibration findings will be presented using an APD detector system in Chapter 5.6.

### 4.3 Imaging using 2-Detectors

GASP was awarded observing time for 4 nights on the Hale 200 inch telescope at Palomar Observatory. The first optical challenge with GASP was to establish a

---

suitable optical design that would demonstrate GASP as an imaging polarimeter, enabling an acceptable FOV for a 5-m class telescope. The obvious approach would be a redesign of the prism-rhomb making it capable of imaging a larger FOV, however, due to lack of funding this was not possible. There were also obstacles encountered using APDs (see Appendix D), which include failing modules and high noise levels measured from the APD array modules. An opportunity to use 2 Andor EMCCD detectors was available by a collaborating group at the California Institute of Technology, therefore GASP was modified for use as an imaging polarimeter.

#### 4.3.1 The Field of View Problem

The focal ratio determines the choice of optics, and depending on the focal length of the mirror, this is a limiting factor to the size of the field of view of the instrument. The optical changes to GASP for an 8-detector system meant that the FOV size was limited by the distance from the prism-rhomb to the collimator. The pupil location was an important factor to consider when moving back to an imaging system, and a number of lens combinations were analysed to find a solution to this problem.

Another factor that must be considered when imaging is pixel scale. This is the ratio of the size of the object imaged (usually in units of arcseconds) to the number of pixels taken up by the object on the detector. It leads to two possible issues that arise in systems such as these, over- or undersampling of the object's point-spread-function (PSF). Images that have blocky or square stars suffer from undersampling. This means that there are not enough pixels covered for each star's image. The number of pixels that make up a star's image is determined by the relationship between the telescope focal length, the physical size of the pixels (in microns), and the size of the star's image (in arcseconds). Oversampling arises when the size of the star is spread out over too many pixels. The larger the pixel, the more sensitive the detector will be for any given focal length, which is also a sampling issue. Oversampling will result in reduced sensitivity, but better resolution.

The size of the prism-rhomb, and focal length of the mirror, define the in-

---

strument FOV. When the main beamsplitting prism-rhomb was moved for an 8-detector system, this meant that the pupil did not fall on the prism-rhomb footprint. Instead the pupil formed before the prism-rhomb, resulting in vignetting and hence reducing the overall field available for imaging. It was necessary to rectify this problem if GASP was to work on a telescope of larger mirror diameter and focal length.

A requirement of any instrument, when observing, is the ability to guide. In particular, calibrating GASP relies on matching pixels across the 4 channels, as well as between the observed target. This means that keeping the target on the same set of pixels at all times is a priority. A larger field will introduce more stars that can be used for guiding. The following section addresses the issue of the pupil and the steps taken to produce a suitable optical design for the mechanical layout.

### 4.3.2 Choice of Telescope Focus

Any optical design work carried out with GASP will require a Zemax prescription including design information for the telescope focus in use. In order to achieve as large FOV as possible, GASP was designed to accept an f/9 beam (platescale of 4.51"/mm) at the Cassegrain focus of the P200, compared to the native f/16, which has a smaller platescale (2.54"/mm). A Zemax ray tracing image for the f/9 set-up can be found in Figure 4.2.

Part of this work required producing a Zemax prescription for the f/9 focus as this was not readily available at Caltech. The original ray tracing drawings for the primary and secondary mirrors were available in the Caltech archives and these were used to achieve a telescope beam that could be accepted by GASP.

### 4.3.3 FOV and Pupil Conjugation

Figure 4.4 shows the GASP prism-rhomb for an f/9 optical set up on the 200 inch telescope at Palomar. The f/9 configuration was based on choice of collimating optics for GASP only. This a general Zemax representation of the beam propagation from the P200. This gives an estimate of the extent of the vignetting that was assumed to exist based on the modifications made for the APD detector system.

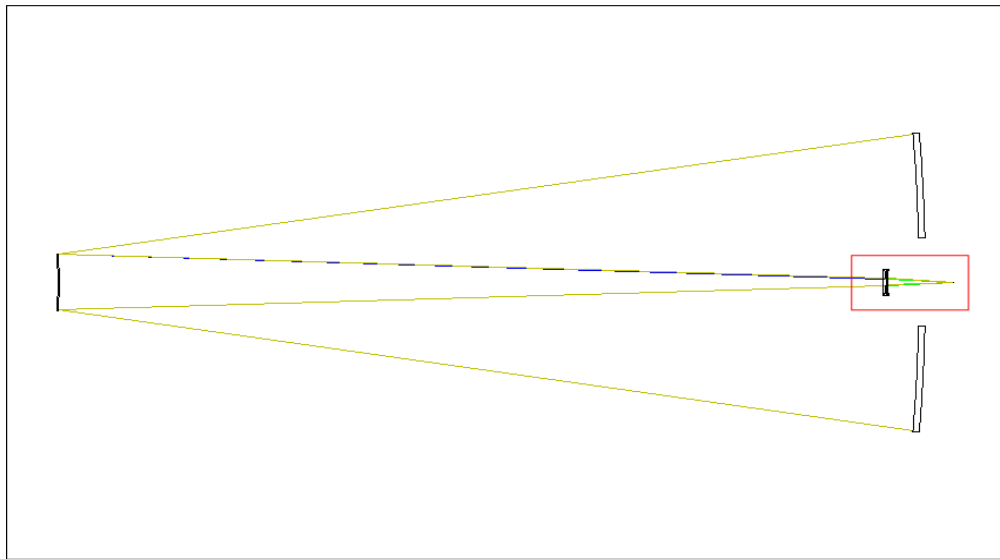


Figure 4.2: A Zemax prescription for the f/9 Cassegrain focus for the Hale 200 inch telescope at Palomar Observatory. Note the extra optics used to convert an f/16 beam to an f/9. This information was found from original drawings of the P200 in the Caltech archives loaned to the group by Paul Gardner, Chief Engineer at Caltech Optical Observatories. The prescription was configured and optimised with the help of Leon Harding.

The pupil size is  $\sim 4.0$  mm and located at the focal length of the collimator. This pupil, for the current GASP set up, is  $\sim 59.0$  mm from the face of the prism-rhomb. This means that the minimum distance between the last element of the collimator to the prism-rhomb centre is  $\sim 100.0$  mm. The off axis light rays are in green and red. Ideally the pupil should land on the centre of the prism-rhomb face. A consequence of this distance is that this divergence continues through the prism-rhomb and reduces the FOV available on the TP. As it stands, the distance from the pupil to the prism-rhomb will also result in a reduced field on the RP. This space was created to make room for the calibration optics, see PSG, ECM and filter wheel in Figure 4.4. It was a reasonable solution, to mount all calibration optics on axis, when GASP was configured for APD detectors.

It was found in Figure 4.4 that the maximum FOV that could be achieved for this configuration is  $\sim 7''$  on the reflected path and  $\sim 6''$  on the transmitted path. There are cases where a larger FOV (multiple targets) must be analysed which requires the use of differential photometry techniques. Other implications

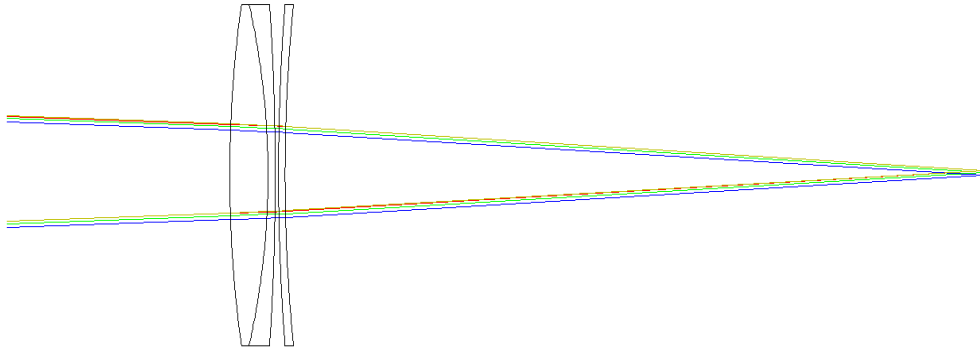


Figure 4.3: A Zemax prescription for the f/9 Cassegrain focus for the Hale 200 inch telescope at Palomar Observatory. This is a zoomed in view of the red box in Figure 4.2. These extra lenses provide the means to change the f-number of the Cassegrain focus from f/16 to f/9.

of a small FOV will result in the inability to guide on sky, or uncertainty that the target in the GASP FOV is correct; which may not be the case if there are unforeseen pointing errors or the need to perform any blind-offsets.

#### 4.3.4 The Collimating Optics

A field lens, a negative concave doublet, is used to extend the distance at which the pupil forms. It reduces the severe off axis angles entering the prism-rhomb, and has the capability of increasing the back focal length (BFL) of the collimating lens. For larger telescopes the focal length, and hence platescale, will always be a limiting factor for the GASP prism-rhomb due to its size. The main purpose of this lens is to conjugate the pupil (i.e. the collimator BFL) to the centre of the prism-rhomb face. This allows an increase in the number of on axis rays to pass through the prism-rhomb, and reduce off axis vignetting. A larger FOV is now possible from the prism-rhomb and its new value is  $\sim 40''$ .

Figure 4.5 is the optical prescription for the field lens and collimating optics used for the Palomar f/9 focus. It was discovered that a combination of two 100

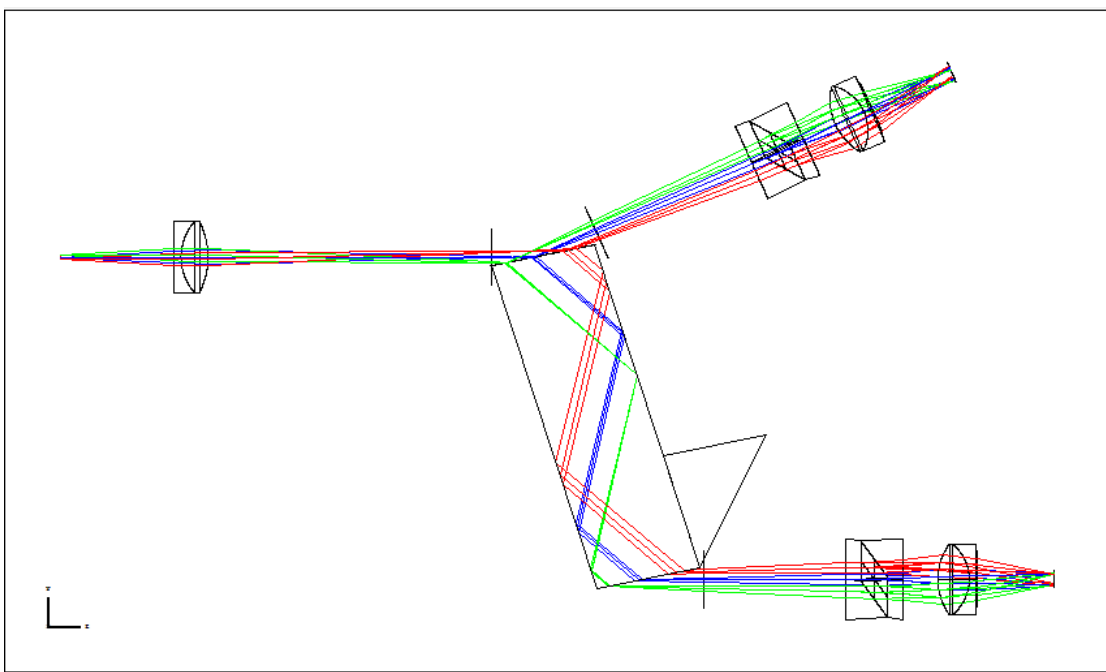


Figure 4.4: Zemax description of how the beam will not remain collimated as it moves past the pupil position. This is an optical description for the 200 inch f/9 telescope focus, using a collimator with a focal length equal to 40 mm.

mm focal length lenses, giving an effective focal length of 50 mm, gave the best solution to increasing the BFL and minimising any distortions in the spot diagrams in combination with re-imaging optics (discussed later).

## 4.4 Final Optical Design for the P200

A description of how the light rays propagate to the detector chip is presented by Figure 4.6 for a complete optical layout of the polarimeter, including the PSA. The GASP prism-rhomb and Wollaston prisms have been included to inspect how well the field lens and collimator work. It is also noted that the AOI of the prism-rhomb was altered to that used by Collins (2012). This AOI used in this configuration was  $78.5^\circ$ , found in Table 3.2. The choice of Wollaston prism was based on what was available in the laboratory. These are two 10 degree Wollaston prisms with a clear aperture of  $\sim 10 - 15$  mm. A re-imaging lens of focal length 30 mm was used to image the pupil onto the chip of the iXon Ultra 897. This gave an unvignetted

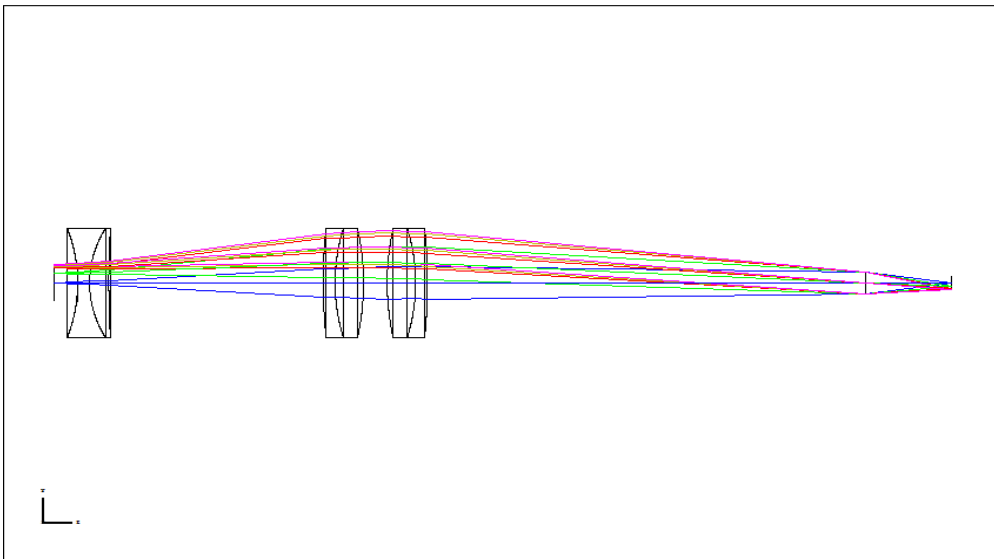


Figure 4.5: Field lens solution for the GASP collimator. Two 100 mm focal length lenses of diameter 25 mm were combined to produce a ‘single’ lens with an effective focal length of 50 mm.

FOV of  $\sim 21''$ . There was difficulty in focusing any other lens onto the chip for a number of reasons. The clear window in front the electronics is located 17 mm behind the front casing in order to protect the chip from damage or dust. The front of the detector itself proved to be quite bulky in design and the mounts to hold the detector in place were required to be of a particular shape and size. This provided a mechanical limitation when mounting the re-imaging lens to the detector. The base of the detector mount was located in such a place that there was a maximum distance in which to position the pillar mount holding the lens tube. Therefore, this focal length was the only available option, which still gave a good outcome for seeing limited spot sizes.

Figure 4.6 provides a more detailed representation of how light propagates through the prism-rhomb. Light rays begin to diverge after the pupil forms. The light rays from the transmitted path diverge through the prism-rhomb, and continue to diverge on exiting the prism-rhomb. Re-imaging systems with demagnification allow the observer to obtain a reasonable FOV and match the pixel scale to the typical seeing of the observatory. Therefore, ideally, a large diameter lens is required to gather all this light and prevent vignetting. It is not normally possible

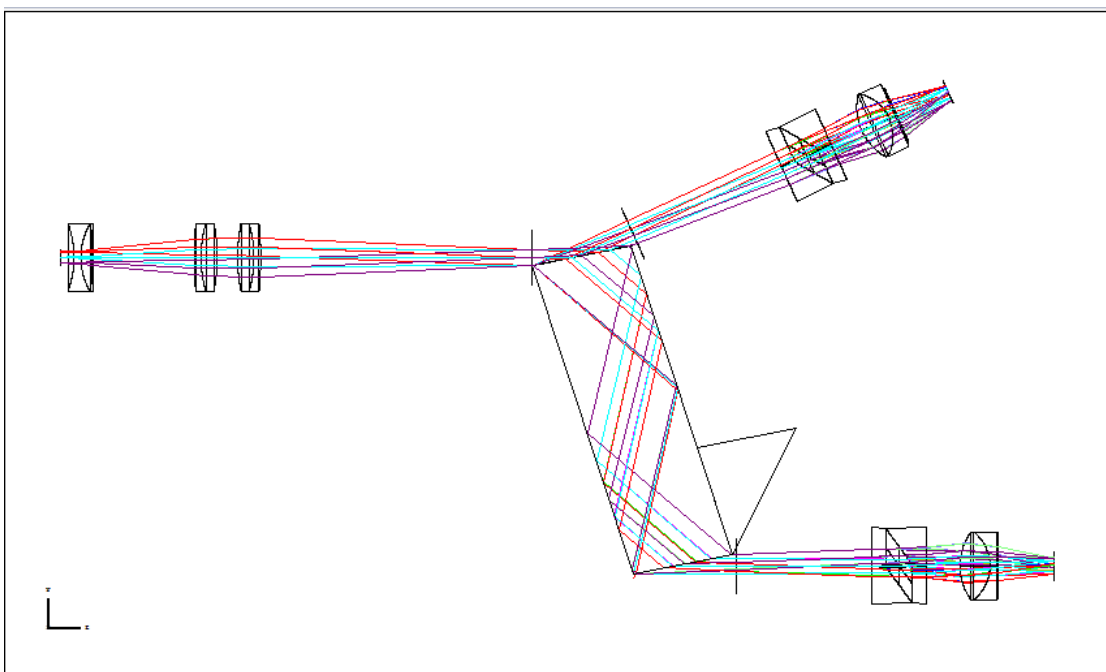


Figure 4.6: Effective focal length collimator lens of 50 mm using a 30 mm lens to re-image at the detector. The unvignetted FOV was found to be  $\sim 21''$ .

to use a fast lens with a large diameter when re-imaging. This is because of the relationship

$$F = \frac{f}{D}, \quad (4.1)$$

which is the f-number of the lens. It is unusual in these kinds of optical systems to have an f-number less than 1. It is also clear that if a lens has an f-number of 1 then its focal length must equal its diameter, resulting in a lens which is quite convex in shape. A fast lens is usually chosen because an instrument, such as GASP, requires an optical demagnification in order to achieve a desired platescale onto a small detector. Therefore, the beam converges with a wider (faster) angle at the detector compared to the beam delivered by the telescope.

---

## 4.4.1 Optical Image Quality

### 4.4.1.1 Spot Diagrams

Spot diagrams are a useful way to examine the optical quality of the spot size of a point source in the sky. In the absence of aberrations, the point source will converge to a perfect image point. The information presented in this section will examine the image size, and quality, of an object in the sky by ray tracing through the GASP system. It is important to determine the quality of the available FOV if there are multiple targets of interest in the case of science. A system is close to the aberration-free quality level if its geometric (ray) spot doesn't exceed the Airy disc boundaries, however, it is important to perform other system checks such as Encircled Energy plots; these will also be examined.

The simulated Airy Disk radius for this optical system is marked by a black circle; it represents the diffraction limit of the system. The wavelength of choice for this analysis is 650 nm as the majority of the targets of interest for this science case will be observed using a filter centred at this wavelength. The RMS radius is the root mean square spot size, and geometrical radius is the distance from the centroid to the furthest ray intersection with the imaging surface. IMA describes the location of the centroid on the imaging surface. OBJ describes the location of the field points in terms of field angles Wang et al. (2011).

Table 4.1: RP1 RMS radial spot diagram values for Figure 4.7; values are in microns and pixels.

Field	1	2	3	4	5	6	7	8	9
$\mu\text{m}$	32.77	13.35	94.29	38.05	26.47	110.51	142.40	137.88	176.65
# pixels	2.05	0.83	5.89	2.38	1.65	6.91	8.90	8.62	11.04

The general layout of a on axis spot diagram is as follows: Photons from the origin of the system (the optical axis) are traced and hit the entrance pupil. The size of the image is indicated as well as its position in the field. In general, on axis spot sizes are ray traced through the centre of the optic used and this is usually an area of the lens with the lowest curvature. The GASP instrument does not

---

work this way. On each path the Wollaston prism uses the same re-imaging lens to focus on the same detector; each beam will be off centre by the same amount for perfect alignment. Off axis spot sizes are selected based on the size of the FOV of the system; they are an angular distance from the optical axis. The same alignment considerations apply to off axis as they do to on axis as two beams must pass through one lens for the GASP instrument.

In general, the bigger the spot diagram, the worse the optics. There are a number of other quality factors that can be determined from examination of the spot diagrams, some of which include image focus quality, optical aberrations inherent to the optical design of the system, vignetting, and distortion. In the case of GASP as an imaging system, it is found that the PSF varies hugely (size and shape) from the on axis position to off axis. These spot sizes give an indication of the size and shape image of a point object, and this should converge to a perfect image point in the absence of aberrations. It is clear that this is not the case for this optical prescription. The spot sizes for each channel are found in Figures 4.7, 4.8, 4.9, and 4.10.

The airy disk is compared in each case ( $\text{Airy}_{\text{radius}} \sim 4 \mu\text{m}$  for each channel) and all measurements are in microns. The values in Table 4.1 shows clearly that the system is not diffraction limited for this channel, and subject to a number of optical aberrations. The PSF appears to be subject to coma and astigmatism<sup>1</sup> (on TP1 and TP2) as we move off axis. Some optical distortions are also evident at all points as the light rays generating the PSF are not radially symmetric. This will cause magnification, and rotation distortions on the transmitted channels.

Table 4.2: RP2 RMS radial spot diagram values for Figure 4.8; values are in microns and pixels.

<b>Field</b>	<b>1</b>	<b>2</b>	<b>3</b>	<b>4</b>	<b>5</b>	<b>6</b>	<b>7</b>	<b>8</b>	<b>9</b>
$\mu\text{m}$	138.08	52.69	69.25	83.08	14.14	22.29	120.59	46.26	67.34
# pixels	8.63	3.29	4.33	5.19	0.88	1.39	7.54	2.89	4.21

---

<sup>1</sup>This astigmatism caused by the prism-rhomb has been examined in detail by Collins (2012).

---

Table 4.3: TP1 RMS radial spot diagram values for Figure 4.9; values are in microns and pixels.

<b>Field</b>	<b>1</b>	<b>2</b>	<b>3</b>	<b>4</b>	<b>5</b>	<b>6</b>	<b>7</b>	<b>8</b>	<b>9</b>
$\mu\text{m}$	146.24	86.52	124.57	143.54	15.02	81.61	129.13	20.58	77.49
# pixels	9.14	5.41	7.79	8.97	0.94	5.10	8.07	1.29	4.84

Table 4.4: TP2 RMS radial spot diagram values for Figure 4.10; values are in microns and pixels.

<b>Field</b>	<b>1</b>	<b>2</b>	<b>3</b>	<b>4</b>	<b>5</b>	<b>6</b>	<b>7</b>	<b>8</b>	<b>9</b>
$\mu\text{m}$	79.53	22.59	123.45	84.34	10.67	140.44	125.78	82.36	144.72
# pixels	4.97	1.41	7.72	5.27	0.67	8.78	7.86	5.15	9.05

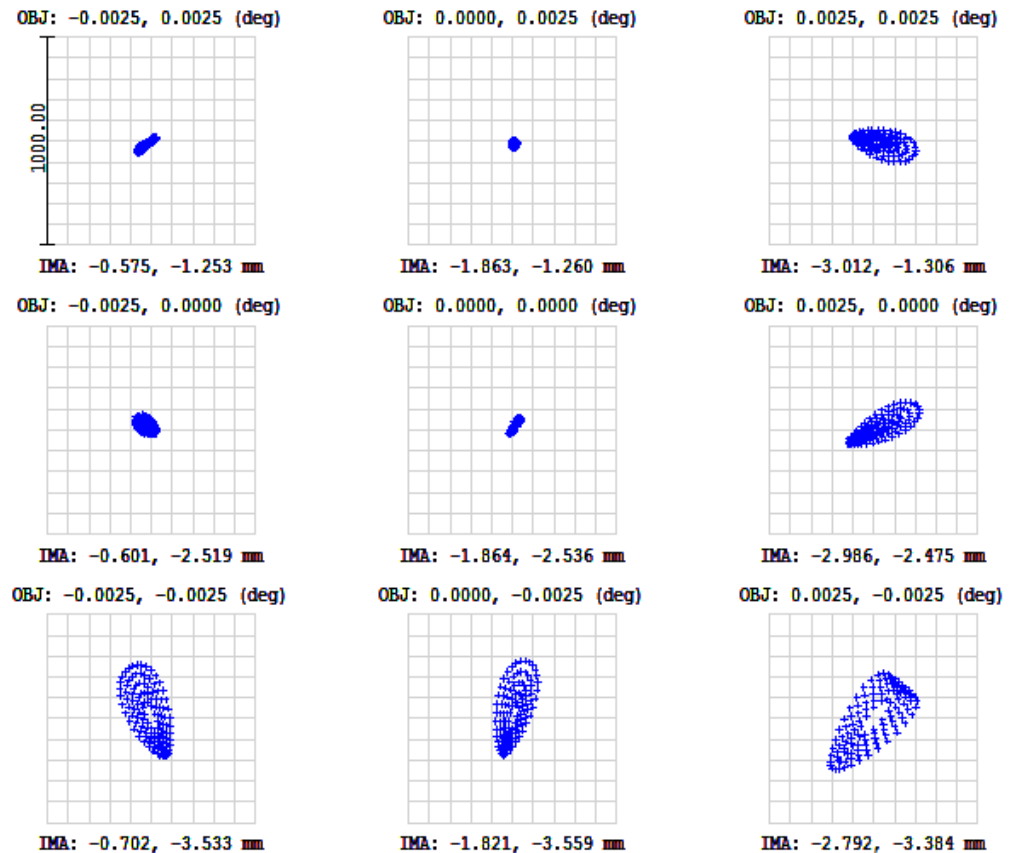


Figure 4.7: Spot sizes for the RP1 channel. The top left corner is the first field point, and are read left to right. The values are given in microns in Table 4.1 and the scale bar is  $1000 \mu\text{m}$ . The Zemax design is optimised based on the optomechanical requirement of the system, but also by giving the best spot size relative to the diffraction limit. The central image refers to the on axis PSF and the outer spot sizes are points on the edge of square FOV of  $\sim 18 \times 18''$ .

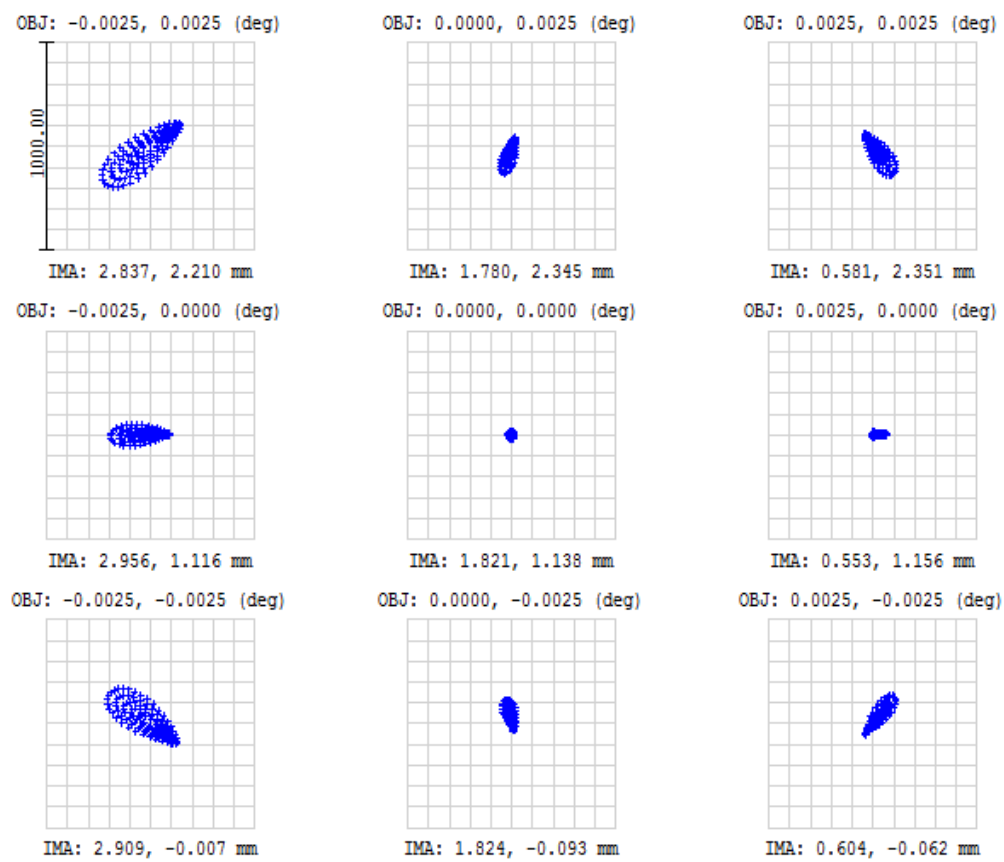


Figure 4.8: Spot sizes for RP2 channel.

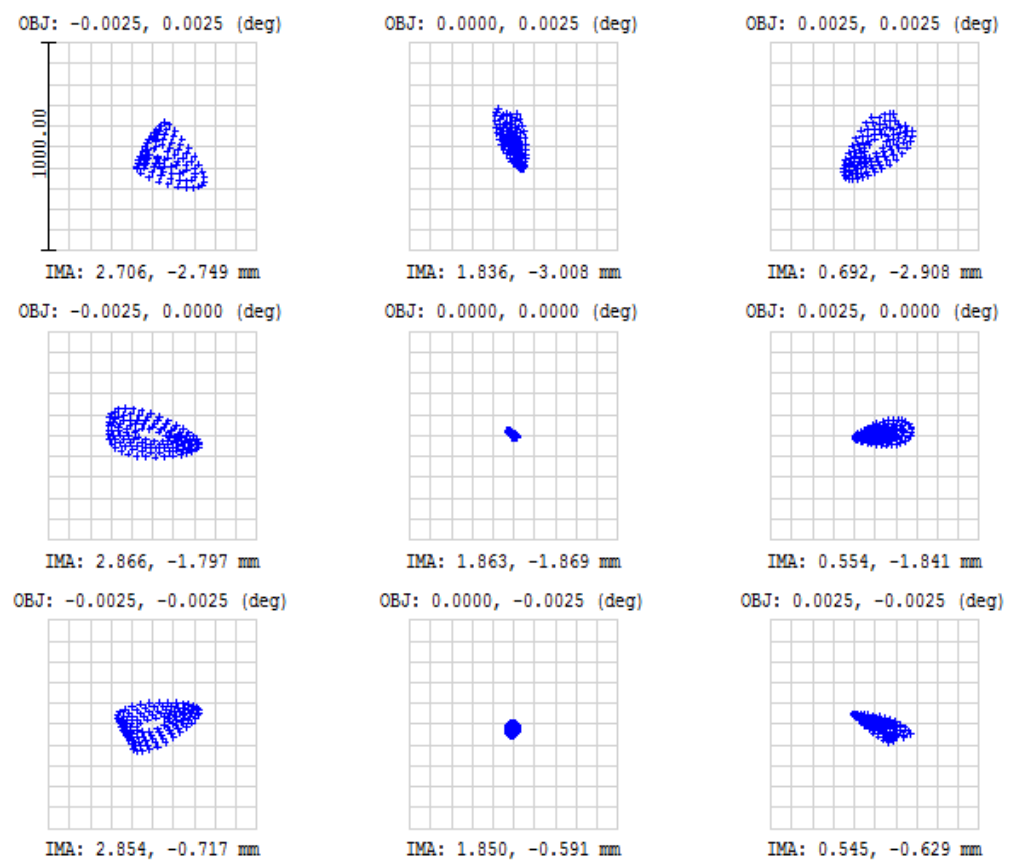


Figure 4.9: Spot sizes for TP1 channel.

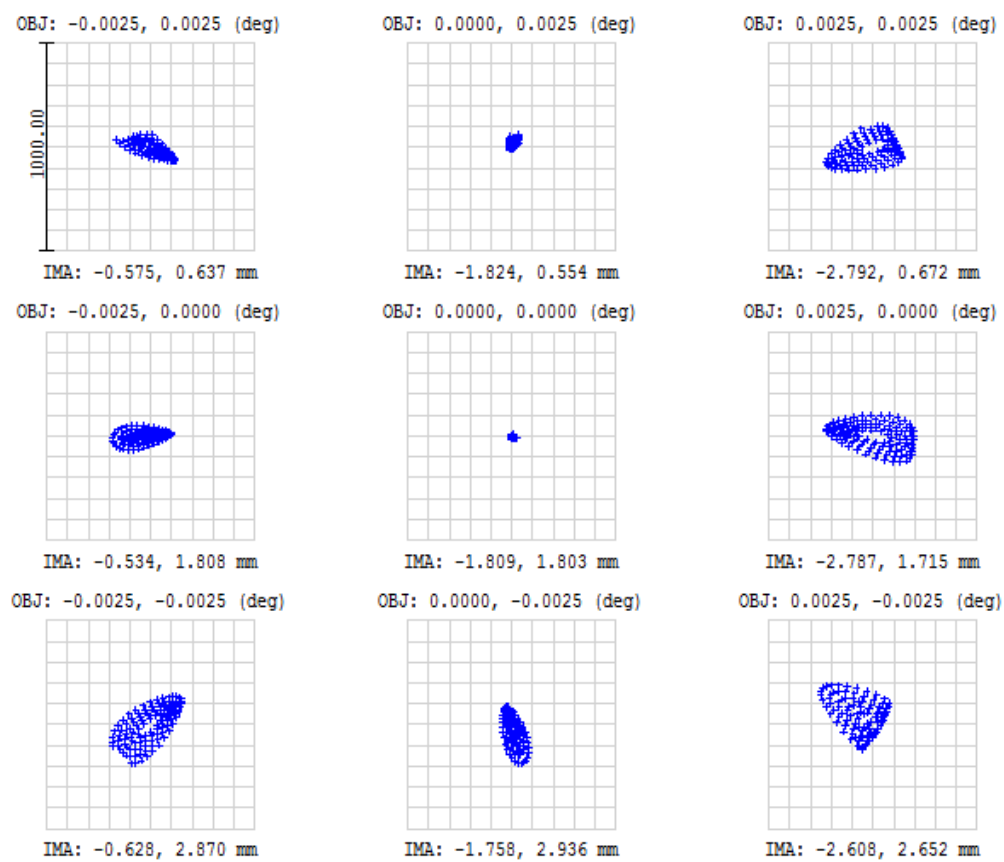


Figure 4.10: Spot sizes for TP2 channel.

---

The values of the spot sizes summarise the limitations of the instrument in terms of the size, and shape, of a target in 3 different field locations. There is a considerable variation in shape between each of the on axis positions; the size of the PSF (in pixels) does not vary greatly, except for the TP2 channel. Within each channel, the PSF appears to have a high variability in size and shape over a small FOV. This leads to questions regarding the variability of the optical aberrations in the system, and distortions as a result of the optics and optical alignment. Looking at each position in the field raises concern for the variation of the PSF. This becomes more evident in Chapter 5.6.

The optical limit of the GASP system has a pixel scale of  $0.14''/\text{pix}$  using the Andor iXon Ultra 897 detectors, which have a pixel size of  $16\ \mu\text{m}$ . Therefore, it is shown that a target size of  $1''$  will cover 7.14 pixels on these detectors. This gives a clearer idea for what area these spot size will cover on these chips. An area this size indicates over sampling of GASP, a large number of pixels for a small area of sky.

#### 4.4.1.2 Encircled Energy

The size and shape of the image pattern is important for the purposes of resolving sources, however for polarimetric/photometric measurements, more valuable information can be obtained from the encircled energy (EE) distribution of the pattern. The encircled energy is the fraction of the total integrated flux in the image contained within a given radius,  $r$ . Real PSFs normally have extended wings, therefore it is good practice to examine how 80%<sup>2</sup> of the flux is distributed in terms of number of pixels (arcseconds). In terms of measuring a polarimetric signal, relative flux values are measured. The following are the EE distributions for each channel of the GASP optical system described in Figure 4.6:

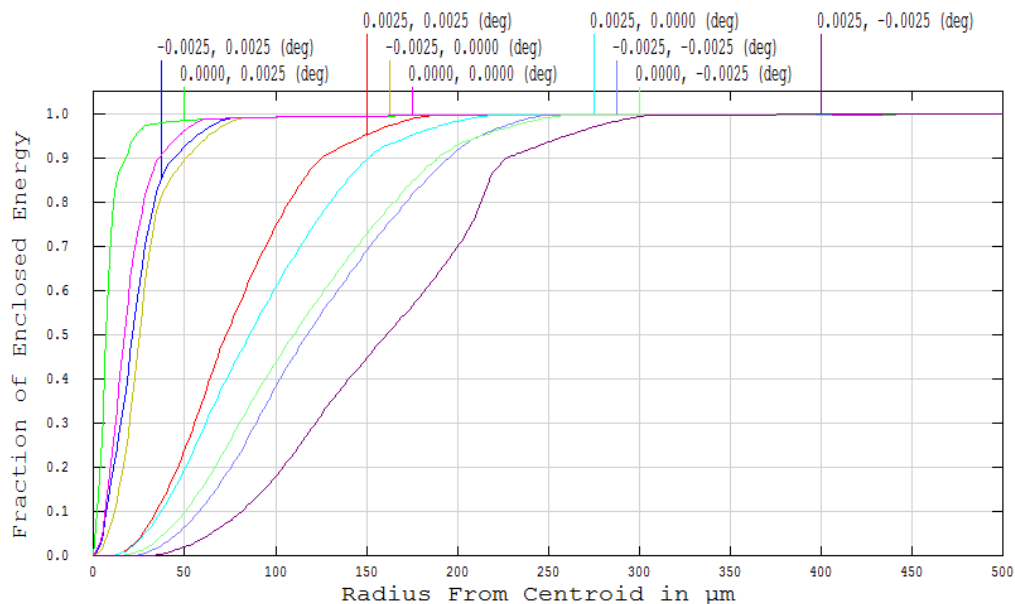


Figure 4.11: Encircled Energy for the RP1 channel. The measured value on the y axis is the fractional percentage. The Zemax design is optimised based on the optomechanical requirement of the system. The plotted lines are colour coded for each position in the FOV, which are indicated by the spot diagrams.

The Encircled Energy Factor measures the fraction of the total energy in the PSF, which lies within a specified radius in the plane of observation or detection. It is a significant image quality parameter and serves as an index of the performance

<sup>2</sup>Typically the radius of the PSF contains 80% of the encircled energy.

---

of an optical system. The radial distribution of energy within the image, called the encircled power, is a classical measure of the quality of the optical system producing that particular image (Srisailam et al., 2001).

It can be found that there is a large variation in each field position for how many microns contain 80% of the flux. This is consistent with the results found when measuring the spot sizes. The same concern is also found when analysing between channels. The on axis image point shape and size is changing between channels, and the optical aberrations (and distortions) are also inconsistent between channels.

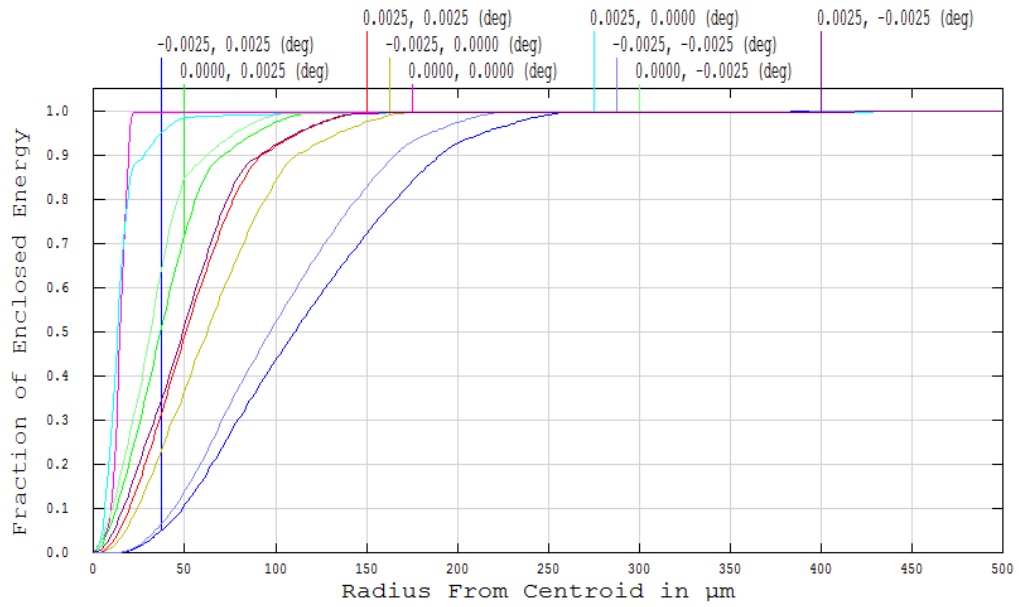


Figure 4.12: Encircled Energy for RP2 channel.

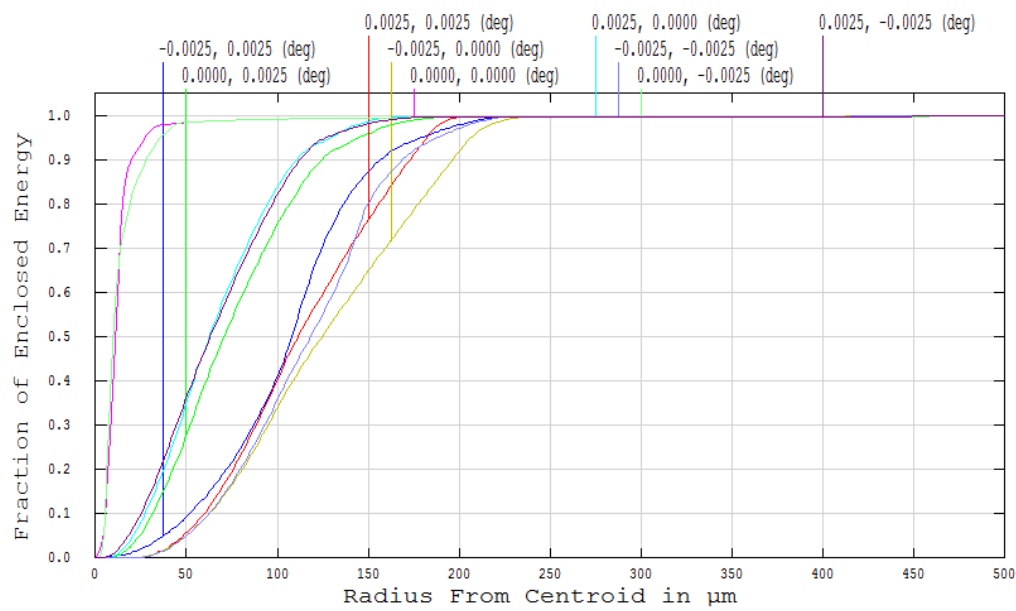


Figure 4.13: Encircled Energy for TP1 channel.

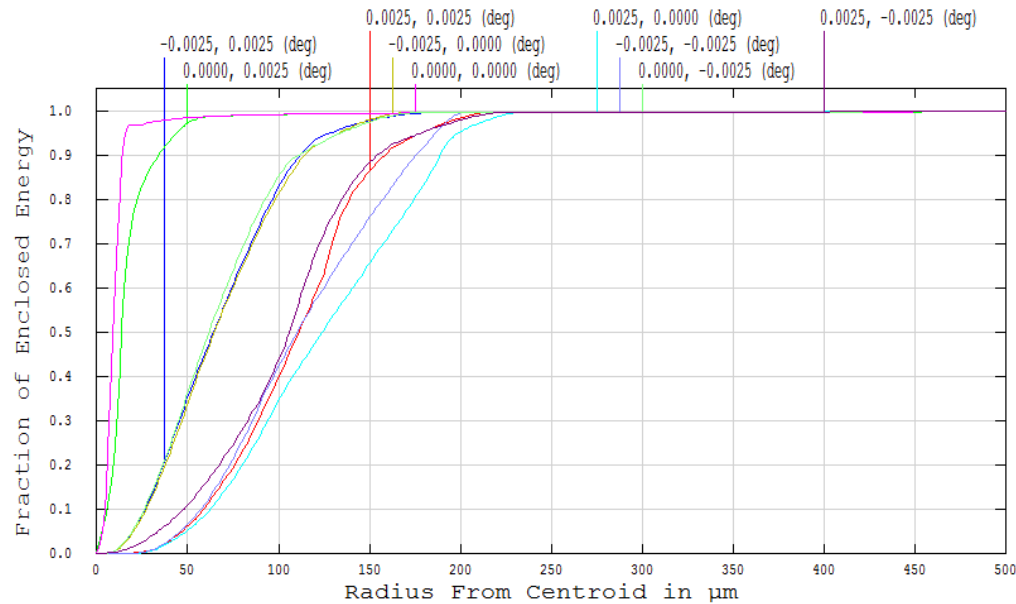


Figure 4.14: Encircled Energy for TP2 channel.

---

An analysis of the spot sizes give a reasonable idea of how the distortion varies, and hence the shape of the PSF, it is also valuable to examine how many pixels contain  $\sim 80\%$  of the flux. The results from this optical design indicate that there is the possibility that there will be difficulties when each channel must be matched, by performing a pixel-by-pixel registration. This will be explained in more detail in Section 5.8.

## 4.5 Pixel Scale and FOV Overlap

A factor when designing any instrument is how well the PSF is sampled, which is largely dependent on the detector pixel size, and also the optics chosen. It has already been explained that GASP is oversampled as an imaging instrument. This is a very difficult problem to solve optically. There are 2 main reasons that make this an issue for the GASP PSA:

1. The pixel size of  $16 \mu\text{m}$  on the Andor iXon Ultra 897 EMCCDs, see Appendix E.
2. The size of the focal length of the 200 inch telescope at Palomar. The focal length of the telescope scales with mirror diameter; larger diameters are necessary for imaging fainter targets.

A pixel scale of  $0.14''/\text{pix}$  was obtained based on the design in Figure 4.6, and that is the limit (optically) for GASP for the iXon Ultra 897s. The size of the lens used to re-image appears to be causing problems due to its focal length and curvature. The light beams that exit the Wollaston prisms strike the lens, not through the centre of the lens, but either side of centre where there is significant curvature.

The re-imaging lens will determine what angular size Wollaston prism is needed in order to avoid image overlap on the chip. A short focal length, fast lens, is generally used to re-image the beam to get demagnification of the focal plane onto a small detector. This usually leads to using lenses that are quite round in shape, as there will be a large surface curvature for fast lenses. The relationship between the re-imaging lens and the Wollaston prism must be accounted for to ensure that

---

both beams pass through a sensible area of the lens. This could lead to light loss if the separation is too great and overlapping if the separation is not large enough. It could also cause image distortion depending on lens type and optics combinations.

The final layout employed at the P200 can be found in Figure 4.15. This is an image of GASP mounted to the telescope at Cass f/9 focus. The beam is delivered to the polarimeter through a shutter, which is obscured from view in this image, and passed to the GASP PSA where 4 beams are imaged by 2 Andor iXon Ultra 897 EMCCDs.

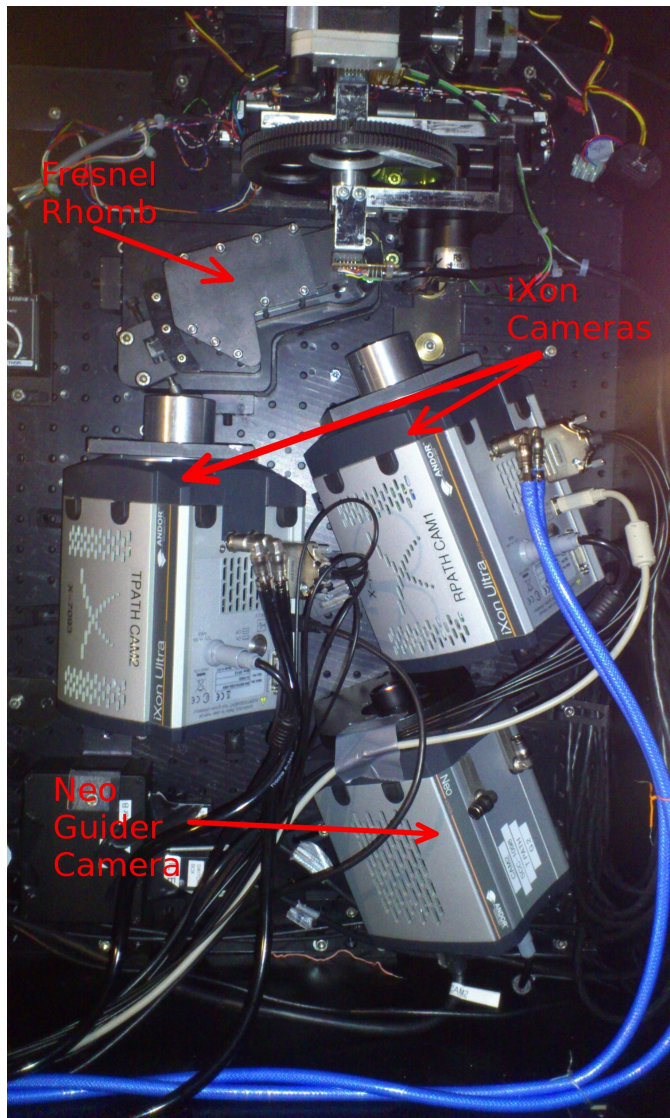


Figure 4.15: The GASP layout while mounted to the Cass f/9 focus of the P200. The image indicates the GASP Fresnel rhomb beamsplitter and detectors used for science and guiding. Calibration optics and filter wheel can be seen in the top section of the image, and the blue tubing was used for cooling of the iXon Ultra EMCCDs.

---

# Chapter 5

## Instrument Calibration & Results

An overview of the difficulties in the calibration of astronomical polarimeters is presented. A description of Mueller polarimetry is discussed as this will become the basis in the development of the Eigenvalue Calibration Method for GASP. The implementation of the Polarisation State Generator built for GASP is also discussed.

The second half of this chapter presents a detailed description of a new analysis technique for GASP applying the ECM on calibration data obtained using two different optical and detector set ups. The first uses Avalanche Photodiodes where the light is fed to the detectors by optical fibres; this is based on the description discussed in Section 4.2. This data analysis was a bench result and will not be discussed in terms of observational results, but as an analysis of the use of the ECM for calibrating GASP. Lastly, an analysis concept is proposed for GASP as an imaging polarimeter and verification results are presented. The data presented in this chapter provides a calibration result that can be applied to observational results, which will be discussed in Chapter 6.

### 5.1 Difficulties in Calibrating Astronomical Polarimeters

A polarimeter is described as ‘complete’ when the PSG and the polarimeter can generate and measure the four states of polarisation of light. The calibration of a polarimetric tool is a two-step process. The optical elements of the system must

---

be precisely orientated with very careful alignment and the behaviour of these optical elements must be easily described and characterised by physical properties (Compain et al., 1999). Therefore, the combination of several measurements in different configurations to determine the main values and shortcomings. Any optical element that has not been fully characterised in the light path, can introduce modifications to the state of polarisation of light.

The behaviour of any optical or electronic device can be distorted by first-order failures, as in the case of a photoelastic modulator (Drevillon, 1993). Therefore, several measurements must be combined in a number of different configurations to determine the main values and the shortcomings. The optical set-up is then adapted to account for these measurements. These aspects of the calibration process have already been reviewed in the literature (Hauge, 1978; Thompson et al., 1980; Azzam and Lopez, 1989). Furthermore, one can notice that usual calibration procedures are difficult to implement *in situ* because of the influence of the optical elements that are necessarily included in the light path (filters, windows, lenses, mirrors, etc.) All these elements can induce modifications of the state of polarisation of light.

## 5.2 Mueller Polarimetry

Polarised light is represented by a Stokes vector, invented by G. G. Stokes in 1852 (Shurcliff and Stanley, 1964; Hecht, 1987; Born and Wolf, 1999). This is simply, a set of 4 numbers and it is described by,

$$\mathbf{S} = \begin{pmatrix} I \\ Q \\ U \\ V \end{pmatrix} = \begin{pmatrix} I \\ I_0 - I_{90} \\ I_{45} - I_{-45} \\ I_{RC} - I_{LC} \end{pmatrix}. \quad (5.1)$$

$I$  is the intensity of the light beam, and  $I_0$ ,  $I_{90}$ ,  $I_{45}$ , and  $I_{-45}$  are the light intensities for the linearly polarised light at  $0^\circ$ ,  $90^\circ$ ,  $45^\circ$ , and  $-45^\circ$ , respectively.  $I_{RC}$  and  $I_{LC}$  are the intensities of right- and left-circularly polarised light, respectively (Tompkins and Irene, 2005).

Light of any polarisation state may be represented by a Stokes vector. It

---

applies equally well to polarised, partially polarised and unpolarised light. It is the simplest method of predicting the result of adding two incoherent beams, and it also provides a simple numerical method of predicting how a beam is affected by the insertion of a polariser or a retarder. The Mueller matrix  $\mathbf{MM}$  of any sample can be found from the linear relationship

$$\mathbf{S}_{\text{out}} = \mathbf{MM}\mathbf{S}_{\text{in}}, \quad (5.2)$$

where  $\mathbf{S}_{\text{in}}$  and  $\mathbf{S}_{\text{out}}$  are, respectively, the Stokes vectors of light entering and exiting the sample (Shurcliff and Stanley, 1964; Collett, 1993).

The linear interaction of light with a sample is described by the  $4 \times 4$  Mueller matrix of that sample (Compain et al., 1999). The overall matrix  $\mathbf{M}$ , of an optical system is the product of all the Mueller matrices for the components of that system. This matrix,  $\mathbf{M}$ , can then be used to find the resultant Stokes vector of the incoming light. This can be seen in Equation 5.3.

$$\mathbf{M} = \mathbf{MM}_n\mathbf{MM}_{n-1}\dots\mathbf{M}_2\mathbf{M}_1. \quad (5.3)$$

Mueller matrices are a very important tool in the laboratory and will be used in more detail in Section 5.5. The simplest optical element that can be represented by a Mueller matrix is the Identity matrix  $I_d$ . Other such examples can be found from (Shurcliff and Stanley, 1964). Only two types of Mueller matrices that have perfectly known theoretical forms (Compain et al., 1999), which will be used in this thesis and these are called reference samples. One such element is a linear polariser  $\mathbf{P}(\tau, \theta)$ , where  $\theta$  is the orientation of the polariser and  $\tau$  is the transmission coefficient:

$$\mathbf{P}(\tau, 0) = \frac{\tau}{2} \begin{pmatrix} 1 & 1 & 0 & 0 \\ 1 & 1 & 0 & 0 \\ 0 & 0 & 0 & 0 \\ 0 & 0 & 0 & 0 \end{pmatrix}. \quad (5.4)$$

Other Mueller matrices may be found by the following relationship (Compain et al., 1999; Tompkins and Irene, 2005):

---


$$\mathbf{P}(\tau, \theta) = \mathbf{Rot}(\theta)\mathbf{P}(\tau, 0)\mathbf{Rot}(-\theta). \quad (5.5)$$

A similar notation has been used here to that by (Lara Saucedo, 2005), where  $\mathbf{Rot}(\theta)$  is represented by the following matrix:

$$\mathbf{Rot}(\theta) = \begin{pmatrix} 1 & 0 & 0 & 0 \\ 0 & \cos(2\theta) & -\sin(2\theta) & 0 \\ 0 & \sin(2\theta) & \cos(2\theta) & 0 \\ 0 & 0 & 0 & 1 \end{pmatrix}, \quad (5.6)$$

where  $\theta$  is the azimuthal angle in degrees. The calibration method that will be described in 5.5 uses the following Mueller matrix for a dichroic-retarder to model the samples used:

$$\mathbf{M}_{DR}(\tau, \psi, \delta) = \tau \begin{pmatrix} 1 & -\cos(2\psi) & 0 & 0 \\ -\cos(2\psi) & 1 & 0 & 0 \\ 0 & 0 & \sin(2\psi)\cos(2\delta) & \sin(2\psi)\sin(2\delta) \\ 0 & 0 & -\sin(2\psi)\sin(2\delta) & \sin(2\psi)\cos(2\delta) \end{pmatrix}, \quad (5.7)$$

where  $\psi$  and  $\delta$  correspond to the usual ellipsometric angles related to the Fresnel coefficients.  $\psi$  refers to a partially polarising effect, and  $\delta$  to a retardance (or phase-shifting) effect due to a reflection off a surface,  $\tau$  is the intensity transmittance (or reflectance) for non-polarised light.

The eigenvalues of  $\mathbf{M}_{DR}(\tau, \psi, \delta)$  are,  $(l_1, l_2, l_3, l_4)$  (Lara Saucedo, 2005) and can be determined from the solutions of the characteristic polynomial equation, which are as follows:

$$l_1 = 2\tau \sin^2(\psi) \quad (5.8a)$$

$$l_2 = 2\tau \cos^2(\psi) \quad (5.8b)$$

$$l_3 = \tau \sin(2\psi) \exp(i\delta) \quad (5.8c)$$

$$l_4 = \tau \sin(2\psi) \exp(-i\delta). \quad (5.8d)$$

### 5.3 The Polarisation State Generator

In order to calibrate a polarimeter of this nature a polarisation state generator (PSG) is required. Its purpose is to generate different states of polarisation to interact with the chosen samples for calibration. The PSG developed for GASP was based on a simple calibration method described in Section 5.4. During the initial design stages of the instrument for this thesis, the PSG was mechanically designed for this method. Light was generated with a Warm White Thorlabs LED with a normalised intensity curve for  $\sim 400 - 750$  nm, which can be found in Figure 5.1.

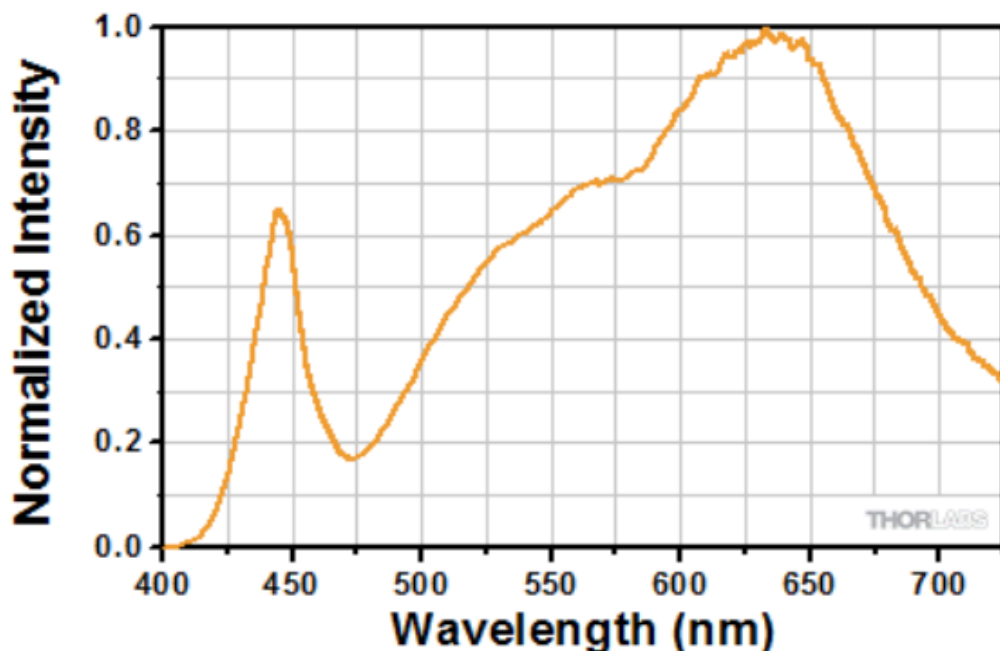


Figure 5.1: An Intensity Spectrum Curve for a Warm White LED sourced from Thorlabs (Tho, b).

There is a variation across the working bandwidth showing that the ideal throughput for alignment and calibration is in the range 600 - 700 nm, which was the optimised design range for the PSA, and for science objective of GASP. The LED had a max power output of 500 mW which made it suitable for alignment and calibration.

The first element of the GASP PSG consisted of a linear polariser mounted

in a rotatory mechanical stage controlled by LabVIEW software on a motorised stage, also controlled by LabVIEW. The second element was a quarter-wave plate (QWP) with its fast axis aligned at  $0^\circ$ .

The linear polariser was anti-reflective (AR) coated with a visible range of 400 - 700 nm with a high extinction ratio (minimum of 1000:1). These types of polarisers are subject to birefringence when under stress. This was minimised by using a stress free retaining ring when housed. This polariser was sourced at Thorlabs; Figure 5.2 is a description of the transmission and extinction ratio of the polariser over a similar wavelength range as the LED.

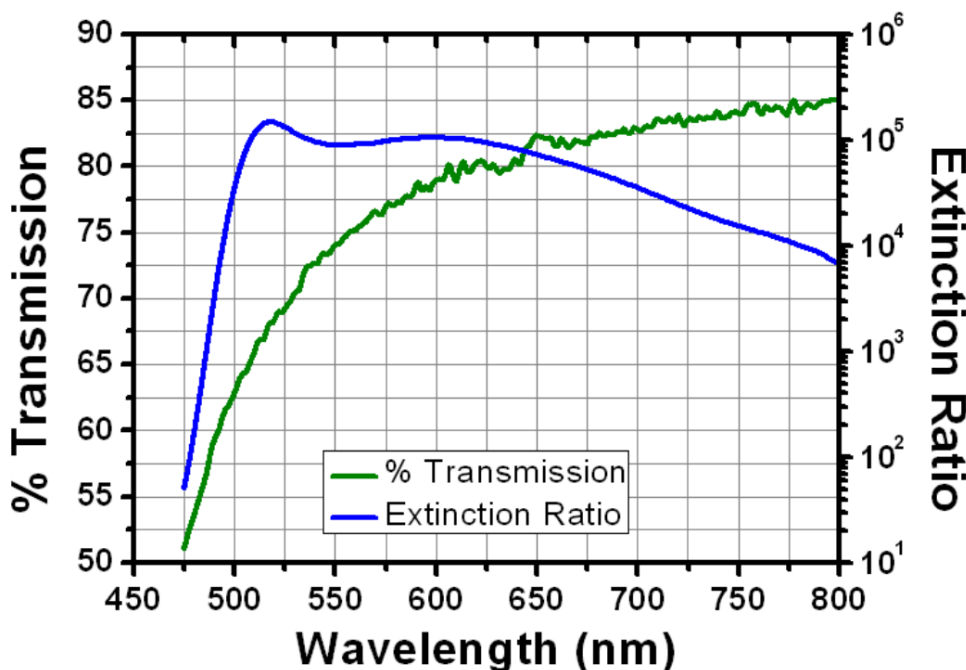


Figure 5.2: Transmission and extinction ratio specifications for a linear polariser from Thorlabs for a range 450 - 800 nm (Tho, a).

The QWP was AR zero-order achromatic wave plate with a visible range of 400 - 800 nm. Due to the high cost of the QWP, and for mechanical compatibility with the rest of the system, a mounted QWP with diameter 25.4 mm was chosen. Both the linear polariser and QWP were Thorlabs products.

The QWP is aligned in the laboratory with its fast axis at  $0^\circ$ . Both the linear polariser and QWP share the same mounting assembly and move in and out of

---

the LED beam in opposite directions. The QWP is centred with respect to the linear polariser on the bench using the same LED used for instrument alignment. The linear polariser is rotated from its known “home position” from  $0^\circ$  to  $171.36^\circ$  in increments of  $10.08^\circ$ , according to the stepper motor in which the polariser is housed. The home position, in the case of the linear polariser, has been measured to be  $\sim -38.8^\circ$ , however, this is not a necessary step in the ECM, which will be explained in Section 5.5. The polariser is rotated in the same way for when the QWP is in position to generate elliptical polarisation states.

## 5.4 The Moore-Penrose Pseudoinverse

In the developing stages of the GASP instrument a pseudo-inverse method was used to determine the system matrix during calibration. This used for a least squares problem presented by the data generated from using an over-determined PSG.

### 5.4.1 Definition

Here we define the notion of a Moore-Penrose pseudo-inverse, or Generalised Inverse, and consider its uniqueness. Let  $m, n \in \mathbb{N}$  and let  $A \in \text{matrix}(\mathbb{C}, m, n)$  be an  $m \times n$  matrix (not necessarily a square matrix). A matrix  $B \in \text{matrix}(\mathbb{C}, m, n)$  is said to be a generalised inverse, or a pseudo-inverse, of  $A$  if it satisfies the following conditions:

1.  $ABA = A$
2.  $BAB = B$

If  $A \in \text{matrix}(\mathbb{C}, n)$  is a non-singular square matrix, its inverse  $A^1$  satisfies trivially the defining properties of the generalised inverse above. The idea of Moore-Penrose pseudo-inverse was introduced by E. H. Moore (H., 1920) in 1920 and rediscovered by R. Penrose (A., 1955, 1956) in 1955. The Moore-Penrose pseudo-inverse is a useful concept in dealing with issues in optimisation, as the determination of a “least squares” solution of linear systems. A mathematical description of this method can be found in Appendix B.

---

## 5.5 The Eigenvalue Calibration Method

A Mueller matrix polarimeter comprises of a PSG, see Section 5.3, which produces a suitable basis set of  $S_{in}$ . A PSA, see Section 3.2.1, determines  $S_{out}$  by measuring the PSG over another set of at least 4 basis states (de Martino, 2004).

The main difficulties encountered while calibrating any polarimeter have been described in Section 5.1. The ECM sets out to eliminate/minimise the main sources of error generally associated with calibration. Three characteristic matrices are described,  $W$  for the entrance arm (PSG),  $A$  for the exit arm (polarimeter), and  $M$ , the Mueller matrix of the sample. The PSG for the GASP design has been modified to that described by Compain et al. (1999). This was based on a previous calibration method discussed in Section 5.4. The PSG, therefore, was not modified for ease of mechanical design. A measurement of

$$I = AMW \quad (5.9)$$

is the basis of the ECM making use of linear algebra.

The ECM has the following advantages (Compain et al., 1999):

1. No assumption is made to the system to be calibrated - except that it must be complete. The precise orientation and position of the various elements that comprise the polarimeter do not need to be known for calibration. All optical elements are included in the matrix representation.
2. The characteristics of the reference samples are completely determined during the calibration without need for secondary measurements. All aspects of the sample are measured during the ECM.  $W$  and  $A$ , when measured, will be a function of the wavelength  $\lambda$ , as will the defining characteristics of the reference samples.
3. The accuracy of the calibration procedure can be evaluated when the ECM is used.

Therefore, according to the above points, the Stokes vectors for the PSG used by GASP does not need to be known prior to calibrating the instrument. It is in fact calculated during the calibration process using Equation 5.9.

---

The general form for the matrices  $A$  and  $W$  are  $n \times 4$  and  $4 \times m$ , respectively, where  $n$  and  $m$  are greater than 4.  $n > 4$  mean that more than four input Stokes vectors are generated, and  $m > 4$  means that the output Stokes vectors are over-determined. This is the case for GASP. The ECM is fully compatible with other size matrices and the dimensions of the intermediate matrices must be adapted (Compain et al., 1999).

### 5.5.1 Mathematical Description

The following description is based on the work by (Compain et al., 1999) and references methods and naming conventions used by (de Martino, 2004) and (Lara Saucedo, 2005).

A linear mapping is described by

$$\begin{aligned} \mathbb{H}_4 : M(\mathbb{R}) &\rightarrow M_4(\mathbb{R}), \\ X &\rightarrow MX - X(aw)^{-1}(amw). \end{aligned} \quad (5.10)$$

$M$  is the Mueller matrix of the reference sample and  $(amw)$  corresponds to experimental measurements.  $\mathbb{H}$  has the property of having  $W$  within its null space, i.e.,

$$\mathbb{H}(W) = 0, \quad (5.11)$$

whatever the value of  $M$ , because without experimental errors  $(aw)^{-1}(amw)$  is equal to  $W^{-1}MW$ . A well chosen set of reference samples for  $\{M_i, \dots, M_n\}$  can reduce the number of solutions to Equation 5.11 to one. And then  $A$  can be deduced from the following:

$$A = (aw)W^{-1}. \quad (5.12)$$

The chosen reference samples for GASP are based on the work carried out by (de Martino, 2004) and (Lara Saucedo, 2005) and are discussed in detail by these references. A mathematical solution to this method can be found in Appendix C.

---

## 5.6 Calibrating GASP

When analysing the results of the ECM, the following equation is used to normalise the system matrix to the first element of the theoretical PSA. This gives a better understanding of any variation in the 16 coefficients, and a comparison between the individual coefficients. The experimental matrix is calculated based on intensity values and it is difficult to interpret the variation in the coefficients without normalisation.

$$A_{\text{norm},i} = \frac{A_i \text{PSA}(1, 1)}{A_i(1, 1)}. \quad (5.13)$$

The calibration method used has been discussed, mathematically, in Section 5.5.1. Calibration data is acquired as follows:

- Input light is generated using an LED, a filter and a linear polariser.
- An ECM wheel contains a set of samples, AIR, a polariser at  $0^\circ$ , a polariser at  $90^\circ$  and a quarter-wave plate at  $30^\circ$ .
- The polarimeter output intensities are recorded for a set of angles ranging from  $-38^\circ$  to  $-209.36^\circ$  in  $-10.08^\circ$  increments for each of the above samples, and is repeated using a quarter-wave plate (QWP) place in front of the linear polariser. Though of course, as has been explained above, it is not necessary to know what these angle are, as long as the same process is repeated for the QWP.
- These intensities are used to extract a system matrix, A and Polarisation State Generator (PSG), W.

## 5.7 ECM with Avalanche Photodiodes

The procedure for gathering data using this detector set up is carried out using the description in the above Introduction. Each APD unit has a dark count, which is measured by the manufacturing company, though it is important to monitor this signal regularly for any changes over time. A background light signal is also

---

recorded using the remaining 4 fibres (not centred on the target field). The dark counts are removed from the target and background signals, and finally the background light is subtracted from the target to remove any reflections or stray light due to any leakage in the instrument. The calibration arm is located on axis, where the light from the collimated LED is mounted external to the main instrument. The data recorded to experimentally measure polarisation in the laboratory uses the same light source, located on the same axis.

The data presented here will discuss the system matrix obtained using GASP as a bench instrument. Some data will also be presented showing how well the ECM performed by using GASP to measure the polarisation of a continuous signal for both polarised and ‘unpolarised’ data.

### 5.7.1 ECM Results

This section presents a detailed description of how the ECM is applied using Avalanche Photodiodes, where the light is fed to the detectors by optical fibres. This laboratory results demonstrates how well the ECM works and how GASP can be used to measure a polarimetric signal. This result was a bench result and will not be discussed in terms of observational results, but as an analysis of the use of the ECM (described above) for calibrating GASP.

A set of calibration data was recorded, using APDs, in the laboratory dated July 2011 and an experimental system matrix, A, shown by..

$$A = \begin{pmatrix} 0.1766 & -0.0901 & 0.1571 & 0.0042 \\ 0.4983 & -0.2010 & -0.4419 & 0.0113 \\ 0.4992 & 0.2503 & 0.1167 & -0.4058 \\ 0.3813 & 0.1826 & -0.0535 & 0.3229 \end{pmatrix}. \quad (5.14)$$

which can be compared to the theoretical PSA,

$$PSA = \begin{pmatrix} 0.1766 & -0.0858 & 0.1544 & 0 \\ 0.1766 & -0.0858 & -0.1544 & 0 \\ 0.2176 & 0.1078 & 0.0008 & -0.1890 \\ 0.2176 & 0.1078 & -0.0008 & 0.1890 \end{pmatrix}. \quad (5.15)$$

---

In the absence of errors, these matrices should match. The matrix is divided into 4 rows. The first 2 rows represent both RP channels, and the second 2 rows are each of the TP channels. Of course, the order of these channels within each path depend on the experimental optical alignment. The first column of the system matrix (and the PSA) represents the gain of the 4 channels of the DOAP, which also includes the gain of each detector. In the discussion comparing each experimental matrix, it will be focused on the gain parameter. This gives the most information regarding the system alignment. The other coefficients are very important, particularly how they are distributed in each row and how their value compares to the PSA; this has been addressed in Section 3.2.1.

The gain of the APDs are a factor in the matrix found in Equation 5.14. The difference in the values in the first column are an indication of these gain variations. There are obvious similarities between A and PSA. Reasons for why these values are not matching exactly are as follows:

- The AOI is not what has been theoretically described.
- Detector gains are assumed to be unity in the theoretical model, this is rarely the case experimentally. Relative gain variation observed in the experimental matrix will be largely due to differences in detector gain values.
- The Wollaston/Foster prisms are aligned at an integer value of  $45^\circ$ .
- The Wollaston/Foster prisms are not aligned at  $45^\circ$  exactly.
- Temperature/pressure variations, which could cause glass contraction/expansion. If this is not uniform across all channels it could result in a change of focus, light losses, incorrect relative gain measurements. This experimentation was beyond the scope of this thesis work<sup>1</sup>.
- Errors in lens focusing.

---

<sup>1</sup>The temperature has been recorded using an ordinary alcohol thermometer placed in the instrument. The temperature variation was never found to vary any more than  $0.5^\circ$  and no systematic was noted in data measurements.

## 5.7.2 Polarimetric Results

The following results have been presented at the Frontiers in Optics Conference, which took place in San Jose CA., 2011 (Kyne et al., 2011). The system matrix A, was used on another data set to produce plots for each of the Stokes parameters for a polarised light source using an LED passed through a glass polariser (Sodium-Silicate glass) and data was recorded for  $\sim 48$  hours. This was a test to see how much variation GASP was subject to over a very long time frame. It was also a check for detector stability as the choice of APD for this system was discovered to be unsuitable in terms of dark counts and electronic noise. The performance of detectors for GASP, and their stability over time was not the work of this thesis. These detectors are used purely for laboratory testing in the context of this work.

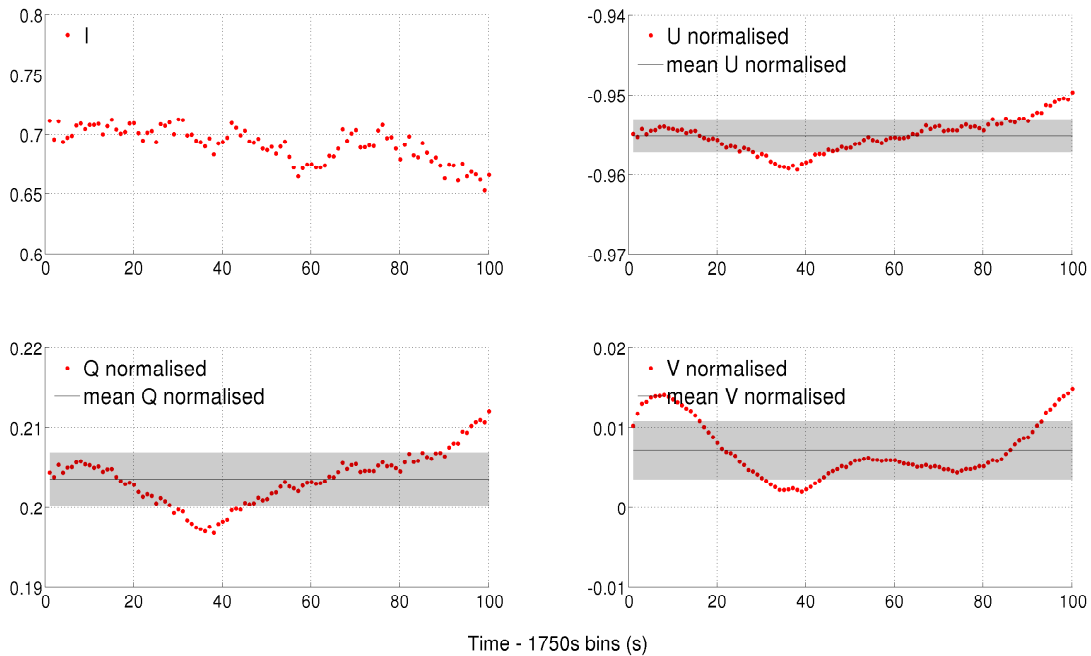


Figure 5.3: Stokes parameters I, Q, U, and V for an experiment passing LED light through a linear polariser to measure the limits of the GASP system using APDs. The Q, U, and V parameters have been normalised to Stokes I to remove any fluctuations in luminosity. A systematic effect is observed on Stokes Q and U, the parameters used to the measurement of the degree of linear polarisation. A different trend is found for V, which suggests an instrumental effect for this laboratory experiment.

---

The parameters Q, U, and V have been normalised to Stokes I to remove any intensity variations over the course of the experiment. A trend is observed in Stokes I; there is a drop in light intensity, which is most likely a result of intensity variation in the LED used over the 48 hour period. In Stokes Q, U, and V, there is evidence of systematic error, as well as random, over this period.

The mean and standard deviation in the values for Q, U, and V are  $0.212 \pm 0.003$ ,  $-0.950 \pm 0.002$ , and  $0.015 \pm 0.004$ , respectively. The standard deviation value is quoted after normalisation, however, there is a visible trend in each of these parameters that suggests a systematic change in the data. This is a possibility as during the experiment a linear polariser was used to generate a polarised signal. The systematic effect shows a drop in value at time point  $\sim 38$  ( $\sim 18.5$  hours) for all Q, U, and V. If the polariser moved, and the movement was not symmetric, then this could induce/reduce linear/circular polarisation. It would also account for the change in polarisation angle seen in Figure 5.4. This systematic error means that the errors quoted for this data set are higher than the random noise, which is visible in this plot.

This systematic error could occur due to the nature of the polariser material. This will be subject to stresses and imperfections over time, and it is possible that the material could also exhibit birefringent properties as a result. Potential reasons for this systematic effect could result from temperature variation causing contraction/expansion of the polariser; the polariser is assumed to be static, this may not have been the case. If the polariser moves during the experiment then not only could polarisation be induced, but any change in angle could also be measured.

This material will be subject to stresses and imperfections over time, and it is possible that the material could also exhibit birefringent properties as a result. Potential reasons for this systematic effect could result from temperature variation causing contraction/expansion of the polariser; the polariser is assumed to be static, this may not have been the case.

Over the time series the mean DOLP was measured to be  $97.66 \pm 0.21\%$ , and the DOCP  $0.72 \pm 0.36\%$ . This is a promising result that indicates GASP has the ability to measure small variations in the linear polarisation error as it fluctuates by about 0.2% over a time series of this duration. The errors quoted are from a

---

combined systematic and random effect and are within very reasonable limits for a linearly polarised signal.

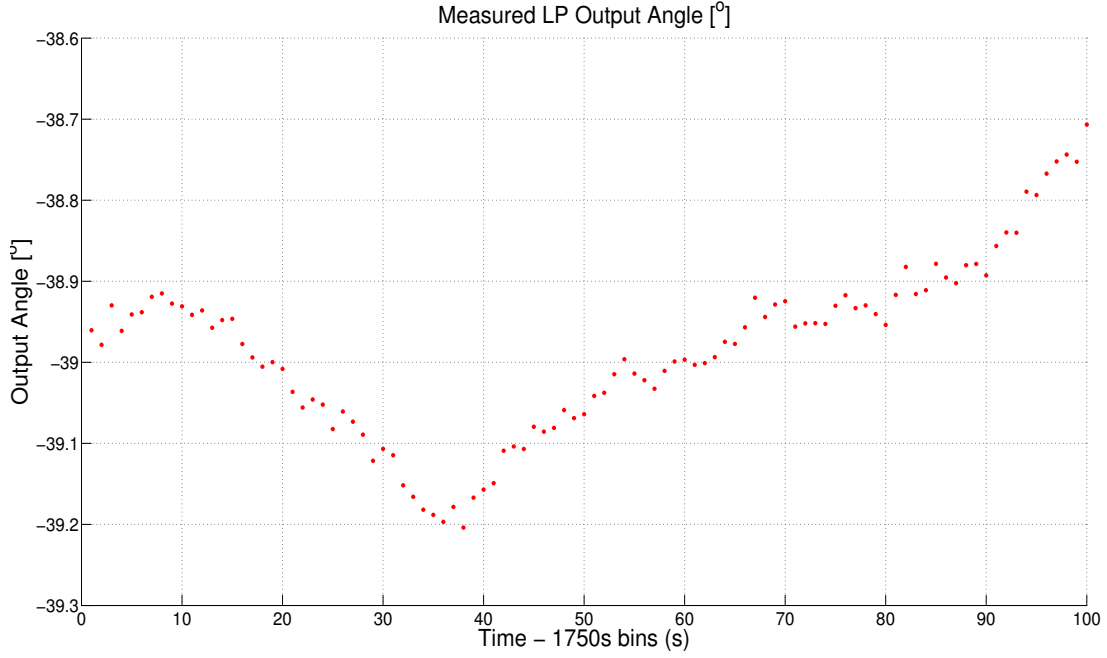


Figure 5.4: Polarisation angle measurement for an experiment passing LED light through a linear polariser to measure the limits of the GASP system using APDs. The drop, and variation, in Stokes Q and U is observed in this plot. There is a variation of  $0.5^\circ$  from beginning to end, which suggests that the polariser is moving. This is not a random effect and over a prolonged period (2 days) it is possible that there was movement in the laboratory, or in the vicinity of the instrument, that could account for this variation.

The polarisation angle of the data set was also measured. This is the azimuthal angle of the linear polariser when placed in the optical axis of GASP. The PA was measured prior to the laboratory experiment; this had a value of  $\sim -38.5^\circ$ . Looking at the plot in Figure 5.6 an angle of  $-38.99 \pm 0.19^\circ$  was measured by the GASP ECM. Again, the ECM has measured the PA to a level of  $0.2^\circ$ , another notable aspect of the ECM performance using GASP. These errors will include any instrumental polarisation effects<sup>2</sup>.

---

<sup>2</sup>A more precise way to measure instrumental polarisation is to use an absolute known polarisation standard (in the laboratory or during observational experiments), this way GASP can be

---

There is variation over the time series ranging over  $0.5^\circ$ . The structure holding the linear polariser was examined and it is very possible that the linear polariser was subject to some movement or wobble within the structure. If this is the case, then the ECM is actually capable of measuring this wobble. If the variation in the polarisation angle is examined on a shorter time scale - in an area where the systematic effect is reduced, or absent - the variation is less than  $0.1^\circ$ . It is a very interesting result and a good indication that GASP is working correctly; it also illustrates the capability of GASP to detect fluctuations in the polarisation angle to a level of  $\pm 0.1^\circ$ . When light of a given polarisation state is passed through the system the output for DOLP, PA, and DOCP is very close to what is expected. Table 5.1 summarises the results of this experiment.

There may also be errors present due to instrumental polarisation effects<sup>3</sup>, however, this is difficult to measure due to the presence of this systematic. One of the primary aspects of using the ECM is to reduce error in optical misalignment of the instrument. It is not capable of removing instrumental polarisation from telescope optics, or atmospheric conditions during observing conditions. The raw intensity data for each of the 4 channels is plotted in Figure 5.5. The drop in Stokes I found in Figure 5.3 can also be found across all 4 channels; an indication that the LED light level has changed during the experiment.

Table 5.1: Linear polariser laboratory experiment using APD detectors to test the GASP ECM.

	DOLP (%)	PA ( $^\circ$ )	DOCP (%)
Expected	100	-38.5	0
LP experiment	$97.66 \pm 0.21$	$-38.99 \pm 0.19$	$0.72 \pm 0.36$

Another experiment carried out using APD detectors was to establish whether compared to an expected result; relying on polarisers in the laboratory for absolutes is not an ideal experiment.

<sup>3</sup>A more precise way to measure instrumental polarisation is to use an absolute known polarisation standard (in the laboratory or during observational experiments), this way GASP can be compared to an expected result; relying on polarisers in the laboratory for absolutes is not an ideal experiment.

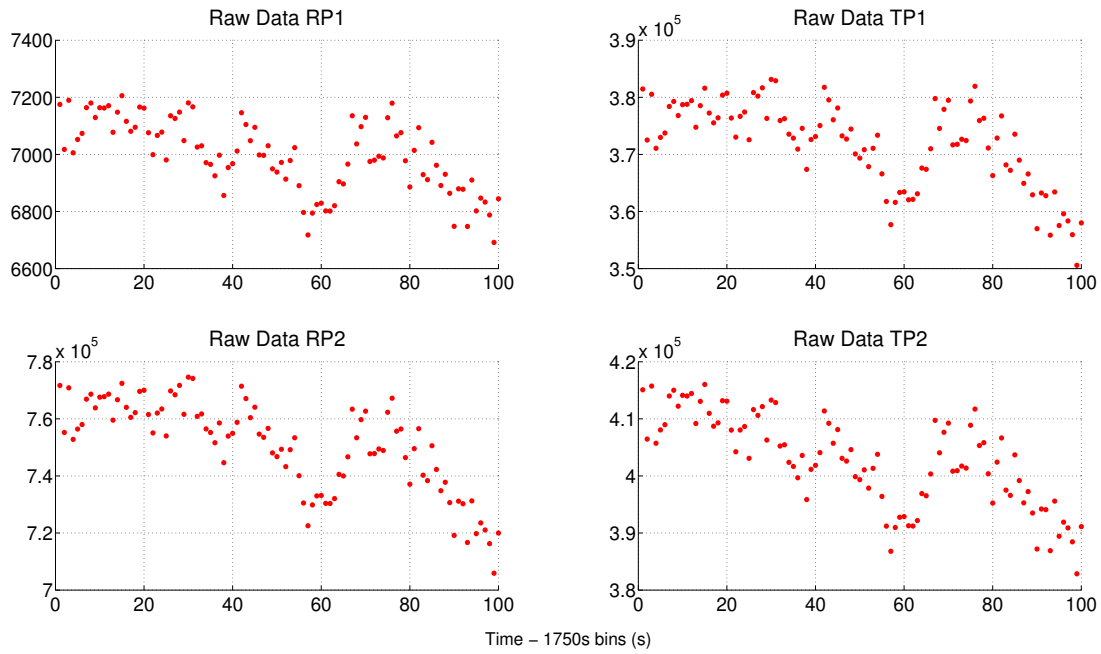


Figure 5.5: Raw intensity data for each of the 4 channels for an experiment passing LED light through a linear polariser to measure the limits of the GASP system using APDs. A drop in light intensity is evident across all channels indicating that the LED light level dropped during the experiment. This is also found in the plot for Stokes I in Figure 5.3.

GASP could make an accurate measurement of an unpolarised source. An unpolarised source is very difficult to produce in a laboratory environment and this experiment was without the use of an integrating sphere<sup>4</sup>. The same system matrix was used to reconstruct the Stokes parameters of this data as that used for the polarised data.

In this case, the LED used in the first experiment was used as an input polarisation state, assuming the output to be unpolarised light. The mean and standard deviation values for Q, U, and V are  $-0.0134 \pm 0.0002$ ,  $-0.0349 \pm 0.0001$ , and  $0.0203 \pm 0.0001$ , respectively. Over the time series the mean DOLP was measured to be  $3.74 \pm 0.01\%$ , and the DOCP  $2.03 \pm 0.01\%$ . This is a more or less inconclusive result without the expected values for DOLP and DOCP from the specifications

<sup>4</sup>An integrating sphere uses the idea of scattering light an infinite number of times within the sphere until the light is ‘mixed’ in such a way that the light exiting the sphere is unpolarised.

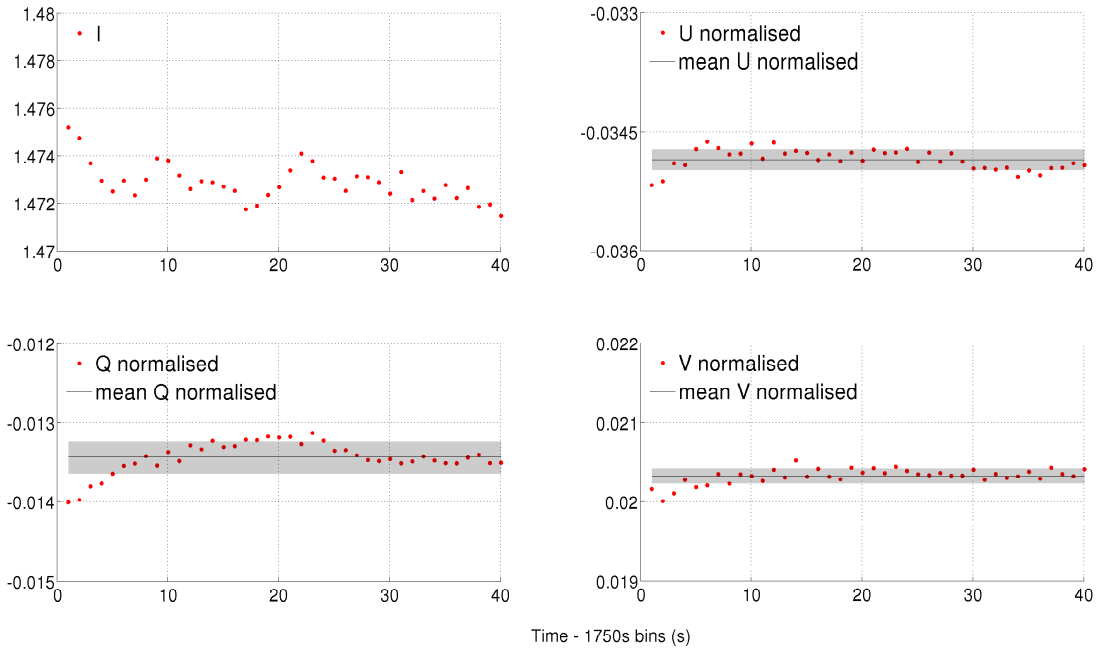


Figure 5.6: Stokes parameters for an experiment passing light from an LED source through GASP to measure the limits of the GASP system for an ‘unpolarised’ using APDs.

of the LED manufacturer. However, it is a result that can be analysed as follows: The result of the ECM concludes that GASP is working within the theoretical limits established by the DOAP design, accepting that the optical alignment of the PSA does not need to match exactly. An experimental measurement of a linear polarisation state is measured within the limits of the expected values. The LED is an incoherent light source that should be capable of producing polarised light. If the results from the linear polariser test are considered a standard measurement, then it can be concluded that the values measured by the ECM are in fact correct for this LED.

It should be noted that there is drop off in Stokes I at the beginning of the time series. There are a number of reasons for this drop in intensity, however, most likely, the reason is that the LED used was not perfectly stable at the beginning of the experiment, producing a steady signal after  $\sim 5$  seconds. As GASP measures a relative signal this has no impact on the final Stokes measurement; however, this drop in intensity is very low, of the order  $10^{-3}$ . It should also be noted that during

---

this experiment no material capable of movement is being used. This is evident from the plots in Figure 5.6 where there is no obvious systematic trend, and the errors are due to random noise effects. Table 5.2 summarises the results of this experiment.

Table 5.2: Unpolarised source laboratory experiment using APD detectors to test the GASP ECM.

	DOLP (%)	PA ( $^{\circ}$ )	DOCP (%)
Expected	0	-	0
'ZERO POL' experiment	$3.74 \pm 0.01$	NA	$2.03 \pm 0.01$

The polarimetric results obtained for an 8-detector APD instrument using a linear polariser show, quantitatively, that GASP is a working polarimeter to a high degree of accuracy; measuring both percentage polarisation (0.2%) and polarisation angle ( $0.2^{\circ}$ ). The instrument has been calibrated and this is confirmed by the Stokes reduction. A factor that must be considered, through rigorous alignment, is to ensure that the optical axis of the instrument matches that of the telescope. This includes matching the height of all optical elements to a central point where the instrument is mounted, and ensuring that all light is incident at  $90^{\circ}$  (where light from the telescope does not travel through any optics off axis).

The results from the polarimetric test using an LED as an unpolarised sources are less conclusive. As there was no integrating sphere available in the laboratory, an LED was used with a diffuser and R Band filter. It is possible that the value of the DOLP for this LED is  $3.74 \pm 0.01\%$ , however, there is no information in the manufacturer specifications, or literature, that confirm the polarimetric results produced with GASP.

It is difficult to measure the degree of linear polarisation at the extremes of its range (0 - 100%), particularly at the minimum value. This is due to a weakly polarised signal, which can be contaminated by scattered light, low SNR, poor seeing, and poor atmospheric conditions.

Due to insufficient laboratory testing of APDs, it was not possible to run veri-

---

fication tests on a set of calibration data. Verification testing on calibration data will be examined later in this chapter for GASP as an imaging polarimeter.

## 5.8 Pixel-by-Pixel ECM using Imaging Detectors

A pixel-by-pixel method of analysis, will be presented in this section using GASP as an imaging polarimeter. The results of this method will be discussed for data recorded at the 200 inch Hale telescope at Palomar Observatory. The observational data recorded will be presented in Chapter 6, with analysis and discussion of the imaging results based on the work presented in these sections to follow. Two methods for registering the calibration data will be discussed in this chapter. Each method will be developed as follows:

1. The techniques used to perform registration and their errors.
2. Registration results in the form of residual errors.
3. The polarimetric results of the ECM through a pixel-by-pixel analysis.

Tyo et al. (2006) explains how image registration, whether for sequential or simultaneous image collection, is a critical issue. Misregistration can result, for example, from separate focal planes that are not looking at the same region of space; it can also result in beam wander from a rotating element. Smith et al. (1999) have suggested that images should be registered to 1/20 of a pixel to achieve less than 0.01 error in DOLP and DOCP results. In Figure 5.7, the authors plot the maximum values of induced DOLP and DOCP as a function of beam wander magnitude. The errors for both 180° and 360° wander are shown. It was found that both DOLP and DOCP increase rapidly as the beam wander diameter increases. This was a technique applied to a dual-beam polarimeter used by the authors, and in the case of GASP this is a error guideline.

Ideally, the alignment should be mechanical. In practice, achieving even a half-pixel alignment mechanically can be difficult - of course this will be dependent on the pixel size of the detector - and software post-processing alignment is frequently

---

necessary. Registration between the channels also includes matching transmission, magnification, and distortion; and is a difficult process, even using post-processing techniques.

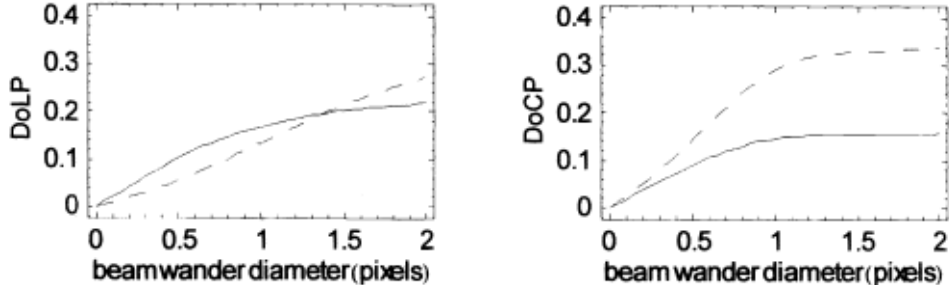


Figure 5.7: Maximum magnitudes of DOLP and DOCP for a square test image. Solid line is for  $360^\circ$  image wander, dashed line is for  $180^\circ$  image wander. The angle of rotation refer to a retarder that is rotated in the beam and induces image wander.

Analysis of the image residuals are a good indication of how well the image sections are registered and hence calibrated. This shows how well the pixels are matched by normalising the input image to the reference image. Equation 5.16, (Ibez et al., 2003), is used to find the normalised flux,  $I_{\text{new}}$ ,

$$I_{\text{new}} = (I - I_{\min}) \left( \frac{R_{\max} - R_{\min}}{I_{\max} - I_{\min}} \right) + R_{\min}, \quad (5.16)$$

where  $I$  is the original flux value, and  $R_{\max}$  and  $R_{\min}$  are the maximum and minimum values are the maximum and minimum values of the reference image used for registration. This way, it is certain that the maximum and minimum values in the input image are matched and scaled accordingly. It is noted that this method of normalisation is best suited when comparing a source, which has a sharp, defined PSF, compared to extended fields.

According to Tyo (2006), to measure the Stokes parameters in an image, the optical intensity must be modulated in time, space, or spectral characteristics and multiple measurements must be made on a pixel-by-pixel basis across the scene. Most existing imaging polarimetry strategies generally suffer from either spatial or temporal misregistration. To avoid the complications of misregistration, these

---

analyses/strategies have severe restrictions placed on the spectral properties of the illumination and/or optical system.

Tyo et al. (2006) discusses the manipulation of polarimetric data reduction for the same pixel across multiple frames. Any motion of the scene in the pixel results in artefacts that have the potential to mask the true polarisation signal. Ideally, two spatial dimensions are desired, but due to this temporal image registration issue, the images must be acquired simultaneously or acquired as quickly as possible to minimise artefacts from platform or scene motion. This is not an issue for GASP as it uses the technique of DOAP that provides the best solution for eliminating these artefacts by the acquisition of multiple images at the same time, however, the issue then becomes spatial registration. Spatial registration of multiple images is complicated by the need to correct for both mechanical misalignment as well as optical ‘misalignment’ arising from aberrations due to separate optical paths. The simplest way to measure the polarisation information is to use separate cameras with separate optics that are aligned to the same portion of the image. This can be done using 2 or 4 imaging detectors, however, they must be matched spatially once data is recorded.

GASP is calibrated using a pixel-by-pixel ECM, to establish a uniform calibration which will be discussed later in this chapter. Errors in focus, image registration, and gain variation can contribute to a non-uniform FOV calibration; if this is the case, then it will not be possible to spatially recover the target’s Stokes parameters correctly, or in any case it will limit the FOV over which the calibration is valid. It is important to establish a uniformly calibrated field for situations when the science goal requires multiple targets in the FOV, or to measure spatial variability in the target. This can be compared to the case when using single photon detectors (1D detector) such as a PMT or APD. In this case, one pixel must be calibrated as all light in the FOV will fall on this pixel. In the case of imaging, the light is divided over multiple pixels, which is dependent on the sampling and sensitivity of the instrument. As the incoming light beam is split 4 ways, every pixel on one channel must be matched to the remaining 3; therefore a pixel-by-pixel ECM will measure how well this matching has been performed, determining how well the system is calibrated.

---

If all 4 channels are well registered polarimetric information may be gathered pixel-by-pixel, or using aperture photometry, which measures the flux of an astronomical target. A pixel-by-pixel analysis is the preferred method of analysis when calibrating imaging polarimeters, particularly when there is division of the incoming beam. This is because each pixel can have different properties, such as gain or noise, or the detector chip may contain dead or saturated pixels (no useful information is gathered). Therefore, by calibrating pixel-by-pixel, these issues can be accounted for, and are able to assess the response of each individual detector (each individual pixel). Averaging over a number of pixels can help to reduce detector variations, however, this will lead to the loss of polarimetric resolution.

## 5.9 ECM Image Registration using Artefacts

GASP calibration data consists of 10 images for every polarisation state of the PSG through each of the ECM samples (described in Section 5.6): This results in 144 images recorded for each path. A single image from each channel can be found in Figure 5.8. Mechanically, the calibration arm is located off axis to the optical axis of the instrument. A plane mirror at  $45^\circ$  is used to redirect the light into the instrument. The process of matching the optical axis of the calibration arm and the optical axis of the instrument is addressed in the laboratory. A resolution target, or a target containing multiple, randomly placed, pinholes can be placed at the instrument focus to map the spatial variability between each of the 4 channels. Alternatively, a light source can be placed along the GASP optical axis, which can then be matched to the off axis calibration beam. Finally, during observations the telescope can be pointed at a crowded star field to compare with the on axis laboratory results. Ideally, if observation time allows, the same target can be placed at focus during twilight as the sun rises, to better compare with the laboratory configuration. This was not an instrument restriction when using APDs. The calibration and laboratory experiments were recorded on the same optical axis, and there was also no need for spatial matching between the 4 channels.

During the observational run at the P200, there were less than ideal observing conditions on 3 out of 4 allocated nights. This limited GASP observing time and a

---

spatial channel comparison was not possible. The instrument was also inaccessible during observing. Closer inspection of the observational data indicated that there were minor disparities in the form of artefacts: these artefacts were a means of matching the calibration channel of RP1 to the remaining 3 channels, RP2, TP1, and TP2, including their subsequent science channels. RP1 was chosen as the reference image for all registration routines.

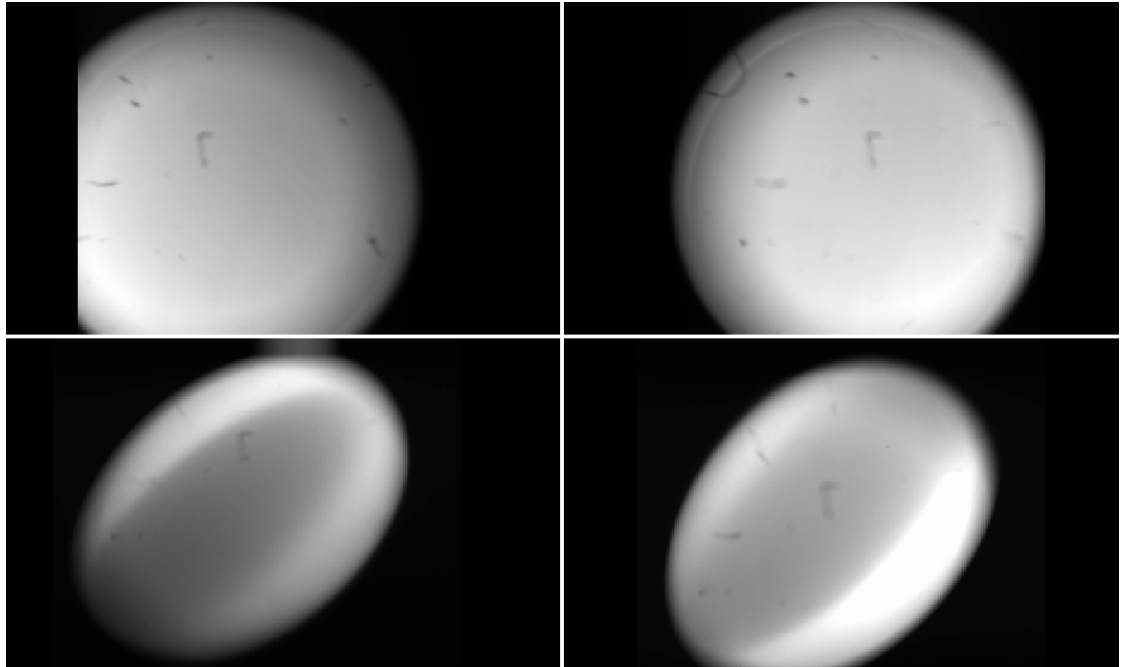


Figure 5.8: All GASP channels for a full frame calibration image. Top LHS: RP1, top RHS: RP2, bottom LHS: TP1 and bottom RHS: TP2.

These artefacts were located in the usable, non-vignetted FOV of the instrument and can be found in Figure 5.9. They are common to all channels, though, as there was some vignetting on the TP channel images, there are less artefacts visible. Due to the fact that it is possible to locate a number of artefacts common to all channels it suggests that they are in fact scratch marks, indentations, or manufacturing defects on the field lens, discussed in Section 4.3.4. It can be assumed that these artefacts pass through the polarimeter, re-imaged by the detector lenses. These artefacts are useful points to perform image registration as they are almost ‘built-in’ to the instrument. The artefacts look well focused on each of the

---

RP images, and less so on one of the TP channels - TP2. This indicates misalignment in focusing the TP channel lens when re-imaging onto the detector chip. The basis of this assumption is that, for example, looking at the image artefact at the top centre of RP1, which resembles an inverted ‘L’: This point appears on RP2, TP1, and TP2. If this point appears in all 4 channels then it must be imaged from the same point in the optical path, i.e. it is a single conjugate point to the imaged artefact. This is true for all common artefacts between channels. If this point is out of focus on one or more channels, it is a result of incorrect alignment and/or focusing of the imaging optics.

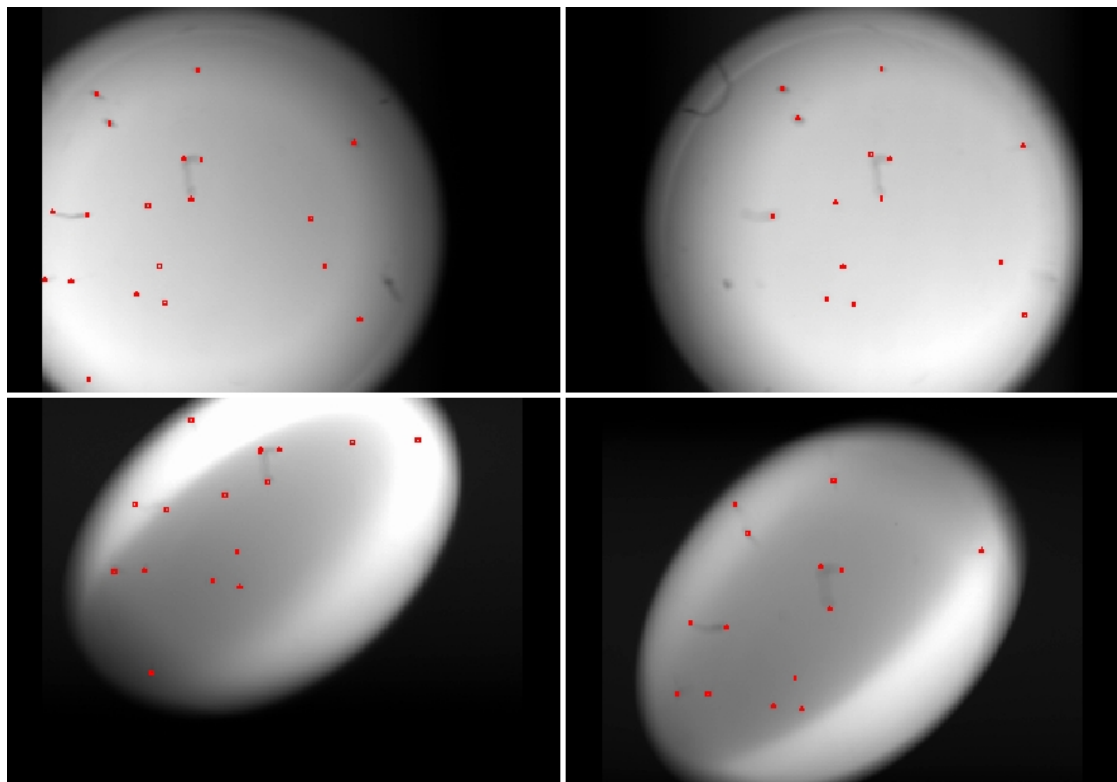


Figure 5.9: All GASP channels for a full frame calibration image. Top LHS: RP1, top RHS: RP2, bottom LHS: TP1 and bottom RHS: TP2.

PyRAF was used to perform all GASP image analysis including bias subtraction, image registration, image combination, and aperture photometry. PyRAF combines the python programming language with the Image Reduction and Analysis Facility (IRAF) software system for the reduction and analysis of astronomical

---

data. PyRAF was used to generate a master bias frame, which consists of 1000 bias frames, averaged using a pixel rejection routine with a  $\sigma$  level of 0.5. All calibration images were debiased using this frame, one for each detector. The same bias frame was used throughout all other data analysis. If the bias frame settings are changed for the calibration data set, then that new frame was used on science data.

Prior to image registration, the normal astronomical analysis routine would use a flat-field to remove any artefacts within a set of data caused by variations in the pixel-to-pixel sensitivity, as a result of the detectors used. In the case of GASP, the ECM procedure takes into account the pixel-to-pixel variation between images. This type of processing would only account for a variation within the image itself, the concern with GASP is the variation between channels, which indicates that pixel-matching is the ultimate requirement. In any case, if this processing was carried out it would be required for both the calibration and science data, in the case of relative measurements this step appears to be unnecessary. Intensity variations in a polarimetric output can be performed after calibration and this will be discussed in Section 5.9.3.

PyRAF was then used to perform image registration using the visible artefacts common to all channels. RP1 was selected as the reference channel and all other calibration, and science, channels are mapped to RP1. These artefacts are not point sources; therefore, it was impossible to choose, and match, their respective centroids, which was performed based on a gaussian/moffat light signal distribution. Instead, line edges, and corners, were selected. It has been noted that there was an element of error introduced by the user's (visual) determination of where an edge/corner begins/ends. This was expected to introduce a systematic error in spatial registration, which has been approximated to be 1 pixel. It was also noted that the RMS results, an output of the *geomap* tool, were an indication of how well these edges/corners were matched image-to-image. These indicated that the selected points were well matched based on the results in Table 5.3.

All data at the Palomar 200 inch telescope was recorded using 2 EMCCD detectors, i.e. both RP channels are recorded on one detector, and the TP channels on the other. Prior to selecting common artefacts, and subsequently image registration, each full frame ( $512 \times 512$ ) image was divided in 2  $256 \times 512$  images

---

- creating 4 channels. The TP channels were ‘prepped’ to make the process of registration to RP1 channel simpler. Figure 5.8 shows that the TP images are flipped along the y axis by  $180^\circ$  and there was a rotation of  $\sim 90^\circ$ . Both these transformations were carried out before final registration, where any remaining rotations were taken care of using the *geomap* geometrical solution.

Note: the  $180^\circ$  is an exact measurement found from the Zemax theoretical model. This is a result of the RP image, which is reflected off the prism footprint (see Figure 4.6) introducing a  $180^\circ$  flip on this channel compared to what enters the polarimeter. There are 2 total internal reflections within the prism that flip the image by  $180^\circ$  twice. As all channels are compared to RP1, the pre-flipping was therefore performed on each TP channel. The  $90^\circ$  comes from the orientation of the Wollaston prism; Zemax cannot be used for this as the experimental alignment does not match the Zemax prescription. The reason for why this is not an issue in the performance of the polarimeter has been address in Section 3.2.1. The reason for the initial  $90^\circ$  rotation was simply, to select image artefact points that matched both TP2 and TP2 to RP1 more easily. An IRAF command called *imlintran* was used to perform the initial flipping and rotating. No skew, scaling or distortion is introduced when carrying out this analysis as every measurement was carried out based on the same reference point. After this step, it became clear, which artefacts were common between RP1 and each of the TP images. There was no difference between the raw image and the flipped and rotated image except in terms of a pixel linear translation. The final registration depends solely on the geometrical relationship between points in the image. All TP images were analysed in this way.

A set of points, per channel, were selected for image registration<sup>5</sup>, and an IRAF command, called *xyxymatch*, was used to perform point matching. This is a useful command as, interactively, the user chooses 3 common points in a triangular configuration on the reference image, and the same 3 points are selected on the input image to be matched. The task selects the remaining matched coordinates that best fit this criterion.

This matching process generates an initial transformation that can be used as

---

<sup>5</sup>This was a factor in determining the order of the polynomial function used and are matched based on a pixel tolerance or triangles relationship.

---

a check of the initial transformation. The matching is stored in a *transform* file, which is fed to a command called *geomap* generating a transform *database*. A registration command called *gregister* takes the original images and registers them using the information stored in the *transform* and *database* files. The minimum function that could be used to fit the data was a 3<sup>rd</sup> order polynomial, which includes higher order distortions in the registration solution. The *geomap* database can generate a function of this order using a minimum of 10 matched points. A data point ‘outlier’ could grossly distort the transformation, therefore RMS value checks should be carried out to find the best combination of points. The RMS value of the fit is only significant in the region where the points are located; however, RMS values of matched points that are higher than 1 pixel are normally rejected.

A 3<sup>rd</sup> order polynomial calculates 6 parameters; linear translation, rotation and scaling for an (x, y) coordinate. It also has the capability of calculating surface distortion factors based on the residuals of the linear fit. *geomap* was used to calculate this polynomial function to register the GASP data. The polynomial solution obtained was assessed based on how well the chosen points fit in terms of RMS values; it was also assessed from the percentage image residuals, which were calculated using Equation 5.16 after registration.

The RMS values for the function are a measure of the distortions specific to the points that are used in the transform, however, they are a useful first order check of the transform generated by *geomap*. Using this transform in a section of the FOV where there are no points means that it is unlikely to give a meaningful registration solution. The removal of any of the above points and re-running *geomap* gave a variation in  $x_{rms}$  and  $y_{rms}$  of  $10^{-3}$  for the RP2 image. In the case of each TP image, where the distortion was visibly worse, removing points the outer FOV gave values for the  $x_{rms}$  and  $y_{rms}$  varied for a range of  $10^{-2} - 10^{-1}$ , see Table 5.4. This reduction possibly indicated that the registration would show improvement, however, as was the case for RP2, it showed no comparable registration difference, particularly in shift, magnification, and rotation. As pixel binning was carried at the  $4 \times 4$  level, these values were greatly reduced. A number of registration combinations were carried all the way through to verify a calibration result based on registration points chosen and ultimately, the removal of any artefact did not alter the calibration matrix. The final registered images can be seen in Figure

---

Table 5.3: Output of the *geomap* fit for artefact registration. These values refer to the data at the pixel level without any binning.

Channel	RP2	TP1	TP2
x shift (pixels)	73.04	29.01	40.19
y shift (pixels)	-3.10	61.89	-11.54
x magnification	0.93	0.94	0.97
y magnification	1.01	0.98	1.01
x rotation ( $^{\circ}$ )	0.27	0.13	0.91
y rotation ( $^{\circ}$ )	0.27	3.58	0.41
$x_{rms}$ (pixels)	0.85	0.58	0.44
$y_{rms}$ (pixels)	0.32	0.53	0.57

## 5.10.

The points used for matching in each of the channels in Table 5.3 are not comparable as the same points were not matched per channel. The RP2 channel used points in the outer edges of the FOV; these same points do not appear in either of the TP images as the FOV was vignetted and too greatly distorted to use any points that appear here. It was reasonable to say that reducing the number of points used in the geometrical transform will yield lower RMS values in this case.

The RP2 channel has been shifted linearly in x and y so that the artefacts now overlap. The overall shape of the FOV is slightly altered but it maintains its circular outline from the LHS as far as the centre, however, the registration starts to breakdown toward the RHS of the image. There are less artefacts for selection in this area of the FOV and any global distortion will not be properly corrected. Looking at the TP channels in Figure 5.8, the FOV has a different shape to that of the RP channels. The main beamsplitting prism causes an astigmatism when it undergoes 2 total internal reflections, which gives this distorted view of each channel. This astigmatism is not obvious when imaging a point source, but it is

---

Table 5.4: Output of the *geomap* fit for the matched TP2 artefact registration. Artefacts were removed in the outer FOV where distortions appeared to grow visually.

Channel	TP2
x shift (pixels)	40.07
y shift (pixels)	-11.51
x magnification	0.98
y magnification	1.01
x rotation ( $^{\circ}$ )	0.95
y rotation ( $^{\circ}$ )	0.41
$x_{rms}$ (pixels)	0.39
$y_{rms}$ (pixels)	0.59

an underlying problem when pixel-matching the entire FOV. When each TP image is registered, see Figure 5.10, it can be seen that the pattern of the FOV is less elliptical and starting to take on a more circular shape. There were fewer points to choose from on the TP images compared to RP2. There is also ‘banding’ of light (where the light intensity on the image appears more localised) on the TP1 and TP2 channels. The light intensity is not being redistributed evenly as on each of the RP channels. This ‘banding’ is not present in the RP data and where it appears in the TP images is where the optical distortion appears worst; this effect has also been found in some of the observational data. In each of the TP images, and to a certain extent RP2, the further out from the centre of each field, the optical distortion grows. This optical effect has been discussed in Section 4.4.1.

Figure 5.11 is a set of registered images, similar to that in Figure 5.10, using different PSG elements for display purposes. The light level for the calibration images is set using the linear polariser. The LED is adjusted until the chip reaches  $\sim$  half pixel-well saturation. A frame is recorded for 0.0045 seconds and averaged over 10 frames. This is the image section that will be used in calibrating the

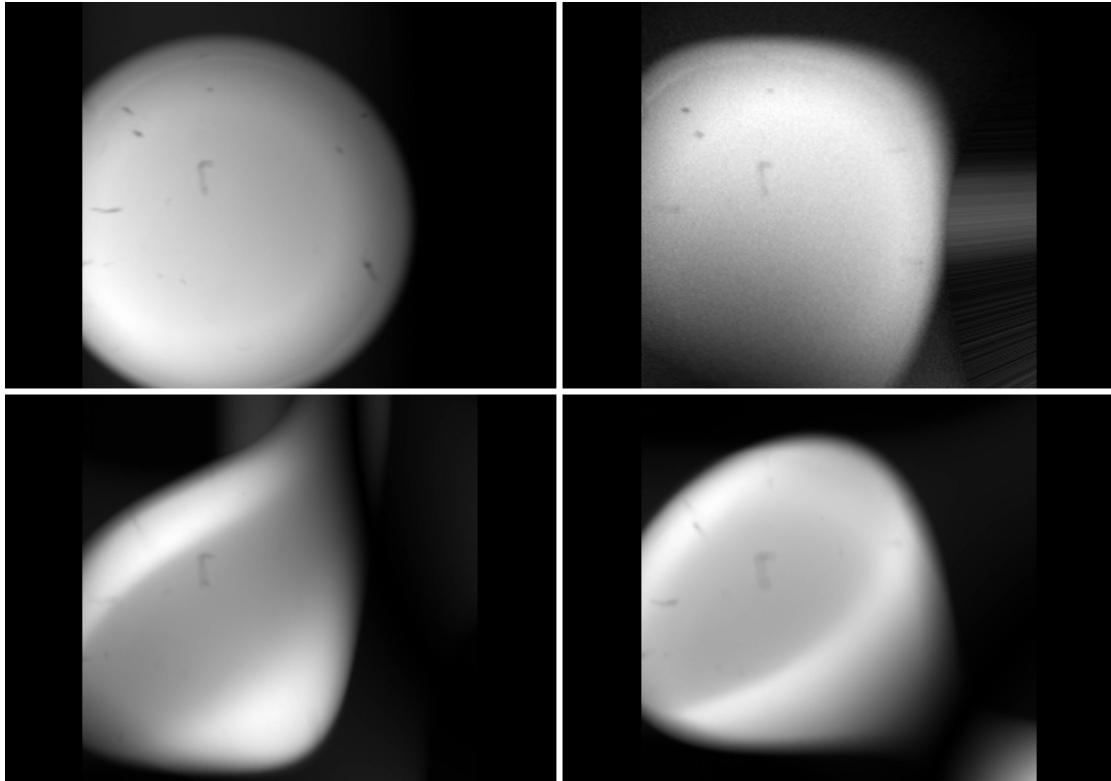


Figure 5.10: All registered GASP channels for a full frame calibration image using the artefacts in Figure 5.9. Top LHS: RP1, top RHS: RP2, bottom LHS: TP1 and bottom RHS: TP2.

instrument pixel-by-pixel.

Due to the processing time required to calibrate the data pixel-by-pixel, subsections of the calibration images were used depending on the location of a target or area on the chip that was of interest. In this section, a region in the centre of the chip will be used to reproduce polarimetric information of science targets. This data has been binned  $4 \times 4$  to reduce processing time, and a secondary objective of binning is to minimise distortion effects.

A closer look at a section of the image on which the ECM will be run (discussed later) show that, there appears to be remaining distortions on the bottom right and top left corner of the image; it suggests that, this area of the field is not as flat as the rest of the image section. This image section was chosen for the purpose of calibration, but also as this section of the FOV contained a number

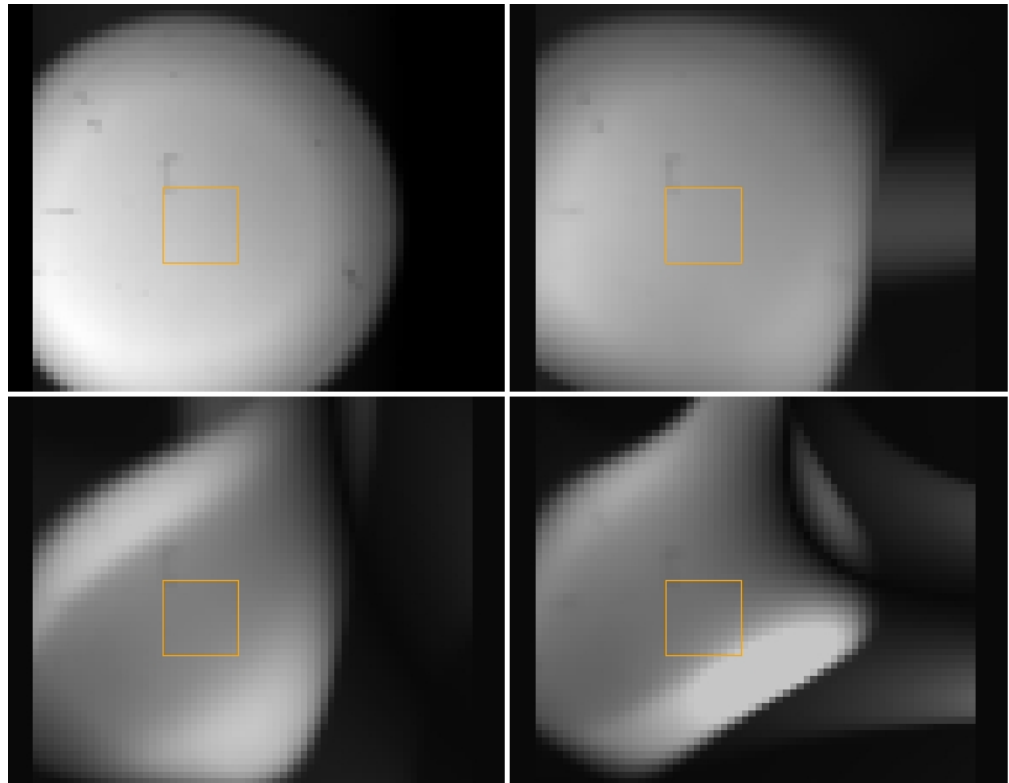


Figure 5.11: All registered GASP channels for a full frame calibration image using the artefacts in Figure 5.9. The section indicated by the orange box is used in calibration to produce a system matrix using the Eigenvalue Calibration Method. This calibration data set has been binned  $4 \times 4$ . Top LHS: RP1, top RHS: RP2, bottom LHS: TP1, and bottom RHS: TP2.

of observational targets from the observation run at Palomar, which would be of interest. The area on TP2 retains some variation in flux in the bottom right corner of the selected FOV. The targets for polarimetric reduction were not found in this area of the field. Unfortunately, there were insufficient image artefacts located in this area, which would have corrected this variation. The main objective of this image analysis was to achieve the best registration solution possible to calibrate every pixel in the image. If this matching is perfect, each pixel should have a similar system matrix to its neighbouring pixel.

---

### 5.9.1 Artefact Residuals

In order to determine how well registered these images are, image residuals (or pixel residuals) are calculated using Equation 5.16. This examines any artefacts left after subtraction, particularly in the case of observational data when using a clearly defined target(s). It also determines the intensity percentage difference per pixel.

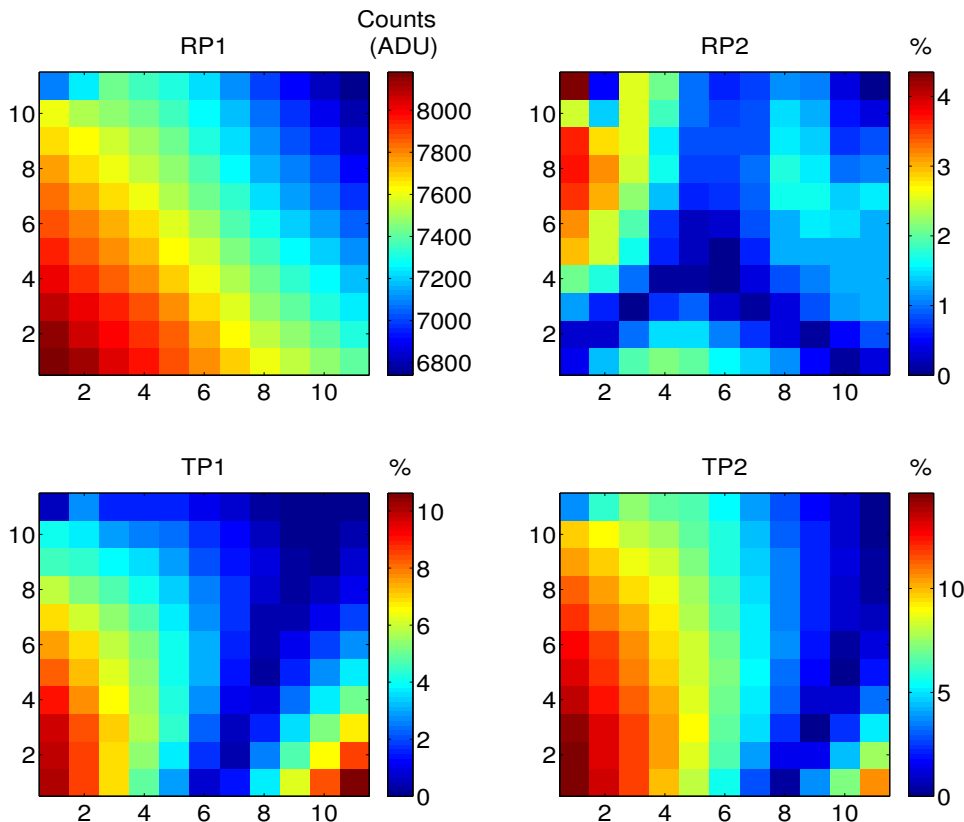


Figure 5.12: Calibration residuals from the section of the image indicated above. The top left corner image show the counts on the RP1 channel to which everything is registered. There is a clear systematic variation present across each field.

On careful examination of Figure 5.12, there appears to be a systematic trend across the calibration channels. The variation in RP2 is thought to be more random than systematic; however, there is a pattern in the bottom half of the residual image that could indicate an effect as a result of improper pixel-matching. The

---

percentage residuals have a maximum value of  $\sim 4\%$ , indicating a close match to RP1. This follows through to the normalised calibration matrix, which can be seen in Figure 5.14, which will be explained in more detail later.

Comparing% residuals to what is calculated in the calibration matrix, it appears that there is very little variation (and little systematic) in RP2 and a very similar pattern is seen in row 2 of the calibration matrix. (Note: For calibration images, RP2 is compared to RP1 for a similar polarisation state.) The pattern present in the residuals in TP1 and TP2 is present in row 3 and 4, respectively. The variation in the gain coefficients is quite high; for TP2 a FOV variation of 0.0378 is found, but for RP2 and TP1 this is 0.0028 and 0.0091, respectively. It is possible that these values could be true pixel gain variations in this FOV, they are not very high; however, it is expected that the pixel residuals of high, or low, gain value should vary randomly across the field, and not produce any discernible patterns. This will be developed in more detail in Section 5.9.2.

### 5.9.2 ECM Analysis & Results of Artefact Registration

After image registration, the calibration images are read into Matlab where the ECM is performed. A code written by David Lara (Lara Saucedo, 2005) has been adapted for the GASP calibration. The same pixel is selected from each path for a series of rotations of the linear polariser and a minimisation routine is used to find the eigenvalues of the intensity matrix, and hence the Mueller matrices of the samples used, see Compain et al. (1999). This is also explained in more detail in Appendix C. Once W is determined A, the system matrix for the experimental set-up, can be calculated.

The GASP Polarisation State Analyser (PSA) for the angle of incidence (AOI) and DOAP configuration is given by Equation 5.15. This is the ideal matrix in the absence of noise. The first column represents the gain of the system (including the detectors used) for each of the channels. This matrix assumes perfect alignment, including the assumption that each of the Wollaston prisms has been aligned to the same angle. If this is not followed for the experimental system, it does not have a negative impact on the experimental matrix. The Wollastons are aligned to  $\pm 45^\circ$  (or an integer multiple of  $\pm 45^\circ$ ). An important consideration is that, once

---

the system has been optically aligned for calibration, it is not modified. The same optical alignment for calibration must be used for science to accurately reproduce any polarimetric information.

Figure 5.13 is an image of the experimental calibration matrix. The first column of the matrix is the gain coefficient for each channel. The first row is a measure for RP1, row 2 - 4, are RP2, TP1, and TP2, respectively. The variation in the gain values and the systematic trend across each coefficient in column 1 is evidence of those seen in the residuals.

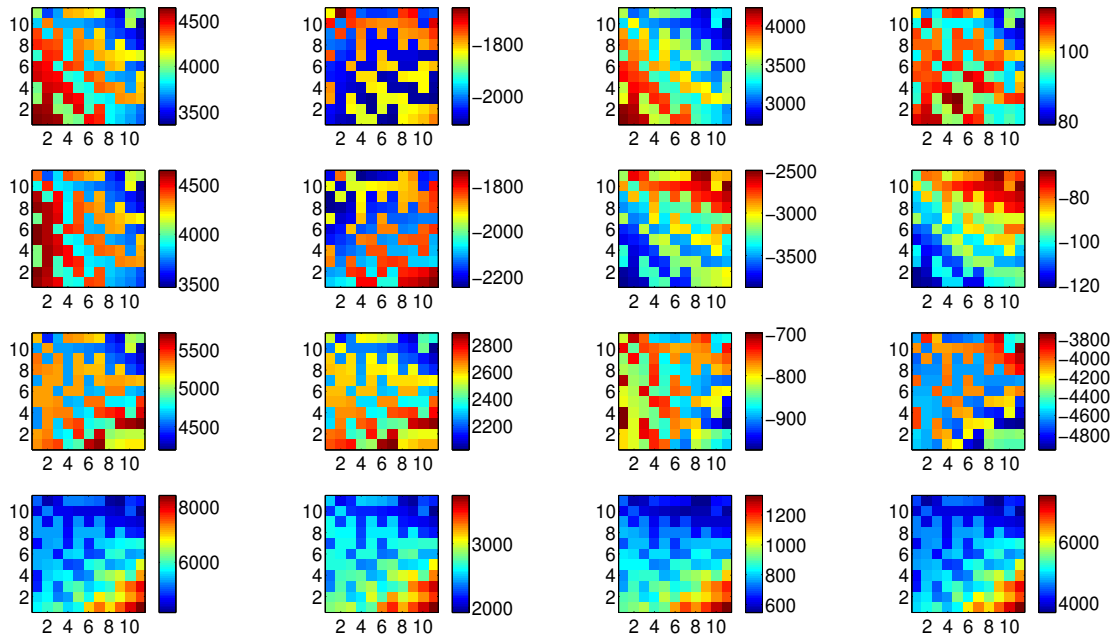


Figure 5.13: The experimental calibration matrix for the image section indicated in Figure 5.11. The calibration images were registered to channel RP1 using artefacts common to all channels.

Figure 5.14 is an image of a normalised version of the calibration matrix in Figure 5.13, for the same image section above. This has been calculated using Equation 5.13.

This matrix contains all the information required to reproduce the entire Stokes vector. It is useful to compare the experimental matrix, to the theoretical, in this form. It can be analysed in this way, remembering that there are certain alignment expectations of the ideal system that may not have been followed experimentally.

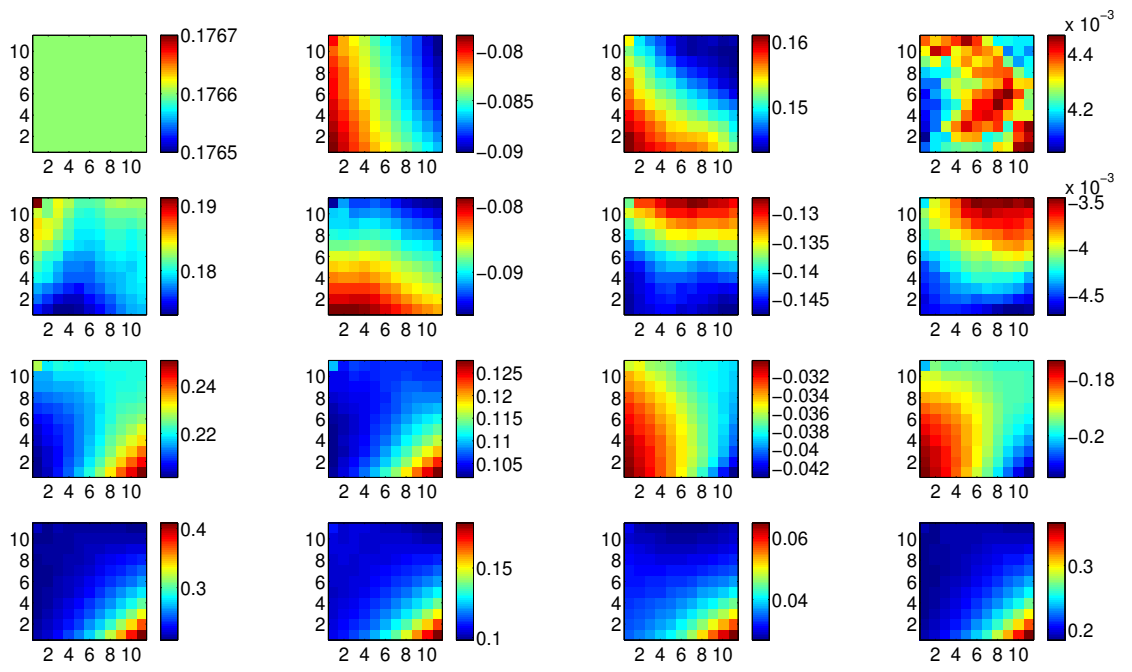


Figure 5.14: The normalised calibration matrix for the image section indicated in Figure 5.11. The calibration images were registered to channel RP1 using artefacts common to all channels. Apart from the clear systematic trend in all gain coefficients the mean values for each are in good agreement with the GASP PSA. The only exception is TP2. This is very clearly a result of the pattern in the bottom right corner, which shows a clear contrast in values to the top left. This pattern is a result of image registration and appears on each of the TP2 coefficients. If this area was ignored, the values would better agree with the PSA. Taking a smaller area of the FOV, or shifting would reduce this pattern, however, there is similar compromise on the TP1 image in the top left corner.

The mean value of the normalised matrix in Figure 5.14 can be found in Equation 5.17. In this case, the error in the FOV will be the combined systematic and random variation in the field.

$$\bar{x} = \begin{pmatrix} 0.1766 & -0.0844 & 0.1508 & 0.0043 \\ 0.1795 & -0.0875 & -0.1397 & -0.0041 \\ 0.2187 & 0.1080 & -0.0359 & -0.1917 \\ 0.2414 & 0.1140 & -0.0350 & -0.2121 \end{pmatrix}. \quad (5.17)$$

It is found that the mean of the normalised matrix is a satisfactory representa-

---

tion of the theoretical PSA found in Equation 5.15. There appears to be a larger deviation on the mean value of TP2 from the theoretical value. It is expected that the gain values for RP1 and RP2 should be quite similar, and the same is true for TP1 and TP2. The reasons for this variation have been discussed at the beginning of this chapter. The mean of the gain coefficient for TP2 varies by  $\sim 0.0378$ , higher than any of the other channels. A variation in pixel values of this magnitude could be an indication that there is a gain variation pixel-to-pixel and this can be a result of incorrect pixel-matching. The ECM measures the gain variation channel-to-channel. If the pixel-matching is not correct this will create a systematic gain variation error. Other sources of error that could result in pattern effects such as these could be imperfections in the polarimetric/optical elements used for the complete polarimeter and the calibration. These inaccuracies can occur as a result of artefacts inherent to experimental equipment, or dust in the system could be an issue. An intensive analysis using Zemax would give a well defined optical description that would allow the observer to limit the level of distortion that increases difficulty in image registration. It is difficult to distinguish, in the case of GASP, as there is no perfect geometrical solution in terms of the optical alignment.

The mean values for RP1, RP2, and TP1 do not deviate largely from what is expected, however, there is a systematic pattern in each of the coefficients in Figure 5.14. A comparison has been made to the pattern in each of the image residuals. An exception in the expected outcome is in the gain coefficient for TP2. This is a clearly defined pattern from the top left corner to bottom right; this pattern is ultimately a result of image registration (other possibilities have been mentioned above) and appears on each of the TP2 coefficients. It is valid to simply ignore this section of the FOV as it will not be used for science target analysis, but would cause problems for extended sources/fields. Taking a smaller area of the FOV, or shifting would reduce this pattern, however, there is similar compromise on the TP1 image in the top left corner. Other areas of the FOV have been explored, however, this was chosen for its location in the interest of science targets.

---

### 5.9.3 ECM Sample Calibration Artefact Registration

It is important to verify how well the system is calibrated: This is done by the reconstruction of the Mueller matrix samples from the ECM. The resultant system matrix of this ECM are used on another set of calibration data recorded for each of the samples AIR, P0, P90, and R30. This indicates how the calibration performs on an independent data set. What is useful about this experiment is that, the data used has been recorded on the same optical axis as the calibration data. The Mueller matrices for these samples are calculated using Equation 5.18,

$$\mathbf{MM}_i = \mathbf{A}^{-1} \mathbf{B}_i \mathbf{W}^{-1}, \quad (5.18)$$

where each  $\mathbf{B}_i$  corresponds to the intensities recorded using the  $\mathbf{MM}_i$  sample,  $\mathbf{A}$  is the system matrix, and  $\mathbf{W}$  is the PSG calculated by the ECM. The image of each sample has been normalised to the first coefficient of the MM (all the pixels in the top left corner image otherwise known as  $m_{1,1}$ ). This is to remove any pixel intensity variation.

Figure 5.15 is an image of the AIR sample used in the ECM analysis. As this is simply a blank slot in the ECM calibration wheel then it is expected that the reconstructed matrix for this sample should be the Identity matrix, this and the mean experimental value are found in Table 5.5. It is found that the results yielded from this sample are showing that the calibration is working very well along the calibration optical axis, where these measurements are recorded. There are some similar systematics present in this matrix to that in the system matrix in Figure 5.14; however, the variation, in particular rows 1 and 3 (RP1 and TP1, respectively) shows very low percentage differences across this FOV. Rows 2 and 4 (RP2 and TP2, respectively) are marginally higher but the mean values show that GASP is measuring the AIR ECM sample very well. It is possible that there are remaining pixel-matching errors, particularly in the case of TP1 and TP2, which were more difficult to register, but this is reasonable based on the results of A matrix. It is noted that in almost all coefficients, an artefact used in registration is reconstructed nicely, in particular  $m_{2,1}$ .

The reconstructed matrices for each of the other samples used, linear polariser at  $0^\circ$  (P0),  $90^\circ$  (P90), and a quarter-wave plate at  $45^\circ$  (R30) show similar system

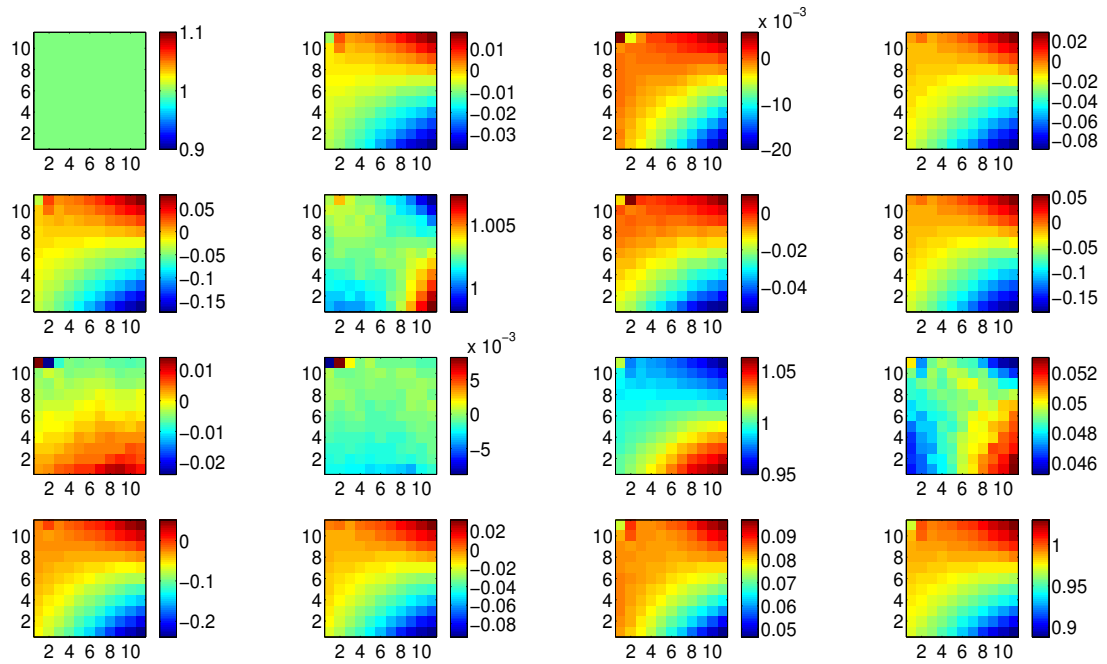


Figure 5.15: The normalised Mueller matrix for the AIR sample for the image section indicated in Figure 5.11. The calibration images were registered to channel RP1 using artefacts common to all channels.

variation and they are also examined. Figure 5.16 is the Mueller matrix for the linear polariser sample P0. The theoretical matrix for this sample can be found in Table 5.6. In the case of both polarisers, the RP2 gain coefficient should report the same result as that of RP1; it is measuring a value within  $\pm 3\%$  as expected. These results indicate that GASP is measuring both the linear and horizontal orientated polarisers quite well, with some variation from the ideal coefficient. These variations can be found in the  $\sigma$  of the value over the FOV, which appears to include some remaining distortions. TP1 and TP2 are also measuring values that are quite close to the expected. Each of these channels should measure a zero value for each coefficient: It is likely that any calibration error could be resulting in coefficient variations of  $\sim 6 - 8\%$ . Any variation in illumination has been accounted for by dividing every pixel of each coefficient by every of the first coefficient. The theoretical Mueller matrix and the mean values for the sample P90 are found in Table 5.7.

A similar trend can be found in the value of the coefficients between P0 and

---

Table 5.5: Theoretical and mean values for the normalised Mueller matrix of the AIR ECM sample; registration performed by image artefacts.

$\mathbf{MM}_{\text{AIR}}$	$\bar{\mathbf{x}}$
$\begin{pmatrix} 1.0000 & 0.0000 & 0.0000 & 0.0000 \\ 0.0000 & 1.0000 & 0.0000 & 0.0000 \\ 0.0000 & 0.0000 & 1.0000 & 0.0000 \\ 0.0000 & 0.0000 & 0.0000 & 1.0000 \end{pmatrix}$	$\begin{pmatrix} 1.0000 & -0.0073 & -0.0036 & -0.0223 \\ -0.0308 & 1.0025 & -0.0152 & -0.0471 \\ 0.0001 & -0.0010 & 1.0023 & 0.0491 \\ -0.0662 & -0.0220 & 0.0782 & 0.9715 \end{pmatrix}$

P90, taking into account the change of sign of the 2<sup>nd</sup> and 5<sup>th</sup> coefficients. Again there are systematic patterns present in the images of the FOV, comparable to those found in the calibration residuals and the normalised calibration system matrix. The difference in the systematic patterns of these polarisers could also indicate inherent characteristics of the individual polarisers, which are not used for the same measurement.

Table 5.6: Theoretical and mean values for the normalised Mueller matrix of the P0 ECM sample; registration performed by image artefacts.

$\mathbf{MM}_{\text{P0}}$	$\bar{\mathbf{x}}$
$\begin{pmatrix} 1.0000 & 1.0000 & 0.0000 & 0.0000 \\ 1.0000 & 1.0000 & 0.0000 & 0.0000 \\ 0.0000 & 0.0000 & 0.0000 & 0.0000 \\ 0.0000 & 0.0000 & 0.0000 & 0.0000 \end{pmatrix}$	$\begin{pmatrix} 1.0000 & 1.0079 & -0.0232 & -0.0008 \\ 0.9554 & 0.9882 & -0.0243 & -0.0005 \\ 0.0018 & 0.0008 & -0.0011 & 0.0015 \\ -0.0765 & -0.0773 & 0.0009 & -0.0002 \end{pmatrix}$

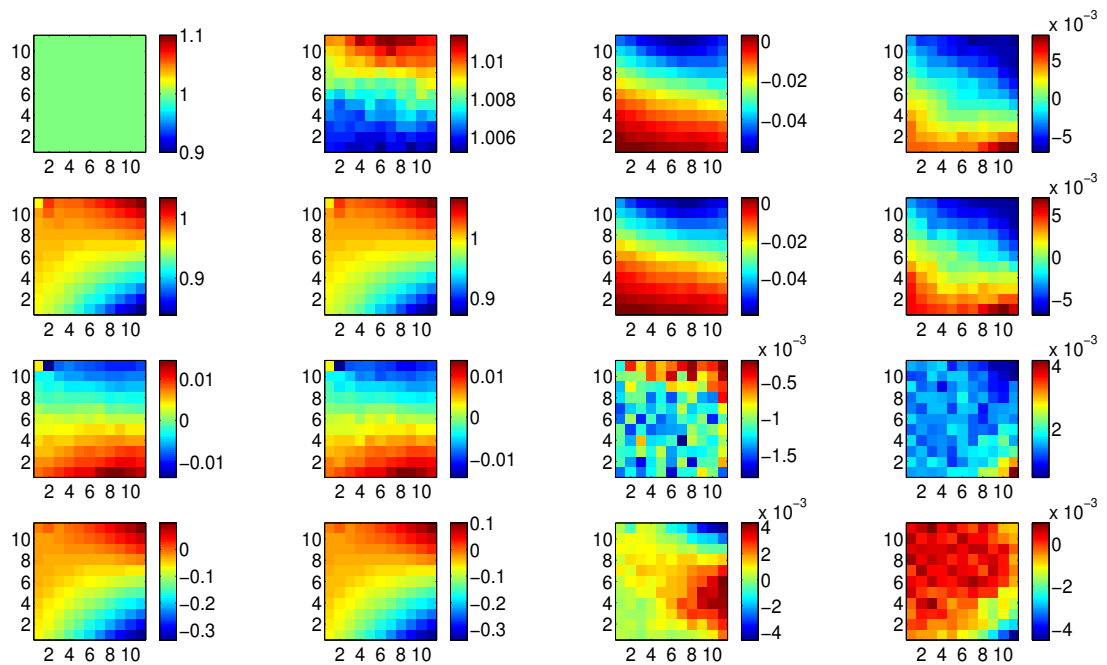


Figure 5.16: The normalised Mueller matrix for the P0 sample for the image section indicated in Figure 5.11. The calibration images were registered to channel RP1 using artefacts common to all channels.

Figure 5.18 is the Mueller matrix for the quarter-wave plate sample R30. The theoretical Mueller matrix should have mean value found in Equation 5.19.

$$\mathbf{MM}_{\mathbf{R}30} = \begin{pmatrix} 1.0000 & 0.0000 & 0.0000 & 0.0000 \\ 0.0000 & 0.2500 & 0.4330 & -0.8660 \\ 0.0000 & 0.4330 & 0.7500 & 0.5000 \\ 0.0000 & 0.8660 & -0.5000 & 0.0000 \end{pmatrix}. \quad (5.19)$$

This sample is more difficult to align (accurately) in the laboratory. If the alignment of this sample deviates from the expected, it will have little (negative) impact on the ECM other than introducing noise. Each of these samples have been normalised to the first element of the MM, the intensity of the matrix and this value is 1. It was found that the actual value to which this QWP was aligned to was  $\sim 38^{\circ}$ <sup>6</sup>. This is not a concern for this system, the same result was found

---

<sup>6</sup>This will be referred to as R30 for convenience.

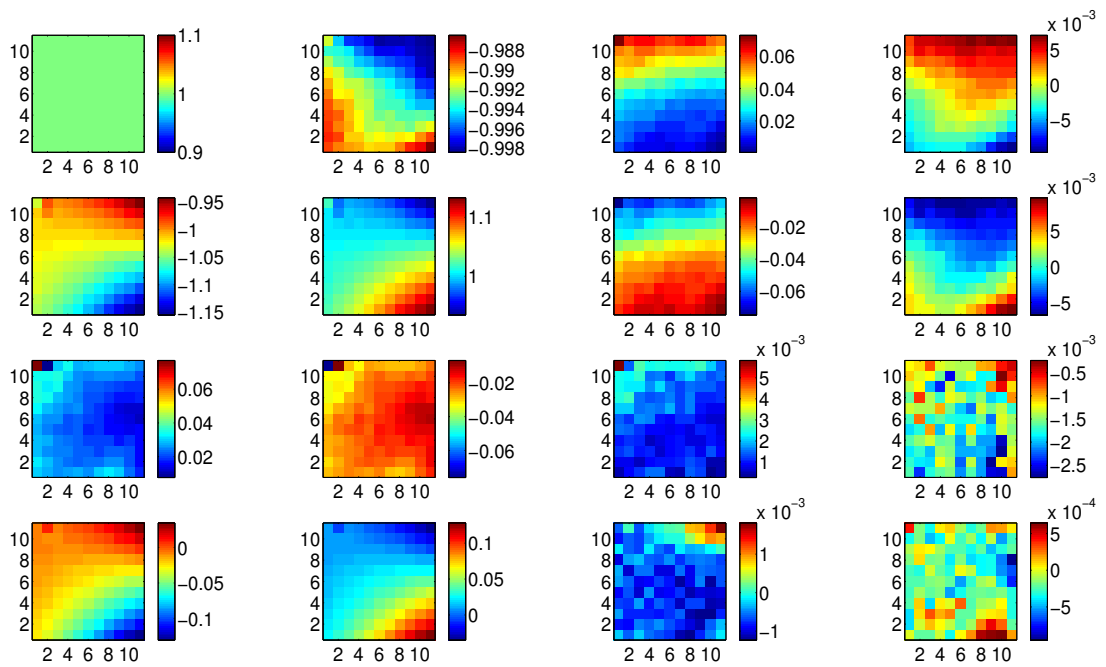


Figure 5.17: The normalised Mueller matrix for the P90 sample for the image section indicated in Figure 5.11. The calibration images were registered to channel RP1 using artefacts common to all channels.

when calibrating the system using APDs. The references de Martino (2004) and Lara Saucedo (2005) explain the investigation performed in the azimuthal angle for the retarder sample. This difference in angle will not create a systematic error, but rather add extra noise to the system. The MM for a QWP aligned to  $38^\circ$  can be found in Table 5.8, which is a better match to the mean. The values for P0 and P90 did not have this concern and were much easier to align in the laboratory. The first column of the MM sample for R30 show variation comparable to the mean in Table 5.8. The variation in the mean values found are at most  $\sim 4\%$ . The image of the matrix in Figure 5.18 indicates that there are remaining pixel-matching errors on each of RP2, TP1, and TP2. These are compared to those in the percentage residuals and the system matrix, however, the variation is low enough to indicate that this sample is calibrated.

The variation from the mean value, in Table 5.8, for each coefficient of each sample's Mueller matrix ranges from  $\sim 0 - 6\%$ . Each coefficient is expected to show a homogeneous pattern with random fluctuations from the ideal case. There

---

are some systematic errors present that conclude that this is not what we see for GASP, however, the mean value of each coefficient indicates that GASP is measuring the Mueller matrix of each sample very well. Some similarities are also found in the systematic variation to that found in Figure 5.14 and the registration residuals. Dust particles can also be a source of variations in the measured irradiance distribution in the ECM samples. This is also a source of error in the calibrated matrix. Therefore, the Mueller samples are divided by the  $m_{1,1}$  coefficient to reduce this error. It is noted that these measurements are taken off axis, the same as that of the data recorded to produce a calibration matrix.

The variation in the system matrix does not appear to be very high, however, there are patterns in certain regions of the field where the values are almost the same, and areas in the FOV where the variation in the value of the coefficient produces a different pattern. There must be a reason for this systematic pattern. There are very similar patterns found in the calibration matrix, rather than a noise pattern, showing a limit to how well the ECM samples can be reconstructed. The results found from verification of these samples indicate that GASP is in fact very well calibrated along its calibration axis showing low level variation, yet indicates consistent systematic patterns like that found in the system matrix.

It is noted that, in the case of using image artefacts, the area of the field, which has been calibrated does not contain any artefacts. The geometrical solution for this area is relying on a solution for the artefacts in the edges of the field that is unlikely to be correct, and could be adding further distortions. Patterns in the registered images in Figure 5.11 is coming through in the residuals as it cannot be removed if that pattern is not present in all images, i.e., it is not real to all images.

Table 5.7: Theoretical and mean values for the normalised Mueller matrix of the P90 ECM sample; registration performed by image artefacts.

$\mathbf{MM}_{\mathbf{P90}}$	$\bar{\mathbf{x}}$
$\begin{pmatrix} 1.0000 & -1.0000 & 0.0000 & 0.0000 \\ -1.0000 & 1.0000 & 0.0000 & 0.0000 \\ 0.0000 & 0.0000 & 0.0000 & 0.0000 \\ 0.0000 & 0.0000 & 0.0000 & 0.0000 \end{pmatrix}$	$\begin{pmatrix} 1.0000 & -0.9931 & 0.0293 & 0.0009 \\ -1.0363 & 1.0241 & -0.0300 & -0.0012 \\ 0.0241 & -0.0231 & 0.0014 & -0.0016 \\ -0.0303 & 0.0298 & -0.0005 & -0.0001 \end{pmatrix}$

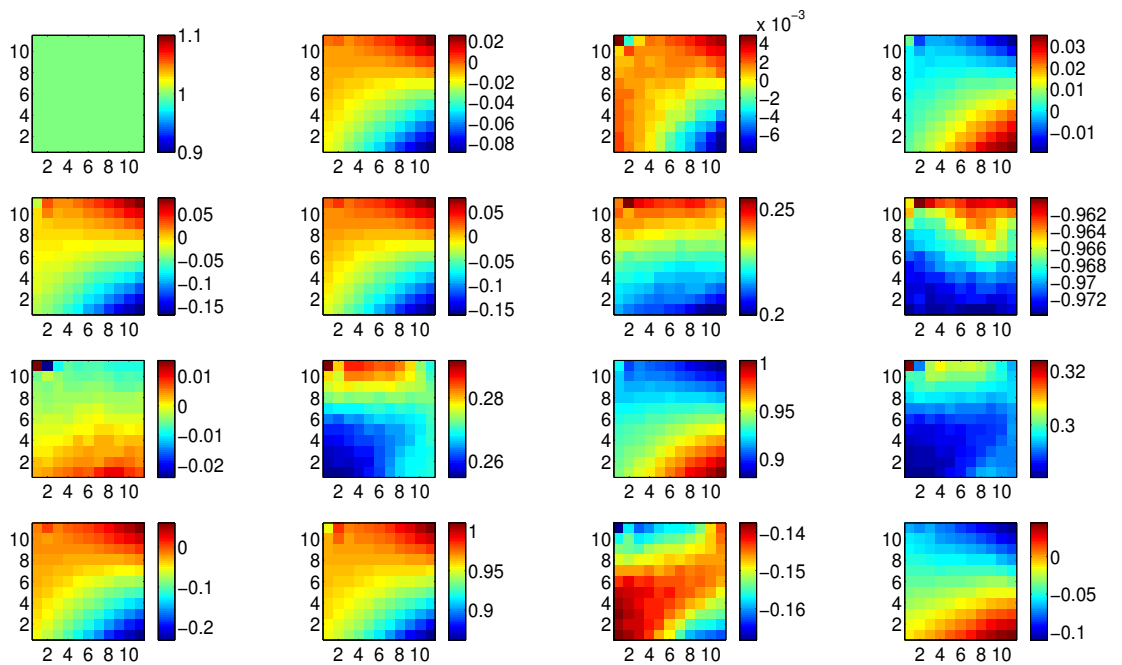


Figure 5.18: The normalised Mueller matrix for the R30 sample for the image section indicated in Figure 5.11. The calibration images were registered to channel RP1 using artefacts common to all channels.

## 5.10 ECM Image Registration using Science Data

Another option that has been explored for image registration uses information from observational data recorded on one of the nights at the P200. A number of polarisation standards were observed and some data from science observations are also used. The centroid of each of these targets was found using the IRAF command *daofind* and a text file was generated, which matched these points for each channel by the user. A second order polynomial solution was generated using *geomap*, as explained in Section 5.9. The data has been binned  $4 \times 4$  to minimise any further image distortion.

It is assumed that the RP1 channel on science data matches the RP1 channel on calibration exactly for this registration method. It is noted that these matched points do not appear in calibration data, as the telescope optical axis is not shared by the calibration optical axis. Angular misalignment of the entrance beam, or mismatching of the respective optical axis centre of the calibration arm could

---

Table 5.8: Theoretical and mean values for the normalised Mueller matrix of the R30 ECM sample; registration performed by image artefacts.

$\mathbf{MM_{P38}}$	$\bar{x}$
$\begin{pmatrix} 1.0000 & 0.0000 & 0.0000 & 0.0000 \\ 0.0000 & 0.0585 & 0.2347 & -0.9703 \\ 0.0000 & 0.2347 & 0.9415 & 0.2419 \\ 0.0000 & 0.9703 & -0.2419 & 0.0000 \end{pmatrix}$	$\begin{pmatrix} 1.0000 & -0.0220 & 0.0001 & 0.0066 \\ -0.0273 & -0.0223 & 0.2259 & -0.9687 \\ -0.0008 & 0.2690 & 0.9357 & 0.2917 \\ -0.0588 & 0.9512 & -0.1482 & -0.0349 \end{pmatrix}$

generate larger error in pixel-matching between the respective channels. Matching the RP1 calibration channel to the RP1 science channel will be discussed in a later section.

The points used for registration are found in Figure 5.19. These points lie in  $\sim 11 \times 11$  pixel area with some variation in the x and y coordinate. The area of interest is the region where the Crab pulsar is located, indicated by the orange box. For the purpose of calibration this FOV is used; in the case of science analysis this area can be moved to give the best calibration output to avoid areas where registration is not uniform. This will be looked at in more detail in the observational work

Table 5.9 give the RMS values for the fit by *geomap*, which is used to find the geometrical transformation. The fit is carried out using a polynomial function of order 2.

The RMS values in Table 5.9 are quite low and show that there is good matching in this area of the chip. This is a very good indication that of the suitability of this fit solution. As this data has been binned  $4 \times 4$ , it is a good idea to check how this fit works at the pixel level. It can be shown that the RMS values are less than a pixel at that level, which is a good result when the aim of the analysis is to match pixels. These RMS values can be compared to those in Table 5.3. It can be seen that, even though this used a simpler 2<sup>nd</sup> order polynomial function, the RMS values are lower. In terms of registration RMS values, the science data points indicate that a better transformation will be generated using the science data.

In order to test the variation in this part of the FOV, the geometrical solution

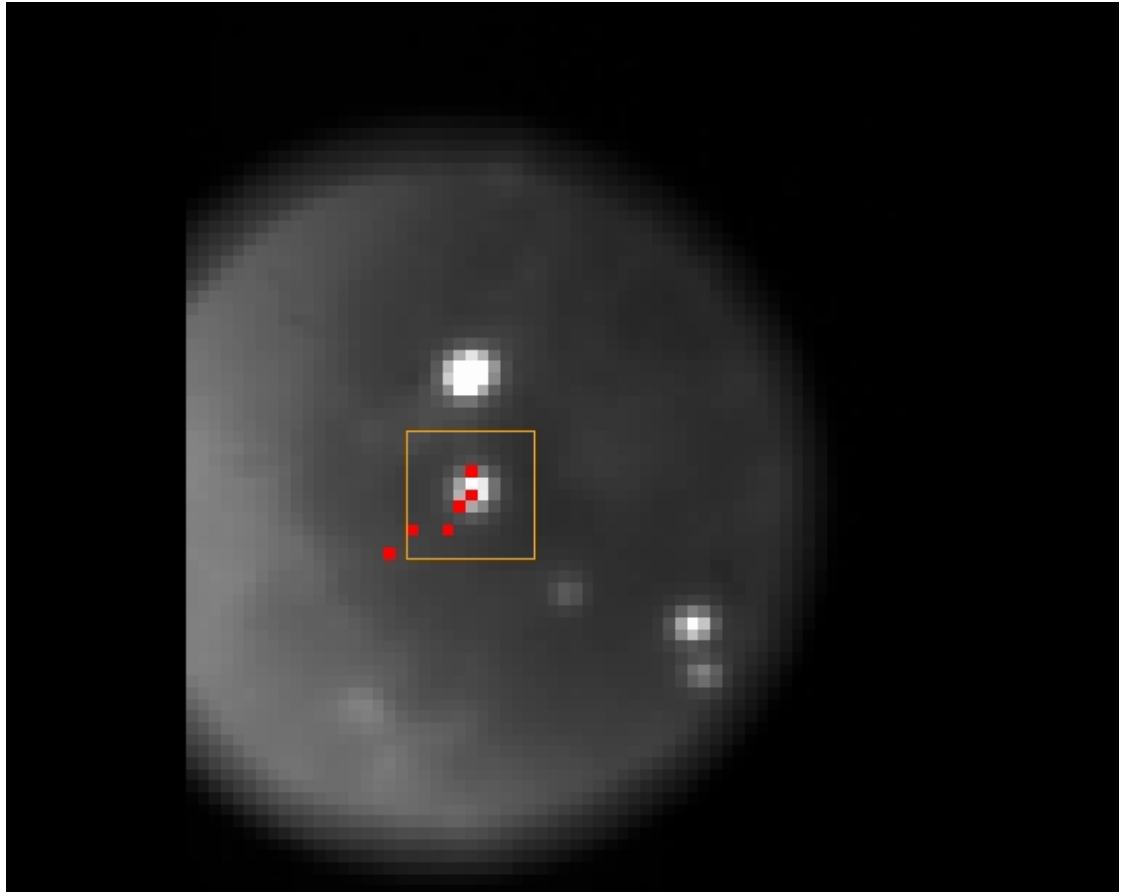


Figure 5.19: This is an image of the Crab Nebula ( $\sim 20''$ ). The points indicated are from a set of data from the first night of observations. This is how they are scattered throughout the field.

produced for all 6 points is tested. One point is removed and a new fit is produced; this fit is then used to find the location of where this removed point would fall, compared to the solution using all 6 points. Table 5.10 gives the coordinate found using all 6 points compared to when that point is removed. The points are numbered according to the values found in Figure 5.20. The LHS column of each channel is the output for registration by all 6 data points, the RHS column is the output from the removal of that particular point. Figure 5.20 gives the location of each point, with  $4 \times 4$  after registration. The values in this table refer to the data at the pixel level without any binning.

It is clear that by the removal of each point, there is some variation in the new

---

Table 5.9: Output of the *geomap* fit using science data points in Figure 5.19.

Channel	RP2	TP1	TP2
x shift (pixels)	84.93	47.42	42.48
y shift (pixels)	-4.32	75.12	-13.88
x magnification	1.09	1.04	1.03
y magnification	1.03	0.91	1.05
x rotation ( $^{\circ}$ )	1.85	-3.14	4.42
y rotation ( $^{\circ}$ )	-6.32	-2.86	-1.07
$x_{rms}$ (pixels)	0.78	0.45	0.40
$y_{rms}$ (pixels)	0.19	0.38	0.54

fit compared to that of the fit produced from using all 6 points. This is expected as there is already limited registration information available in only 6 points. These points are all within  $\sim 15$  pixels, though it can be seen that the variation worsens in points that are located further away than the main cluster, in particular point 1, and the RMS values also decrease in Table 5.11. Table 5.11 shows a similar analysis on all channels where the RMS values are given for the geometrical when a point is removed. In this case when point 1 is removed the RMS values in each TP image decrease, which match the trend in Table 5.10. These results show that there is large variation over a small FOV. This is comparable to the results found by Smith et al. (1999) where small changes in beam wander or pixel misregistration result in large polarimetric errors - 0.05 pixel error compares to  $\sim 1\%$  DOLP and DOCP. The results of the GASP registration show that, if any individual point is not used:

- It is not possible to register that section of the field.
- It is possible to use the new fit to register the removed point but with error as it is field dependent.

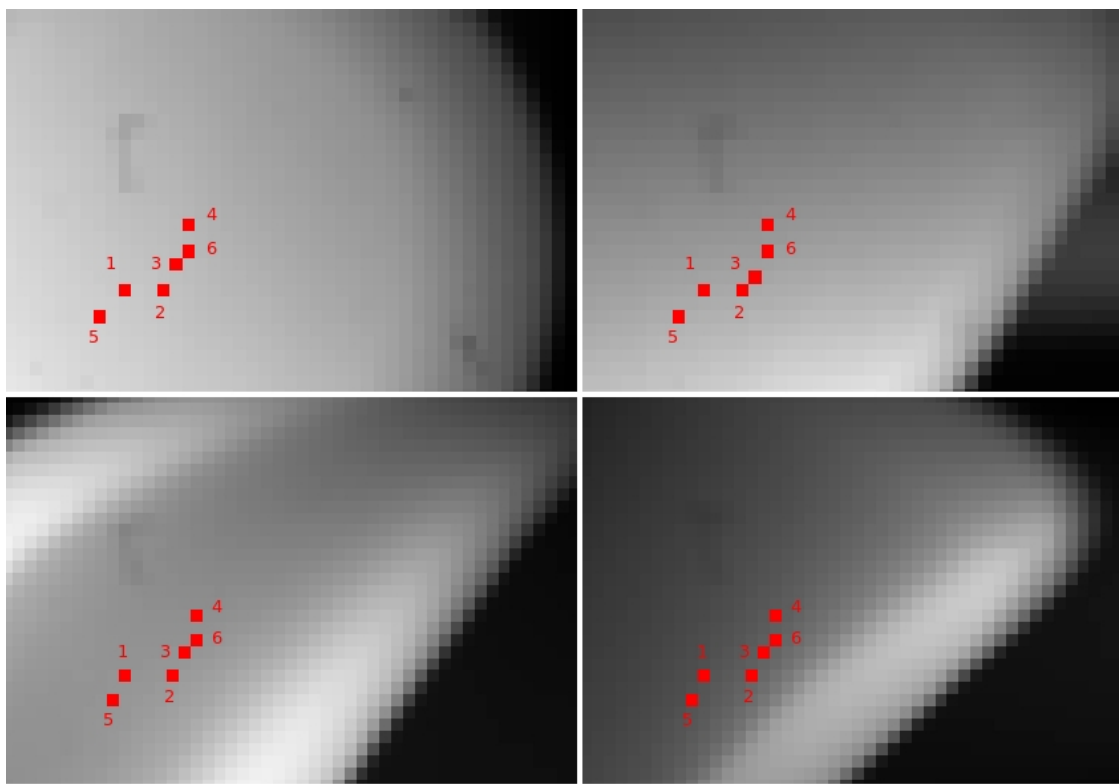


Figure 5.20: The final registered channels for calibration. The points indicated are from the set of science data used for registration from the first night of observations. This is how they are scattered throughout the field after registration - the points have been passed through the IRAF task *geoxytran*, which uses the geometric fit to find the new coordinate location.

- Depending on field location the removal of the point can improve/disimprove the registration.
- It can be assumed that, based on these results, any part of the FOV without matched points is not well registered.

Figure 5.21 shows the registered images for the final geometrical registration solution using all 6 data points. The LHS column of each channel is the output for registration by all 6 data points, the RHS column is the output from the removal of that particular point. Figure 5.20 gives the location of each point, with  $4 \times 4$  after registration. The RMS values in this table refer to the data at the pixel level without any binning.

---

Table 5.10: Output of each of the *geomap* fits. The coordinates are given for each channel after registration.

Point #	RP2		TP1		TP2	
	6 point fit	point removed	6 point fit	point removed	6 point fit	point removed
1	78.2,227.4	83.0,226.9	77.8,227.5	96.5,215.8	77.9,227.3	135.8,294.9
2	91.8,226.8	90.8,227.1	92.7,226.1	92.8,225.2	92.5,227.1	92.3,227.8
3	96.8,233.8	97.0,233.7	97.0,234.3	97.3,234.5	97.2,234.0	97.5,234.0
4	98.3,248.8	95.4,249.3	99.5,248.2	100.6,246.9	99.4,249.2	100.1,251.3
5	71.7,218.3	70.5,218.5	71.7,218.3	70.5,217.8	71.7,218.3	70.8,219.4
6	100.6,240.0	101.3,239.9	98.7,240.7	98.3,241.0	98.8,239.3	98.6,238.9

Based on the theoretical work done by Smith, RMS errors such as these indicate that it is possible that GASP will show large polarimetric variation pixel-to-pixel. If the 6 points are used to calibrate GASP an error for all 6 RMS parameters (x and y for each of the 3 channels registered) gives a resultant pixel error of  $\sim 0.3$  pixels (propagation of the RMS errors in all 3 channels). This is for this area of the FOV. According to Smith et al. (1999), this could result in a  $\pm 6\%$  error (the results in Figure 5.7 are not linear) in the DOLP and DOCP. However, this analysis is a first-order approximation and other factors will have to be included. The calibration is also affected by this misregistration and this will create further error in the polarimetric results. Smith relates the misregistration directly to an error in percentage polarisation. The polarimetric errors are calculated using the expressions in Appendix A. Further analysis is required to establish how this misregistration contributes to error in GASP calibration and polarimetric results.

It is noted that this analysis was not carried out using image artefacts as there were not enough available points in the FOV of interest. The artefacts used for registration were not located in clusters, but randomly distributed in the outer field.

The central region of the images appear to be well registered, however, looking

---

Table 5.11: Output of each of the *geomap* fits. The RMS values are given for each channel after registration.

Point #	RP2		TP1		TP2	
	x <sub>RMS</sub>	y <sub>RMS</sub>	x <sub>RMS</sub>	y <sub>RMS</sub>	x <sub>RMS</sub>	y <sub>RMS</sub>
1	0.50	0.19	0.16	0.29	0.29	0.24
2	0.49	0.02	0.50	0.19	0.43	0.43
3	0.84	0.15	0.41	0.40	0.22	0.6
4	0.09	0.13	0.34	0.10	0.42	0.06
5	0.88	0.22	0.53	0.43	0.48	0.60
6	0.50	0.19	0.12	0.29	0.28	0.24

from the centre out to the edges of the field the matching deteriorates. This is expected given the limited number of matched points from the analysis above.

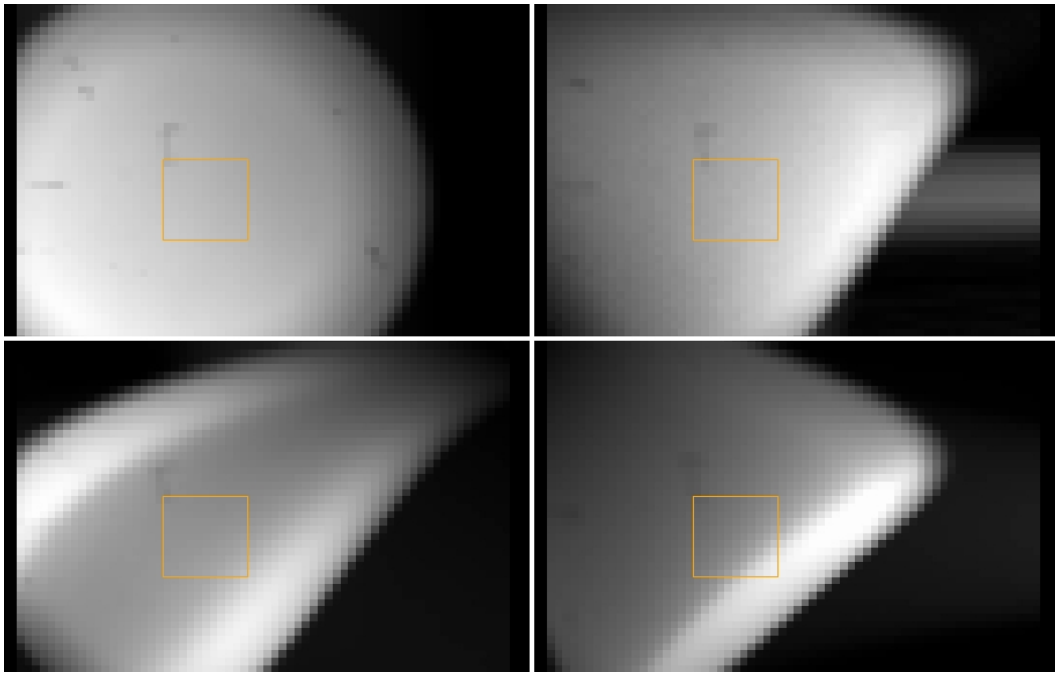


Figure 5.21: All registered GASP channels for a full frame calibration image that have been spatially registered using science data points in Figure 5.19. The section indicated by the orange box is used in calibration to produce a system matrix using the Eigenvalue Calibration Method. This calibration data set has been binned  $4 \times 4$ . Top LHS: RP1, top RHS: RP2, bottom LHS: TP1 and bottom RHS: TP2.

### 5.10.1 Science Residuals

These calibration images are compared to RP1 calibration channel. A systematic trend is observed when analysing the residuals. The residual percentage for RP2 channel have increased compared to registration by image artefacts. It appears to have a banding across the observed field compared to using image artefact registration. A comparison can be drawn to the variation across the FOV in RP1, though this pattern is rotated by  $90^\circ$ . It is uncertain what is causing this pattern. The area where the residuals reach their maximum covers a very small area of the FOV. A similar trend is seen for TP1 and TP2, which have an elliptical pattern within the field. There is also some banding pattern, meaning that the residuals are not the remaining noise pattern that would be expected after normalisation and subtraction. These patterns are found in the raw data images, which shows that this particular area of the FOV is not perfectly registered.

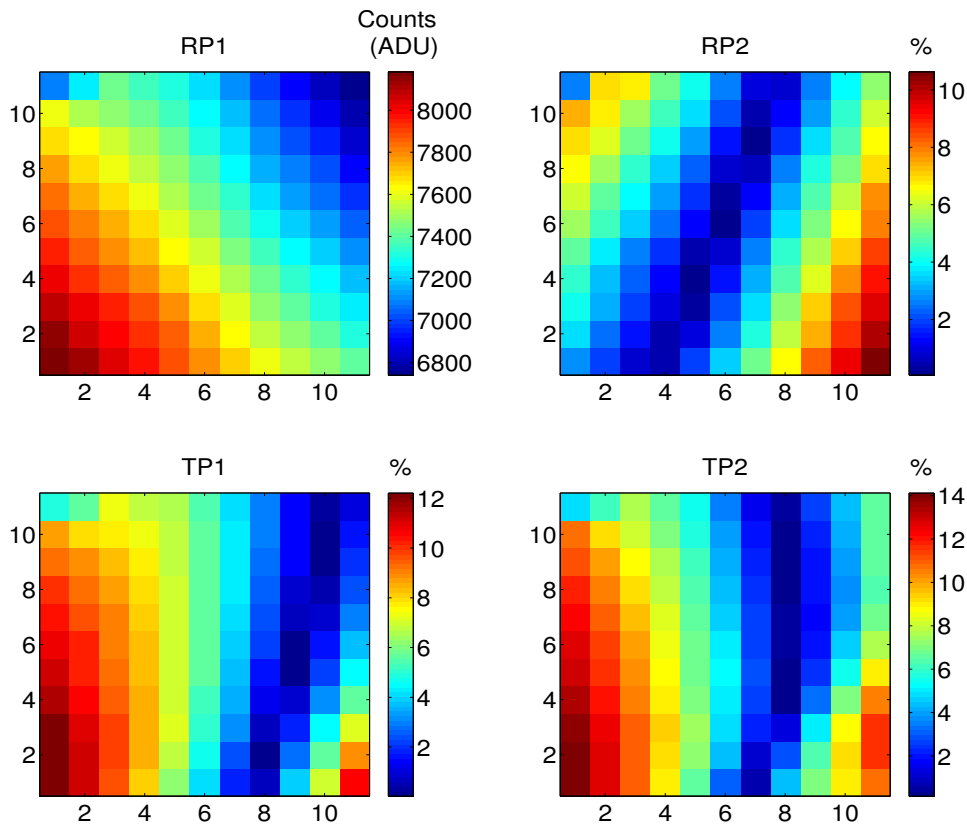


Figure 5.22: Calibration residuals from the section of the image indicated above. All 4 channels have been registered to the calibration image RP1 channel based on science points from Figure 5.19.

The variation in the mean value of the RP2 gain coefficient increases, based on the trend observed, to 0.015 compared to the registration with artefacts. There is also a change in both the TP1 and TP2 channels, and looking at the system matrix in Figure 5.24, it is clear that there is more variability on both TP1 and TP2 gain coefficients, with variation of 0.017 and 0.071, respectively. This will be developed further in the next section. It is difficult to compare both methods of registration as there are advantages and disadvantages to both. Small changes in the mean values of the calibration matrix are not indicative of a better calibration.

---

### 5.10.2 ECM Analysis & Results of Science Data Registration

The results from artefact registration were showing reasonably accurate results that indicated that GASP was calibrated. However, the points used for calibration were not located in the FOV of interest and the registration analysis was repeated for a science data registration technique. These data points are found in Figure 5.19. The idea behind using this method is that this part of the field contains a number of points that can be matched on all channels to RP1 channel, from the first night of observations at the 200 inch. There are 6 matched points meaning a polynomial of order 2 is the most complex function that can be used. The geometrical fit has been discussed above. A comparison can be drawn to the GASP theoretical PSA found in Equation 5.15.

Figure 5.23 is an image of the calibration system matrix generated from this registration solution. It has already been explained that the first column of the matrix gives the gain for each channel. The first row is a measure for RP1, row 2 - 4, are RP2, TP1, and TP2, respectively. There is a variation in the gain values and the systematic trend across each coefficient in column 1. These are comparable to the trends found in the image residuals where the patterns observed are nearly identical.

Figure 5.14 is an image of the normalised calibration system matrix for the same image section in Figure 5.23.

Equation 5.20 contains the mean values of the normalised matrix in Figure 5.24, which give a better understanding how the calibration matrix compares to the theoretical. The variation in the mean value of each coefficient contain a combination of the systematic and random variation in this FOV.

$$\bar{x} = \begin{pmatrix} 0.1766 & -0.0846 & 0.1520 & 0.0043 \\ 0.1996 & -0.0966 & -0.1586 & -0.0046 \\ 0.2254 & 0.1126 & -0.0366 & -0.1964 \\ 0.2810 & 0.1315 & 0.0422 & 0.2477 \end{pmatrix}. \quad (5.20)$$

On examination of the variation across the FOV for the normalised matrix, like the matrix in Figure 5.14, the gain values for RP1 and RP2 should be quite

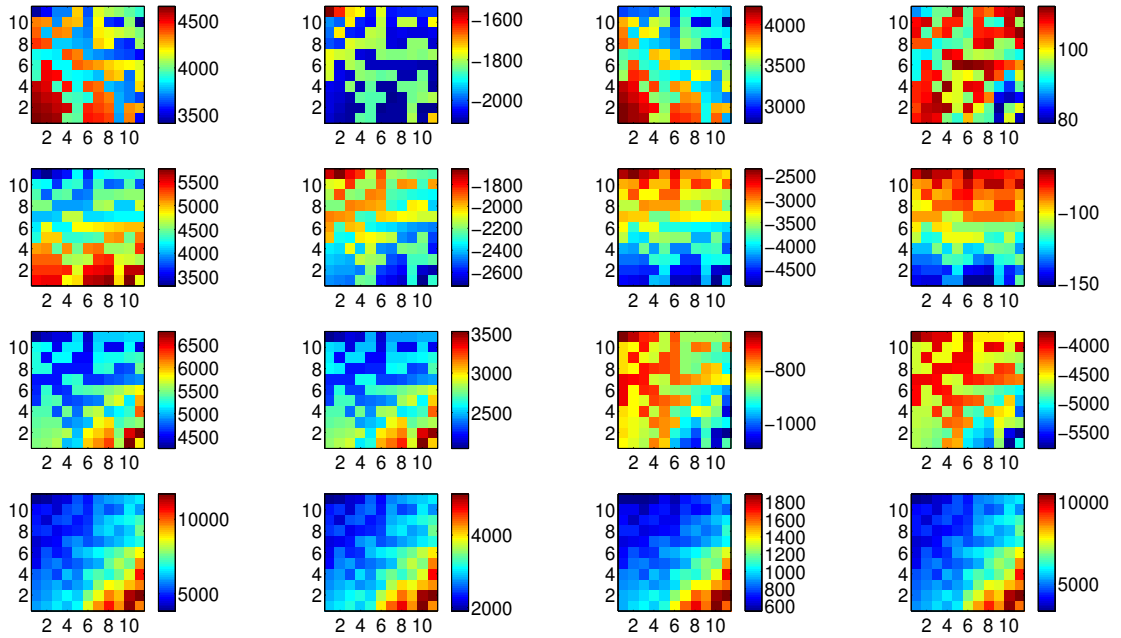


Figure 5.23: The experimental calibration matrix for the image section indicated in Figure 5.11. The calibration images were registered to channel RP1 using science data.

similar, and those for TP1 and TP2. There is a larger difference in the mean value for each of the gain coefficients for this matrix compared to that found using image artefacts, when compared to the theoretical matrix to which each of these has been normalised. However, it is difficult to compare this to the theoretical given the differences that will exist in optical alignment. The mean values found for this calibration matrix are showing a similar trend to those found in the matrix found when calibrating using APDs. It must be noted that there will be a gain variation between each set of detectors used in calibration.

The pattern found in each of the coefficients, particularly on TP2, are images of that area of the FOV of each channel, which is expected. In the absence of variation in luminosity in the field, of each channel, a more random pattern would be observed. In the coefficients where the values are expected to be low ( $\sim 0$ ), a pattern will be less evident where the random errors are approximately equal to the systematic, taking into account alignment variation in the theoretical PSA.

The variation in the mean values found in Equation 5.20 are comparable to

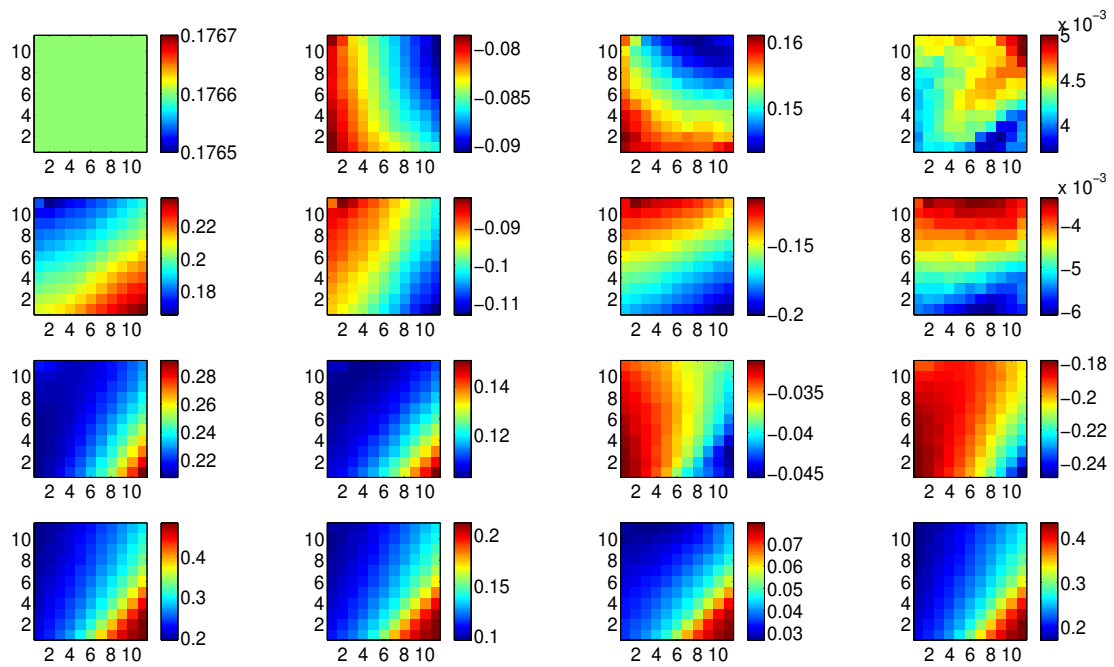


Figure 5.24: The normalised calibration matrix for the image section indicated in Figure 5.11. The calibration images were registered to channel RP1 using science data.

those found in Equation 5.17, containing both systematic and random errors. Some remaining error in pixel-to-pixel matching is a likely cause of these values. It is possible that these are a good representation of the distribution of coefficient values in this area of the FOV due to the fact that actual science targets are used for matching. As there was for registration using image artefacts, this has resulted in the observed systematic pattern in each of the coefficients in Figure 5.24.

### 5.10.3 ECM Sample Calibration using Science Data Registration

The results of the ECM samples are analysed resulting in similar conclusions for the registration solution using image artefacts. A systematic trend persists, though the pattern differs to that using artefacts, as a different solution for geometrical registration is used, nonetheless the pattern emerging in the normalised system matrix is evidence of that found in the residuals of registration. The expected

---

values for these MM have been discussed in Section 5.9.2.

The Mueller matrix for the AIR ECM sample is found in Figure 5.25. The results for this sample are greatly improved compared to that using image artefacts with respect to the difference in systematic trend. The  $\sigma$  have also improved and appear to be as low as 0.5%. There is evidence of a systematic effect on each of the TP images, particularly TP2. This is consistent with the fact that there is more observed distortion on this path, which makes image registration more difficult. The theoretical and mean value for the second to last coefficient is quite high, and again this is indicative of the difficulty in image registration. The same is found for the last TP1 coefficient.

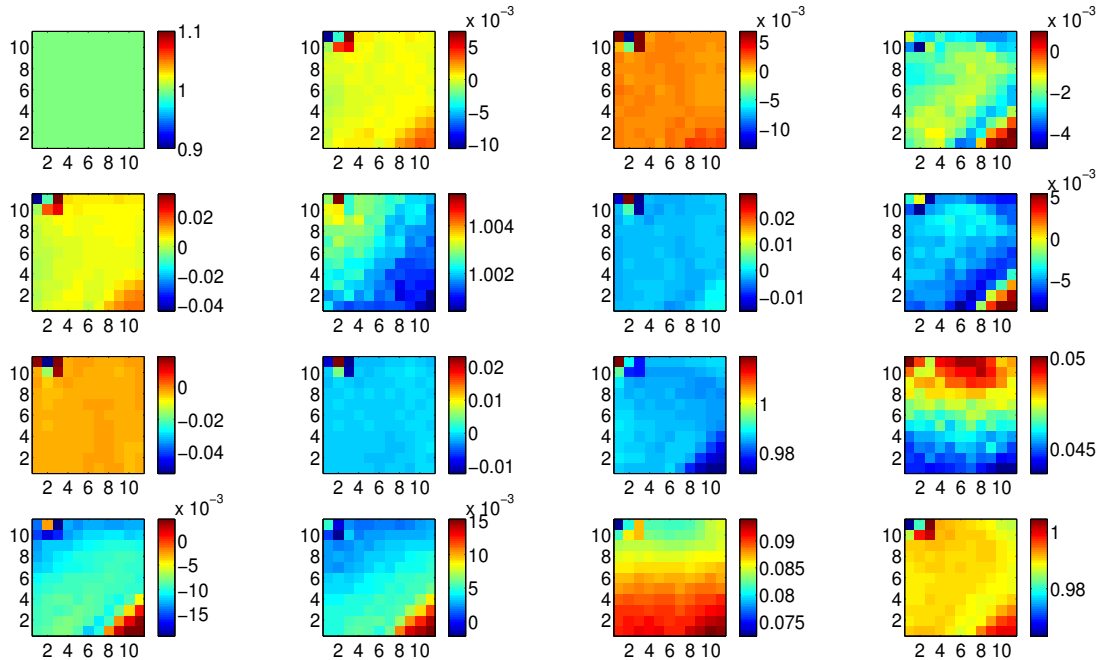


Figure 5.25: The normalised Mueller matrix for the AIR sample for the image section indicated in Figure 5.11. The calibration images were registered to channel RP1 using science data.

Figure 5.26 and 5.27 are the Mueller matrices for the linear polariser sample P0 and P90. These samples have similar MM, with the exception of sign. Again, the results found using this registration method are improved and the variation is low on each channel, however, the values for the 3<sup>rd</sup> coefficients on rows 1 and 2 are higher than expected. This could be for a number of reasons, image registration,

---

Table 5.12: Theoretical and mean values for the normalised Mueller matrix of the AIR ECM sample; registration performed using science data points.

$\mathbf{MM}_{\text{AIR}}$	$\bar{\mathbf{x}}$
$\begin{pmatrix} 1.0000 & 0.0000 & 0.0000 & 0.0000 \\ 0.0000 & 1.0000 & 0.0000 & 0.0000 \\ 0.0000 & 0.0000 & 1.0000 & 0.0000 \\ 0.0000 & 0.0000 & 0.0000 & 1.0000 \end{pmatrix}$	$\begin{pmatrix} 1.0000 & 0.0004 & 0.0014 & -0.0020 \\ 0.0043 & 1.0021 & -0.0018 & -0.0045 \\ -0.0032 & -0.0008 & 0.9854 & 0.0467 \\ -0.0094 & 0.0046 & 0.0873 & 0.9902 \end{pmatrix}$

or imperfections in the polarisers used. There is a trend on each of the TP rows (3 and 4). The top left and bottom right corner show larger variation compared to that in the centre of the FOV. Again, this is most likely as a result of an absence of registration points in those areas. To a good extent, the P0 and P90 experimentally determined Mueller matrices correspond with their corresponding theoretical matrices.

Table 5.13: Theoretical and mean values for the normalised Mueller matrix of the P0 ECM sample; registration performed using science data points.

$\mathbf{MM}_{\text{P0}}$	$\bar{\mathbf{x}}$
$\begin{pmatrix} 1.0000 & 1.0000 & 0.0000 & 0.0000 \\ 1.0000 & 1.0000 & 0.0000 & 0.0000 \\ 0.0000 & 0.0000 & 0.0000 & 0.0000 \\ 0.0000 & 0.0000 & 0.0000 & 0.0000 \end{pmatrix}$	$\begin{pmatrix} 1.0000 & 1.0075 & -0.0166 & 0.0015 \\ 0.9848 & 1.0169 & -0.0175 & 0.0017 \\ -0.0004 & -0.0014 & -0.0011 & 0.0015 \\ 0.0044 & 0.0049 & -0.0000 & 0.0003 \end{pmatrix}$

The results found for the horizontal polariser in Figure 5.26 are comparable to those in Figure 5.27. The mean value is compared to the theoretical in Table 5.13. The variation appears to be very similar and the probable systematic effect of registration is also present in this image. However, compared to the method using image artefacts, registration by science data point has produced Mueller samples that appear to be very well calibrated. These Mueller matrices show a cleaner variability compared to those using image artefacts and the areas showing systematic variation are clearly evidence of errors in the calibration matrix.

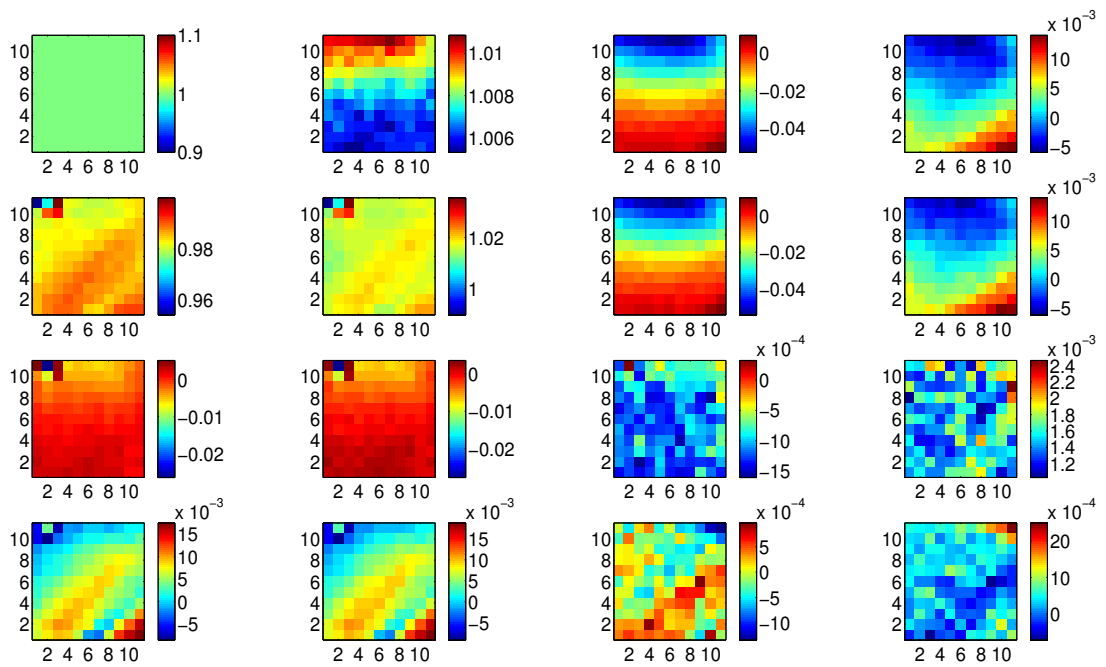


Figure 5.26: The normalised Mueller matrix for the P0 sample for the image section indicated in Figure 5.11. The calibration images were registered to channel RP1 using science data.

Figure 5.28 is the Mueller matrix for the sample R30. In the same way as using image artefacts, it has been concluded that this sample has been aligned to an angle of  $\sim 38^\circ$ . Just like the figures above, there is a low systematic trend present and any evidence of one can be compared to that in the system matrix and image residuals.

Looking at this image, the TP coefficients, rows 3 and 4, register the highest variation for all coefficients, however, this value is about 1%, which does compare to the values found for the image residuals after registration. Any variation is most likely to be a result of incorrect pixel-matching which is due to an insufficient number of data points; this has been discussed when registering with image artefacts.

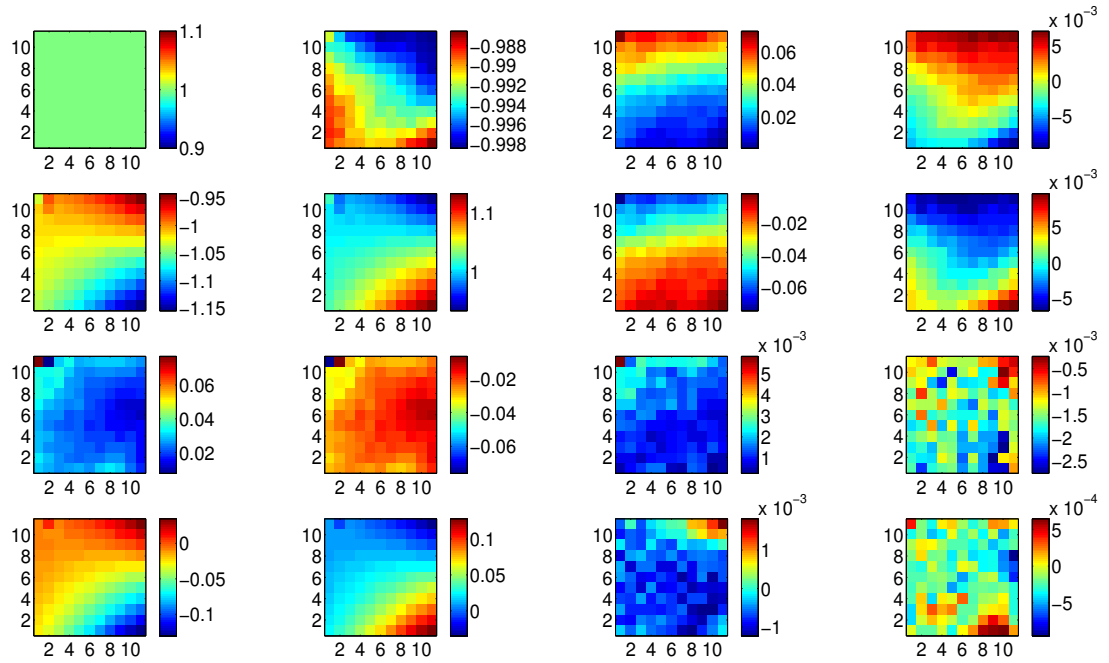


Figure 5.27: The normalised Mueller matrix for the P90 sample for the image section indicated in Figure 5.11. The calibration images were registered to channel RP1 using science data.

Table 5.14: Theoretical and mean values for the normalised Mueller matrix of the P90 ECM sample; registration performed using science data points.

$\text{MM}_{\text{P90}}$	$\bar{x}$
$\begin{pmatrix} 1.0000 & -1.0000 & 0.0000 & 0.0000 \\ -1.0000 & 1.0000 & 0.0000 & 0.0000 \\ 0.0000 & 0.0000 & 0.0000 & 0.0000 \\ 0.0000 & 0.0000 & 0.0000 & 0.0000 \end{pmatrix}$	$\begin{pmatrix} 1.0000 & -0.9930 & 0.0238 & -0.0002 \\ -1.0091 & 0.9969 & -0.0242 & -0.0005 \\ 0.0190 & -0.0181 & 0.0012 & -0.0017 \\ -0.0017 & 0.0010 & -0.0002 & -0.0002 \end{pmatrix} [1.5ex]$

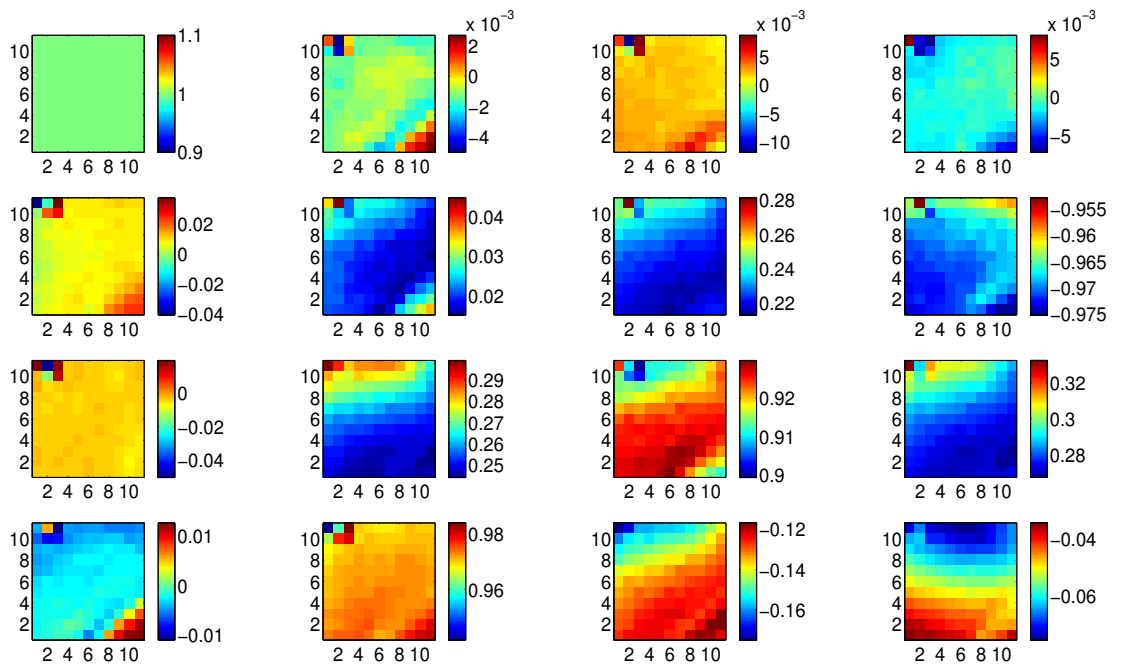


Figure 5.28: The normalised Mueller matrix for the R30 sample for the image section indicated in Figure 5.11. The calibration images were registered to channel RP1 using science data.

As has been discussed in Section 5.9.2, the variation from the mean value for each coefficient of each Mueller matrix is well within the expected values for each of the RP1, RP2, TP1, and TP2 channels. It can be concluded that registration by science data points has produced a more accurate calibration result with lower variation across the FOV and a better matched experimental Mueller matrix. A pattern still remains in the FOV of a number of coefficients in each of the samples for AIR, P0, P90, and R30. The same pattern is found in Figure 5.24 for the respective channels. The reason for this pattern can also be referenced in Figure 5.19 where there are insufficient points, and the areas absent of points are showing this trend.

The results of the geometrical solution for registration by both image artefacts, and science data have both shown positive results in terms of calibration along the calibration axis. It is concluded that using science data points produces better calibration results even with the assumption that these points in fact appear in the calibration data. The results of the calibrated ECM samples are a clear indication

---

Table 5.15: Theoretical and mean values for the normalised Mueller matrix of the R30 ECM sample; registration performed using science data points.

$\mathbf{MM_{P38}}$	$\bar{\mathbf{x}}$
$\begin{pmatrix} 1.0000 & 0.0000 & 0.0000 & 0.0000 \\ 0.0000 & 0.0585 & 0.2347 & -0.9703 \\ 0.0000 & 0.2347 & 0.9415 & 0.2419 \\ 0.0000 & 0.9703 & -0.2419 & 0.0000 \end{pmatrix}$	$\begin{pmatrix} 1.0000 & -0.0010 & 0.0023 & -0.0014 \\ 0.0083 & 0.0212 & 0.2259 & -0.9689 \\ -0.0040 & 0.2593 & 0.9217 & 0.2823 \\ -0.0020 & 0.9720 & -0.1346 & -0.0545 \end{pmatrix}$

that GASP is calibrated using a pixel-by-pixel method using the ECM.

## 5.11 Stability of the ECM

It is important to measure the stability of an instrument's performance, and account for changes in the environment (or system) that could cause variations in that performance. The system matrix was observed over a period of a few days to verify the polarimetric stability of GASP. The ideal case would be to perform multiple calibrations in a uniform laboratory environment but this was not possible for the time frame of this experiment. The imaging polarimeter design was used to perform this stability test and 3 sets of calibration data are examined over a period of 5 - 6 days. Registration is performed using the science data points method as it yielded the most positive results for calibration verification.

In each case the calibration is performed using a similar LED light level and exposure time. The filter used is R Band, from a set of Johnson filters, centred at  $\lambda = 650$  nm. The bandwidth is 100 nm. Data is recorded and analysed in exactly the same way for each system matrix produced.

Table 5.16: iXon Ultra 897 detector settings for the calibration data presented in this section, and chapter.

Frame size (pixels)	512 × 512	
Exposure Time (s)	0.0045	
Amplifier (%)	Electron Multiplying	
	RP	TP
Sensitivity ( $e^-/\text{ADU}$ )	4.84	5.16
Readnoise ( $e^-$ )	81.34	88.85

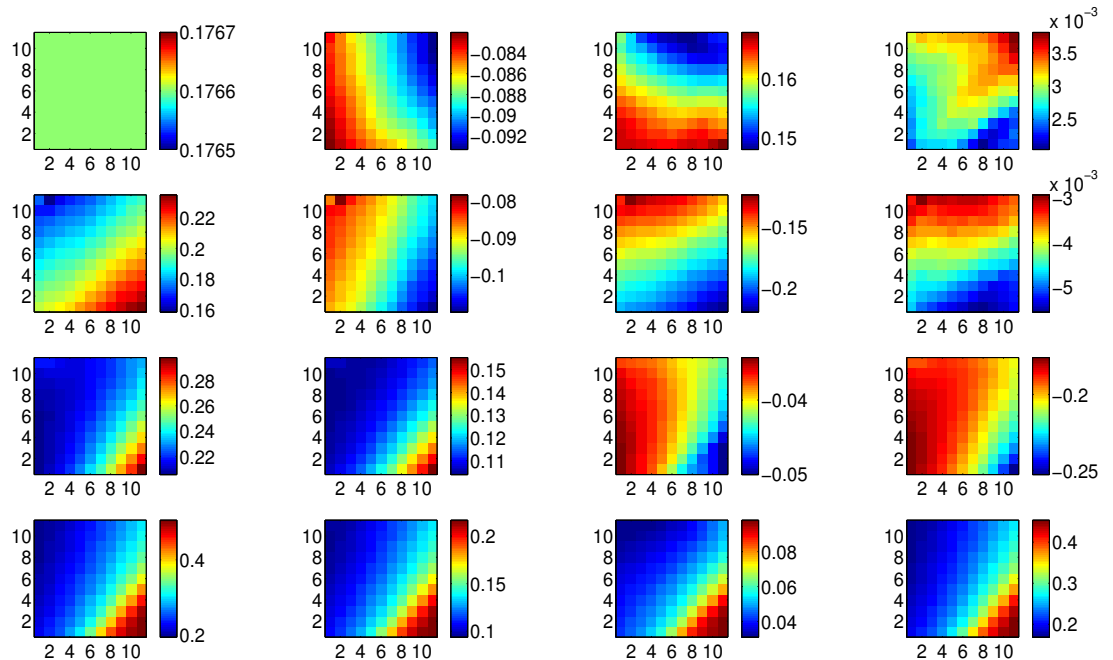


Figure 5.29: A calibration data set recorded using the settings in Table 5.16. This calibration matrix was produced from data recorded at the beginning of observation Night 3 at the Palomar 200 inch telescope.

---


$$\bar{x} = \begin{pmatrix} 0.1766 & -0.0874 & 0.1584 & 0.0029 \\ 0.1961 & -0.0936 & -0.1723 & -0.0042 \\ 0.2266 & 0.1146 & -0.0399 & -0.1961 \\ 0.2864 & 0.1311 & 0.0507 & 0.2517 \end{pmatrix} \quad (5.21)$$

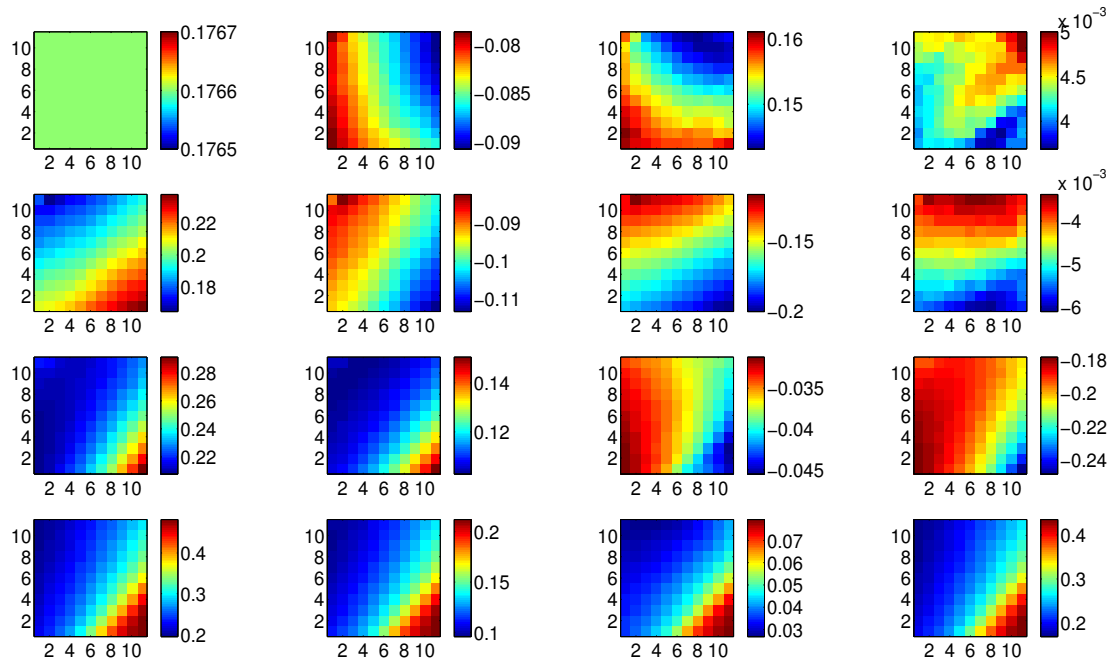


Figure 5.30: A calibration data set recorded using the settings in Table 5.16. This calibration matrix was produced from data recorded  $\sim 10$  hours after the data presented in Figure 5.29.

$$\bar{x} = \begin{pmatrix} 0.1766 & -0.0846 & 0.1520 & 0.0043 \\ 0.1996 & -0.0966 & -0.1586 & -0.0046 \\ 0.2254 & 0.1126 & -0.0366 & -0.1964 \\ 0.2810 & 0.1315 & 0.0422 & 0.2477 \end{pmatrix} \quad (5.22)$$

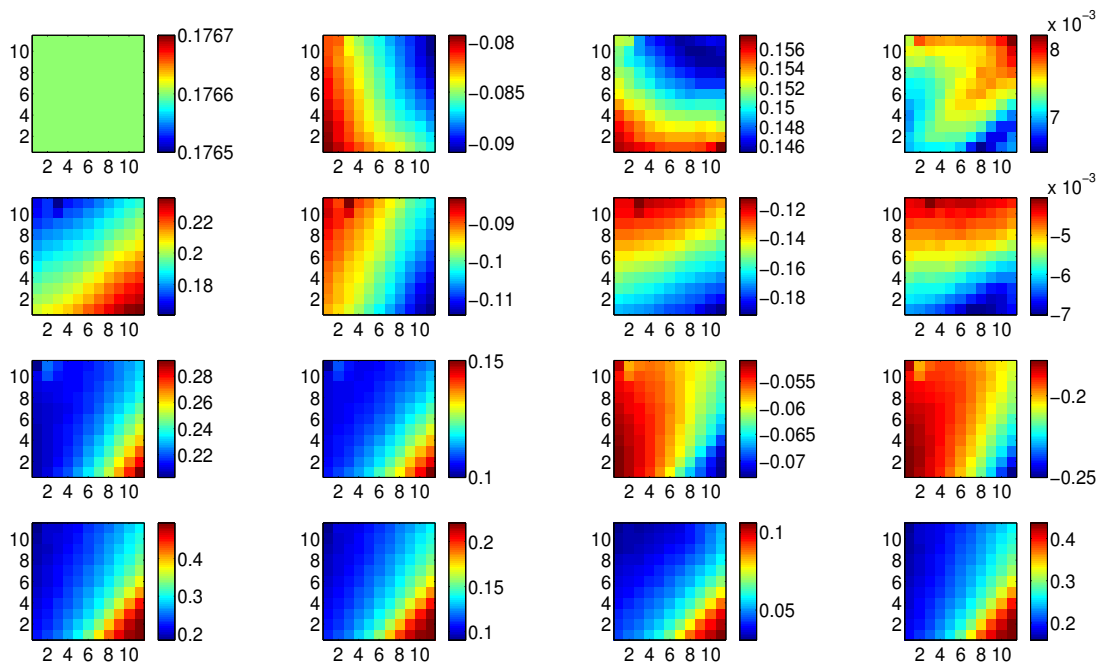


Figure 5.31: A calibration data set recorded using the settings in Table 5.16. This calibration matrix was produced from data recorded  $\sim 6$  days after the data presented in Figure 5.30.

$$\bar{x} = \begin{pmatrix} 0.1766 & -0.0851 & 0.1506 & 0.0074 \\ 0.1973 & -0.0985 & -0.1498 & -0.0054 \\ 0.2257 & 0.1134 & -0.0585 & -0.1987 \\ 0.2814 & 0.1329 & 0.0515 & 0.2456 \end{pmatrix} \quad (5.23)$$

Looking at Equations 5.21, 5.22, and 5.23, it is clear that the calibration stays very stable over this period of 1 week. It should be noted that the data recorded producing the image in Figure 5.31 was done after GASP was removed from the telescope. The variation found between the same matrix gain coefficients is of order 1 - 2%. Coefficients where the values are expected to be close to zero value exhibit higher percentage difference levels; these coefficients will be more influenced by random noise variations, from the detector used, than those with larger values. The largest variation between the 3 matrices appears to be on the TP2 channel, or row 4, where the registration has shown less accuracy: The variation on the gain coefficient reaches 2% in each case. The percentage difference on the second

---

coefficient on each of the first and second rows appear higher, as do the values for the third coefficient on the third and fourth rows. Looking at the theoretical PSA in Equation 5.15, these values approach zero. This, again, stands true that any random fluctuations matrix-to-matrix will appear as a higher percentage difference.

It is the conclusion of this section that GASP has shown a consistent calibration over a period of 6 days while the instrument was subject to movements of the telescope and temperature variations in the telescope dome compared to that of the Caltech laboratory. It is not possible to analyse any influence of temperature change as this was not monitored, but it is an important point to note for these results. Variation in the gain coefficients could potentially be influenced by temperature fluctuations. Theoretically, the effect of random noise fluctuations on a polarimetric signal have been investigated for GASP by Collins (2012). Further Monte Carlo simulations were beyond the scope of this work, however, it is an important experimental investigation to consider regarding the stability of the calibration in a uniform environment.

### 5.11.1 ECM Calibration Verification using Science Data Registration

The data used in Section 5.10.3 was also used to perform verification tests to examine the performance of the polarimeter. A Stokes reduction analysis is performed on the AIR sample used as part of the ECM. The polarimetric results of sample are more straight forward to predict as the AIR sample does not require any alignment in the laboratory.

The first stage of the test consists of rotating a linear polariser through  $180^\circ$  of the AIR sample. The intensity variation of the linear polariser, as a function of input angle, can be found plotted in Figure 5.32. As the angle of the polariser changes, the polarising beamsplitters (Wollaston prisms) will each measure an orthogonal component of the light resulting in a sinusoidal pattern for each channel.

Figure 5.33 shows the polarimetric behaviour of the data in Figure 5.32, as a function of input angle. The DOLP is expected to be constant at 100%. Theoretical plots for these data can be found in Collins (2012) where a more detailed analysis of these tests can be found. The expected DOCP should give a constant

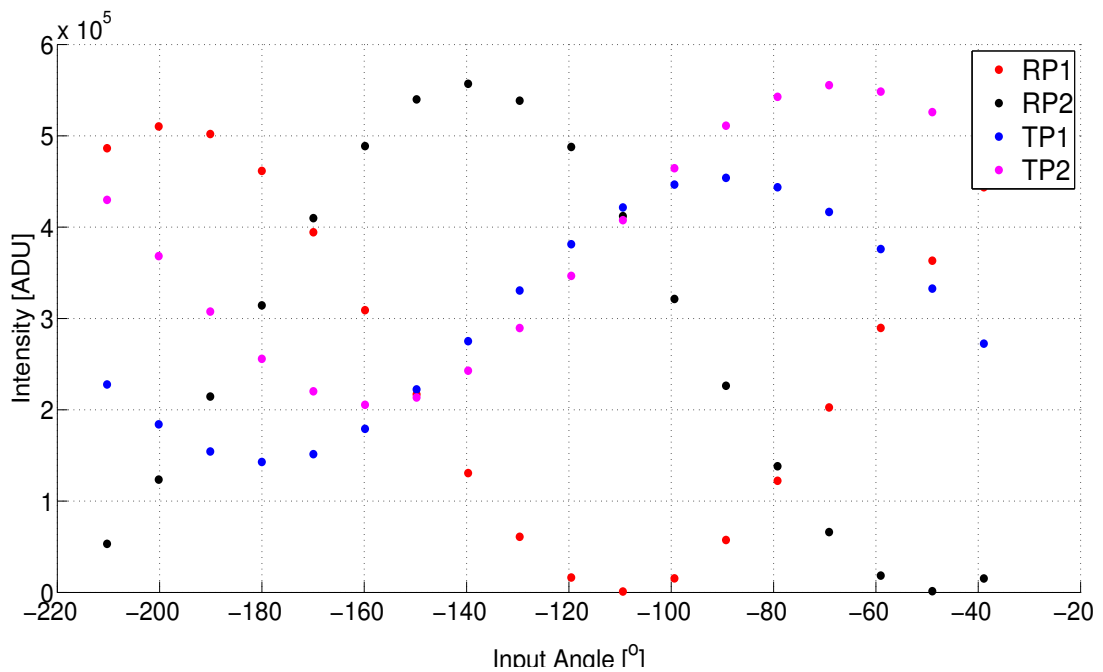


Figure 5.32: Raw intensity plots from a calibration verification test using GASP as an imaging polarimeter for an experiment using a rotating linear polariser.

measurement of 0%. The linear polariser could introduce a certain level of circular/elliptical polarisation depending on the quality/condition of the glass polariser used during the experiment. The polarisation angle (PA) follows a linear trend with the input angle. The input angle, the angle of the linear polariser, is measured by GASP and plotted as the output PA. The plot for the PA must be read right to left as this is how the linear polariser was rotated. It is noted that the PA is modular 180° in plots such as these.

Errors are found in the experimental data at the maximum value for the DOLP; at times the values fluctuate above 100%. This is not a possible measurement, however, it could be a result of error from registration, which has been discussed earlier in the chapter. It is possible that this error is a result of a gain calibration variation on one, or both detectors. If there is any minor misalignment to the optical setup, between data acquisition, an error such as this could occur.

Figure 5.34 is a plot of the raw data, as in Figure 5.32, with the addition of a quarter-wave plate (QWP) as the linear polariser was rotated. A sinusoidal plot

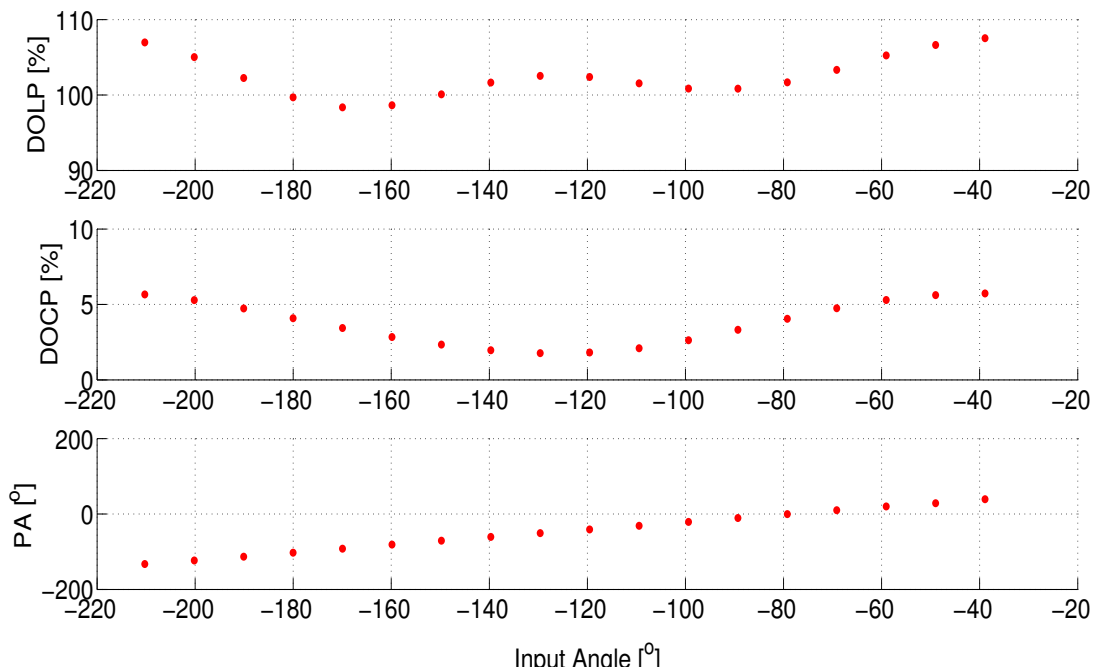


Figure 5.33: Polarimetric results from a calibration verification test using GASP as an imaging polarimeter for an experiment using a rotating linear polariser.

is observed as expected.

The results of the Stokes reduction using the linear polariser with the QWP can be found in Figure 5.35. The linear polariser makes an angle with the quarter-wave plate, which remains constant at  $0^\circ$ . As the polariser rotates, this angular offset between the two optics changes, which will cause the linear/elliptical and circular polarisation to vary as a function of angle. As the linear polariser approaches integer angles of  $45^\circ$ , it will produce circular polarisation. This is because the quarter-wave plate is offset by an angle of  $45^\circ$ . The DOLP approaches 0% while the DOCP approaches 100% for left- or right-circular polarisation (positive or negative). The reverse occurs when the polariser is at  $0^\circ$  or  $180^\circ$  where the DOLP approaches 100% and the DOCP drops to 0%.

The polarisation angle is behaving as expected. As the quarter-wave plate is aligned to  $0^\circ$  and will produce a polarisation of 0 or  $90^\circ$  depending on the rotation of the linear polariser, which rotates through  $180^\circ$ .

These results are a close representation for what should occur theoretically.

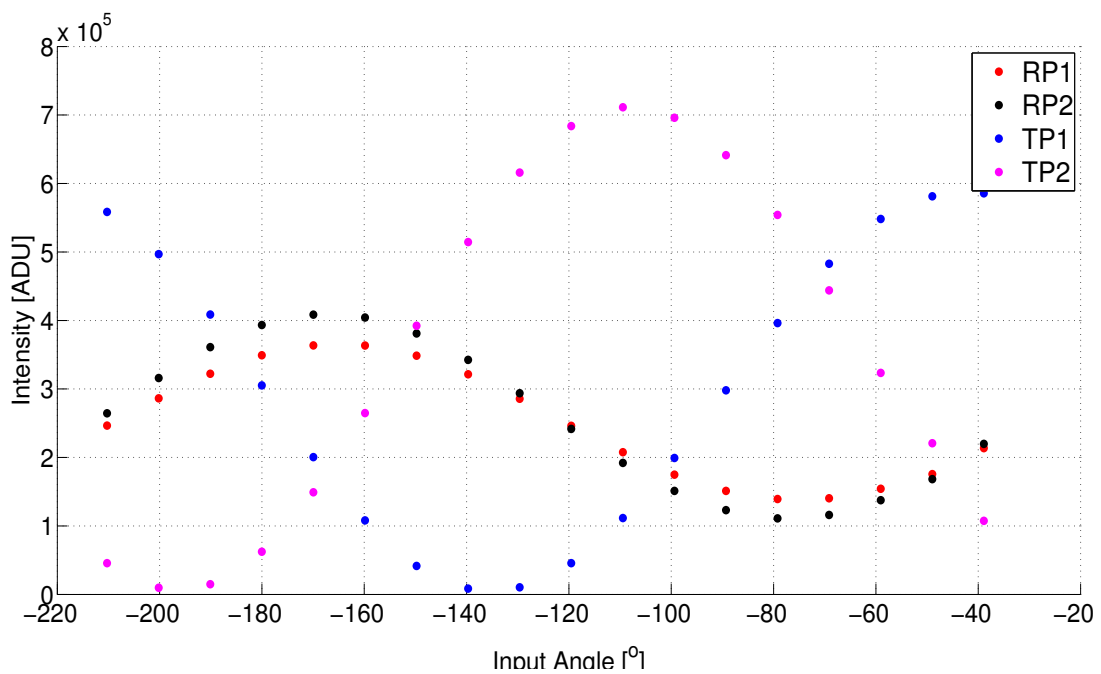


Figure 5.34: Raw intensity plots from a calibration verification test using GASP as an imaging polarimeter for an experiment using a rotating linear polariser and a quarter-wave plate.

The polarisation calibration elements are aligned in the laboratory, however, their alignment is subject to error, and therefore the offset of the quarter-wave plate with respect to the linear polariser may not be as expected. The important point to note from these verification results is that when the DOLP is high, the DOCP is low. It is also noted that errors occur when approaching maximum and minimum polarisation limits. There are a number of reasons for why this may occur. A lower value of DOLP could be measured if the rotation resolution of the polariser was changed. 0% DOLP is difficult to measure when the source (as for the LED experiments at the beginning of this chapter) may have some intrinsic polarisation. A weakly polarised signal will be dominated by any nearby polarised signal, by low SNR, or systematic errors from the instrument and post-processing such as image registration.

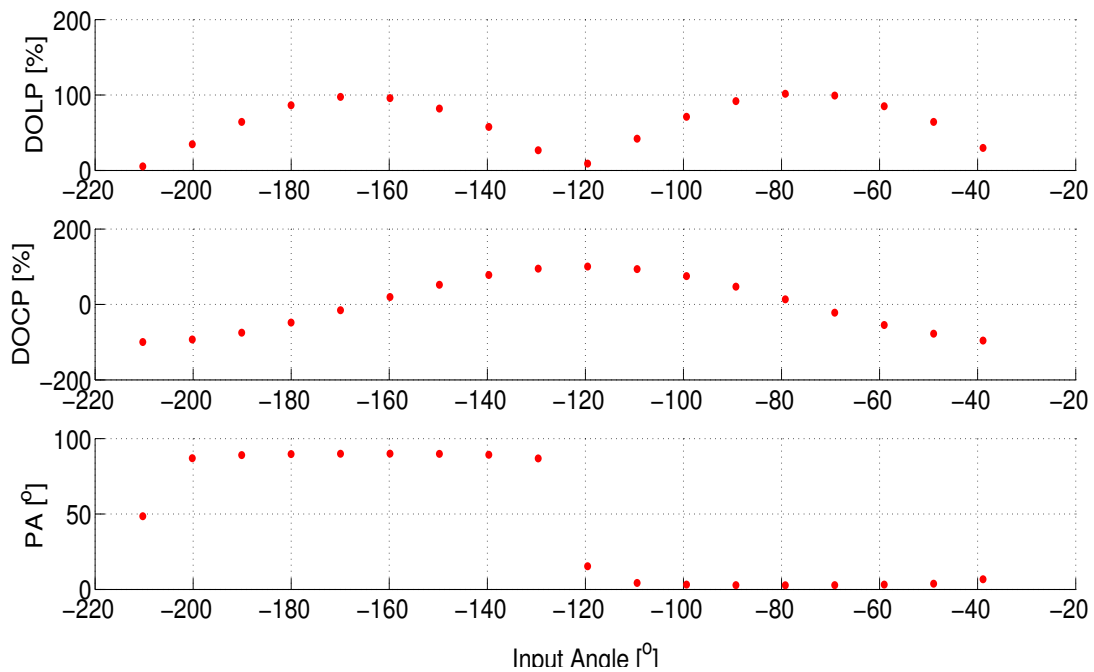


Figure 5.35: Polarimetric results from a calibration verification test using GASP as an imaging polarimeter for an experiment using a rotating linear polariser and a quarter-wave plate.

## 5.12 Concluding Remarks

Conclusive results that GASP works as a DOA polarimeter can be found in the ECM results and laboratory experiments carried out using APD detectors. A comparable system matrix to the theoretical PSA was obtained and reasons have been presented for any deviation in these matrices. The ECM results has been bench tested on experimental data using a linear polariser to generate a polarisation state with an expected DOLP value of 100%. The polarisation angle was measured and yielded quantitative results for the accuracy of the ECM ( $\sim 0.2\%$  DOLP,  $0.1^\circ$  in the absence of systematic error), measuring a possible mechanical movement in the system. An experiment was also carried out using an LED with the assumption that this light is unpolarised. However, as there is no polarimetric information made available by the manufacturer, this is a measurement made by GASP, as the same system matrix was used to great effect on polarised data.

The data processing requirements using APDs are far less than that of imaging.

---

This is evident in the APD analysis as there was no need for image registration following acquisition, unlike that using the data sets from November 2012 at Palomar. Imaging polarimetry involves the measurement of the partial/full Stokes vector on a pixel-by-pixel basis across a scene (Tyb, 2006). The work carried out with GASP employed this method of analysis, measuring the full Stokes vector.

It has been explained, using both methods above, that the components of a photon of light entering the polarimeter for analysis are matched using a well defined geometrical solution. Image registration can be performed in many different ways using a wide variety of functions, but they all require a good sample of matched data points between an input and reference image.

On examination of the calibration data, a number of artefacts were found in the surrounding FOV. These artefacts were not densely scattered across the field, but were more localised in the edges (sparse at the centre FOV) of each channel, particularly each TP channel. However, these artefacts were available data points that could be matched based on their edges and corners, rather than assuming centres. It has been noted that there is an element of error introduced by the user's determination of where an edge/corner begins or ends and this must be taken into account as an added systematic error in spatial registration. It is also noted that the results of the RMS results using *geomap* are an indication of how well these edges/corners have been matched image-to-image.

The matched data points, or artefacts, were tested under a number of conditions by varying the choice of function, and examining the RMS values. This has been discussed in detail but it was concluded that the choice of combination of artefacts had no impact on the final geometrical solution used in terms of RMS or image residual values. On examination of the final calibration results errors in residuals, a systematic variation in the FOV show a correlation with improper image registration. However, calibrated data for each of the ECM samples have shown that, in spite of the limitation of this method, it can reconstruct each Mueller matrix to a reasonable degree of accuracy ( $\sim 5\%$  variation of the mean). This is also found using points that are not in the area of interest of the FOV. The image area used for calibration (where most of the observational targets were located) did not contain any image artefacts, and so an assumption is made that a geometrical solution for a different area of the field can be used. There are rea-

---

sions to suggest that the errors found here indicate large optical distortions in the field, leading to the systematic patterns found. To properly model the distortion variation on the chip, one would require multiple frames of a moderately crowded field, which was not available for this particular data set.

An alternative method was also explored using science data information found by matching points from one of the nights observations. This also gave image residuals that showed systematic error, which were also present in calibration system matrix results. These data points do, in fact, appear in an area of interest in the calibration field; however, they do not actually appear as points in calibration data. The results of this method show improved calibrated ECM samples, leading to concluding that this has shown that GASP is in fact calibrated along its calibration optial axis. The systematic patterns are less evident, and the patterns that are present are indicative of the areas of the FOV which lack registration points. A first-order analysis has been discussed, related to work by Smith et al. (1999), for how error propagation will occur through misregistration. Further analysis of GASP as an imaging polarimeter is required to establish a more accurate error through calibration and polarimetric reduction.

There are other errors that could corrupt calibration, apart from image registration. These are difficult to distinguish in the case of GASP as there is no perfect geometrical solution in terms of the optical alignment. Other inaccuracies can occur as a result of artefacts inherent to experimental equipment, or dust in the system could be an issue. An intensive analysis using Zemax would give a well defined optical description that would allow the observer to limit the level of distortion that increases difficulty in image registration.

GASP has also shown a consistent calibration over a period of 6 days. This has included many movements of the telescope on sky and while unmounting. There is the possibility that temperature variations in the telescope dome compared to that of the Caltech laboratory could cause instability, however this was not possible to analyse as it was not monitored. The main source of the variation in the system matrix is concluded to be that of random fluctuations in the detector, however some systematic effects are found on the TP2 channel that also present here. These have been discussed and concluded to mostly likely be a result of insufficient points for image registration. The error found here will be a combination of this random and

---

systematic variation.

It is the conclusion of this chapter's analysis that the ECM works excellently using DOAP for the GASP polarimeter. The results of the APD polarimetric analysis provide a certainty of the accuracy of the ECM when reconstructing the Stokes vector.

The calibration results for GASP as an imaging polarimeter were less accurate albeit, a more difficult system in terms of analysis. Two registration methods were examined, both showing positive calibration results across a selected field. Reconstruction of the Mueller samples indicate the instrument is calibrated correctly when it produced accurate values for the coefficients of each sample with a low level of variation for the science data registration method. This is clear when looking at the results in Section 5.9.2 and 5.10.2 by examining the Mueller matrix samples reconstructed by the ECM.

Calibration verification results give an indication of the instrument's capability of measuring a range of values for the DOLP and DOCP. The measurement for the polarisation angle show how GASP can remeasure the input angle after calibration. The minimum DOLP values measured could indicate possible limitations for the instrument at this level of polarised signal; comparisons can be drawn with the unpolarised LED experiment. A close representation of the theoretical results were found, however, a more detailed analysis of these tests can be found in Collins (2012).

A redesign of the imaging optics is a future consideration, fully mapping the theoretical distortions to improve the results of calibration. Secondary to this, remodelling the GASP PSA to reduce the constraints placed on optimisation of retardance of the prism could yield a more flexible design. The optical/geometric distortion is varying from the centre of the chip to the edge; and there are not enough points to model this distortion: This has been explored in Section 4.4.1. Theoretically the distortion could be modelled by binning the data, however a problem occurs whereby image resolution is lost, resulting in the loss of common points, between the frames. There is a further complication in a difference between calibration and science channels. It became clear during the initial stages of image registration, that the optical axes of calibration and science were not matched well enough, and this is a requirement for the ECM; this problem can be solved by

---

registering every frame to one reference frame in calibration. This did not appear to be a great concern when using these science points to match calibration frames in the FOV of interest, but it is clear that some improvements can be made. Less error will be introduced when the verification data for the ECM samples has been recorded on the same axis as the calibration data; pixel-matching between axis is not required here. Some observational results are presented in Chapter 6. Based on the results in this chapter, the method of registration using science data points appears to yield the most positive result.

---

# Chapter 6

## Observational Results

### 6.1 Introduction

GASP embarked upon a 4 night observing campaign in November of 2012 at the Palomar Hale 200 inch telescope. From the 4 observing nights allocated, only 2 nights yielded data due to bad weather conditions and high humidity. GASP was used as an imaging polarimeter using detectors capable of imaging at a speed of 1000 frames per second (fps). The results presented in this chapter include a number of polarisation standards to test the performance of GASP as a polarimeter and find, if any, a value for any instrumental polarisation.

Polarimetric measurements of a set of data taken at twilight are also presented. These data were recorded while the telescope was pointed at the Zenith. The data was recorded for approximately 35 minutes while the Sun was rising using a Johnson R Band filter. One of the objectives of this experiment was to measure the change in the polarisation angle of the Sun as a function of this 35 minute period.

All polarimetric reductions in this chapter were performed in a similar way to the calibration verification test in Chapter 5.6 whereby the Mueller matrix of each ECM samples was reconstructed to measure how well GASP was calibrated. The following expression is used to calculate the Stokes vector,  $S$ , of the Zenith data:

$$S = A^{-1}I, \quad (6.1)$$

where  $I$  represents the intensity recorded by each channel,  $i_1 - i_4$  and  $A$  is the

---

calibration matrix for each section in the same area of the field sampled for the Zenith flat-fields. It is noted that this science data has been recorded on a different axis to that of the calibration data. Data binning is carried out to reduce any offset was introduced by this discrepancy. The calibration result produced in Section 5.10.2 were successful using a registration technique with science data points and this result is used in Equation 6.1. It is noted that there were remaining registration errors found in the calibration analysis that could lead to error in science data polarimetric analysis over the FOV. A pixel-by-pixel analysis is carried out in this chapter, however, to reduce any remaining error a method of aperture photometry is also explored.

Two methods of polarimetric analysis will be used to present this data, which will be dependent on the experiment or observation carried out. A pixel-by-pixel analysis was used in Chapter 5, and will be used on a set of Zenith flat-field data. Polarimetric analysis using aperture photometry will also be used on these flat-fields and on a number of polarisation standards observed on the same night.

## 6.2 Polarisation Standards

GASP observed two polarisation standards on the fourth observation night at Palomar. The polarimetric information, from the literature, can be found in Table 6.1. The analysis to follow was carried out using aperture photometry. The image quality of the data sets was not sufficient to perform a pixel-by-pixel analysis. This type of analysis was not necessary to characterise the stability and performance of the polarimeter.

The observation logs from Night 4 of the GASP observing run in November 2012 show that the seeing reached about  $2''$  in the early stages of the night, once the dome was open. There was also poor observing conditions for the 2 days previous to Night 4 where Palomar Mountain experienced snow, rain and heavy fog. It was late into the night before the dome could be opened as the humidity was quite

---

<sup>1</sup>Observations at  $\theta = 177.1^\circ$  at 529 nm; Sun elevation of  $-5.9^\circ$ .

<sup>2</sup>Cronin et al. (2006)

<sup>3</sup>Integrated data.

<sup>4</sup>Phase averaged.

Table 6.1: Integrated polarimetric information in the literature for targets observed by GASP at the P200 in November 2012.

Target	Filter	V Mag	DOLP (%)	PA ( $^{\circ}$ )	Ref
HD12021	B	8.86	$0.11 \pm 0.02$	$160.10 \pm 5.21$	Schmidt et al. (1992); Turnshek et al. (1990)
BD25727	R	9.50	$6.39 \pm 0.04$	$32.6 \pm 0.2$	Turnshek et al. (1990)
	V		$6.15 \pm 0.09$	$32.6 \pm 0.4$	Turnshek et al. (1990)
Skylight flat	R	-	$73.9 \pm 1.4^1$	$\sim 25^2$	Gehrels (1962), see also Cronin et al. (2006); Ugolnikov and Maslov (2009)
Crab pulsar	V	16.5	$5.2 \pm 0.3$	$105.1 \pm 1.6$	Moran et al. (2013) <sup>3</sup>
			$5.4 \pm 0.1$	$96.4 \pm 0.2$	Slowikowska et al. (2009) <sup>4</sup>
Trimble 28	V	-	$1.6 \pm 0.2$	$147.5 \pm 3.7$	Moran et al. (2013)
Crab pulsar & Knot	IR	-	$9.8 \pm 0.1$	$109.5 \pm 0.2$	Slowikowska et al. (2009)

high, and remained high for a time after the dome opened. This lead to a settling period, in terms of the seeing, for the telescope, and hence observations recorded by GASP. It is not known how much cloud cover occurred on the same night, however, it was noted to be intermittent. The seeing improved towards the end of the night. The last recorded value was  $1.2 - 1.5''$ . Polarimetry is basically a very accurate differential photometry technique and polarimetric observations require stable observing conditions, if not the degree of polarisation will be overestimated. This means that any changes in the seeing and transparency of the atmosphere should be minimal and, overall, occur slowly during the observation.

The radial plots from the polarisation standards indicate that this is consistent with the recorded values for the FWHM. It was difficult to focus the telescope during periods of poor seeing. The polarisation standard HD12021 was recorded at the beginning of the night. The standard BD25727 was recorded at a later stage

---

when an improvement in seeing was observed, 2 hours later.

The radial aperture size used was approximately equal to the FWHM of the target. An aperture of this size contains almost 70% of the target's flux, excluding scattered flux in the target wings. Due to poor seeing, and detector oversampling, the target observed tended to cover a large area of the FOV. The registration has been shown to be non-uniform therefore, it was necessary to reduce the area chosen for photometry to prevent further error from blurring of the PSF. It has been discussed that the spatial results from the calibration varied outward from the centre of the FOV.

### 6.2.1 Data Reduction

Table 6.2 contains the observation notes for each polarisation standard observed on Night 4. There is a time lag in observing where the atmospheric conditions changed; this makes it difficult to account for instrumental polarisation effects.

Table 6.2: Observational logs summary for the polarisation standards observed by GASP on Night 4.

Target	Filter	Exp Times (s)	# Frames	UT recorded
BD25727	V	2	30	06: 29: 08
	R	2	60	06: 31: 46
HD12021	V	2	30	04: 37: 28
	R	2	30	04: 40: 02

The choice of aperture size has already been discussed. Figure 6.1 shows all four GASP channels and the choice of aperture for photometry. The image quality for HD12021 after data reduction is not ideal. There is a remaining scaling and rotation difference on TP1 and TP2 compared to RP1. The data was binned  $4 \times 4$  post-processing to reduce this error but the optical distortions are greater than what can be rectified in software. A sky background level was removed but it was found not to have any significant effect on the polarimetric signal; the SNR was

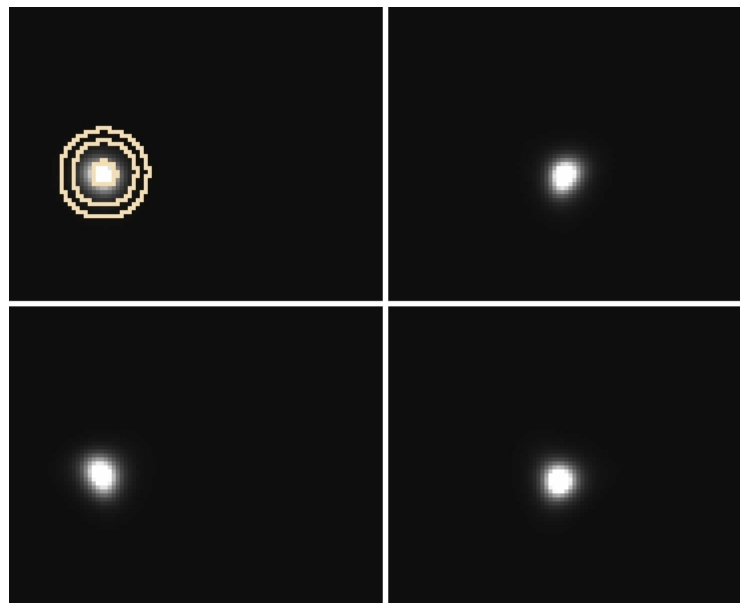


Figure 6.1: Registered images for polarisation standard HD12021 taken in a clear filter. The RP1 images displays the location of the radial aperture (3 pixels), annulus (8 pixels) and dannulus (3 pixels). Sky background subtraction was found to make very little difference to the polarimetric measurements. The data has been binned  $4 \times 4$  post-processing. Top LHS: RP1, top RHS: RP2, bottom LHS: TP1 and bottom RHS: TP2.

measured to  $\sim 800$  per channel.

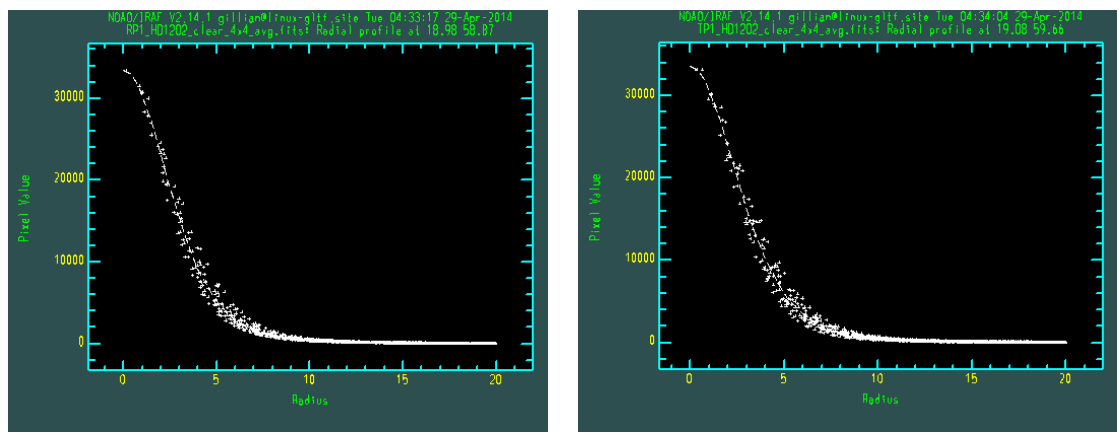


Figure 6.2: A radial profile plot for the RP1 (LHS) and TP1 (RHS) channels of HD12021 for the registered images. These plots are found from the images in Figure 6.1. The size of the radial aperture chosen for photometry is equal to the FWHM of this target, which is almost identical in both channels. It is noted that the FWHM varies from 4 - 6 pixels for the duration of this observation.

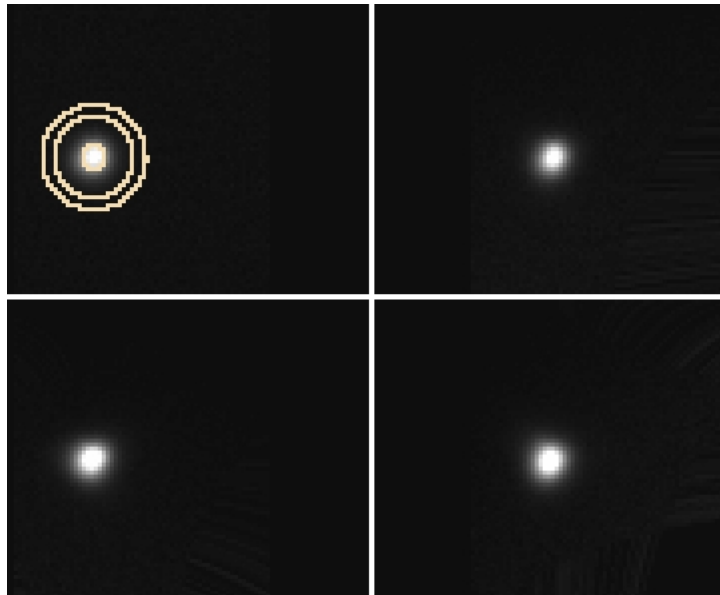


Figure 6.3: Registered images for polarisation standard BD25727 taken in the R Band filter. The RP1 images displays the location of the radial aperture (3 pixels), annulus (10 pixels) and dannulus (3 pixels). Sky background subtraction was also found to have minimal variation on this target’s polarimetric measurements. The data has been binned  $4 \times 4$  post-processing. Top LHS: RP1, top RHS: RP2, bottom LHS: TP1 and bottom RHS: TP2.

Figure 6.2 gives the radial plots for HD12021 on the RP1 (LHS) and TP1 (RHS) channels. A PSF is fitted to this target giving the FWHM radius of about 3 - 4 pixels. There is some scatter on the fitting as the fit approaches the target wings. This could indicate that the image is properly in focus, or a poor level of seeing. There is some variation in shape, mostly registration error, when comparing TP1 to RP1. This is not observed in the radial plots.

The image quality in Figure 6.3 is improved compared to HD12021. The HD12021 target on TP1 and TP2 show greater distortion than the BD25727 images on the same channels. BD25727 has less residual error from registration, based on image quality. Each channel is higher on the chip than HD12021, which shows that field position is a function of the optical distortion present in the system. However, in each case, the data is calibrated. To avoid errors from data reduction in spatial polarimetry, aperture photometry finds a mean flux value for the target per channel.

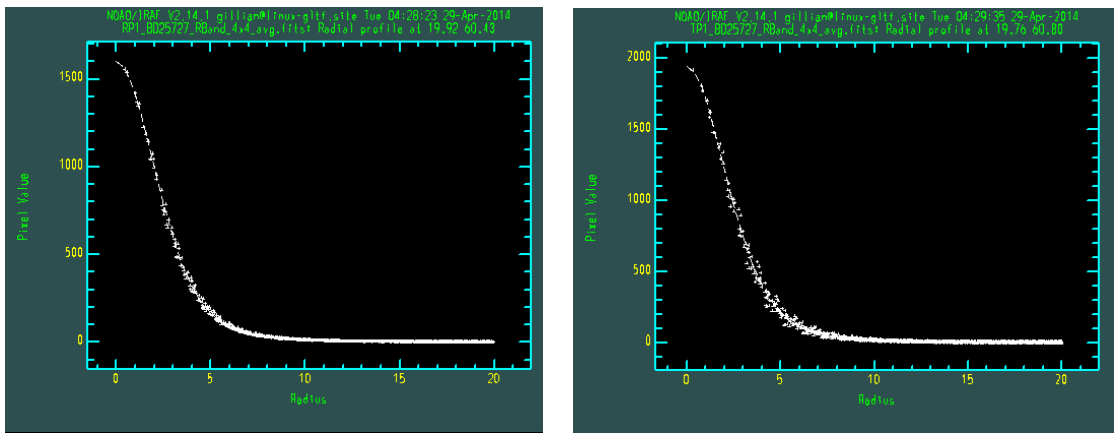


Figure 6.4: A radial profile plot for the RP1 (LHS) and TP1 (RHS) channels of BD25727 in the R Band filter for the registered images. These plots are found from the images in Figure 6.3. The size of the radial aperture chosen for photometry is equal to the FWHM of this target, which is almost identical in both channels.

The radial plots for BD25727 show a tighter PSF fit compared to HD12021 resulting from minimal errors in focus or seeing on this target. TP1 shows some scatter but overall a closer fit compared to HD12021. It is noted that the SNR for BD25727 was not as high as that from HD12021. These plots do not indicate that there is any variation in profile or shape between the channels. RP2 and TP2 are identical to their respective paths. These plots indicate that about 80% of the light from the target lies within the FWHM and is sufficient for polarimetry.

The raw intensity plots for the HD12021 data sets, see Figures 6.5 and 6.6, show large fluctuations in intensity as a function of time. The level cloud cover or atmospheric turbulence was not recorded, but the measured seeing was high,  $\sim 2''$ . The time series plots give some information regarding the behaviour of the source over time, but a change in seeing is indicated by the temporal stability of the FWHM of the target. Error bars have been omitted for all of the plotted time series'. The level of error that can be plotted is either, a SNR error, or a standard deviation in the time series. The time series' have been plotted to investigate the level of atmospheric variability for that data set.

Regarding HD12021, measuring a value of zero percent is a difficult undertaking with any polarimeter, including unknown effects as a result of poor observing conditions. The polarimetric results from this target demonstrate that there is a

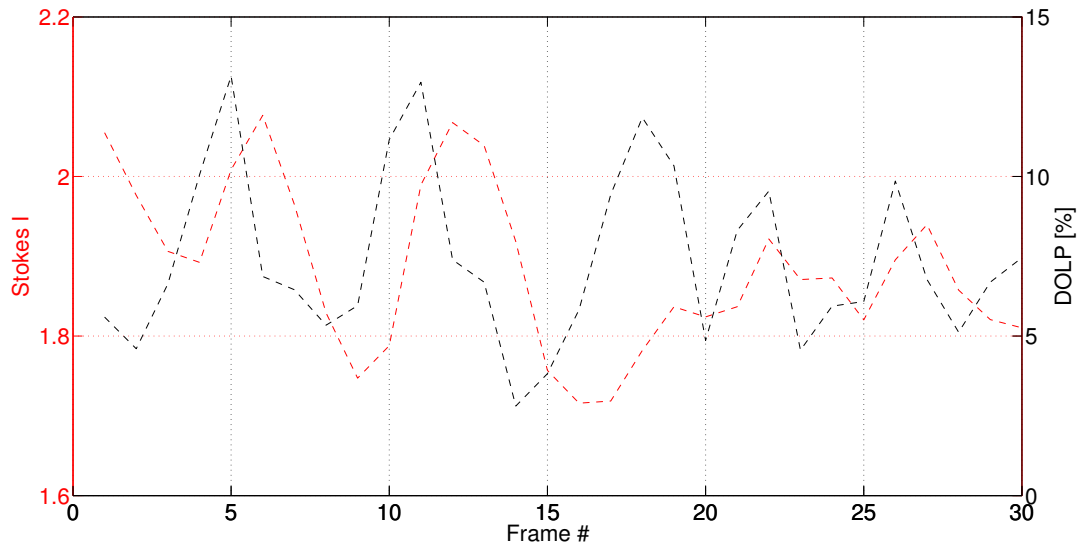


Figure 6.5: A plot of Stokes I and the DOLP for the polarisation standard HD12021 in the clear filter. There is a large variation,  $\sim 20\%$  of the maximum value, in Stokes I as a function of time (x axis refers to frame number). This variation could indicate movement of clouds, or the target moving in and out of focus.

strong possibility of an instrumental polarisation effect: this will be discussed in Section 6.2.2. It is noted that GASP has already demonstrated in the laboratory that it can measure a value as low as 3.7%.

The error measured on these targets is calculated from the SNR. Each target is quite bright, 8/9 magnitude, and the errors quoted are low indicating a SNR error; the instrumental polarisation must be calculated separately. A weakly polarised target will be dominated by any other polarised signal present in the data. There is also a possibility of induced polarisation due to poor observing conditions.

The DOCP is also plotted as a function of time. The variation is quite large, and comparable to the plot for DOLP in Figure 6.5. A changing/turbulent atmosphere could be an indication of this variation. The R Band filter is also plotted in Figure 6.8. Using a filter could block some of the light that is causing this increase in polarisation as the mean value for DOCP in R Band is lower than that in clear.

The results of the polarisation standard BD25727 are more promising. Each set of data in each filter is plotted as a function of time in Figures 6.9 and 6.10. There is higher variability in the Clear filter compared to R Band, and Stokes I in

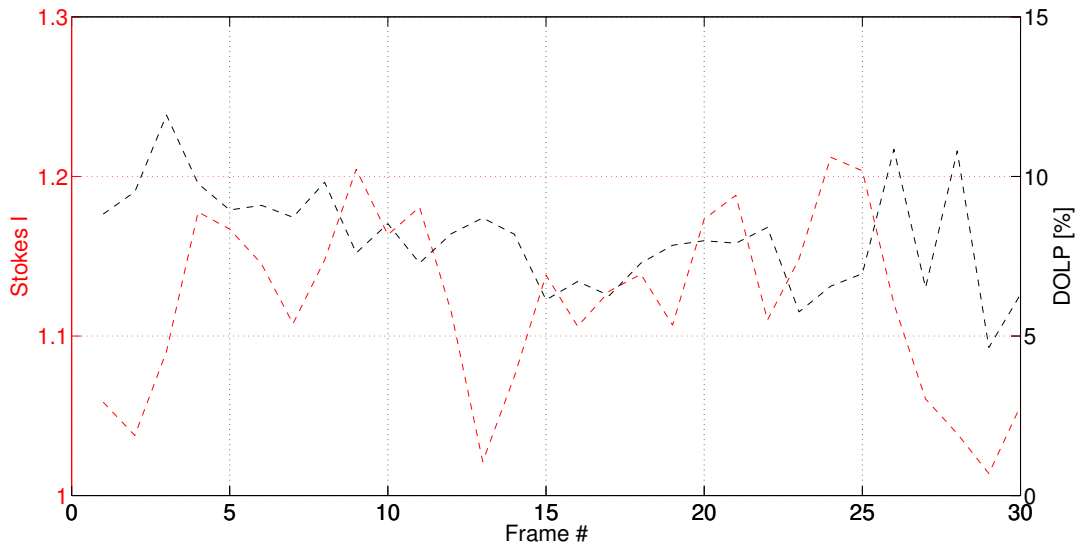


Figure 6.6: The same as Figure 6.5 but using the R Band filter. Less variability is observed but Stokes I is much lower due to the filter. The value in the DOLP jumps higher as Stokes I drops. This could be related to scattering light from transmission through a variable atmosphere.

R Band shows a trend of increasing flux against decreasing DOLP. The R Band filter shows some improvement in stability for Stokes I. This data was recorded during a period when the seeing had improved. The errors found are quoted but these refer to the Poissonian error due to the level of counts in photometry, it does not include any error from registration, which has been discussed in previous reports, and is difficult to measure. The polarisation angles have been corrected for telescope orientation. This was done using a set of Hubble Space Telescope (HST) data and computing the rotation of the GASP RP1 image compared to the HST for normal sky orientation. The polarimetric results for each target are summarised in Table 6.3.

The expressions used to find the errors in Table 6.3 can be found in Appendix A.

---

<sup>5</sup>See reference above.

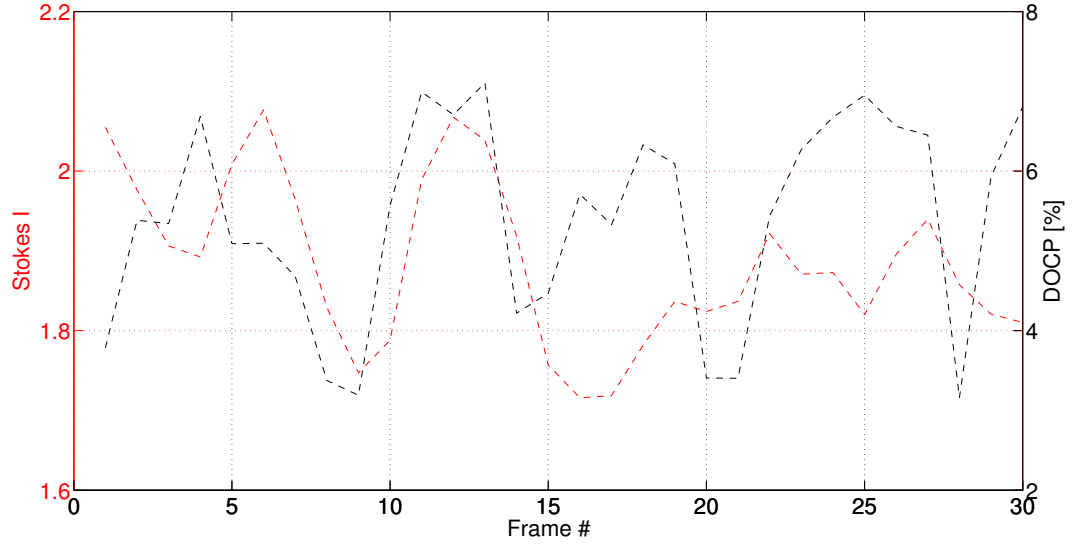


Figure 6.7: A plot of Stokes I and the DOCP for the polarisation standard HD12021 in the clear filter. The x axis refers to frame number. This variation could indicate movement of clouds. There is also the possibility of a change in target focus over time.

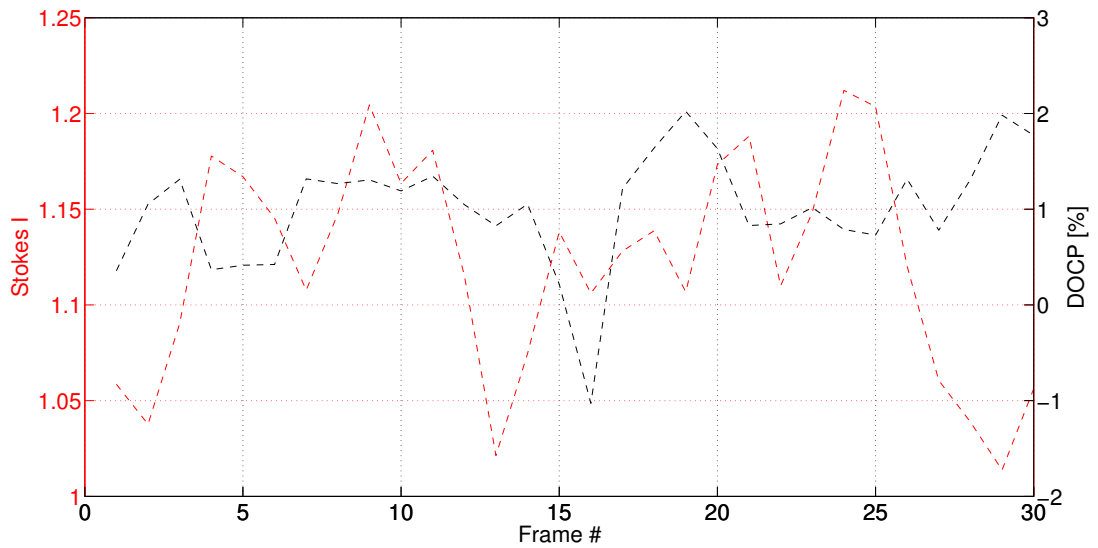


Figure 6.8: The same plot in Figure 6.7 but using the R Band filter.

Table 6.3: Polarimetric results for the polarisation standards observed by GASP on Night 4. Sky subtraction has been performed on each set of data. Polarisation angle has been corrected for telescope orientation. The difference in aperture size taken is a result of a changing FWHM for each target in each filter. A radial aperture equal to the radius of the FWHM was used. The expected result for the polarisation standards, including filter if given by there reference, is also stated.

Target	Filter	Source	Radial aperture size (pixels)	DOLP (%)	DOCP (%)	PA ( $^{\circ}$ )
HD12021	GASP	R	4	$7.35 \pm 0.07$	$1.01 \pm 0.15$	$53.76 \pm 0.71$
		V	4	$6.82 \pm 0.20$	$5.42 \pm 0.13$	$87.84 \pm 0.57$
	Expected <sup>5</sup>	B	-	$0.11 \pm 0.02$	-	-
BD25727	GASP	R	2	$6.65 \pm 0.49$	$-0.89 \pm 0.28$	$29.26 \pm 1.43$
			-	$6.39 \pm 0.04$	-	$32.6 \pm 0.2$
	GASP	V	3	$7.10 \pm 0.12$	$-0.19 \pm 0.16$	$33.48 \pm 0.70$
			-	$6.15 \pm 0.09$	-	$32.6 \pm 0.4$

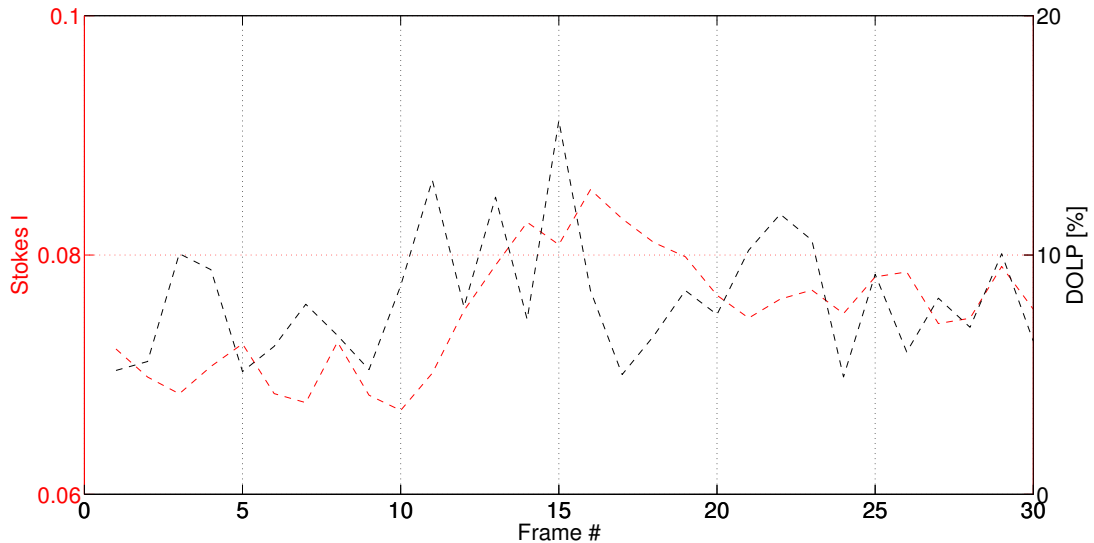


Figure 6.9: A plot of Stokes I and the DOLP for the polarisation standard BD25727 in the clear filter. There is some variation in Stokes I, which seems to follow a more random pattern of variation with DOLP compared to HD12021. Each measurement is plotted as a function of time (x axis refers to frame number).

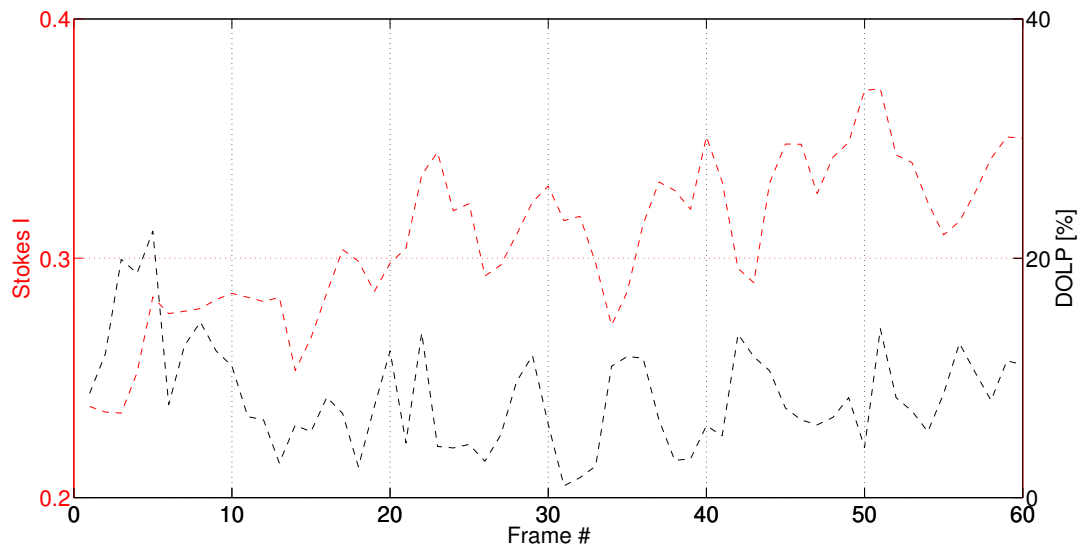


Figure 6.10: A plot of Stokes I and the DOLP for the polarisation standard BD25727 using the R Band filter. Some variability is observed and Stokes I is higher. This could be a result of improved observing conditions. As Stokes I increases the value in the DOLP begins to drop, fluctuating around its mean value.

The DOCP is also plotted as a function of time for BD25727. The variation is quite large, and comparable to the plot for DOLP in Figure 6.5. A changing/turbulent atmosphere could be an indication of this variation. The R Band filter is also plotted in Figure 6.8. Using a filter could block some of the light that is causing this increase in polarisation as the mean value for DOCP in the R Band is lower than that in clear.

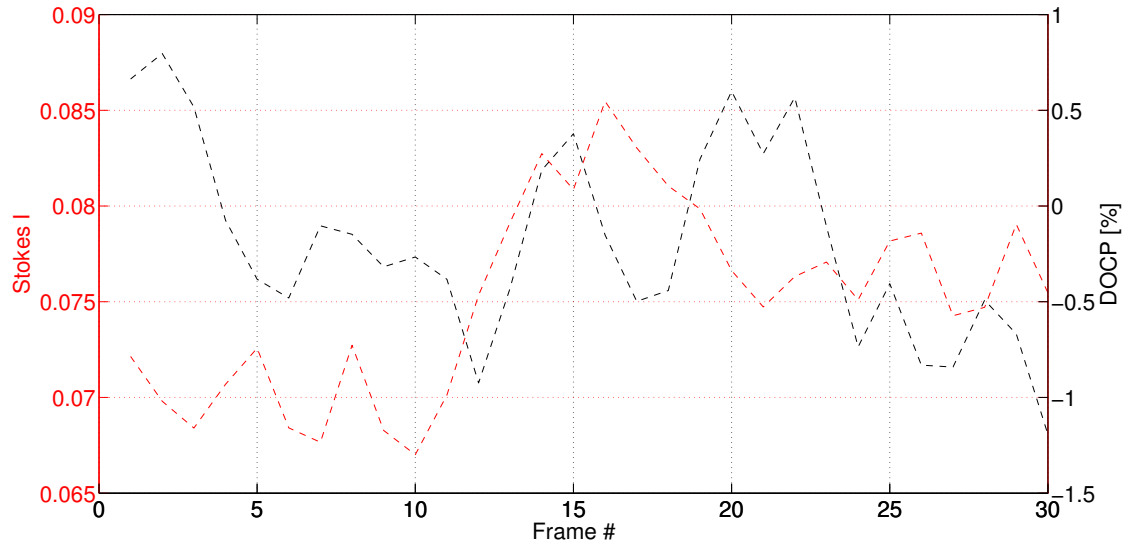


Figure 6.11: A plot of Stokes I and the DOCP for the polarisation standard BD25727 for a clear filter. The x axis refers to frame number. This variation could indicate movement of clouds, or the target moving in and out of focus due to seeing variation.

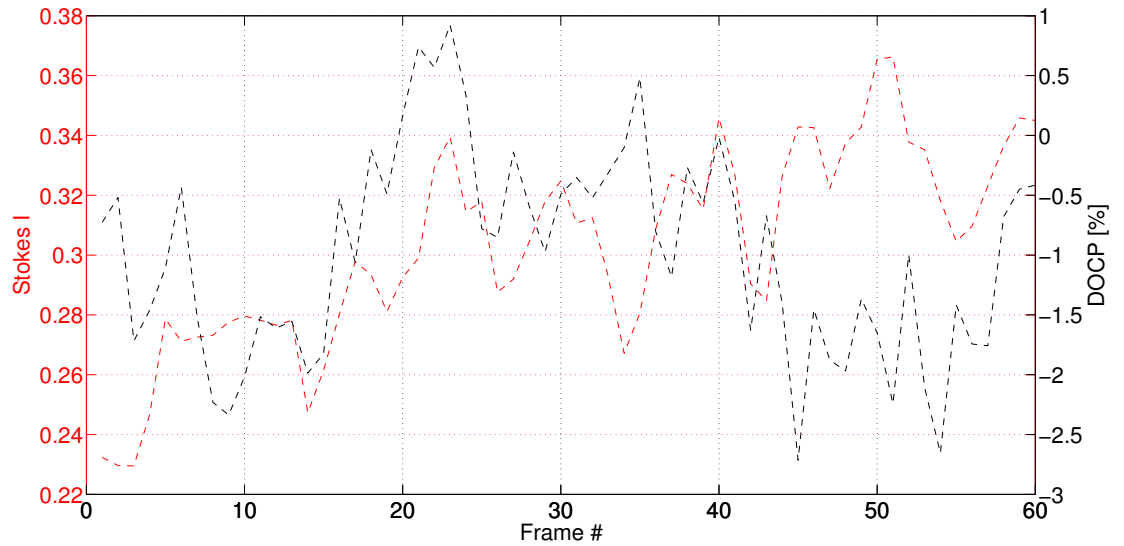


Figure 6.12: The same plot in Figure 6.7 but using the R Band filter.

---

### 6.2.2 Instrumental Polarisation

Taking the above analysis into account the instrumental polarisation must also be calculated. In order to do this, a zero polarisation standard must be observed. It is not accurate to assume that all optics preceding the PSA do not introduce some polarisation. The calibration method outlined in Chapter 5 explains how no assumption is made about the optical system as long as it is not altered between calibration and experimental work. However, to show the effect of instrumental polarisation, all optics before the PSA, which include telescope mirrors, and f/16 to f/9 lenses, can introduce an artificial polarisation which will depend on the position in the field.

In order to measure instrumental polarisation the first observation must be of a 0% polarisation standard. Ideally, a number of zero standards would be required to accurately determine the instrumental polarisation of GASP on a particular night. In this case, the observational result from polarisation standard HD12021 can be used. It is not certain what is causing a measurement of  $\sim 6\%$  polarisation. It has already been discussed that atmospheric effects could be a factor however it is more likely to be an instrumental error.

According to Patat and Romaniello (2006), it is important to note that the instrumental polarisation is not removed by the sky background subtraction. It is also discussed that instrumental polarisation is independent of the object's intensity. Based on an instrumental polarisation  $p$ , and instrumental polarisation angle  $\varphi$ , Patat and Romaniello (2006) showed that,

$$P = \sqrt{P_0^2 + p^2 + 2P_0p \cos 2(\chi_0 - \varphi)}, \quad (6.2)$$

where  $P$  is the observed polarisation, and  $P_0$  and  $\chi_0$  are the expected polarisation and polarisation angle, respectively.

From this expression, it is clear that when  $P_0 \gg p$ , then  $P \simeq P_0$ . In the case that an object and the measured instrumental polarisation are comparable ( $p \simeq P_0$ ), the observed polarisation is approximately given by,

$$P = \sqrt{2}P_0\sqrt{1 + \cos(2(\chi_0 - \varphi))}. \quad (6.3)$$

---

The main difference between instrumental polarisation and a polarised background is that the latter is effective only when the background is  $\gtrsim I$  (Patat and Romaniello (2006) discuss this in more detail), while the former acts regardless of the object intensity; the important element in the measurement is its polarisation. The authors also discuss how an average instrumental polarisation can be calculated when a known source of a particular polarisation is observed.

HD12021 was used to measure the instrumental polarisation as it is a zero polarisation standard. Equation 6.3 is used for  $p \simeq P_0$  as well as the information from Table 6.1 for the clear filter observation. The DOLP that should have been measured by GASP is  $0.07 \pm 0.2\%$ . Therefore, it is expected that if HD12021 was observed again, in similar conditions, that it would measure a value for the DOLP of  $6.82 \pm 6.80\%$ . Applying this to BD25727, for the same filter, the instrumental polarisation was calculated to be  $\sim 6.8\%$ . Equation 6.3 is used as  $p \simeq P_0$ , i.e. the instrumental polarisation is equal to the expected value in the literature, and this gives a DOLP of 7.01%, which is in agreement with what was observed by GASP.

For the R Band filter, the measured instrumental polarisation was 7.35% for HD12021. This gives an expected DOLP of 0.062%. The instrumental polarisation in R Band was also used to determine the expected DOLP for BD25727. It was found that  $P_0 < p$ . The DOLP measurement obtained by GASP for BD25727 is the expected value from the literature. This indicates that there is no instrumental polarisation effect acting on this data, or that the value has changed. If Equation 6.3 is applied for  $p \geq P_0$ , the DOLP was found to be 11.92%. The polarisation is overestimated; however, if GASP repeated the measurement for the DOLP of this target, using this filter, 11.92% is an acceptable upper limit for this level of instrumental polarisation. As can be seen in Table 6.3, GASP has calculated a value of  $6.65 \pm 0.49\%$ .

The results of this instrumental polarisation calculation indicate that either the instrumental polarisation has changed over the course of the night, or that this calculation is only valid for sources, which are weakly polarised where GASP overestimates the polarisation. The atmospheric variation between these targets could also lead to an error in using this instrumental polarisation.

---

### 6.2.3 Conclusions

It is difficult to judge the result of the polarisation standard HD12021. The seeing and general observing conditions changed quite rapidly as the night progressed. Data from another polarisation standard would have been required immediately after HD12021 to measure any instrumental polarisation effect. Polarimetry is a very accurate differential photometry technique and requires stable observing conditions. The level of polarisation will be overestimated if not. It is almost certain that HD12021 is not circularly polarised - and any measure of DOCP from this source implies instrumental or, more likely atmospheric errors and can be found from the variation in the time series.

The results from BD25727 are more promising and give an idea of any instrumental polarisation towards the end of the night. Some atmospheric instabilities are also present in this data. Variation in polarisation as a function of passband is unknown and has not been measured in the laboratory accurately. The variability in the polarimetric results for each standard, for non-ideal observing conditions, demonstrate that GASP is performing well on Night 4. It is not a limitation of the instrument as GASP has been found to measure polarisation at lower values (the LED calibration experiments).

HD12021 was used to determine the instrumental polarisation for this observation night in both the clear and the R Band filter. Acceptable results from these instrumental DOLP values were determined for the polarisation standard BD25727. To determine a more accurate estimate for the instrumental polarisation, a larger number of polarisation standards is required per night of observation.

---

## 6.3 Zenith Flat-Field Observations

A series of images were recorded, over a 35 minute period, at twilight on the last night of observations during the Palomar November observing campaign. Data was recorded continuously as the Sun was rising. By taking data like this we can measure how the polarisation of the sky changes with respect to the elevation of the Sun over time, i.e. we expect that the polarisation of the sky will increase over time. This type of experiment gives valuable information of how well registered the GASP data is, and measures the limit of the polarimetric variation over the FOV. It is also a very interesting experiment to perform using GASP to determine a measurement of the degree of linear polarisation, and change in polarisation angle, of the twilit sky over time.

Some outstanding registration problems were evident in certain areas of the FOV based on the results found in Sections 5.9 and 5.10. This analysis will help by confirming the performance of the GASP calibration. The Zenith data was recorded as 3 data cubes<sup>6</sup>. The first was binned for 48 frames (48 seconds) and is the first image in the figures to follow. Images 2 - 11 are averaged over 200 frames (3.3 minutes). The final image, where the sky was the brightest for this data set, is an average of 134 seconds of data.

The conclusion of Chapter 5 was that the registration technique using science data points gave the best polarimetric results when verification of the data was carried out. This method, with some variation, is what is used to register the science data presented in this chapter. Registration of calibration data is performed by, firstly using the science data points in Figure 5.19 to match RP2, TP1, and TP2 to RP1 for the science images; secondly, the solution for image artefacts that match RP1 science to RP1 calibration are used to match science to calibration. These artefacts can be found in Figure 5.8.

The registration of RP1 science to RP1 calibration was at the sub-pixel level for pixel shift and no magnification difference is found. The angular rotation is also much less than 1°: This does not change the results of the final calibration registration, and the calibration matrix is unaltered compared to that found in Figure 5.24. The results of the *geomap* fit can be found at the end of this section

---

<sup>6</sup>A data cube is a single FITS file containing header information and N number of images.

---

Table 6.4: *geomap* output for matching RP1 science to RP1 calibration.

x shift (pixels)	0.32
y shift (pixels)	0.60
x magnification	1.00
y magnification	1.00
x rotation ( $^{\circ}$ )	-0.12
y rotation ( $^{\circ}$ )	0.13

in Table 6.4. The points, found in Figure 5.19, lie in  $11 \times 11$  pixel area with variation in the y coordinate, but little in the x. The area of interest is the region where the Crab pulsar is located, indicated by the orange box.

---

### 6.3.1 Science Data Pixel-by-Pixel Analysis

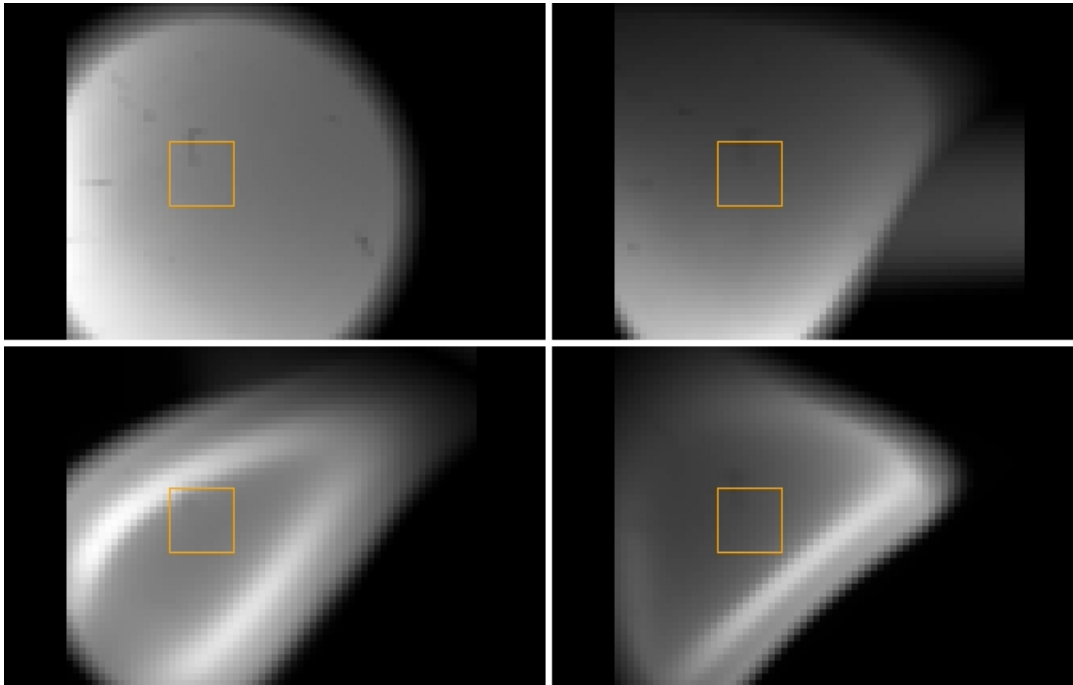


Figure 6.13: All registered GASP channels for a full flat-field frame using science data points and image artefacts. A pixel-by-pixel analysis will be analysed in this chapter on the area indicated by the orange box. Top LHS: RP1, top RHS: RP2, bottom LHS: TP1 and bottom RHS: TP2.

This section uses the geometrical registration solution in Section 5.10 to register the Zenith flat-field data. The system matrix found in Figure 6.14 is used to perform the Stokes reduction.

This method makes use of science data found in Figure 5.19, which has been addressed in detail in Section 5.10.

These points are not found in the calibration data therefore, an assumption is made that the science points in RP1 science channel are matched to those in RP1 calibration channel, and so the same geometrical solution can then be used on RP2, TP1, and TP2 calibration channels as those on their respective science channels. To reduce this assumption the RP1 calibration channel is also mapped to the RP1 science channel and this solution is also used on the RP2, TP1, and TP2 channels, as these have already been mapped to RP1 science. As has already

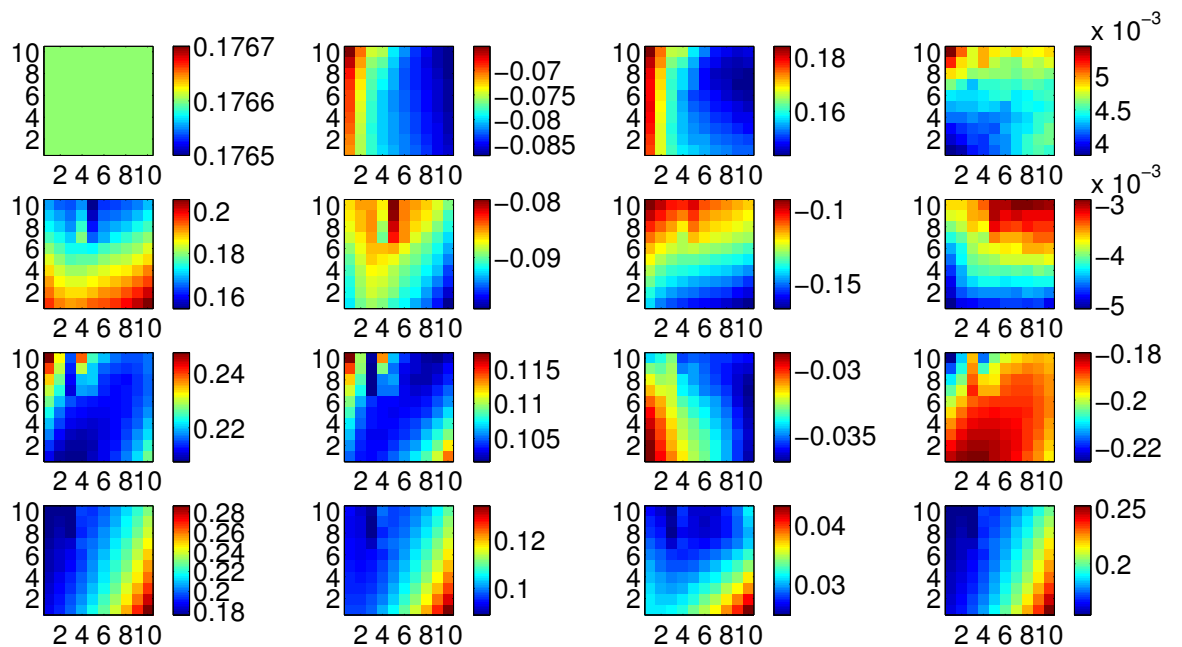


Figure 6.14: The experimental calibration matrix for the image section indicated in Figure 6.13. The calibration images were registered to channel RP1 using science data.

been discussed, this process has no impact on the final result and this is evident based on the results in Table 6.4.

The location of the orange box in Figure 6.13 was chosen for a number of reasons. It spans a region that includes the coordinates of the targets on Nights 1 and 4. These points were used for image registration and so this area will be registered using a solution that is matched with this location. Other locations of the field were examined to find an area with minimal variation. There is a banding at the top RHS of the TP2 channel where there is a gradual gradient, in a diagonal direction, from this banding. This banding is present in all locations of the TP2 field and cannot be removed/reduced.

Taking a look at the image registration residuals, RP1 calibration channel is used as the reference channel and the variation of counts across the field is shown for pattern comparison in the residuals. RP1 shows an inhomogeneity across the field. This could indicate that the light is not distributed in a uniform way across the optics/prism-rhomb, and this is inherent to optical systems such as what

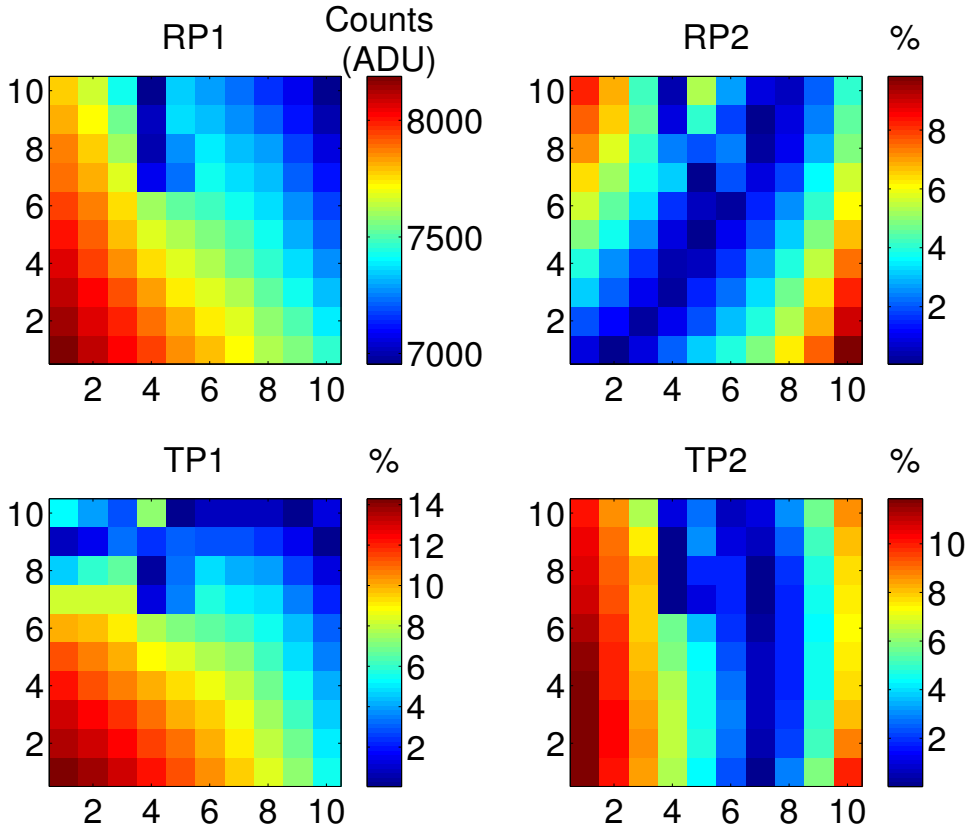


Figure 6.15: Image residuals for the flat-field section indicated by the orange box for RP1 (top left image) in Figure 6.13: Science data points are used to perform the image registration. The colour bar indicates the percentage intensity remaining when the normalised channel is removed from the normalised reference channel, RP1 calibration channel.

has been developed for GASP (see Section 4.4.1). This variation/inhomogeneity appears to be present across each path, however, the registration should take care of the variation on the 3 registered channels compared to the reference. As the polarimetric result is dependent on a relative intensity measurement, as long as the variation across the field is comparable to each subsequent channels, any inhomogeneity should not have a negative impact on the result.

There appears to be a decrease in the percentage residuals on RP2 compared with using image artefacts; however, this is only valid for a small area in the FOV and the pattern across the field is more evident. In the case of RP2, TP1, and

---

TP2 the systematic error is a banding or elliptical pattern for each TP image and a striped or banding for RP2.

### 6.3.1.1 Polarimetric Results

Table 6.5 is an approximation of the expected variation in polarisation angle over the time frame for which GASP recorded the Zenith flat-fields. The results that follow will be compared to this table. A known value for the variation in DOLP is not known at this time but is compared to the absolute value in Table 6.1.

Table 6.5: Expected polarisation angle variation over the same 35 minute period of observation by GASP for Zenith flat-field data. The first time is not usable as we are measuring from this value: The  $\Delta PA$  values are measured from here.

Flat-field	1	2	3	4	5	6	7	8	9	10	11	12
Time (mins)	0.47	2.45	5.75	9.05	12.35	15.65	18.95	22.25	25.55	28.85	32.15	35.55
$\Delta PA$ ( $^{\circ}$ )	-	0.42	0.69	0.69	0.69	0.69	0.69	0.69	0.69	0.69	0.69	0.71

The values for time in Table 6.5 were calculated from the time-stamps in the header (data information) files. The Sun moves  $1^{\circ}$  in 4 minutes, however, the altitude of Palomar Mountain must also be taken into account. The elevation was  $+32.3^{\circ}$ . Therefore, taking the cosine of the elevation, the actual change in PA is  $0.84^{\circ}$  in 4 minutes. The times given in Table 6.5 are the midpoints of the recorded data - taking into account delays in acquisition due to stoppages.

A theoretical description can be determined for the behaviour of the DOLP. The following expression, known as the Rayleigh Sky Model, gives the value for the degree of linear polarisation calculated as a function of the absolute angle for a reflected beam of light,

$$DOLP(\gamma) = \frac{1 - \cos^2 \gamma}{1 + \cos^2 \gamma}. \quad (6.4)$$

In this case,  $\gamma$  refers to the scattered angle, which is formed between the pointing (telescope) and the Sun. The polarisation angle,  $\theta = 90^{\circ} - \gamma$ , or the angle

---

formed by the Sun with the Zenith. It is found that as the scattered angle in Figure 6.16 increases, the DOLP also increases. It can also be shown that if the DOLP was plotted as a function of increasing (absolute)  $\theta$  the value of DOLP will decrease. A detailed experiment of how this model describes the E vector was carried out by Suhai and Horváth (2004).

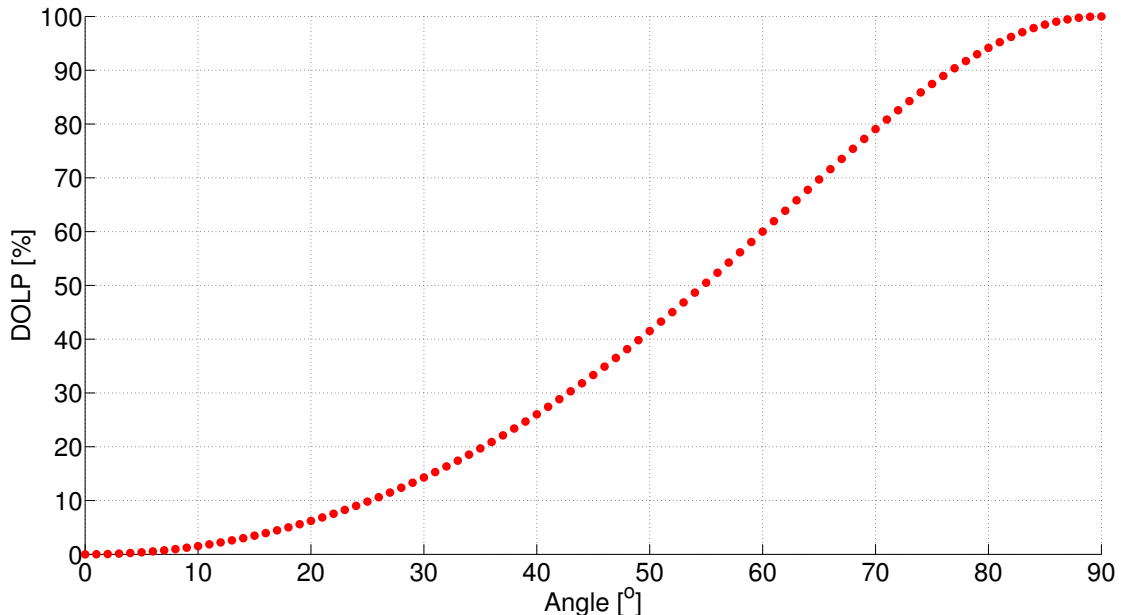


Figure 6.16: A plot of the DOLP as a function of scattering angle according to Equation 6.4. The DOLP is observed to change more rapidly after  $\sim 20^\circ$ , slowing down from  $\sim 80^\circ$ . These angles refer to absolute values, and not  $\Delta\gamma$  values.

Stokes reduction was run for the flat-fields registered using science data points. The results for the DOLP can be found in Figure 6.17; the DOLP, DOCP, and PA are measured over a 35 minute period at twilight, as the Sun was rising. There is a clear systematic trend in the DOLP across the  $6 \times 6''$  square FOV. It is unclear what is causing this trend, however, it has been found that the calibration matrix, in Figure 6.14, shows a very similar pattern in this same location for the gain coefficients on RP2, TP1, and TP2. The reconstructed Mueller matrix ECM samples also show these trends, to a lesser effect.

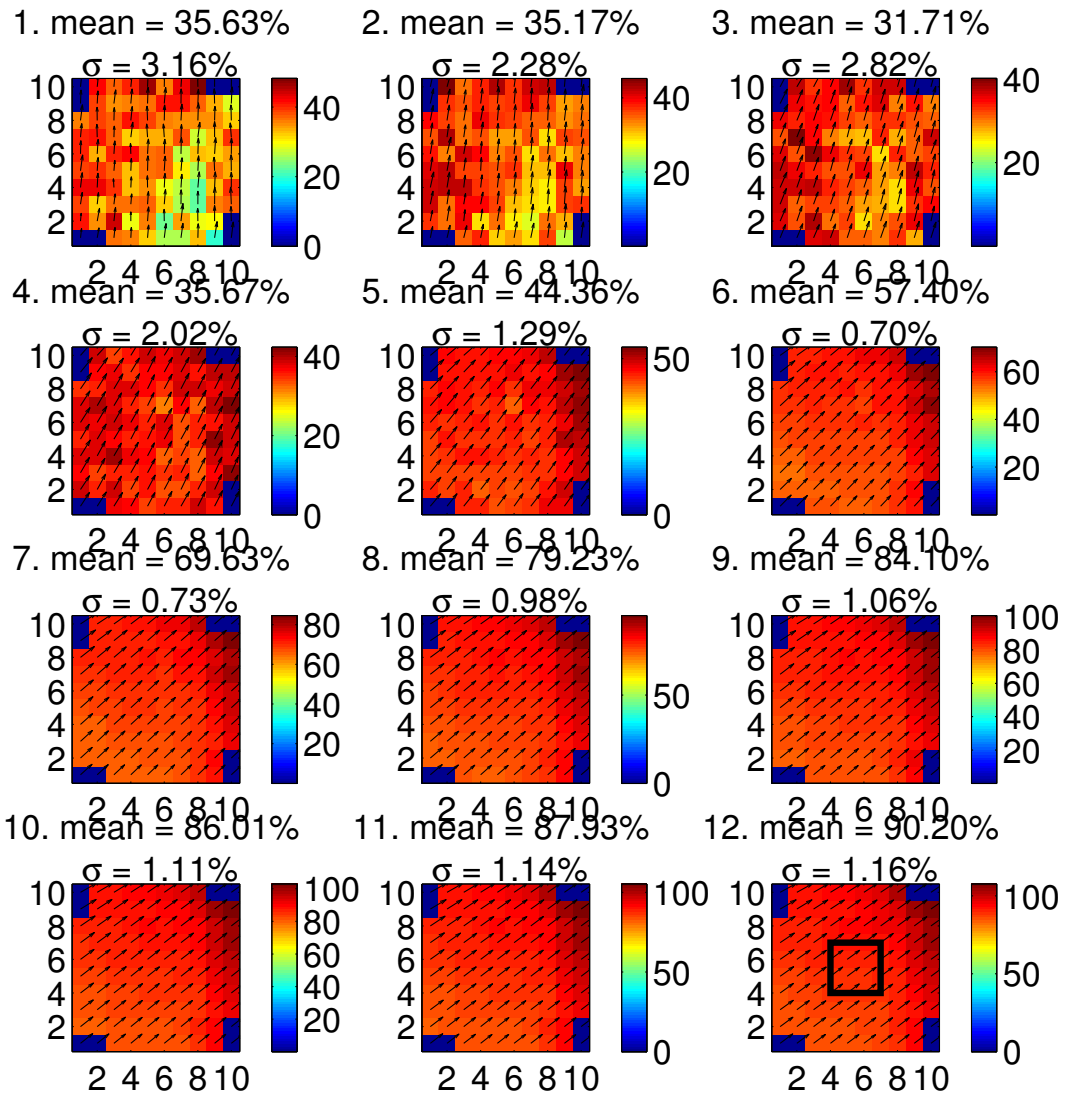


Figure 6.17: Degree of linear polarisation found using a registration method by science data points. The mean and  $\sigma$  values are given in the title of each flat. The image has been flipped and rotated compared to the images in Figure 6.13 to match the telescope correction. This is the reason for the blue pixels at each corner of the image. The PA vectors are also plotted. The  $\sigma$  value refers to the random and systematic error over the FOV of interest in Figure 6.13 for the  $3 \times 3$  pixel area indicated by the rectangle on the final image.

---

It is also observed that, over time, a systematic effect becomes evident. This could be a result of the change in light level as the Sun rises. It is a possibility that when fewer photons strike the EMCCD there is a combined effect from random, and systematic variations. This also gives an incorrect gain representation of the flat-field for each of the GASP channels, which is difficult to discern in this data with an uncertainty such as pixel-matching. This raises a concern where there could be an intensity threshold below which it is not possible for GASP to make a sensible polarimetric measurement. The bias frame, that is removed from this data (and calibration data), was carefully examined and it was found not to show systematic variation across the FOV comparable to what has been found in the residuals in Figure 6.15. Any gain error will be a result of calibration, and additionally in any science data. Insufficient pixel-to-pixel matching is the mostly probable cause due to a lack of registration points in the location of these patterns. This was also observed in the calibration matrix, and MM samples.

A similar trend in the pattern for the polarisation angle (PA) is found in Figure 6.18. The mean and  $\sigma$  values are taken from the  $3 \times 3$  pixel area highlighted in the last frame in Figure 6.17. Quite a low error value has been found here in a reasonably flat section of the field, comparable to the same area in the polarimetric measurements for the PA and DOCP. The same areas of the FOV as those for DOLP show a gradual gradient in the pattern, particularly from the bottom left to top right corner. This area is also present in the registered TP2 images and appears in the calibration matrix and reconstructed Mueller matrices of the ECM samples. It is noted that the polarimetric results have been flipped and rotated to account for the telescope orientation on the sky. This has not been performed for the calibration measurements. The pattern is visible from top left to bottom right of this image, as it is in Figure 6.17 if the image was flipped  $180^\circ$  along the y axis. The variation in pattern is a close match to the image of the TP1 gain coefficient in Figure 6.14. A comparison can also be made between the gain coefficient for the polarisation angle and RP2. This makes sense as the gain coefficient for RP2 and TP1 are used to calculate the values for Stokes Q and U respectively when calculating the PA.

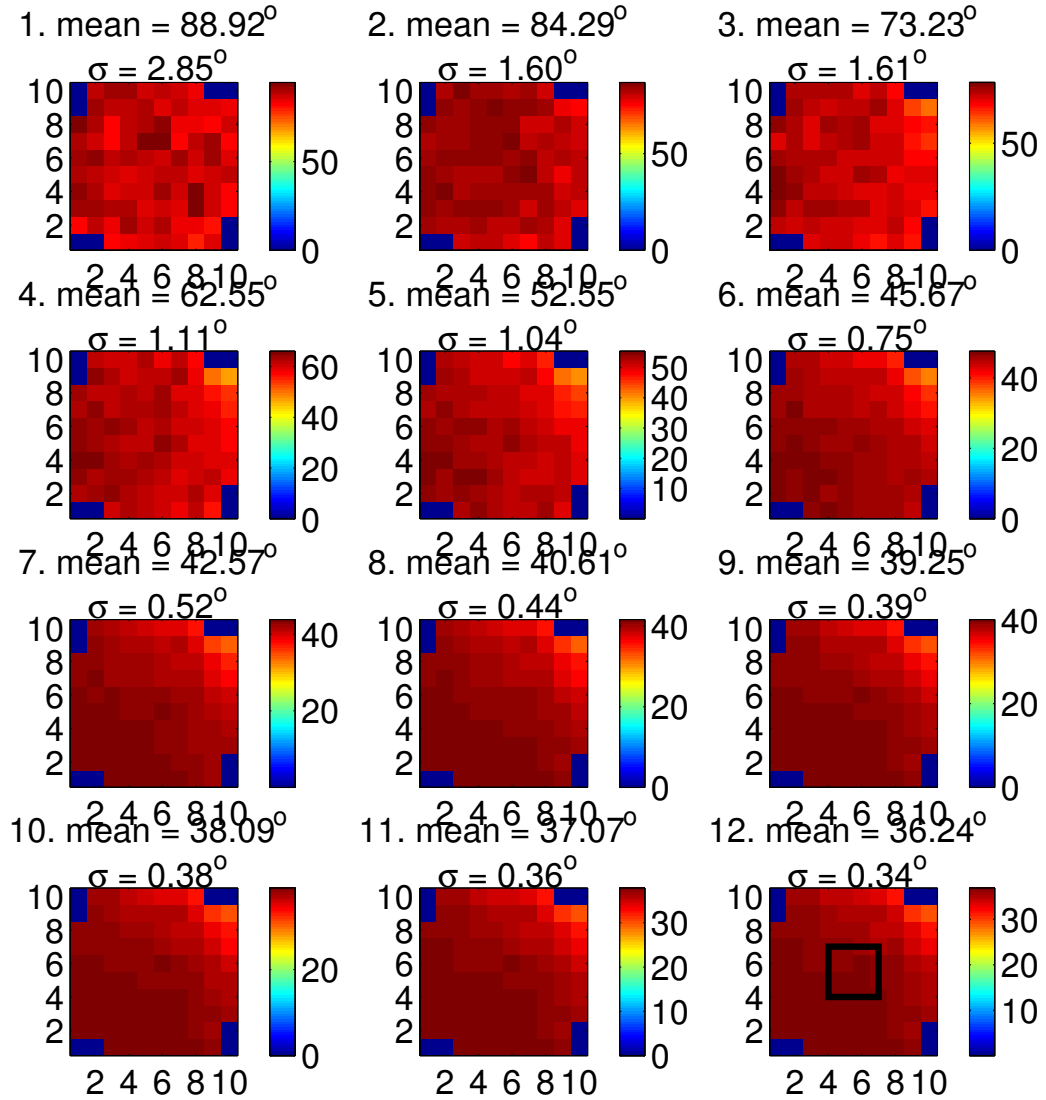


Figure 6.18: Polarisation angle found using a registration method by science data points. The mean and  $\sigma$  values are given in the title of each flat. The image has been flipped and rotated compared to the images in Figure 6.13 to match the telescope correction. This is the reason for the blue pixels at each corner of the image. The  $\sigma$  value refers to the random and systematic error over the FOV of interest in Figure 6.13 for the  $3 \times 3$  pixel area indicated by the rectangle on the final image.

---

It has been discussed in Chapter 5 that errors in misregistration can lead to large errors in measured values for DOLP and DOCP. The GASP system has been compared to work carried out by Smith et al. (1999) where, if GASP measures a pixel error of  $\sim 0.3$  pixels (propagation of the RMS errors in all 3 channels for  $4 \times 4$  binning), this could result in  $\pm 6\%$  error in the DOLP and DOCP. An error for the PA has not been stated by the authors. There is variation in the pixel-to-pixel values measured by the GASP system that are comparable to this result, showing that the errors found in image registration will result in variation of this order. It is also noted that, there are points in the FOV used that do not have matched points channel-to-channel - the misregistration errors are not known for these positions but are expected to be similar to those stated.

The first 6 frames show a combination of random and systematic error in the results for the DOLP. This has not changed when measuring the PA and the conclusions are the same in terms of the calibrated gain of the system. It has been discussed, above, how the polarisation angle varies over time, from frame-to-frame. As indicated in Table 6.5, over a 35 minute period the expected change in angle of the Sun with respect to the Earth is  $\sim 6.3^\circ$ . This means that from start to finish we expect to see a swing of this size angle.

Similarly, the pattern in the images for the DOCP in Figure 6.19 show a systematic variation. The highlighted area in the final frame measures the DOCP at  $0.7 \pm 0.3\%$  and appears relatively flat, which indicates that GASP is measuring a low level of circular polarisation, almost zero, and a reasonable  $\sigma$  variation. This area is used as outside the total blue section there is an indication that the field is less flat (where the colour map changes from blue to red, left-to-right). There is a large increase in DOCP and the visible shape in the bottom right corner is altered compared to the left-hand-side. This corner could be showing quite a large variation in optical distortion not corrected by geometrical registration. It is also noted that this pattern exactly matches that of the TP2 gain coefficient in Figure 6.14, which measures the Stokes V parameter. This pattern is also found in the raw image and flat-field residuals for TP2 images.

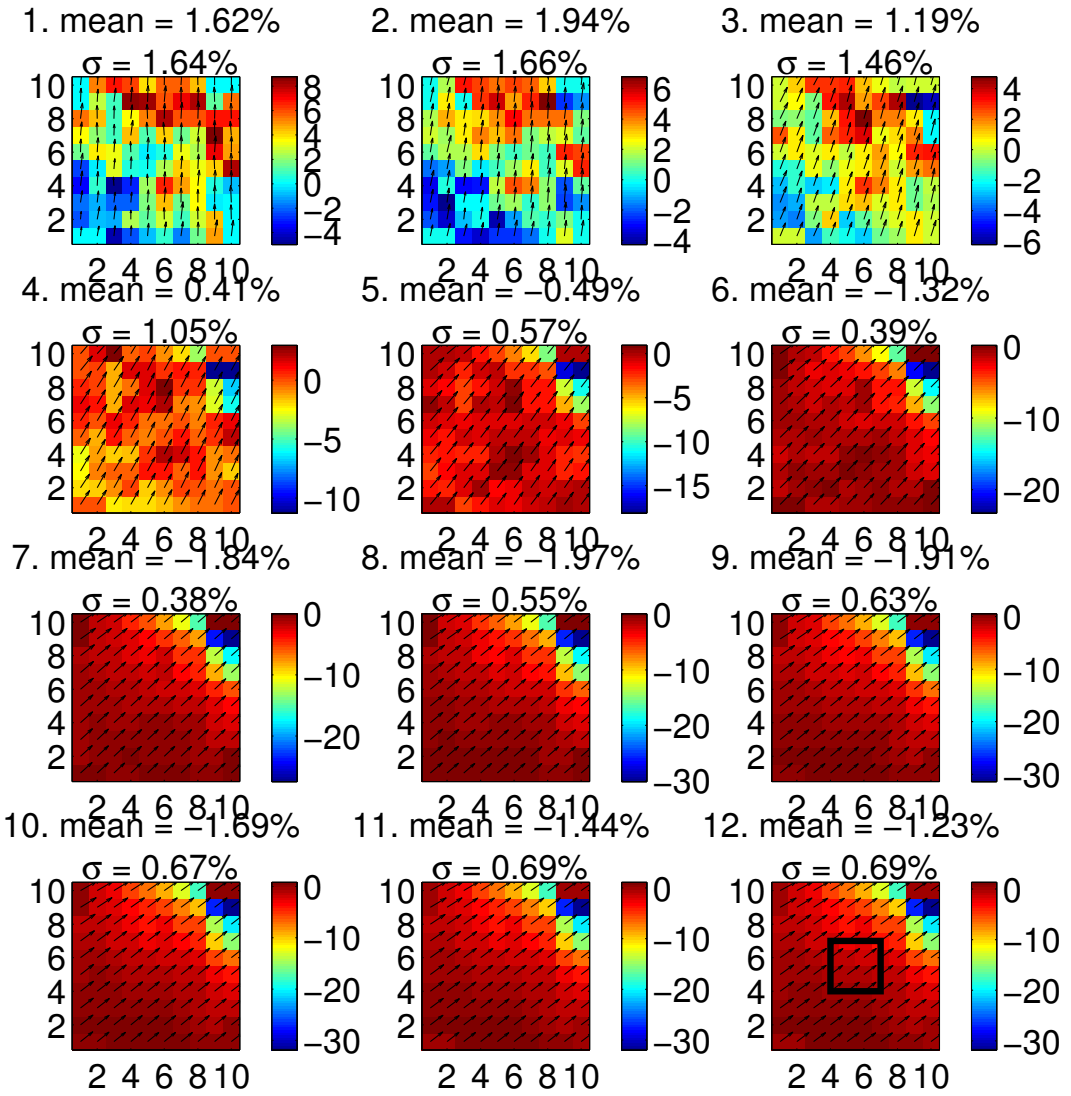


Figure 6.19: Degree of circular polarisation found using a registration method by science data points. The mean and  $\sigma$  values are given in the title of each flat. The image has been flipped and rotated compared to the images in Figure 6.13 to match the telescope correction. The  $\sigma$  value refers to the random and systematic error over the FOV of interest in Figure 6.13 for the  $3 \times 3$  pixel area indicated by the rectangle on the final image.

---

Table 6.6: Mean polarimetric results for Zenith flat-field data using a pixel-by-pixel analysis for the  $3 \times 3$  pixel area in the final image of each polarimetric measurement. The  $\Delta PA$  values are also given.

<b>Flat-field</b>	<b>1</b>	<b>2</b>	<b>3</b>	<b>4</b>	<b>5</b>	<b>6</b>	<b>7</b>	<b>8</b>	<b>9</b>	<b>10</b>	<b>11</b>	<b>12</b>
Time (mins)	0.47	2.45	5.75	9.05	12.35	15.65	18.95	22.25	25.55	28.85	32.15	35.55
DOLP (%)	35.63	35.17	31.71	35.67	44.36	57.40	69.63	79.23	84.10	86.01	87.93	90.02
DOCP (%)	1.62	1.94	1.19	0.41	-0.49	-1.32	-1.84	-1.97	-1.91	-1.69	-1.44	-1.23
PA ( $^{\circ}$ )	88.92	84.29	73.23	62.55	52.55	45.67	42.57	40.61	39.25	38.09	37.07	36.24
$\Delta PA$ ( $^{\circ}$ )	-	4.63	11.06	10.68	10.00	6.88	3.10	1.96	1.36	1.16	1.02	0.83

It is concluded that an error in the calibration in this area of the field, which is mostly likely a result of registration, has not been capable of removing this pattern in the reconstructed degree of circular polarisation. The results in Table 6.6 are measurements of the mean in the highlighted  $3 \times 3$  pixel area in the final image of each polarimetric measurement. A variation in the polarisation angle of  $\sim 52^{\circ}$  over the course of the observation. Realistically, this value should be measured for when there are less influences from random variations as a result of detector noise. There appears to be a significant increase in the light level at frames 5 - 6, which gives a change in the PA of  $\sim 7^{\circ}$ . This is higher than expected for the length of time this data block represents. The lowest frame-to-frame variation in PA observed is  $0.83 \pm 0.10^{\circ}$ <sup>7</sup>. The  $\Delta PA$  value is decreasing over time, approaching  $0.83^{\circ}$ . This measured value is close to the expected value for this time block. The expected variation is  $0.71^{\circ}$ . It is possible that if more data was recorded that this value would eventually be reached. A decrease in the change in polarisation angle over time has been found. The full set of data is presented here; however if data had been recorded for a further 10 - 30 minutes this value could reach a terminal value for  $\Delta PA$ . It is possible that this measurement is dependent on a high level of counts per pixel, and that when frame 7 or frame 8 is reached, there are enough

---

<sup>7</sup>Errors quoted are based on the Poissonian statistics for the  $3 \times 3$  pixel area

---

photons to overcome the noise floor of the detector.

The value for the DOLP increases in value between frames 4 - 9, where there is a significant change in light level. However, the  $\Delta$  value, frame-to-frame, for the DOLP reaches a terminal value between frames 9 and 10. From frame 9 onwards, the  $\Delta$ DOLP is 2%. It is still uncertain, from a limited set of data over time, whether this value would continue to grow at this speed. The trend in DOLP over time, and as a function of PA is in good agreement with the Rayleigh Sky Model. The difficulty in measuring low levels of DOLP has been discussed in Section 6.2. In this analysis it is clear that the initial measurements for the DOLP are mostly at the noise level, which will cause the polarisation to be overestimated.

A similar trend is found for the DOCP. The measured value changes by 1 - 2% around the expected value of 0%, eventually converging at 0%. This value changes slowly, by 0.2% in the final frames reaching a value of  $-1.23 \pm 0.3\%$ . A combined result of both random and systematic error in the initial frames could cause this behaviour; however, these errors are difficult to discern. However, each polarimetric measurement is producing results indicating that GASP is working. There is a possibility that, there is a limitation in the instrument in terms of variability over the FOV, however, there are remaining errors for image registration, and the calibration matrix is a good representation of where this error is derived. The results of the pixel-by-pixel analysis are mostly positive in terms of the values measured and that there is reason to suspect that a more uniform measurement could be obtained with improved registration analysis.

An important remark, which could indicate discrepancies during analysis of this data, is that GASP was calibrated along its calibration axis by reconstructing the Mueller matrix ECM samples. This analysis was reproduced on a set of Zenith flat-fields. It was found that the science axis and calibration axis do not match exactly, but this could be overcome using image binning. It was also considered that if registration is performed a second time, using the artefacts in both RP1 science and RP1 calibration, it would account for this variation; however, it has not significantly altered the polarimetric results compared to registering only by science data points. The reason for this is clear by the results of registration found in Table 6.4.

The variation found (over the entire FOV) in each of the polarimetric results

---

are within the error limitations in misregistration outlined by Smith et al. (1999). It is also noted that, if the FOV area chosen was moved a number of pixels up in y, and to the left in x, it may be possible to reduce the pattern effect in the bottom right corner of the field found in all polarimetric results.

### 6.3.2 Science Data Aperture Photometry Analysis

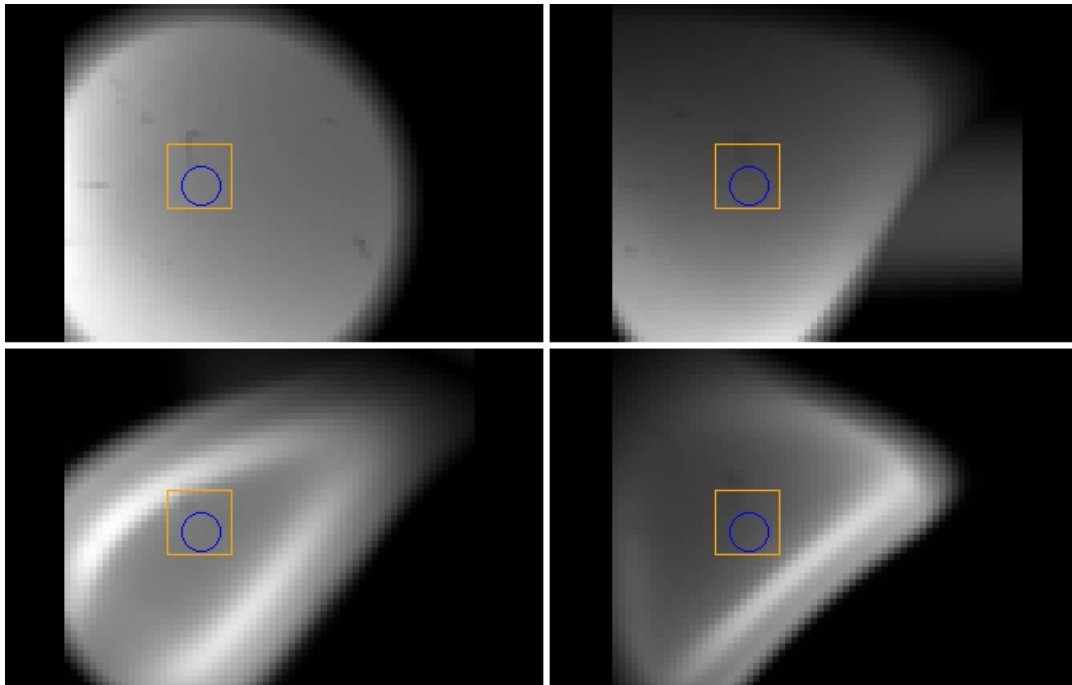


Figure 6.20: All registered GASP channels for a full flat-field frame using science data points and image artefacts. The chosen FOV is indicated by the orange box. The blue aperture was selected for aperture photometry analysis as it had a uniform (flat) distribution of flux on each channel. The radial size of the aperture is 3 pixels ( $5''$ ). Top LHS: RP1, top RHS: RP2, bottom LHS: TP1 and bottom RHS: TP2.

In addition to the registration outlined above, a set of coordinates were obtained for data recorded of the Crab pulsar (without any binning) and an area of the field was chosen with this at the centre that allowed  $4 \times 4$  binning. An aperture was then selected that covered a radial FOV of interest, the analysis of which will be presented below. This approach was chosen to avoid/reduce the clear systematic

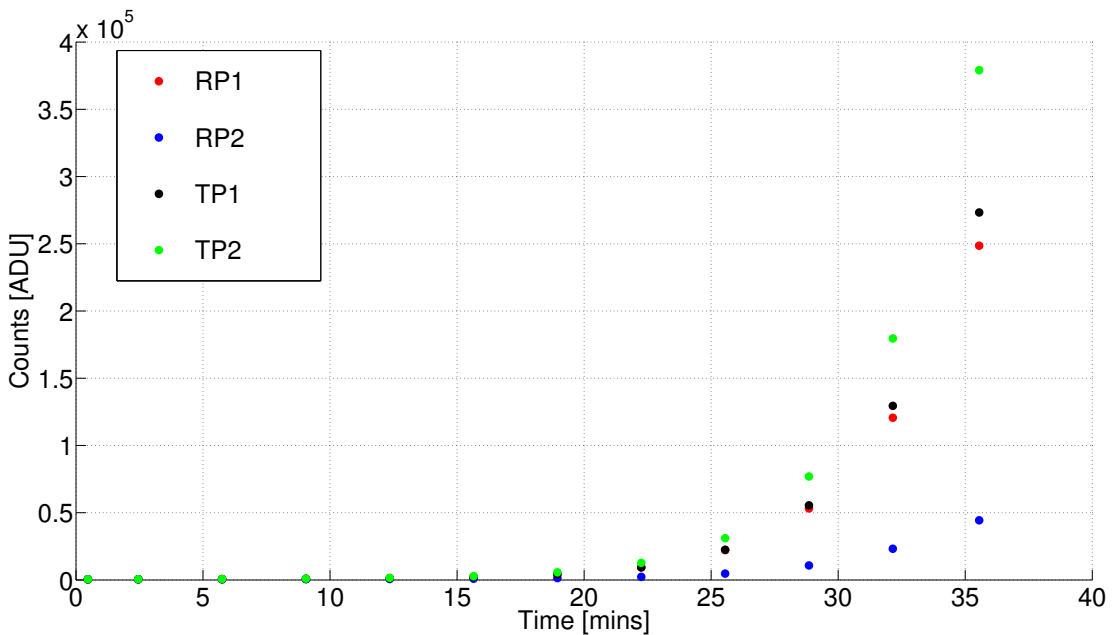


Figure 6.21: The raw intensities, after bias subtraction and registration, for each GASP channel as a function of time. The light level is low (no significant Sunlight) for the first 4 - 5 frames on each channel. The values measured range from 500 to 900 counts,  $\sim 2 - 3$  times that of the bias level. These data values are extracted from a set of data that have been averaged in time according to the values in Table 6.5. It is assumed that the intensity value is an average value for that data set and represents the value at the midway point of the recorded data. This plot is produced using the blue aperture in Figure 6.20 and uses a 3 pixel radial aperture, which corresponds to a FOV of 5".

error evident in the pixel-by-pixel analysis above. This same set of coordinates and size aperture were used on calibration data images to produce a calibrated matrix for Stokes reduction. This aperture can be found in Figure 6.20.

The raw data plots for this 3 pixel radial aperture are displayed in Figure 6.21. This is a plot of the change in intensity as a function of time (see Table 6.5), over a 35 minute period at twilight, as the Sun was rising.

It is observed that each of the TP channels show little variation compared to each other; this is expected for low levels of DOCP when the calibration gain variations are examined. Taking an example of a linear polariser (which theoretically should yield a DOLP result of 100%), depending on the azimuthal angle of the polariser, a result of 100% linear polarisation will always be obtained. Figure 6.22

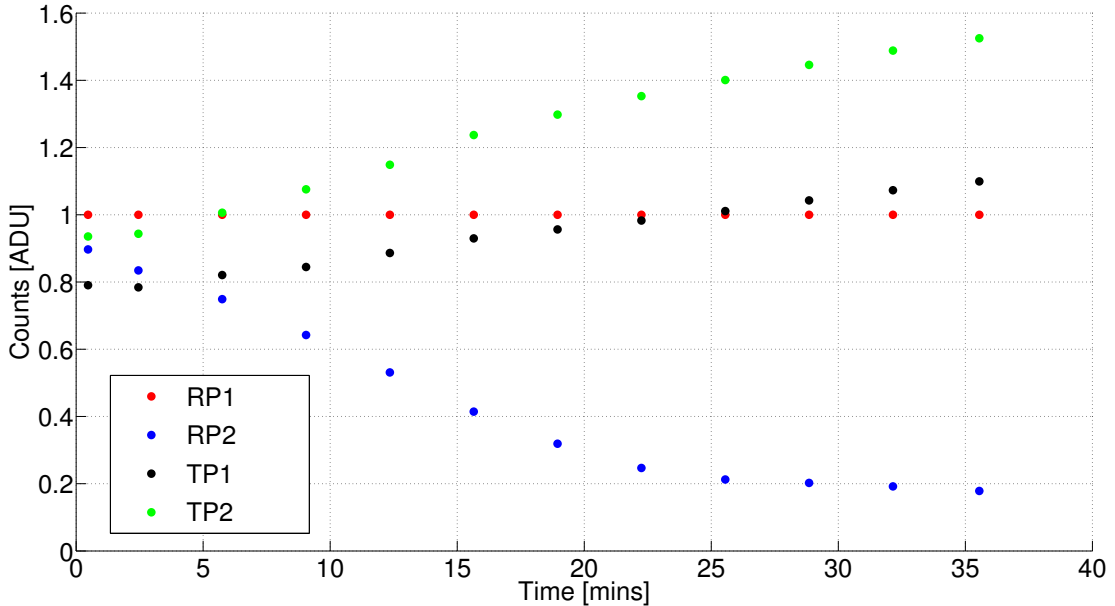


Figure 6.22: The raw intensities from Figure 6.21 after each channel is normalised to RP1 channel. This data refers to the blue aperture in Figure 6.20 and uses a 3 pixel radial aperture, which corresponds to a FOV of 5".

is a normalised version of this plot to better describe the relative rate of change. The measured intensity on each RP channel can be varied with respect to each other by rotating the polariser itself, or the entire GASP instrument. However, if the DOLP increases over time this is a result of the absolute angle that the Sun makes with the Zenith. Depending on the orientation of GASP, RP1 and RP2 channel will measure the orthogonal components of the polarised beam; depending on this azimuthal angle it cannot be assumed that each RP channel will increase in intensity at the same rate.

### Polarimetric Results: 3 pixel radius

Figure 6.21 is a plot of the change in intensity as a function of times (see Table 6.5), over a 35 minute period at twilight.. This data was plotted for aperture #1 in Figure 6.20. Referring back to the plot in Figure 6.21, which plots the raw intensities for each of the 4 GASP channels; these values are found using

aperture photometry for a 5" FOV after bias subtraction and image registration. It is found that from frame 1 - 4 the light level is low and displays little variation until frame 5, where the counts (ADU) are (on average) greater than 1000. It is possible that with light levels as low as these that extracting a polarimetric signal may be difficult due to a combination of random and systematic error. The values measured are 2 - 3 times that of the bias level. These data values are extracted from a set of data that have been averaged in time according to the values in Table 6.5. It is assumed that the intensity value is an average value for that data set and represents the value at the midway point of the recorded data.

Figure 6.23 is a plot of the change in DOLP, DOCP, and PA over the same period as that for Figure 6.21.

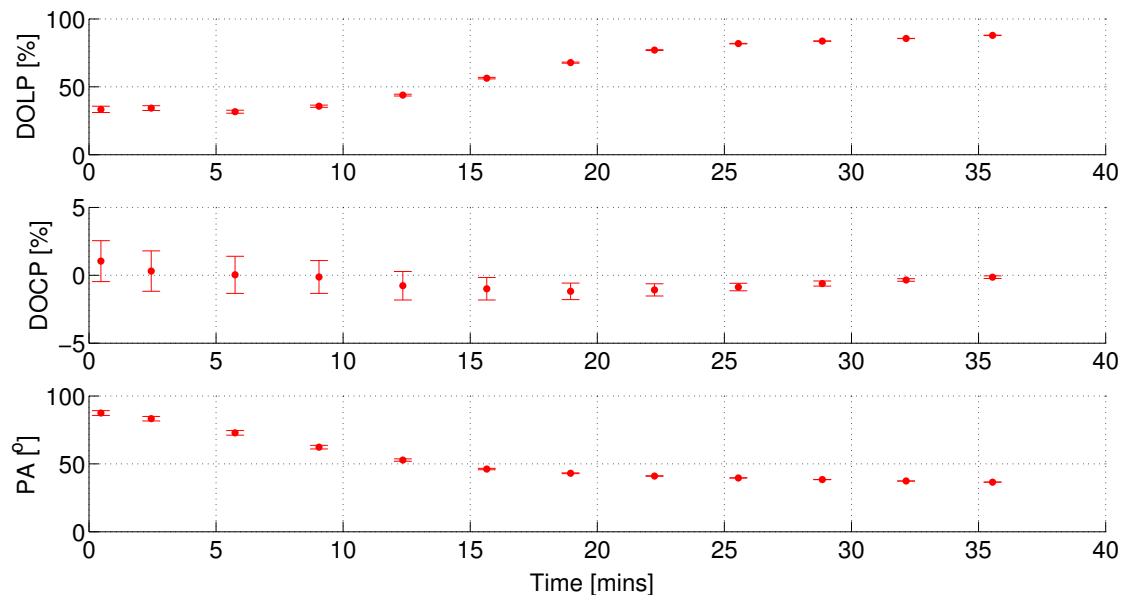


Figure 6.23: Degree of linear and circular polarisation and polarisation angle values found using a registration method by science data points. The x axis is the value for elapsed time according to the image time-stamps. This is a plot of the variation of each of these polarimetric values for each flat-field. It is assumed that the polarimetric value is an average value for that data set and represents the value at the midway point of the recorded data. This data refers to the blue aperture in Figure 6.20 and uses a 3 pixel radial aperture, which corresponds to a FOV of 5".

The x axis values are plotted in minutes and indicate the time midway through the recording of that data block. The values for each data point can be found in

---

Table 6.7. It is assumed that the polarimetric information found is that at the halfway stage of recording that data block, i.e. it measures the mean value of that time block. The error bars show clearly that the first half of the data is dominated by low SNR. The polarisation angle measurements have been corrected for telescope orientation. The PA varies as expected if compared to Figure 6.16. The angle plotted on the x axis of this figure is equal to  $90^\circ - PA$ .

Table 6.7: Mean polarimetric results for Zenith flat-field data using a method of aperture photometry for a 3 pixel radial aperture.

<b>Flat-field</b>	<b>1</b>	<b>2</b>	<b>3</b>	<b>4</b>	<b>5</b>	<b>6</b>	<b>7</b>	<b>8</b>	<b>9</b>	<b>10</b>	<b>11</b>	<b>12</b>
Time (mins)	0.47	2.45	5.75	9.05	12.35	15.65	18.95	22.25	25.55	28.85	32.15	35.55
DOLP (%)	33.38	34.30	31.66	35.72	43.91	56.36	67.81	77.06	81.83	83.68	85.59	87.86
DOCP (%)	1.05	0.31	0.03	-0.12	-0.77	-0.99	-1.18	-1.08	-0.87	-0.61	-0.35	-0.14
PA ( $^\circ$ )	87.46	83.29	72.82	62.29	52.78	46.14	43.06	41.02	39.62	38.45	37.39	36.52
$\Delta PA$ ( $^\circ$ )	-	4.17	10.47	10.53	9.51	6.64	3.08	2.04	1.39	1.17	1.06	0.87

The results in Table 6.7 show that variation can be found in the polarisation angle over time to be  $35^\circ$ . Again, this value should be measured for when random variations appear to be overcome by an increase in light hitting the detector. The light level between frame 4 and 5 gives a change in the PA of 7, and the lowest frame-to-frame variation in PA observed is  $0.87 \pm 0.03^\circ$ ,  $\sim 0.16^\circ$  from the expected. In the case of the pixel-by-pixel analysis, the same concern exists. There is a variation in the PA, which is difficult to disentangle from random noise fluctuations, however, the same trend is found; as the light increases (more photons hitting the detector) the value for  $\Delta PA$  starts to reach a terminal value - it is decreasing faster. If more data was acquired this trend could be more conclusive. The final value for  $\Delta PA$  has shown a degradation here compared to a pixel-by-pixel approach. The expected value is  $0.71^\circ$ , however, GASP is showing that perhaps in the absence of random error (where higher SNR is achieved), this value could

decrease further. It is assumed that the data recorded by GASP is a mean value of the images recorded for the time period indicated and have to be plotted this way in Figure 6.23. The low SNR is evident from the error bars and this will also be the error on  $\Delta\theta$  as a function of time.

The value for the DOLP and the PA, using aperture photometry, is comparable to the pixel-by-pixel method showing minimal change. The value of the measured DOLP by aperture photometry, like that for a pixel-by-pixel method, appears to reach a terminal  $\Delta$  value at frame 9. It was expected that, the value for  $\Delta$ PA would reduce, by averaging a smaller area of the FOV. The variation found for both methods of analysis is higher than expected for this time block. The value of the DOLP at these recorded times is not known, however, the DOLP is varying with the same mean as that of the pixel-by-pixel analysis. The DOCP also shows variation, however, it is approaching 0%. There is some improvement over a pixel-by-pixel analysis approach.

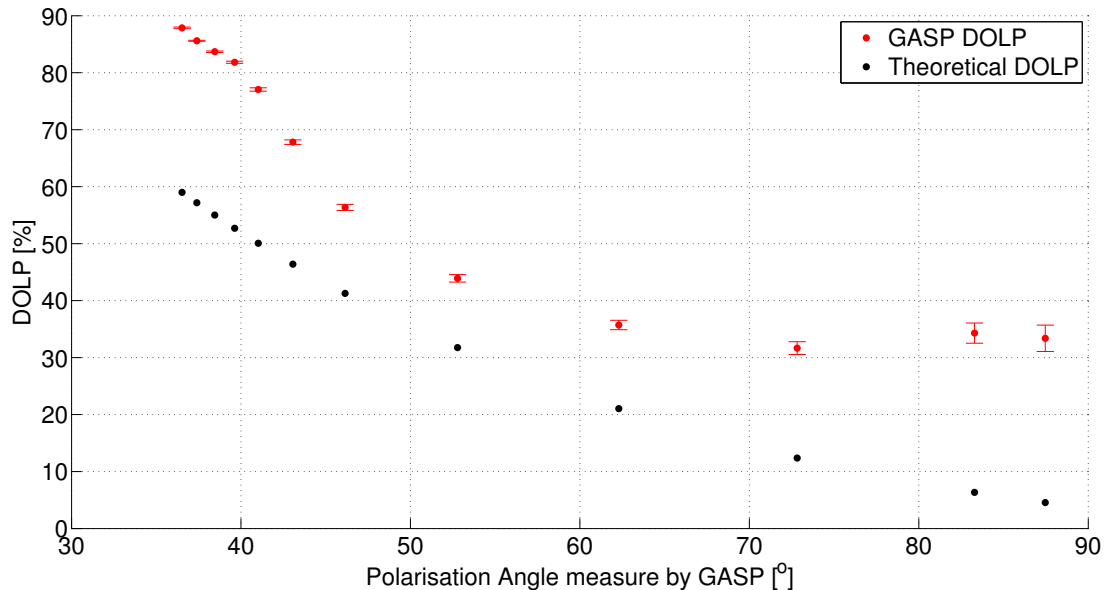


Figure 6.24: Degree of linear polarisation as a function of polarisation angle measured by GASP. The theoretical plot is generated by Equation 6.4 where  $\gamma = 90^\circ - \text{GASP PA}$ .

Figure 6.24 is plotted to test how accurately GASP has measured the DOLP assuming the polarisation angle is correct. The polarisation angle is not calcu-

---

lated using Stokes I and is therefore not related to intensity variations. It will be affected by low SNR or atmospheric turbulence. The residuals are large  $\sim 20\%$ . It is possibly an effect of the instrumental polarisation, which could have changed throughout the night. As in the case of measuring 0% polarisation, the polarisation will also be overestimated approaching 100% polarisation. The theoretical plot is based on the Rayleigh Sky Model in the absence of random and systematic error. It is also possible that the polarimetric signal measured by GASP includes polarisation from light other than that which has been Rayleigh scattered.

## 6.4 Concluding Remarks

A set of Zenith flat-fields were recorded on observation Night 4 at the Palomar 200 inch telescope. The image analysis, including registration techniques developed, in Chapter 5 were used in this chapter. It was found that registration using science data points gave a better calibration solution and this method was carried through to science analysis.

The results found in this chapter indicate that there are remaining errors in the spatial registration using science data points; this is evident in the spatially reconstructed Stokes analysis for the Zenith flat-fields, after bench calibration. If pixel-matching (or indeed position matching) is not exact, the ECM will not work to great effect. The calibration data has been registered using science data positions and using image artefacts between RP1 science to RP1 calibration. The overall pixel variation across a small FOV ( $10 \times 10$  pixels, or  $6 \times 6''$ ) is expected to appear flat, polarimetrically, where the pixel-to-pixel variation is expected to be no higher than the random errors on each pixel. The pixel-by-pixel polarimetric results in this chapter, in a small suitable area of the FOV (with minimal distortion), show stable pixel-to-pixel measurements for the DOLP, DOCP, and PA.

Errors in registration will lead to errors in measured values for DOLP and DOCP across the larger FOV. The registration results in this work have been compared to a publication by Smith et al. (1999) whereby, if pixel errors of 1.2 pixels are found from combined registration error in all GASP channels, this could result in  $\sim 10\%$  error in the DOLP and DOCP, worst case. An error for the PA

---

has not been stated by the authors, but it is expected. Variation of this order has been observed in the GASP system, which indicates that the errors found in image registration can explain the variation in the polarimetric results obtained using a pixel-by-pixel calibration method. This is also noted in the systematic patterns found in the images for the DOLP, DOCP, and the PA. The variation in the PA was found to match very well with the expected from the theoretical plots of DOLP versus scattering angle. The lowest  $\Delta$ PA observed was found to be  $0.83 \pm 0.03^\circ$ ; the  $\Delta$ PA value is approaching this  $0.83 \pm 0.03^\circ$  over time, where the expected value in this time block is expected to be  $0.71^\circ$ . The polarimetric measurement appears to be intensity dependent and low SNR for the initial frames give large errors on the PA measurements. Further observations are required, with larger SNR intensity measurements. Error in registration has lead to an error in obtaining more conclusive spatial polarimetric results.

The trend observed in Figure 6.16, of DOLP versus scattering angle, can be used as a first order check. The DOLP varies as a function of scattered angle. The reverse trend is found for DOLP versus PA. If the exact PA is known the DOLP can be calculated. If further observational data were obtained, the  $\Delta$ DOLP ( $\sim 2\%$ ) could eventually reach 100%. The behaviour of the DOCP is a little stranger. It approaches 0 and passes through this value, resulting in a mean value of  $\sim 2\%$ . Errors in registration of TP2 have been discussed as a reasonable source to this discrepancy.

Another analysis approach was explored using aperture photometry, which can be found in Figure 6.20. The results of this analysis show some disimprovement in the expected value for the  $\Delta$ PA when a small area is selected and the intensity is averaged. However, an improved result for the DOCP was found where it approaches a zero value as the sky brightens, though in both analyses the DOCP shows variation over time. There is a variation in the spatial polarimetric results from this data set. An aperture was selected in an area that was uniform in intensity and compared to a pixel-by-pixel analysis. Based on this observation if another aperture in a different location was selected, it could/not lead to an improvement in the polarimetric measurements.

Any remaining error comes from registration in the calibration data, which is currently at its limit. This is also true when matching calibration data to

---

science data in terms of pixels. If this step of the analysis is incorrect, then further systematic error will be introduced to the final polarimetric result. The science data can be well registered inside the already accepted parameters of the current registration solution (see *geomap* RMS values in Tables 5.3 and 5.9). It is concluded that the registration solution used in this analysis was sufficient to perform accurate polarimetric analysis.

It is concluded that the Zenith flat-field polarimetric results (using a calibrated instrument) have shown that GASP has measured meaningful, time varied values for the PA, where remaining errors have been explored in the discussion above. The experimental DOLP follows the same trend as the expected theoretical DOLP as a function of either the scattered or polarisation angle. Using aperture photometry has proven that it is possible to reduce the effects of error in registration to measure a value that approaches 100% as the Sun rises. The results of the analysis have shown that GASP is clearly capable of measuring a changing polarimetric signal with SNR error limits.

---

# Chapter 7

# Observation Results for the Crab Pulsar

## 7.1 Introduction

This chapter will present an analysis of the Crab Nebula and the visible targets observed on the fourth night of observation at the 200 inch telescope on Palomar Mountain. The analysis was carried out using aperture photometry and will be compared to the results found in the literature, which can be found in Table 7.2.

GASP observed the Crab Nebula in R Band using full frame data. The pulsar and a nearby star, Trimble 28, were also observed at a frame rate  $> 1000$  fps. The observing specifications for these data sets can be found in Table 7.1.

Table 7.1: Observational logs summary for the Crab Pulsar observed by GASP on Night 4.

Data set	Filter	Exp Times (s)	EM gain	Temperature <sup>1</sup> (°C)	# Frames	UT recorded
Integrated	R	30	10	- 85	10	13: 06: 23
1000 fps	V	0.00074	300	- 60	1000000	11: 57: 00

The polarimetric reductions in this chapter follow the same procedure outlined in Chapter 6. The data is binned  $4 \times 4$  to reduce any remaining scaling/distortion

---

<sup>1</sup>Refers to stabilised temperature reading from FITS header.

---

after image registration. The calibration result produced in Section 5.10.2 were successful using a registration technique with science data points and this result is used in Equation 6.1. A pixel-by-pixel analysis is not carried out in this chapter. It was found that there were errors in a pixel-by-pixel calibration analysis after image registration. These errors will propagate through to the polarimetric analysis on science data. However, the optical resolution of the instrument was not sufficient to carry out any spatial polarimetry measurements. Aperture photometry is used to perform Stokes reductions, using the same methods in Chapter 6.

Table 7.2: Integrated polarimetric information from the literature for the Crab Nebula. The pulsar has a magnitude of 16.5.

Target	Filter	DOLP (%)	PA (°)	Ref
Crab pulsar	V	$5.2 \pm 0.3$	$105.1 \pm 1.6$	Moran et al. (2013) <sup>2</sup>
Trimble 28	V	$1.6 \pm 0.2$	$147.5 \pm 3.7$	Moran et al. (2013)
Crab pulsar	V	$5.4 \pm 0.1$	$96.4 \pm 0.2$	Słowińska et al. (2009) <sup>3</sup>
Crab pulsar & Knot	IR	$9.8 \pm 0.1$	$109.5 \pm 0.2$	Słowińska et al. (2009)

## 7.2 Polarisation of the Crab Pulsar: Integrated Data

An image of the Crab Nebula is found in Figure 7.1. A radial aperture was chosen equal to the FWHM of the target, where over 80% of the light is found. Little variation in the polarimetric measurements was found as a function of changing radial aperture. It is noted that, in the case of the nebula, an aperture size of 3 pixels contains photons from the pulsar and Trimble 28. However, this was the only possible available area of the FOV that was well registered on all channels. The

---

<sup>2</sup>Integrated data.

<sup>3</sup>Phase averaged.

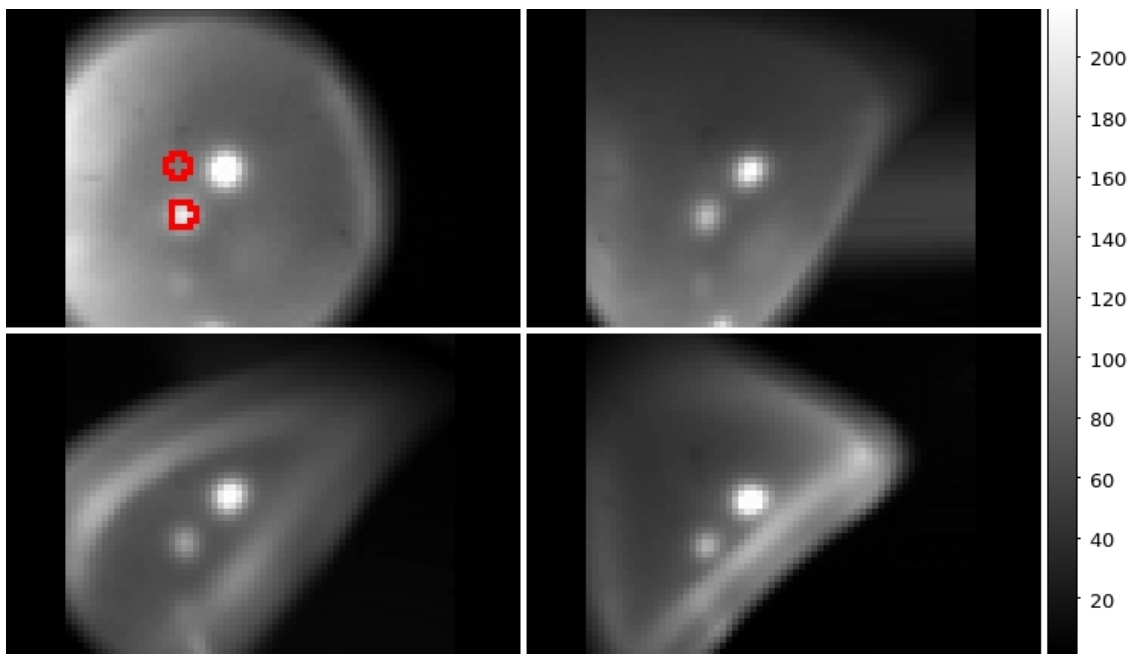


Figure 7.1: The location of the apertures used in photometry, for the pulsar and nebula, are shown in red. The polarimetric information of the Crab pulsar and nebula will be analysed at these points. The data has been registered and binned  $4 \times 4$ . This data was recorded at the end of the night, before the Zenith flat-fields. The aperture in this plot has a 2 pixel radius. Top LHS: RP1, top RHS: RP2, bottom LHS: TP1 and bottom RHS: TP2.

radial plots for the pulsar and Trimble 28 can be found in Figure 7.2. The radial profile plot, for both targets, indicate that the wings extend into the area where the aperture of the nebula is taken. These plots also show that the wings of the targets themselves are bleeding into each other. This could lead to contamination of a more weakly polarised signal, as is the case for the pulsar and the nearby Knot.

The radial profiles of both the pulsar and Trimble 28 can be found in Figure 7.2.

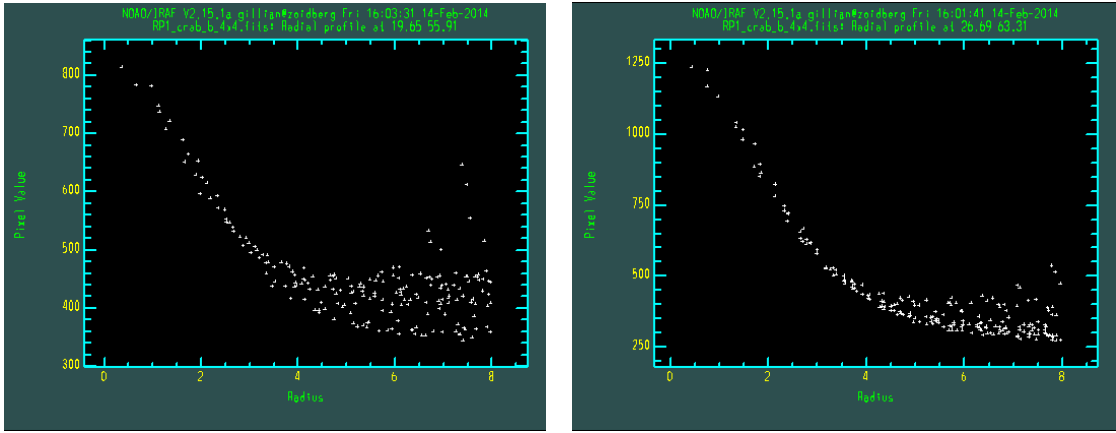


Figure 7.2: A radial profile plot for the Crab pulsar (LHS) and Trimble 28 (RHS) for the registered RP1 image. This image is found in Figure 7.1. The wings of the profile appear to lie exactly in the area occupied by the nebula and it is therefore difficult to distinguish between nebula and overlapping targets. It is also true to say that the wings of each target extend into the aperture of the nearby target.

The results of the pulsar are comparable to those found by Słowikowska et al. (2009) and Moran et al. (2013), found in Table 6.1. It has been found by Moran et al. (2013) (private communication) and Weisskopf et al. (1978) that the expected DOLP and PA of the nebula are in the range of 15 - 20% and  $\sim 150^\circ$ , respectively. The GASP results for the pulsar and the nebula are close to the expected, however, the angle of the nebula is much lower. This signal is most likely a combination of nebula and sky and it is not possible to remove the sky background from this data. The DOCP is not known at this time.

It is also important to note that Trimble 28 may be located behind the nebula and this could lead to a circular polarisation measurement. This is not a measurement that has been previously recorded in the literature. The location in the field is also important - the area covered by each of these targets is in the field shown in Figure 7.1. The area for the target, which measures the polarimetric information for the nebula does not cover an area occupied by the Wisps measured by Moran et al. (2013).

As both the Crab pulsar and the surrounding nebula are polarised, it is difficult to determine a suitable location in which to take a measurement of the nebula. Image registration was found to be variable in the field and polarimetric measure-

---

ments of Trimble 28 (expected DOLP of 2% with a space based telescope) and the nebula (expected DOLP of 15 - 20%). However, the polarimetric measurements for the Crab pulsar agree well with what both Słowińska et al. (2009) and Moran et al. (2013) have found. The pulsar PA, measured by GASP, is not in agreement with these authors. It is found to have changed by 15°.

Sky subtraction was not carried out on this data set. It was not possible to select an annulus and dannulus around both the pulsar and Trimble 28 (the other star in the field, top right of the pulsar) that did not overlap the nearby star. If a larger annulus was chosen this would sample non-calibrated sections of the FOV from each TP image. This sections can be seen from the banding on the upper LHS of TP1, and the lower RHS of TP2. It was also not possible to find a flat section of sky that was common to all channels, for sky subtraction. It is believed that the background FOV is composed of counts from both sky, nebula, and any atmospheric turbulence on the night. It is therefore difficult to separate a sky background measurement from a nebula measurement. It has been discussed that the PA of the nebula does not match with the expected value. It is thought that this data is not only measuring the nebula, but a combination of sky background and flux from the nearby targets.

Table 7.3: Polarimetric information for each of the targets indicated in Figure 7.1. A radial aperture equal to the FWHM was used, however, any variation caused by seeing/atmosphere must be taken into account when making comparisons to the literature.

Target	Aperture Size (pixels)	DOLP (%)	DOCP (%)	PA (°)
Crab Pulsar	2	$9.55 \pm 0.53$	$-1.23 \pm 0.40$	$85.26 \pm 1.40$
Trimble 28	3	$6.54 \pm 0.30$	$-5.56 \pm 0.45$	$60.89 \pm 2.68$
Nebula	3	$10.42 \pm 0.49$	$-6.00 \pm 0.80$	$55.98 \pm 2.77$

---

### 7.2.1 Concluding Remarks

The results of these data are not fully conclusive regarding Trimble 28 and the section of nebula analysed. There are no measurements for DOCP in the literature for the Crab Nebula. The DOCP value for Trimble 28 and the nebula are closely matched, which could indicate that the nebula is circularly polarised and that Trimble 28 is located behind the nebula. The linear polarisation measurement is higher than expected by 3 - 4% compared to work by Moran et al. (2013). If there is light contamination from the pulsar, this will also affect the polarisation angle.

In the case of an instrumental polarisation effect for the pulsar and Trimble 28, the target HD12021 is used for the R Band filter. The Crab pulsar & Knot result from Słowińska et al. (2009) is used as the expected measurement. Using Equation 6.2 a DOLP value of 10.23% is calculated, which is in good agreement with the actual value of 9.55% measured by GASP. This indicates that the polarimetric measurements for the Crab pulsar are found not be largely affected by instrumental polarisation, mostly likely as the pulsar is strongly polarised compared to a zero polarisation standard. The same analysis is performed for Trimble 28. The result for Trimble 28 is unclear as the expected value measured by Moran et al. (2013) is less than the instrumental polarisation from HD12021. This indicates that it is likely that the instrumental polarisation has changed. As this is the only known polarimetric measurement for Trimble 28, it cannot be used as a zero or low level polarisation standard. However, if the instrumental polarisation from HD12021 is used Equation 6.3 must be used and a value of 0.1% is determined.

## 7.3 Polarisation of the Crab Pulsar: Phase Resolved Data

Figure 7.3 are images of each channel for the phase-averaged data. In particular, it is noted that the level of extension of the wings of the Crab are quite high. A number of data sets were recorded of the Crab pulsar at a frame rate  $> 1000$  fps. One of these data sets will be examined in this section. Observational information for this data can be found in Table 7.1

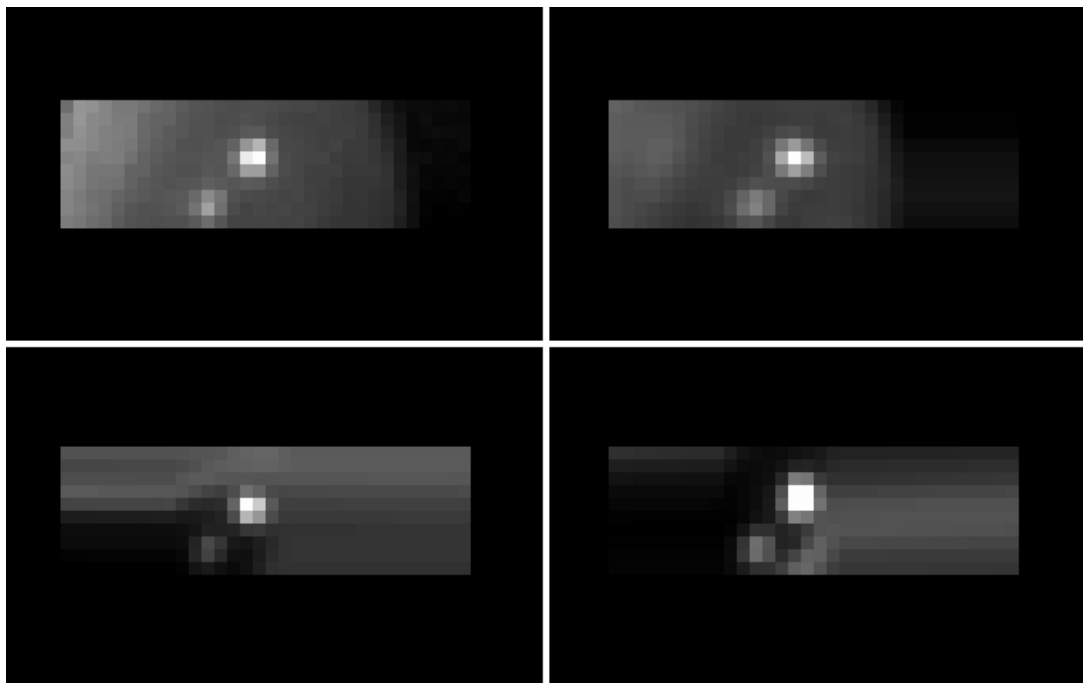


Figure 7.3: Each image, on each channel, is summed and averaged for 200,000 images for an exposure time of 0.00074 seconds. Each registered channel contains the Crab pulsar and Trimble 28. A 1.5 pixel radial aperture was used to obtain polarimetric information for the Crab pulsar, and Trimble 28. This data was binned  $8 \times 8$  and windowed during acquisition. Top LHS: RP1, top RHS: RP2, bottom LHS: TP1 and bottom RHS: TP2.

### 7.3.1 EM Gain & Bias Level

The bias acquired for the 1000 fps data used the same acquisition parameters as that for its respective science data. This data has been taken at a frame rate of  $\sim 1100$  Hz, with an exposure time, per frame, of 0.00074 seconds and an EM gain of 300. The master bias was created using 1000 bias frames, which have been averaged using a pixel rejection routine with a  $\sigma$  level of 0.5. It is noted that there is a temporal instability, which can occur in the iXon Ultra 897 EM detectors when acquiring data. It is due to small changes in heat generation of the driving electronics within the detector head and can cause some drift in the bias level. It is noted in the Andor literature that this is often particularly observable during long kinetic series. Andor claim that any drift in the bias level can be corrected by using the Baseline Clamp option. Baseline Clamp corrects each individual image for any

---

bias drift by subtracting an average bias signal from each image pixel and then adding a fixed value to ensure that the displayed signal level is always a positive number of counts. As such, the bias is expected to remain at steady value during a fast kinetic series. This can be shown in Technology (2013). It is also noted that bias level is susceptible to variation at different EM gain settings, however, the iXon Baseline Clamp corrects for this, ensuring the bias level is clamped no matter what EM gain setting is selected. The expected performance is noted, however, some variation from this ideal detector behaviour was found for a set of data recorded by GASP.

When data acquisition began the TP detector took some time to achieve stability. The temperature could not be maintained at the optimum level of  $-90^{\circ}\text{C}$ ; a level of  $-60^{\circ}\text{C}$  gave more consistent results. The first 10,000 frames (approximately) recorded noise due to this instability.

The raw data was analysed using photon counting analysis methods to measure the EM gain at different positions in each path over time. The inverse-slope measurement used by, Mackay et al. (2010), was implemented on GASP data.

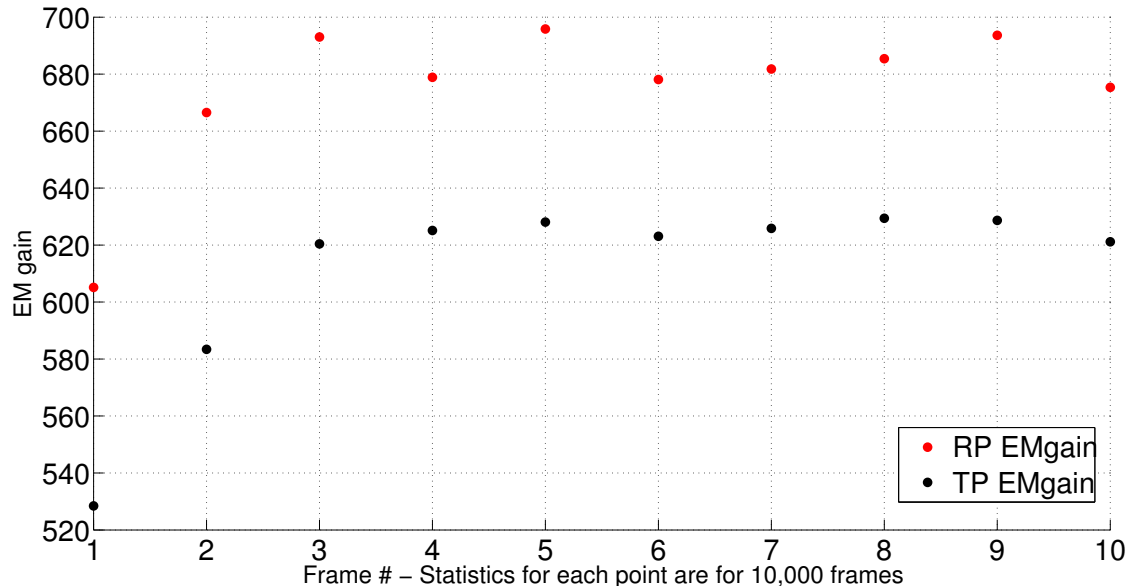


Figure 7.4: This is a plot of the variation in EM gain over the duration of each data set per GASP path. The RP:TP EM gain is 1.1:1. Each detector was set to an EM gain of 300.

---

Figure 7.4 plots the variation in EM gain for both GASP paths as a function of time. It is clear that the measured EM gain by the inverse-slope method is not measuring the EM gain assumed during acquisition. The EM gain measurement from both detectors become more stable over time, however, there is a disparity in measured gain between both cameras. The measured EM gain on the RP detector is 1.1 times higher than that of the TP detector. This could occur for a number of reasons:

- Temperature fluctuations and instabilities. The temperature recorded in the image header file is taken at the beginning of acquisition, however, the temperature throughout may have not remained stable over time. The EM gain requires a particular temperature in order to work optimally.
- The TP camera displayed signs of failing to acquire sensible data at the beginning of acquisition. This could be a sign of difficulty in maintaining a high frame rate of 1100 Hz.

Another observation from this data is bias variation. The following plots show the inverse-slow method implemented for this GASP data. Figure 7.5 is a pixel count frequency distribution for a set of 10,000 images at the beginning of acquisition for the RP detector. The bias level is found from the peak value of the curve on the LHS. A trendline is fitted to the data and the inverse of the slope gives the EM gain for this data block.

The RP detector was found to remain relatively stable regarding bias level. The EM gain grows over time, eventually reaching stability. The TP detector shows some inconsistencies when compared to the RP detector. The problem of the variable EM gain has been addressed in Figure 7.4 where an offset was found compared to that set in software, and compared to the RP detector. However, the TP detector bias level was also found to vary over time.

Figure 7.6, like Figure 7.5, shows the EM gain and bias level for three blocks each using 10,000 science frames. The detector bias level was found to vary over the times series for this detector. The first block shows a bias level of 175 ADU. This is not expected from the data based on laboratory tests. At the midpoint of acquisition, the analysis found the bias level to drop by 40%. This is a considerable

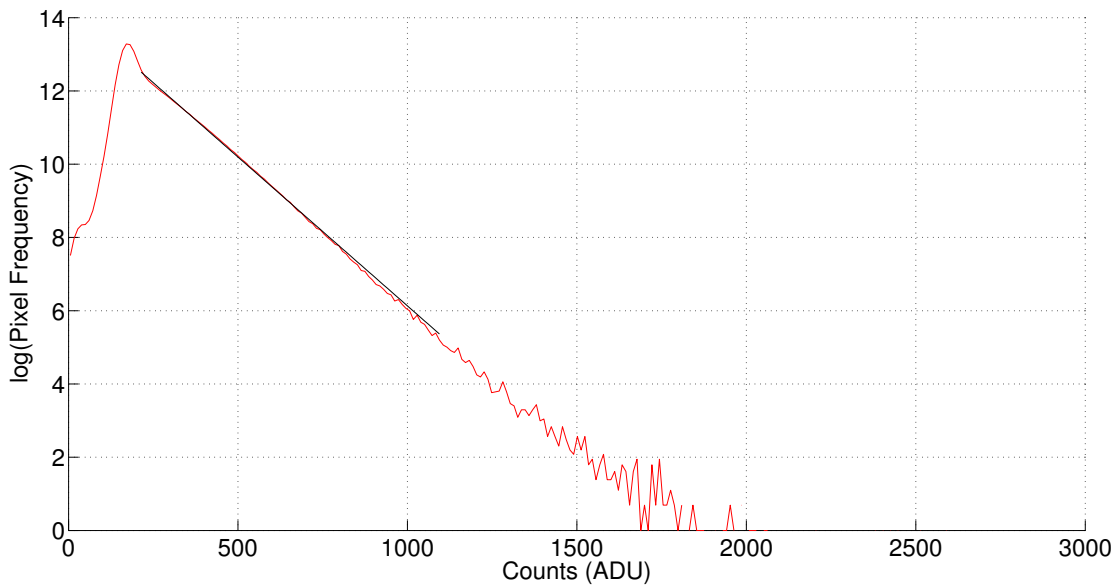


Figure 7.5: This is a plot of 10,000 RP science frames used statistically to determine the EM gain using the inverse-slope method. The gain found for these frames was  $\sim 600$  and the bias level, which is the peak of the curve on the LHS, is 170 ADU.

drop after 5 minutes of recording. The bias level remains at 105 ADU for the remainder of the data set.

The level of bias measured from each detector does not match laboratory bias frames recorded at close to a 0 second exposure using the same acquisition parameters as the science data. It was not possible to perform any further experiments on these detectors as they were on loan to the project. A laboratory recorded bias frame was scaled to match the levels found above for data bias subtraction. As the TP detector was found to change over time, two separate bias frames were used for the data block. Aperture photometry was used to extract the counts from the pulsar using a radial aperture of 1.5 pixels.

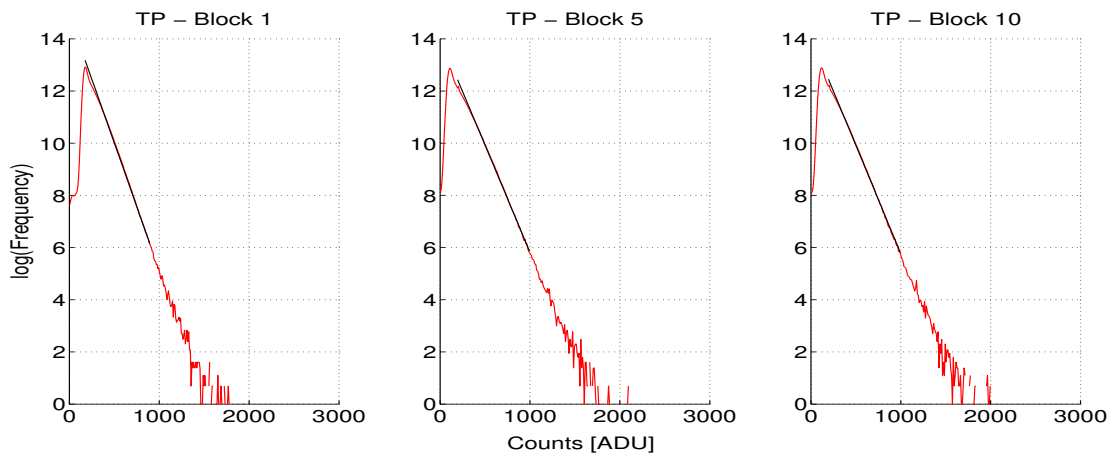


Figure 7.6: This is a plot of a series of EM gain plots for the TP. Each plot is generated using 10,000 TP science frames from the beginning middle and end of the data cube. The EM gain is calculated using the inverse-slope method. The EM gain value found for these frames was 580, 630, and 620, respectively. The bias level is found from the peak value on the LHS of the gain curve. It was found to vary from beginning to end throughout this data cube. Block 1 has a bias level of 175 ADU, and block 2 and 3 have a bias level of 105 ADU.

On closer examination of the bias subtracted TP channels the intensity time series was observed to drift, or slope downward near the beginning of the data block. This can be found in Figure 7.7. The first 300,000 frames show unstable variation in the data, and there is a decreasing slope from the 200,000 - 300,000 frame. These frames may need to be rejected from the polarimetric analysis. Observational logs recorded that there were a number of detector instability events from the TP camera and this is confirmed from this analysis.

The plots for the RP1 and RP2 channel are also plotted. There appears to be a difference in RP1 to RP2 in terms of the minimum value of the noise floor. As any value close to 0 ADU will essentially be a noise measurement, it should match in each camera. There could be a bias variation channel-to-channel. This seems unlikely due to the fact that each channel uses the same detector, but it could lead to channel-to-channel gain inaccuracies .

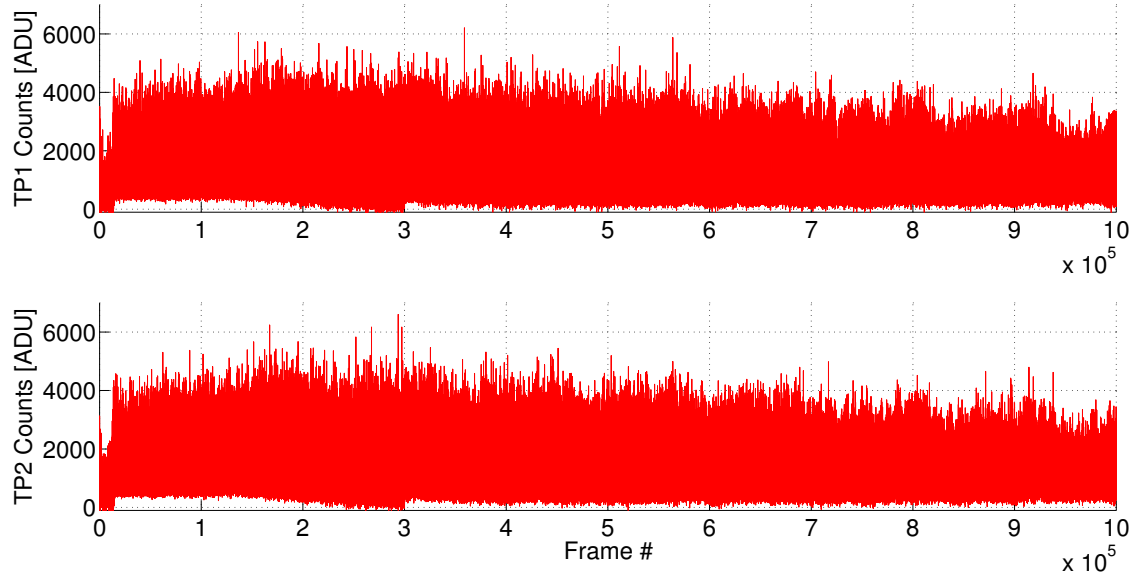


Figure 7.7: This is a plot of 1 million TP1 and TP2 science frames after bias subtraction. The bias was calculated using the inverse-slope method when investigating the level of EM gain that was applied during acquisition. A different bias frame was used for the first 300,000 frames compared to the remaining. This was based on the observations above of a decreasing bias over time. Aperture photometry was performed for a 1.5 pixel radial aperture.

### 7.3.2 Timing Analysis

This data was acquired using 2 iXon 897 Ultra detectors at a frame rate of approximately 1000 fps. The specifications for these detectors can be found in Appendix E. These detectors are designed to operate off their own built in clock and each frame is triggered internally. There is a functionality that allows for external triggering and this was implemented during data acquisition, however, this only allowed the first frame to be triggered, the remainder of the kinetic series was triggered by the internal clock.

The Crab pulsar has a period of 33 ms or 29.69 Hz. In order to achieve phase resolved measurements of the pulsar lightcurve, data acquisition is required to be equal or better than a millisecond resolution. As well as a detector that can acquire at this speed, accurate timing measurements are also necessary. The Andor iXon 897 Ultra can be triggered externally, but the GASP project did

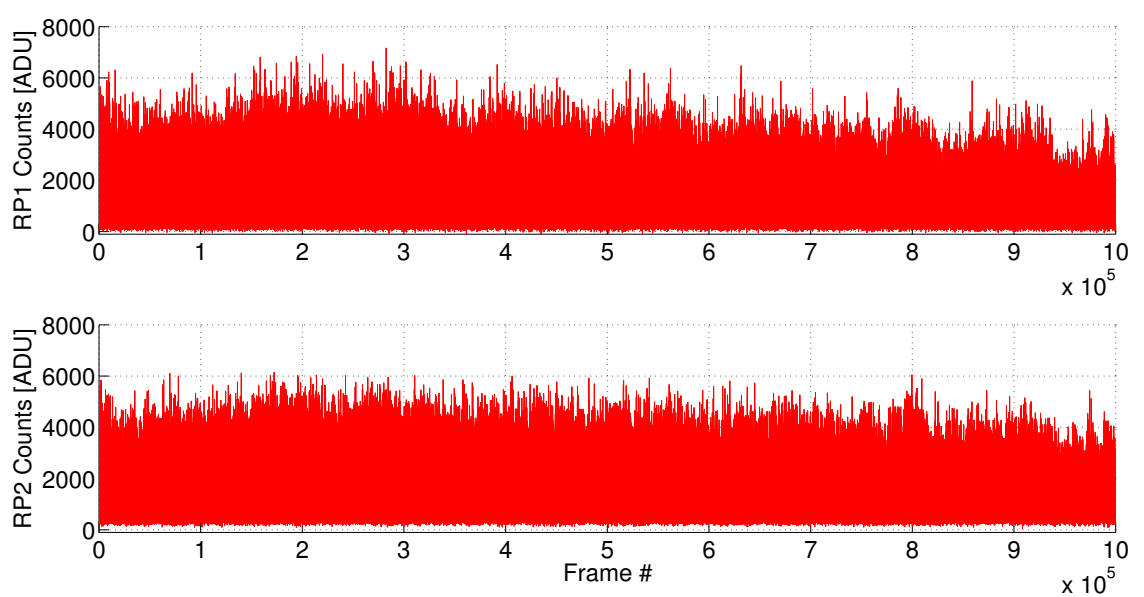


Figure 7.8: This is a plot of 1 million RP1 and RP2 science frames after bias subtraction. The bias was calculated using the inverse-slope method when investigating the level of EM gain that was applied during acquisition. There is a difference in RP1 to RP2 in terms of the minimum value of the noise floor.

not have the means to trigger each frame at a known and constant frame rate. A Symmetricom XLi Time and Frequency System unit was used to trigger each detector, simultaneously, at a known GPS time. This unit has a resolution at the nanosecond time scales, which is well within the required limitations of this timing analysis. Once triggered, each detector imaged at a frequency controlled by its internal clock. The problem with imaging in this way is that any drift in the detector frame rate cannot be measured. It is a functionality, which is not built into the hardware of these detectors. Due to time and budget constraints, a simple set up within the polarimeter was devised to perform accurate timing. A flashing LED was positioned behind the GASP PSA and connected to the same output port of the Symmetricom unit as each of the iXon detectors. The trigger sent from the Symmetricom unit was programmed to send a trigger to the LED every 60 seconds where it would flash and this could be detected when running aperture photometry. The same trigger was also fed to each iXon. Once triggered they were free to run off their own clocks, but every 60 seconds the LED flash would appear in a captured frame. It was found that the LED had a decay rate

---

and the flash would persist for approximately 3 frames. These frames would be disregarded in the timing and polarimetric analysis.

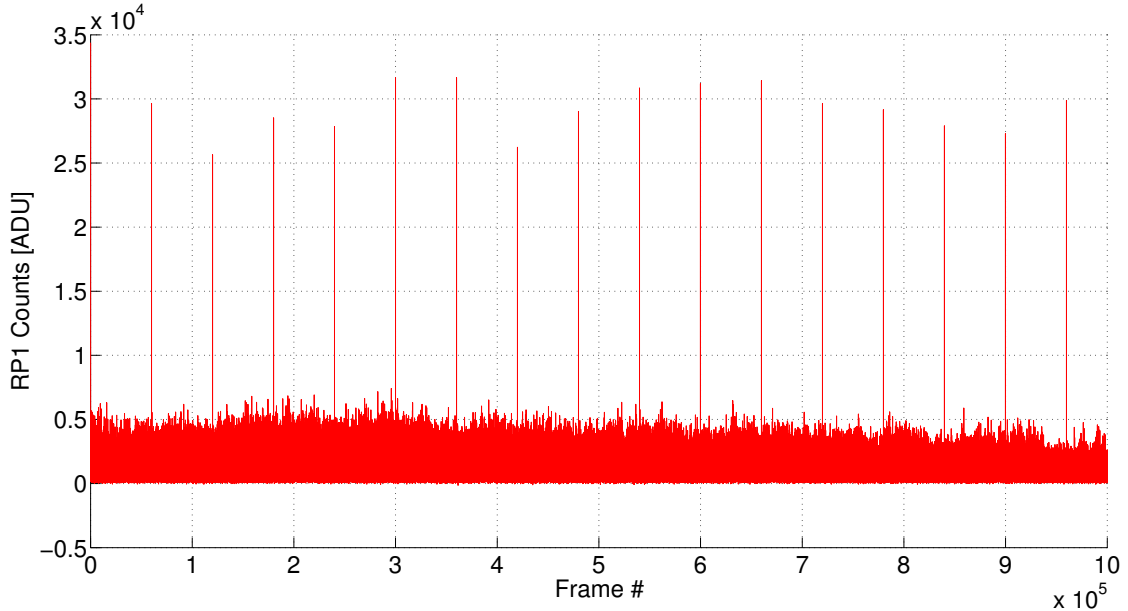


Figure 7.9: This is a plot of 1 million RP1 science frames after bias subtraction. The spikes present in the data are the result of a flashing LED, which was triggered to flash every 60 seconds. The same plot was found for the RP2 channel.

The suspected detector temporal frame rate drift was found to be true when analysis was carried out on the data in Figure 7.9 compared to Figure 7.10. The first to last initial LED flash (the flash decays over 3 frames) was measured to last for 960 seconds. In the case of RP1 and RP2 this consisted of 959,859 frames however, for TP1 and TP2 962,246 were recorded. This shows that the TP detector was imaging at a slightly faster frame rate compared to the RP detector. This would have been a more difficult analysis routine without the flashing LED however, a time step can be calculated from these data to perform a Fourier analysis and hence, data phase folding.

Using the information from these data sets a power spectrum can be generated from the fast Fourier transform (FFT) of the flux in ADUs plotted against a frequency series where the maximum value is the Nyquist frequency for this data in Hz.

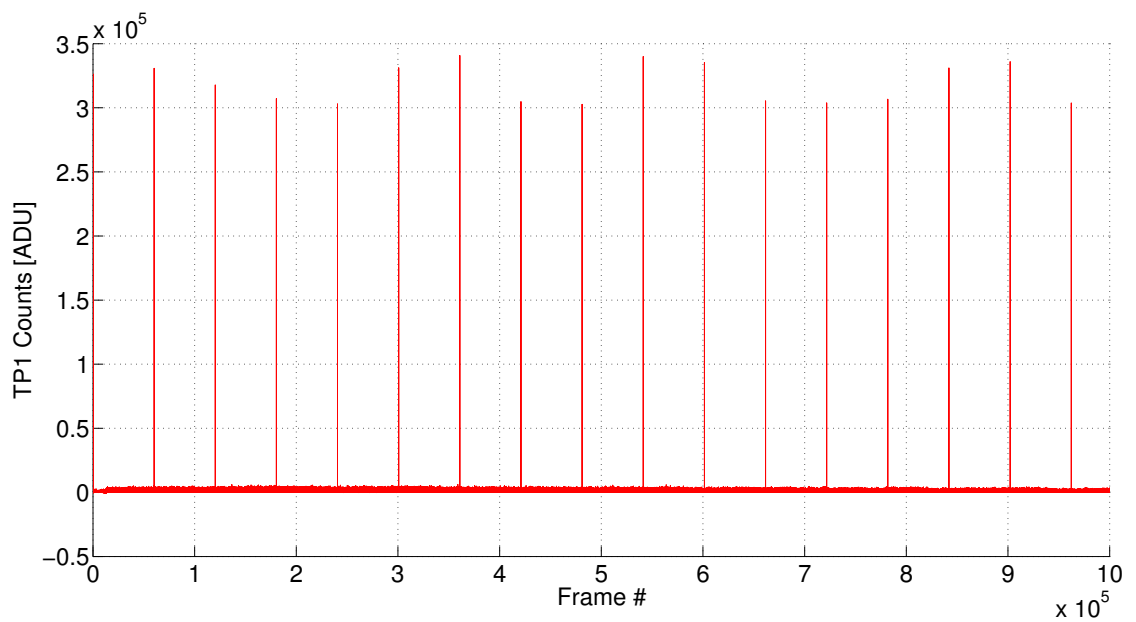


Figure 7.10: This is a plot of 1 million TP1 science frames after bias subtraction. The spikes refer to a flashing LED triggered to flash every 60 seconds. The same plot was found for the TP2 channel.

The frequency analysis of the pulsar was carried out as confirmation of the timing analysis using the flashing LED. It has proven that the measured time step can be used to accurately phase fold each channel. The accuracy of the timing analysis time step is limited by the frame rate resolution. The frequency measured at the 3<sup>rd</sup> or 4<sup>th</sup> harmonic is compared to the mean value measured by Jodrell Bank on the same week that GASP was observing. This frequency was 29.694779 Hz. There is an error of  $\sim 1$  mHz, which is acceptable for the frame rate at which these detectors were imaging. There will also be a frequency error between the iXon detectors as each was imaging at different frame rates with respect to the other detector.

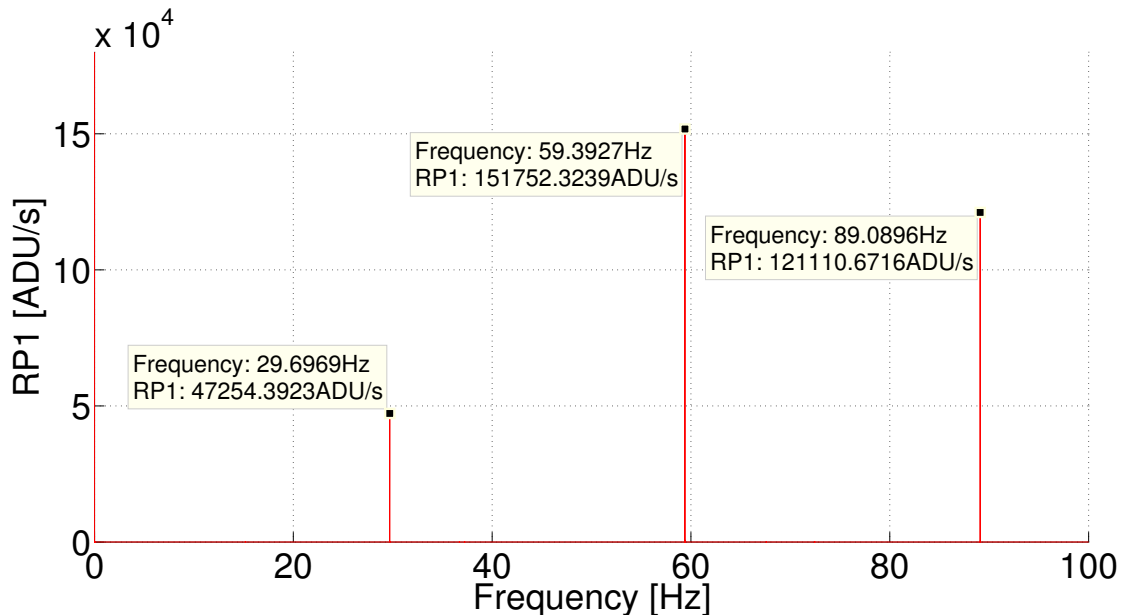


Figure 7.11: This is a power spectrum for the first 3 harmonics of the Crab pulsar from the RP1 science frames in Figure 7.9 after bias subtraction. The same plot was found for the RP2 channel. The known frequency of the Crab pulsar is  $\sim 29.69$  Hz and it is clear that this is the pulsar. The characteristic increase in power on the 2<sup>nd</sup> harmonic is also evident. Higher harmonics are used data phase folding.

### 7.3.3 Polarimetric Results

The data from RP1 and RP2 was phase folded using a frequency of  $f_{RP} = 29.69658$  Hz, and for TP1 and TP2  $f_{TP} = 29.69656$  Hz. The maximum peak was found on each channel from these frequencies. As each detector was operating at a different frame rate, the data also needed to be phase shift. RP1 was taken as a reference and TP1 and TP2 were shifted in phase by -0.0856. A plot of the overlayed channels can be found in Figure 7.13.

Sky background subtraction has not been carried out for this data set. It has already been discussed that there was some difficulty in determining a level of sky in the integrated data in Section 7.2. In this case the sky background level was not uniform and difficult to distinguish nebula from sky. A similar trend was observed with this phase resolved data however, further analysis on a frame-by-frame basis will be required. The polarimetric results that follow have not been sky subtracted.

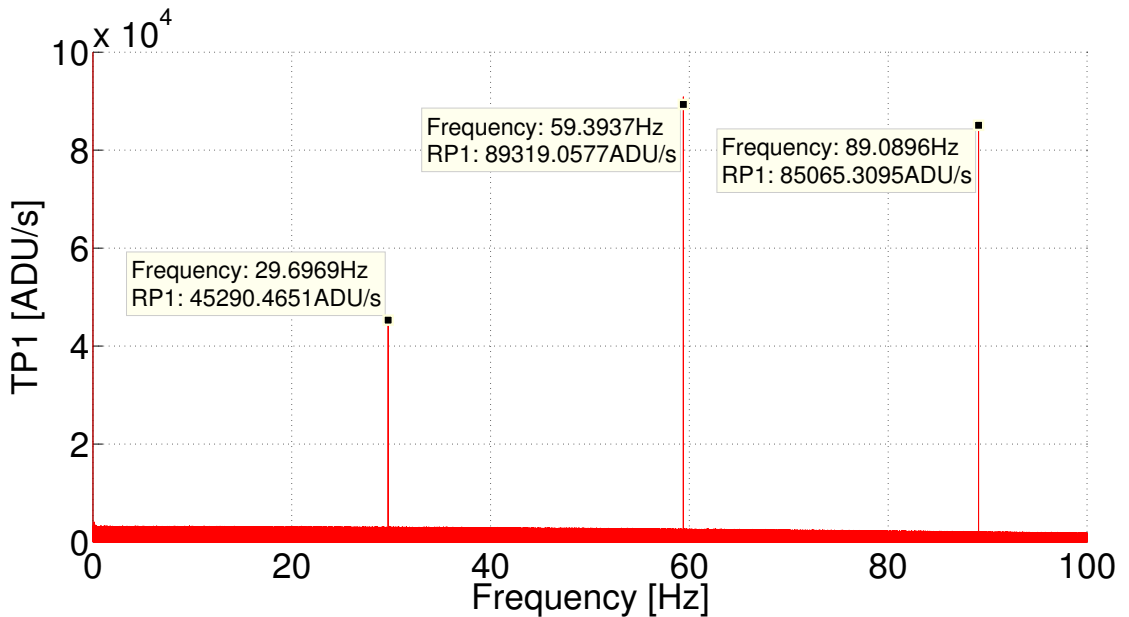


Figure 7.12: The same as Figure 7.11 but for the TP1 channel from the bias subtracted data in Figure 7.10. The same plot was found for the RP2 channel. As in the RP1 channel, the frequency of the Crab pulsar was measured to be 29.6969 Hz for the  $1^{st}$  harmonic. To achieve more precision higher harmonics are used when phase folding the data.

It is noted that at this stage in the analysis, each of the TP lightcurves appear to be lower than what is expected from the optical alignment of the instrument. It is possible that this is expected in the case of the pulsar, however, it seems unlikely. The TP, optically, receives a larger percentage of light than RP. The value of TP/RP for this data set is equal to 0.94. In the case of the integrated data at the beginning of this chapter, the value for  $TP/RP \simeq 1.04$ . The EM gain variation between the paths has been accounted for in Figure 7.13. In the data reduction section of this analysis there was concern for the variation in the bias level throughout the data set, particularly on the TP detector. This was accounted for in data reduction, however, there may be further error that is not clear from the raw counts. The polarimetric reductions are plotted in Figures 7.14, 7.15, and 7.16.

The data is calibrated in the same way as the integrated Crab pulsar data. It is possible that inconsistencies in the settings between science data and calibration

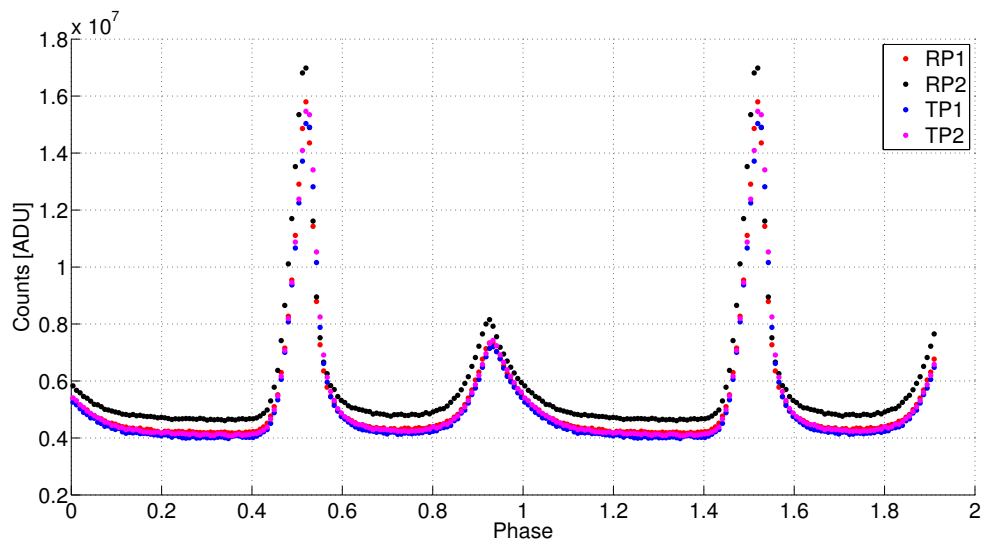


Figure 7.13: A plot of all phase folded lightcurves for the Crab pulsar from the set of debiased data in Figures 7.8 and 7.7. The data in TP was phase shifted -0.0856.

could lead to error in the gain, which appears to be present. However, if the error was a result of calibration then it is most likely due to an optical change in the system. This was shown not to be the case in Chapter 5 from the Mueller matrix verification experiments.

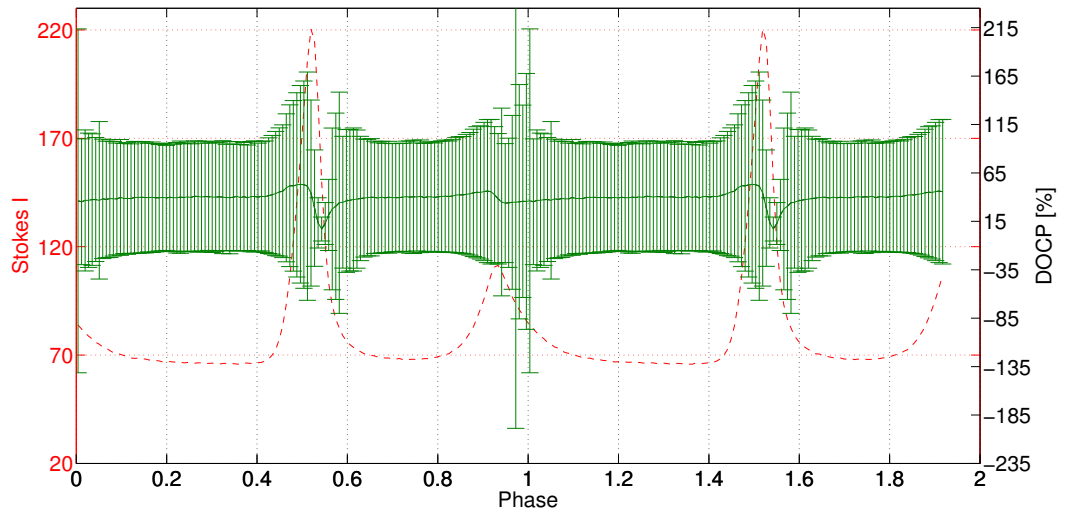


Figure 7.14: A plot of the DOLP and Stokes I as a function of phase. The Stokes analysis was performed using the phase folded lightcurves in Figure 7.13. Error bars are plotted.

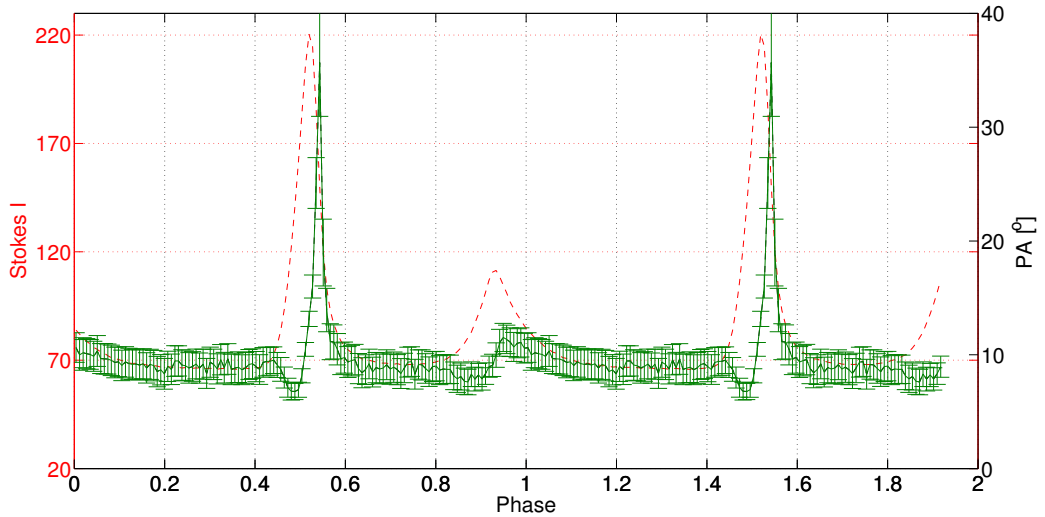


Figure 7.15: A plot of the PA and Stokes I as a function of phase. The expected swing in PA is what is plotted in this figure, however, the range of values is much lower and the mean PA is not what has been produced by the integrated data, or in the literature. Error bars are plotted.

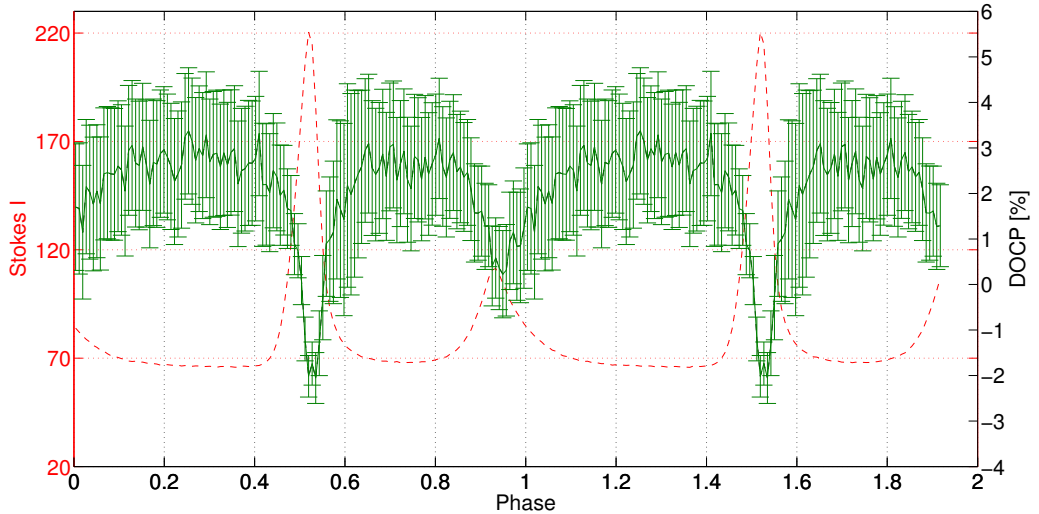


Figure 7.16: A plot of the DOCP and Stokes I as a function of phase. The value for this parameter is not known. The measured DOCP by the integrated data is lower than the mean value in this plot, however, it is possible that the DOCP has been measured more accurately as it is not dependent on Q and U, which are used for the DOLP and PA. Error bars are plotted.

An errors analysis has been performed on this data, however, more analysis will be required to investigate the errors caused by the bias and EM gain on the polarimetric signal. This will also affect the level of error on each point in the phase. The data has not been barycentred. The data is not compared to radio observations at this time, particularly as this data set is approximately 11 minutes in length, insufficient to affect the phase of the lightcurves plotted in Figure 7.13.

---

### 7.3.4 Concluding Remarks

There are clear errors in each of the polarimetric plots for this set of Crab data. The swing of the polarisation angle is the correct shape. An ‘S’-shaped swing is expected. It also agrees with the swing found by Słowińska et al. (2009), which can be found in Figure 7.17.

The overall shape of the DOLP measured by GASP is not correct. The magnitude of the percentage polarisation is close to the expected range but the background, or DC component (described in more detail by Słowińska et al. (2009)), is underestimated by this data. This analysis was performed for a 1.5 pixel radial aperture. It is possible that this aperture is large enough to measure the flux from the pulsar on the RP detector, but the TP is underestimated due to remaining registration error in the form of a scale variation. Background subtraction is not performed on this data. It is possible that this could lead to another source of error in the DC component.

There have been a number of issues found in the performance of the TP detector, which have been addressed. The instrument works well when performing timing measurements at very fast frame rates, however, it is possible that these parameters could have caused the TP to malfunction during data acquisition, in particular when using high EM gain. Further analysis of data sets with lower EM gain settings could provide more information regarding detector performance. The results from the polarimetric analysis of the integrated data are more promising and indicate that it should be possible to measure phase resolved polarimetric information from this target. It is clear that there are remaining errors in the detector acquisition.

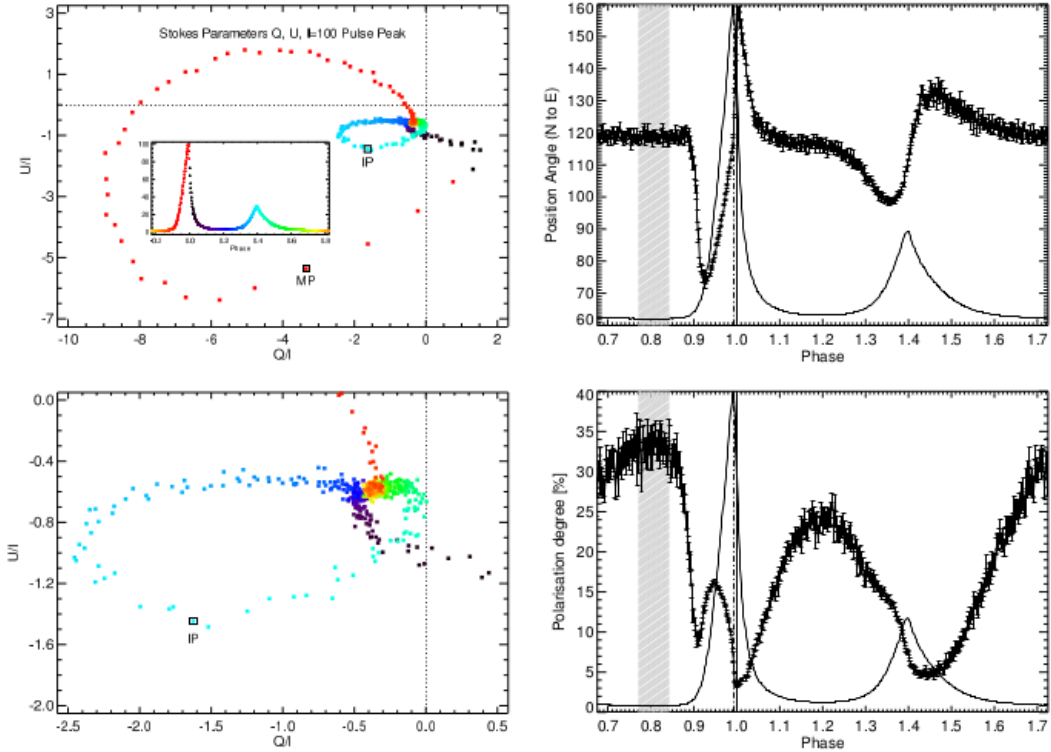


Figure 7.17: Left column: Stokes parameters  $Q$ ,  $U$  as a vector diagram. Colours refer to the pulse phases as indicated in the input box of upper panel. The scale is such that  $I = 100$  at the maximum light. Phases of the main and inter pulse maxima are indicated with black open squares. Points belonging to the main and inter pulse follow in a counter-clockwise direction on outer and inner ellipses, respectively. Bottom panel shows a zoomed region around the IP phases. The dashed lines indicate the origin of the scaled  $Q$ ,  $U$  coordinates. Any error in background polarisation would correspond to a shift in the origin in this plot. The lower plot shows a zoomed region of the upper panel. Right column: The Crab pulsar position angle as a function of rotational phase. Changes of PA are aligned with the main pulse maximum of the optical light (vertical dot-dashed line), but also with the zero phase, i.e. with the radio phase of the main pulse (vertical solid line). The Crab pulsar polarisation degree as a function of rotational phase (bottom panel). Minimum of  $p$  is for the radio phase (vertical solid line), and not for the maximum phase of the optical main pulse (vertical dot-dashed line). The pulse profile (solid line) and DC phase range (dashed region) are indicated also Słowińska et al. (2009).

---

# Chapter 8

## Conclusions & Future Work

The work presented by this thesis has consisted of establishing a suitable optical design for an imaging division of amplitude polarimeter, and the implementation of an improved calibration method to limit instrument systematic error. The results of this calibration method were presented using a number of analysis techniques, including image registration and methods of polarimetric reduction.

A set of polarimetric results are presented from an observing run on the 200 inch telescope at Palomar Observatory. A number of polarisation standards were reduced in order to measure the polarimetric sensitivity of the instrument as well as any instrumental polarisation. Science observations for a set of Zenith flat-fields were reduced to measure both the sensitivity, and the temporal stability of the polarimeter. Further science results from observations of the Crab pulsar and its surrounding nebula were also presented in order to compare with what has been found in the literature.

### 8.1 Laboratory Instrument Calibration Conclusions

The overall design of the polarimeter and prism-rhomb has been presented in Chapter 3 from the work in Collins (2012) and a publication (Collins et al., 2013). The use of the polarimeter as a lab instrument, and a scientific motivation for the use of GASP as an observational instrument is presented by the authors. A number of optical design parameters were addressed in Chapter 4 to use GASP as

---

an imaging polarimeter. When this work began, GASP was in the design stages as an 8-detector polarimeter using APDs. The optics of this system were finalised and laboratory bench testing of the alignment and calibration were carried out.

It was with this system that the Eigenvalue Calibration Method, or ECM, was adapted for use with GASP; this is presented in Chapter 5 using APDs, and EMCCDs for imaging polarimetry. The ECM is explained in greater detail in this chapter, but it was part of the work of this thesis to establish a suitable method of calibration that eliminated any errors introduced as a result of inaccuracies in alignment. As has already been stated, the use of the ECM has the following advantages:

1. No assumption is made to the system to be calibrated other than that it must be complete.
2. The precise orientation and position of the various elements do not need to be known in order to calibrate.
3. All optical elements are included in the matrix representation.
4. The characteristics of the reference samples are completely determined during the calibration without need for secondary measurements.  $\mathbf{A}$ , when measured, will be a function of the wavelength  $\lambda$ , as will the defining characteristics of the reference samples.
5. The accuracy of the calibration procedure can be evaluated when the ECM is used.

The results of calibration, using APDs, are presented in Chapter 5.6. An excellent result from the ECM was found in the laboratory indicating that GASP works well as a DOA polarimeter. A comparable system matrix to the theoretical PSA was obtained with reasonable explanations given for any deviation in these matrices. The ECM system matrix,  $\mathbf{A}$ , was tested on linearly polarised light to great effect and the ECM measures absolute values for the DOLP, DOCP, and PA, with variation in these values as low as 0.2% and 0.1° (in the absence of systematic error), respectively. The results of this experiment also showed a systematic error

---

in the Stokes parameters, which indicates that GASP was measuring a possible mechanical movement in the system. An experiment was also carried out using an LED, assuming that this light was unpolarised. These results also show reasonable variation in the final results over time (same order as above) without any systematic error, however, there is the possibility that GASP is measuring some instrumental polarisation; without documented results for the polarisation of the LED this is an uncertain result.

The FOV and pixel scale of the instrument were a concern when switching from a 1- to a 2D detector system, and were reviewed when designing an optical prescription in Zemax for the use of GASP with EMCCDs. At the end of this chapter GASP is presented as an imaging polarimeter, using DOAP, which has a suitable FOV for a 5-m class telescope. It creates this FOV in a way that may be adaptable for larger (or smaller) diameter telescopes using imaging detectors.

In order to calibrate GASP as an imaging polarimeter it is necessary to spatially register the 4 GASP channels to a reference frame, - 1 of the 4 channels is selected to be the reference). It has been discussed, in detail, the implications of misregistration and errors that can occur as a result. Two methods of registration were explored, both yielding positive verification that GASP was calibrated at Palomar. These methods used either, a set of artefacts present in all channels (less on each TP channel), or a combination of coordinates from one of the observation nights. There were difficulties in using both methods for various reasons discussed, however, the conclusion of both registration methods indicated that there was insufficient information, in the form of available targets, to perform accurate registration.

The results of the second registration method show improved calibrated ECM samples, concluding that this has shown that GASP is in fact calibrated along its calibration optical axis. There were remaining systematic patterns in the resultant Mueller matrices, and the patterns that are present are indicative of the areas of the FOV, which lack registration points. A first-order analysis was also discussed regarding error propagation as a result of misregistration.

Other errors can also lead to a corruption in the calibration of the instrument, apart from image registration. Unfortunately, these are difficult to distinguish (in the case of GASP) as there is no perfect geometrical solution in terms of the optical

---

alignment. Artefacts inherent to experimental equipment, or dust in the system could lead to inaccuracies.

GASP has also shown a consistent calibration over a period of  $\sim$  6 days, including many movements of the telescope on sky and while unmounting. The possibility that temperature variations in the telescope dome compared to that of the Caltech laboratory could cause instability, however this was not monitored. There are a number of sources of the variation in the system matrix. It was difficult to discern these errors and it was concluded that, depending on the light intensity striking the detector (dependent on the calibration or current experiment) random fluctuations in the detector and systematic effects (mostly like due to misregistration) are the source of error.

## 8.2 Observational Calibration Conclusions

Two polarisation standards were observed on the fourth night at Palomar. The polarimetric information, from the literature, can be found in Table 6.1. The analysis performed used aperture photometry for a more accurate measure of the polarisation. Spatial polarimetry was not a requirement of these types of targets and the resolution of the instrument was not sufficient to carry out any spatially varying analysis. The observation of polarisation standards is a necessary step on any observation night using a polarimeter to test the limitations and stability of the instrument, as well as measuring the instrumental polarisation as a function of time.

The results of the polarimetric analysis by GASP show that the zero polarisation standard HD12021 does not agree with the expected. It is taken that, in spite of less than ideal observing conditions, that this target is measuring the instrumental polarisation at this stage in the night (Patat and Romaniello, 2006). The polarimetric results for the DOLP, DOCP, and PA from the 6% standard BD25727 were more acceptable as this target is not weakly polarised and was observed at a later stage in the night. Each target varied as a function of time within their respective data sets for both a clear and R Band filter.

The results of the instrumental polarisation analysis demonstrated that there was a change in this measurement from the beginning of the night toward the end of

---

observation. It is also a measurement that is dependent on the source being weakly polarised, in which case the polarisation will always be overestimated. Overall, the results from this analysis show that GASP is measuring acceptable levels of polarisation within instrumental limitations but a larger number of polarisation standards is required per night of observation to ensure a better estimate.

### 8.3 Science Conclusions: Zenith Flat-Fields

A set of Zenith flat-fields were analysed using GASP when it was known to be calibrated. These were recorded on observation Night 4 at the Palomar 200 inch telescope. The results found indicate remaining geometric registration errors using science data points; also found from bench calibrations. It has been discussed, in previous chapters, that errors in misregistration will lead to errors in measured values for DOLP and DOCP. Pixel errors due to misregistration of 0.3 pixels are found, which could result in  $\pm 6\%$  error in the DOLP and DOCP for  $4 \times 4$  binning. This level of variation has been observed in the Zenith flats indicating that the errors found in image registration can explain the variation in the polarimetric results obtained using a pixel-by-pixel calibration method.

Analysis of the capability of GASP to operate as a spatial, imaging polarimetry was performed. This showed a variation of 1% DOLP and a  $0.3^\circ$  PA over the field when the SNR of the data was maximised. A small area of the field was shown to be well registered for the limits and error discussed in Chapter 5.

The variation in the PA was analysed, where the lowest  $\Delta$ PA observed was  $0.83 \pm 0.03^\circ$ ; the  $\Delta$ PA value is approaching this value over time, where the expected value in this time block is expected to be  $0.71^\circ$ . All time blocks are expected to show this  $\Delta$ PA and a number of possibilities for where this error may occur have been explored.

The expected value in the DOLP is not recorded, however, as observed in the PA, it appears to approach a terminal  $\Delta$  value. The  $\Delta$ DOLP shows  $\sim 2\%$  variation in the last 5 frames and if more observations were obtained, this could continue to decrease at this rate. The measured value for the DOCP was found to be  $\sim 0.7\%$  for the data set, for a pixel-by-pixel method.

Further analysis was carried out using a method of aperture photometry. Po-

---

larimetric results were obtained using an aperture displayed in Figure 6.13. The results of this analysis showed some improvement in the expected value for the PA, but no significant difference in the DOLP. An improvement was found for the value of DOCP, though with some temporal variation. This was a successful analysis method for this polarimetric value to reduce remaining distortion observed on TP2 - the calibration channel, which measures the circular polarisation. The reasoning behind using aperture photometry was valid as this chosen aperture demonstrated an improvement in the polarimetric output and the variation from pixel-to-pixel is reduced by averaging.

Some conclusions were drawn due to the observed errors in the science observational analysis. The polarimetric results appear to show a dependence on intensity, or value of SNR. The first 6 Zenith frames indicate that there are random and systematic errors present and this is impossible to disentangle. Until the SNR rises, the measured values for DOLP, DOCP and the PA show high variation frame-to-frame. Possible errors in the timing/time-stamps of the iXon detectors could show that the  $\Delta$  values found for the PA are closer to the expected result. Finally, remaining systematic errors are most likely due to misregistration.

It is concluded that by using a number of analysis techniques it is possible to reduce the calibrated GASP science data to produce meaningful polarimetric measurements and compare them to a time varying expected value based on the geometric position of the Sun relative to the Earth while observing at Zenith. These results match well with what is expected from the Rayleigh Sky Model. Further observations, for extended periods and higher SNR, could improve the results found from this work.

## 8.4 Science Conclusions: Crab Pulsar

Science results of the Crab Pulsar and Nebula are presented. The first set of data examined the polarimetric information from the Crab Nebula and determined the polarisation of the pulsar and a nearby star Trimble 28. The polarimetric results measured for the pulsar are in good agreement with what has been found in the literature. It was found that the measurement for the nebula was most likely contaminated by light from the pulsar and Trimble 28. If a larger FOV was

---

available, this could have been investigated further.

In the case of an instrumental polarisation, the standard HD12021 was used to investigate if the value for the DOLP measured by GASP is valid. As the pulsar is expected to have a strong polarised signal, it is unlikely to be affected by instrumental polarisation. The DOLP of Trimble 28 was investigated by Moran et al. (2013) and was found to be 1.6% polarised. It is possible that the instrumental polarisation could have changed over the course of the night and if still high could affect the value of Trimble 28 measured by GASP. If HD12021 is used, the DOLP is underestimated compared with Moran et al. (2013). A more comprehensive analysis of the instrumental polarisation is required over the night to determine a more accurate measurement.

Phase resolved polarimetric analysis was carried out for the Crab pulsar, which was imaged at a frame rate  $> 1000$  fps. The results of this analysis have shown inconclusive information. When compared to the literature (Słowińska et al., 2009), there are disparities in the shape of the DOLP curve as a function of phase. The off-pulse region is underestimated and it is possible that errors in the TP detector, which has been discussed in Chapter 7, have lead to this error. Inconsistencies in the bias offset and EM gain have been found from the raw data and have been difficult to remove/reduce. The overall shape of the PA matches well with the expected ‘S’-shaped curve, however, the mean value, and range over the swing are not correct. If compared with the results from the integrated data, there is a clear difference in the total counts from photometry between the RP and TP channels.

Further investigation of the EM gain and bias settings could provide more information regarding detector performance, particularly by reducing data sets that vary the EM gain parameter. It is also possible that increasing the aperture size in photometry could be effective.

## 8.5 Future Instrumentation & Experimentation

The choice of detector plays a large role in the scientific motivation in the development of any instrument. In the case of GASP, the most suitable detector for most observational endeavours are APDs, if no spatial polarimetric information

---

is required. In terms of data analysis, using APDs would reduce the need for conditioning the data prior to performing any calibration. There is no need for registration. The light from a single source (astronomical or otherwise) is focused on to the fibre and subsequently the focused signal is measured by the APD sensor. The FOV of the fibre is chosen to match the seeing limit of the telescope. All the light from the source is focused on to one pixel and measured as one signal. Any optical distortions will not have an impact on an APD pixel in the same way that it will when imaging a larger FOV.

In the case of imaging, to properly model the distortion variation on the chip, one would require multiple frames of a moderately crowded field, which was not available for this particular data set. There is also the added issue of the difference between calibration frames and real science frames. It is understood that the optical axes of calibration and science do not match perfectly, and this is expected for the ECM; this misalignment can be solved by registering every frame to one reference frame in calibration. Image binning has also been found to reduce this offset.

Another reason for using APD detectors is if the scientific motivation requires information read out at fast frame rates. This is a feature of APDs that is not readily available from most imaging detectors due to the large readout noise trade-off that occurs as a result. The use of EMCCDs greatly reduces this problem, however, there are still limitations to how fast most detectors can operate, see Appendix E. An advantage of using imaging detectors is that, if a suitable resolution can be achieved, far more detail can be extracted from the polarimetric results. Fine details in the surrounding FOV can be imaged, or discovered by using an ECM pixel-by-pixel calibration. Features that are not distinguishable by optical imaging, it may be possible to uncover new information using polarimetry in this way.

### 8.5.1 Recommendations

There are a number of tests that can be run in the laboratory with GASP to test its calibration, stability, and limitations/precision. A number of these tests were performed during the course of this work, however, there are other experiments that can yield more information.

---

It was found that there was a compromise in the FOV of the instrument when using GASP on a larger diameter telescope. The size of the prism is the limiting factor. It accepts a pupil size of  $\sim 4.5$  mm therefore, if the platescale of the telescope is not very large, the FOV of the instrument will scale the same way. In the case where a 5 m telescope (and larger) is a necessary factor in the science observation goal, an overall improvement in optical quality is required. In order to produce a larger FOV, the simplest solution is to design a larger prism with less constraints placed on the optimisation of the quarter wave retardance of the glass and geometric design. This was an important factor in designing the current prism-rhomb, however, further optical designs could be explored to reduce this constraint.

An important requirement when using GASP as an imaging polarimeter is that images must be registered accurately. This can be addressed in the design stages of the polarimeter. In order to reduce the extent of software post-processing a suitable optical design, where optical aberration and distortion is minimised, is required. This is possible using the optical design software Zemax. A suitable set of optics to improve the image quality will aid in pixel-matching to reduce the pixel errors across all channels, which has been discussed in Chapter 5 and by Smith et al. (1999).

In the laboratory, an object must be placed at the focus of the instrument, which contains a large number of points that are randomly distributed. If this is not available, a USAF resolution test target can be used. Defined lines and edges can be compared, however, using a gaussian/moffat fit to obtain the centre of a target is recommended. A frame must be recorded for each channel with a high SNR to give good target-to-background contrast and reduce noise improving PSF fitting. A set of matched targets is created for each channel and a geometrical transformation is defined, this will register any subsequent images recorded on that specified channel.

Theoretically the distortion could be modelled by binning the data, however a problem occurs whereby image resolution is lost, resulting in the loss of common points, between the frames. There is a further complication in a difference between calibration and science channels. It became clear during the initial stages of image registration, that the optical axes of calibration and science were not matched well

---

enough, and this is a requirement for the ECM; this problem can be solved by registering every frame to one reference frame in calibration. This did not appear to be a great concern when using these science points to match calibration frames in the FOV of interest, but it is clear that some improvements can be made.

Once the registration has been established, calibration can be performed on each of these targets to examine how the calibration varies over the field. This can be done by performing the ECM (as discussed in this work) for each field location. Alternatively, the entire FOV can be flooded to test the calibration at the pixel level. Similar analyses of the Mueller matrix ECM samples (see Section 5.10.3) can be performed to verify the results of calibration. This should be carried out over an extended period to test the stability of the calibration. It has been carried out in this work to good effect, however, it is important to test the stability in a uniform environment and test the precision of the calibration through verification. It is also important to test the stability when the calibration is subject to environmental changes such as temperature. This is particularly important in the case when GASP is used for the purpose of observing. If temperature fluctuations cause instabilities, then this will have an effect on the stability of the measured Stokes parameters. According to the results in Section 5.11 some environmental changes were documented while observing with GASP, which show that the calibration shows good stability over an extended period of 6 days. Further work is recommended.

Some theoretical (and experimental) experimenting could be carried out to test the sensitivity of GASP to errors in the image registration, and how this will propagate through to a final value for DOLP, DOCP, and PA. This has been done by Smith et al. (1999) and similar approach can be used for GASP. An error in the misregistration in RMS pixel values can be modelled and passed through the system calibration procedure, giving errors in the final Stokes vector.

Further sensitivity testing in the laboratory can be performed to test GASP's ability to measure low levels of polarisation. A number of different polarisation states can be mixed, or an integrating sphere can be used to generate unpolarised light. This will provide valuable information, in the laboratory, on the limitations of GASP in measuring extreme low or high levels of linear/circular polarisation. Variation in bias (noise fluctuations) effects will also provide significant information

---

regarding the errors that GASP is subject to at low light levels. These errors could have a large effect on the calibration and propagate through to the final measured Stokes parameters. Is there a minimum intensity cut-off where the calibration will not yield positive results?

It is the concluding recommendation of this thesis work, to consider redesigning the optical prescription of the main prism-rhomb to improve the image quality of the final output of the system. Furthermore, a suitable combination of optics can limit the distortions that are clearly evident in the images presented from this work. If this is implemented correctly, with a well aligned system, it is certain that the final outputted images can be registered with less constraints from optical aberrations and imperfections in alignment resulting in distortions. It is also necessary to use a source at the focus of the instrument, which is designed to have a crowded field of points with a random distribution, e.g. a resolution target would provide enough information. This can then be used to match points between all 4 channels, to ensure that every pixel is matched correctly.

---

## Appendix A

# Polarimetric Expressions

The relationship between the calibration and the Stokes vector of input light is given by

$$\begin{pmatrix} I \\ Q \\ U \\ V \end{pmatrix} = \begin{pmatrix} a_{1,1} & a_{1,2} & a_{1,3} & a_{1,4} \\ a_{2,1} & a_{2,2} & a_{2,3} & a_{2,4} \\ a_{3,1} & a_{3,2} & a_{3,3} & a_{3,4} \\ a_{4,1} & a_{4,2} & a_{4,3} & a_{4,4} \end{pmatrix}^{-1} \cdot \begin{pmatrix} i_1 \\ i_2 \\ i_3 \\ i_4 \end{pmatrix}. \quad (\text{A.1})$$

The Stokes vector can be used to calculate how highly polarised the light is in terms of linear and circular polarisation. It can also be used to calculate the polarisation angle of the light - the direction in which the polarised signal of the light is travelling. The following equations show how the Stokes parameters can be used to calculate the (fractional) degree of linear polarisation (DOLP), degree of circular polarisation (DOCP), and the polarisation angle (PA):

$$\text{DOLP} = \frac{\sqrt{Q^2 + U^2}}{I} \quad (\text{A.2})$$

$$\text{DOCP} = \frac{V}{I} \quad (\text{A.3})$$

$$\text{PA} = 0.5 \left( \arctan^{-1} \frac{U}{Q} \right). \quad (\text{A.4})$$

The following are the equations used for the calculation of the (fractional) abso-

---

lute errors in the DOLP, DOCP, and PA. They are calculated using the normalised mean Stokes vector, where Stokes I has a value of 1 and the standard deviations are based on the normalised Stokes parameters. If Stokes I is 1, then the standard deviation on Stokes I will be 0.

$$\Delta\text{DOLP} = \sqrt{\frac{(Q\Delta Q)^2(U\Delta U)^2}{Q^2+U^2}} \quad (\text{A.5})$$

$$\Delta\text{DOCP} = \Delta V \quad (\text{A.6})$$

$$\Delta\text{PA} = 0.5 \left( \frac{(\Delta U Q)^2 + (\Delta Q U)^2}{Q^2 + U^2} \right) \quad (\text{A.7})$$

---

## Appendix B

# Pseudo-inverse Calibration Method

One of the main applications of the Moore-Penrose pseudo-inverse, namely to optimisation of linear least squares problems, which will be used by GASP during calibration. Let  $A \in \mathbb{C}^{m \times n}$  and  $y \in \mathbb{C}_m$  be given and consider the problem of finding  $x \in \mathbb{C}_n$  satisfying the linear equation

$$Ax = y. \quad (\text{B.1})$$

If  $m = n$  and  $A$  has an inverse, the (unique) solution is, evidently,

$$x = A^{-1}y. \quad (\text{B.2})$$

In the other cases, the solution may not exist or may not be unique. We can, however, consider the alternative problem of finding the set of all vectors  $x' \in \mathbb{C}_n$  such that the Euclidean norm  $\| Ax' - y \|$  reaches its least possible value. This set is called the minimising set of the linear problem Equation B.1. Such vectors  $x' \in \mathbb{C}_n$  would be the best approximations for the solution of Equation B.1 in terms of the Euclidean norm, i.e., in terms of “least squares.” As we will show, the MoorePenrose pseudo-inverse provides this set of vectors  $x'$  that minimise  $\| Ax' - y \|$ .

---

## Appendix C

# ECM Mathematical Solution

When an appropriate set of reference samples ( $M_{1-4}$  in the case of GASP) has been chosen it is useful to choose a matrix formulation to solve a set of linear equations. Each of the samples are described by  $M_i$  for  $i = 1,2,3,4$ , where  $M_1$  constitutes a reference sample for air and is equal to the identity matrix. These samples correspond to a set of intensities  $B_i$  for each  $M_i$ . The first measurement yields,

$$B_0 = AW. \quad (C.1)$$

Next, the DRs, i.e.  $M_i$  for  $i = 2-4$ , are measured. From the raw data matrices  $B_i$  the following matrices can be calculated,

$$C_i = B_0^{-1} B_i = W^{-1} M_i. \quad (C.2)$$

Equation C.2 has the same eigenvalues as  $M_i$  and these provide the real values for  $\tau_i$ ,  $\psi_i$ , and  $\delta_i$ , which is independent of the DR azimuthal angle,  $\phi_i$ .  $W$  is then determined from the unique solution of the set of equations:

$$M_i W - WC_i = 0. \quad (C.3)$$

A linear operator  $K$  is built so that its only eigenvector associated with a zero eigenvalue is  $W$ .  $K$  is defined based on both the experimentally known matrices  $C_i$  and the values of  $\tau_i$ ,  $\psi_i$ , and  $\delta_i$ . Working towards a solution for  $W$  the unknown angles  $\phi_i$  are determined from the requirement that one of the eigenvalues of  $K$

---

actually vanishes.  $\mathbf{K}$  is found from the solution to the following equation,

$$\mathbf{K} = \mathbf{H}_1^T \mathbf{H}_1 + \dots + \mathbf{H}_n^T \mathbf{H}_n \quad (\text{C.4})$$

where  $\mathbf{H}$  is the matrix that represents the linear mapping  $\mathbb{H}_M$ . The matrix  $\mathbf{K}$  is a positive symmetric real matrix, so it can be diagonalised. The eigenvalues of  $\mathbf{K}$  are sorted in such a way that

$$\lambda_1 > \dots > \lambda_{n-1} \gg \lambda_n \approx 0 \quad (\text{C.5})$$

where  $n$  depends on the size of the matrix  $\mathbf{K}$ , which is a direct result of the number of  $B_i$  samples measured. The value for  $n$  can be found from Equation C.3. This is the solution to the calibration problem from a mathematical point of view, however, this does not take into account the physical limitations. That is, the equality  $\mathbb{H}_M(\mathbf{W}) = 0$  can never be exactly verified. Because of the limited experimental precision,  $\mathbf{W}^{-1}(aw)^{-1}(amw)$  is always slightly different from  $\mathbf{MW}$ . This fact imparts peculiar properties to eigenvalues in Equation C.5 of  $\mathbf{K}$ . They are all different from zero except  $\lambda_n$ , the smallest, which should theoretically be null and which is close to zero in reality.

According to (Compain et al., 1999), it is necessary to ensure a good balance among the non-zero eigenvalues of the matrix  $\mathbf{K}$ . The eigenvalues of  $\mathbf{K}$  being sorted, as in Equation C.5, the accuracy is maximum when

$$\frac{\lambda_{n-1}}{\lambda_1} \quad (\text{C.6})$$

is maximum. The parameters  $\tau_i$ ,  $\psi_i$ , and  $\delta_i$  can be experimentally determined because the eigenvalues of a matrix product are independent of the product order. Consequently, one can identify the theoretical eigenvalues of  $\mathbf{M}$  to the eigenvalues of the product of measured matrices  $(aw)^{-1}(amw)$ . The eigenvalues of  $\mathbf{P}(\tau, \theta)$  and  $\mathbf{M}_{\text{DR}}(\tau, \theta, \delta)$  (see Section 5.2), are found to be  $\lambda_{r1}, \lambda_{r2}, \lambda_{c1}, \lambda_{c2}$ , the real and complex eigenvalues of  $(aw)^{-1}(arw)$ . This leads to

$$\begin{aligned} \tau_p &= \text{trace}[(aw)_{-1}(apw)] & \tau_r &= 0.5(\lambda_{r1} + \lambda_{r2}) \\ \delta_p &= 0.5 \arg\left(\frac{\lambda_{c1}}{\lambda_{c2}}\right) & \psi &= \arctan\left(\sqrt{\frac{\lambda_{r1}}{\lambda_{r2}}}\right), \end{aligned} \quad (\text{C.7})$$

---

where the trace is equal to the sum of the eigenvalues.  $r$  and  $p$  denote the type of sample used.  $r$  for the dichroic retarder, and  $p$  for the linear polarisers. If  $\theta$  has the correct value, all the eigenvalues of  $\mathbf{K}$  are non-zero except one, see Equation C.5. On the other hand, when we depart from the actual value, the null space of  $\mathbf{K}$  is empty and the system has only a trivial solution, which is the null matrix because all the eigenvalues are non-zero. As a consequence, we obtain the value of  $u$  by minimising the amplitude of the smallest eigenvalue of  $\mathbf{K}$  with respect to the other eigenvalues:

$$\theta \text{ is verified when } \frac{\lambda_n(\theta)}{\lambda_{n-1}(\theta)} \text{ is minimised.} \quad (\text{C.8})$$

The solution for  $W$  is the eigenvector of  $\mathbf{K}$  associated with the smallest eigenvalue of  $\mathbf{K}$ . Finally,  $A$  is calculated by

$$A = B_0 W^{-1}. \quad (\text{C.9})$$

---

## Appendix D

# Avalanche Photodiode Specifications

SPCM stands for Single Photon Counting Module. GASP used these detectors, including array modules, for laboratory based experiments, the results of which can be found in Chapter 5.6. All technical data sheets and reports can be found through Elmer (2013).

The SPCM-AQR is a self-contained module that detects single photons of light over the 400 - 1060 nm wavelength range - a range and sensitivity that often outperforms a photo-multiplier tube (PMT). The SPCM-AQR-IX uses a unique silicon avalanche photodiode with a circular active area that achieves a peak photon detection efficiency of more than 65% at 650 nm over a 180- $\mu\text{m}$  diameter. The photodiode is both thermo-electrically cooled and temperature controlled, ensuring stabilised performance despite ambient temperature changes. Count speeds exceeding 10 million counts per second (Mc/s) are achieved by the SPCM-AQR-1X module. There is a ‘dead time’ of 50 ns between pulses. As each photon is detected, a TTL pulse of 2.5 V (minimum) high in a  $50 \Omega$  load and 35 ns wide is output at the rear BNC connector. To avoid a degradation of the module linearity and stability, a case temperature between 5° and 40° should be maintained.

The photon count decreases at higher incoming light levels. The count at which the output rate starts to decrease is called the saturation point. As an extreme example, if the module is exposed to intense light the count rate will fall to zero.

The SPCM-AQR-WX-FC has an ‘FC’ fibre-optic receptacle pre-aligned to the optical detector. The photon detection efficiency of connector equipped modules is



Figure D.1: SPCM-AQR unit used to measure counts from one of the GASP DOAP channels.

about 95% of that quoted for standard modules. Fibre shielding When used with optical fibres, both the fibre itself and the connector shrouds must be completely opaque; otherwise, stray light will increase the count rate.

One peculiarity of silicon avalanche photodiodes is that as an incoming photon is detected, a small amount of light is emitted from the avalanche region. The emitted light has a broad spectral distribution. In most cases, this is not a problem. However, it can cause some confusion if another detector is monitoring light, or if the optical system is such that light emitted from the SPCM-AQR is reflected back on itself. If these photons return 35 ns after the initial event, they will be detected.

In the dark, the module generates random counts that follow a Poisson distribution. In a Poissonian process, the standard deviation is equal to the square root of the average count. In this specification, the ‘dark count variation’ refers to the stability of the average count of the module.

Another module utilised by GASP is found in Figure D.2. Each photodiode is both thermo-electrically cooled and temperature controlled, ensuring stabilised performance despite changes in the ambient temperature. The SPCM-AQ4C card uses an improved circuit with a peak count rate  $> 4$  Mc/s for short bursts of time



Figure D.2: SPCM-AQ4C array unit used to measure counts from one of the GASP DOAP channels.

on all 4 channels and a count rate of 1.5 Mc/s for continuous operation.

The SPCM-AQ4C requires + 2 V, + 5 Volt, and + 30 V power supplies. The output of each channel - a TTL pulse that is 4.5 V high (into a  $50\ \Omega$  load) and 25 ns wide - is available at the card edge behind the circuit board. Each TTL pulse corresponds to a detected photon. All input and output signals are available at the card connector. To avoid a degradation of the module linearity and stability, the heat sink temperature should be kept between 5° and 40° during operation.

---

## Appendix E

# iXon Ultra 897 Specifications

Photon Counting in EMCCDs is a way to overcome the multiplicative noise associated with the amplification process, thereby increasing the signal to noise ratio by a factor of root 2 (and doubling the effective Quantum Efficiency of the EMCCD). Only EMCCDs with a low noise floor can perform photon counting. The approach can be further enhanced through innovative ways to post process kinetic data. Andor designs incorporate back-illuminated sensors offering up to 95% Quantum Efficiency (QE). All technical data sheets can be found from Technology (2013).

Andor offer specific application requirements, such as providing effective charge purging immediately prior to acquisition, specific coatings, coupling to fibre optic scintillators and also specific interface requirements. As of now the Andor iXon brand has been prevalent across a variety of demanding applications, such as photon counting, lucky astronomy, adaptive optics, Bose Einstein condensation (BEC) / ion trapping, single molecule detection / nanotechnology, neutron tomography, X-ray/Gamma tomography, plasma diagnostics, Raman detection, sono- and thermo-luminescence detection.

Facilitated by a fundamental redesign, the new iXon Ultra platform takes the popular back-illuminated  $512 \times 512$  frame transfer sensor and overclocks read-out to 17 MHz, pushing speed performance to an outstanding 56 FPS (full frame), whilst maintaining quantitative stability throughout. The status of ‘Ultimate Sensitivity’ is also preserved in this model, offering thermo-electric cooling down to -100° and industry-lowest clock induced charge noise.

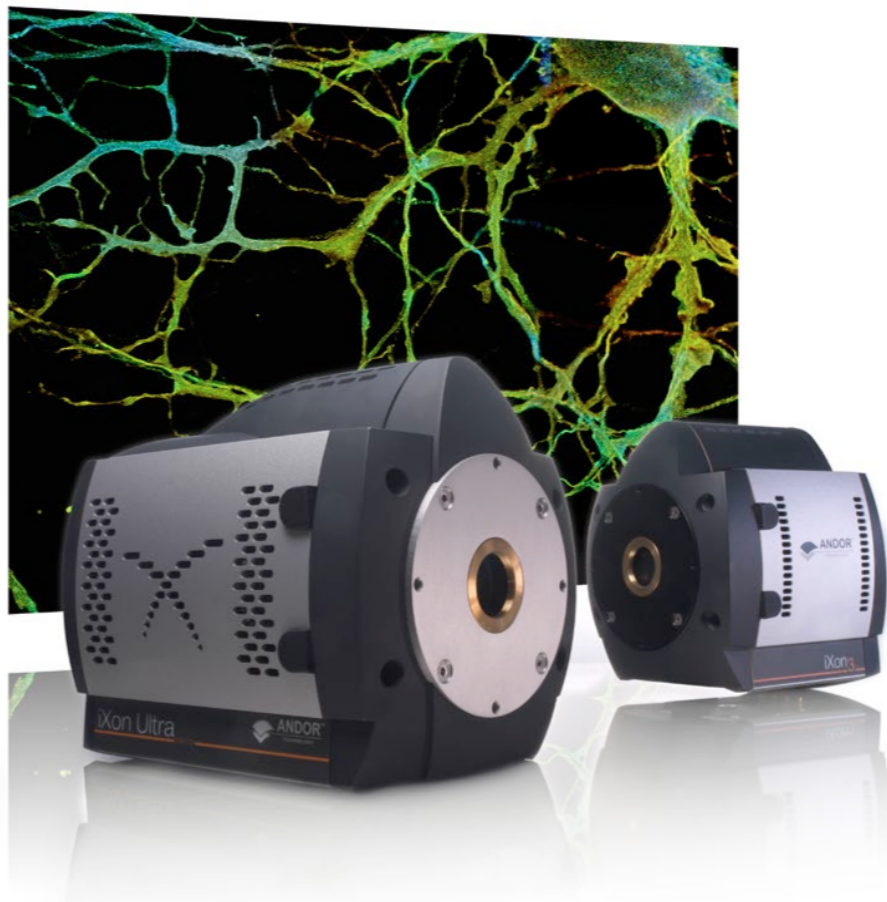


Figure E.1: iXon Ultra 897 EMCCD detector used to record image data from 2 GASP DOAP channels simultaneously.

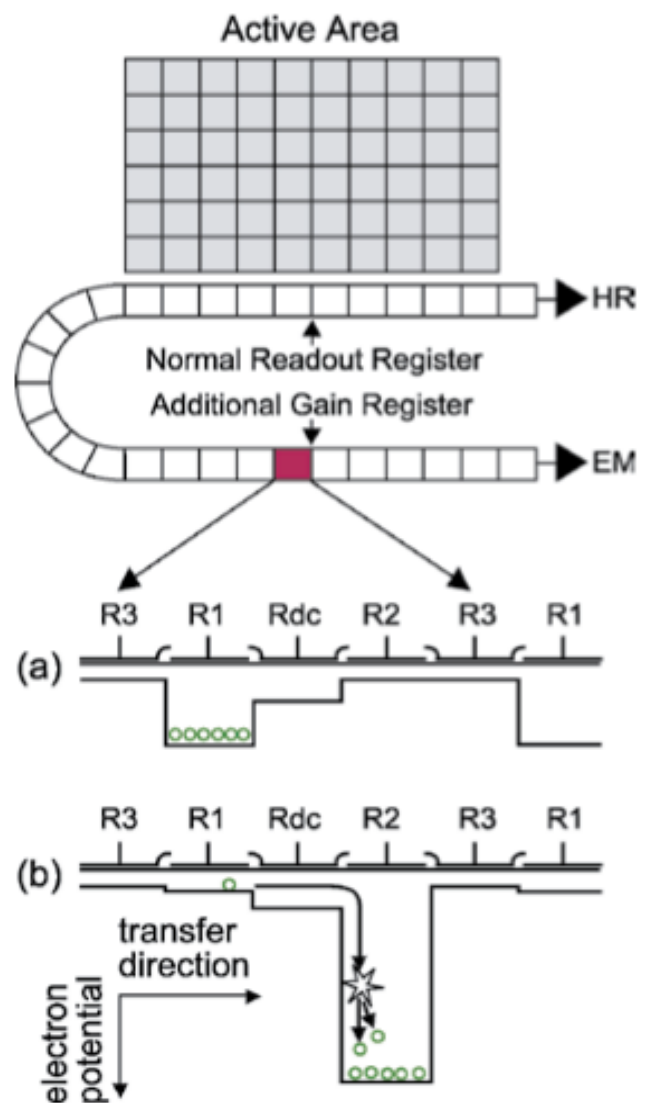


Figure E.2: Readout process and EM application for conventional and electron multiplication amplifier.

---

Table E.1: iXon Ultra 897 Key Specifications.

Active Pixels	512 × 512
Pixel Size (W × H; $\mu\text{m}$ )	16 × 16
Image Area (mm)	8.2 × 8.2
Active Area Pixel Well Depth (e-)	160,000
Max Readout Rate (MHz)	17
Frame Rates (frames per sec)	56
Read Noise ( $e^{-1}$ )	98 17 MHz 66 10 MHz <b>&lt; 1 with EM gain</b>
QE max	> 90%

---

# Bibliography

*Thorlabs Catalog 2010.*

*Thorlabs Catalog 2012.*

A., P. R. (1955). A generalized inverse for matrices.

A., P. R. (1956). On best approximate solution of linear matrix equations.

Abdo, A. A. (2013). In preparation.

Abdo, A. A., Ackermann, M., Atwood, W. B., Bagagli, R., Baldini, L., Ballet, J., Band, D. L., Barbiellini, G., Baring, M. G., Bartelt, J., and et al. (2009). Fermi Large Area Telescope Observations of the Vela Pulsar. *Astrophysical Journal*, 696:1084–1093.

Abdo, A. A. et al. (2010). Fermi-LAT Observations of the Geminga Pulsar. *Astrophysical Journal*, 720:272–283.

Agol, E. and Blaes, O. (1996). Polarization from magnetized accretion discs in active galactic nuclei. *Monthly Notices of the Royal Astronomical Society*, 282:965–976.

Alpar, M. A., Ankay, A., and Yazgan, E. (2001). Pulsar Spin-down by a Fallback Disk and the P-P Diagram. *Astrophysical Journal Letters*, 557:L61–L65.

Alpar, M. A., Cheng, A. F., Ruderman, M. A., and Shaham, J. (1982). A new class of radio pulsars. *Nature*, 300:728–730.

Angel, J. R. P. and Stockman, H. S. (1980). Optical and infrared polarization of active extragalactic objects. *Annual Review of Astronomy & Astrophysics*, 18:321–361.

- 
- Arons, J. (1983). Pair creation above pulsar polar caps - Geometrical structure and energetics of slot gaps. *Astrophysical Journal*, 266:215–241.
- Arons, J. and Scharlemann, E. T. (1979). Pair formation above pulsar polar caps - Structure of the low altitude acceleration zone. *Astrophysical Journal*, 231:854–879.
- Azzam, R. (1982). Division-of-amplitude photopolarimeter (doap) for the simultaneous measurement of all four stokes parameters of light. *Optica Acta: International Journal of Optics*, 29(5):685–689.
- Azzam, R. and Bashara, N. (1988). *Ellipsometry and Polarized Light*. North Holland.
- Azzam, R., Elminyawi, I., and El-Saba, A. (1988). General analysis and optimization of the four-detector photopolarimeter. *josa*, 5:681–689.
- Azzam, R. M. A. and Lopez, A. G. (1989). Accurate calibration of the four-detector photopolarimeter with imperfect polarizing optical elements. *Journal of the Optical Society of America A*, 6(10):1513–1521.
- Baring, M. G. (2004). High-energy emission from pulsars: the polar cap scenario. *Advances in Space Research*, 33:552–560.
- Blandford, R. D. and Romani, R. W. (1988). On the interpretation of pulsar braking indices. *Monthly Notices of the Royal Astronomical Society*, 234:57P–60P.
- Blaskiewicz, M., Cordes, J. M., and Wasserman, I. (1991). A relativistic model of pulsar polarization. *Astrophysical Journal*, 370:643–669.
- Born, M. and Wolf, E. (1999). *Principles of Optics, 7th Edition*. Press Syndicate of the University of Cambridge.
- Caraveo, P. A. (2000). A Sociological Study of the Optically Emitting Isolated Neutron Stars. In Kramer, M., Wex, N., and Wielebinski, R., editors, *IAU Colloq. 177: Pulsar Astronomy - 2000 and Beyond*, volume 202 of *Astronomical Society of the Pacific Conference Series*, page 289.

- 
- Chanan, G. A. and Helfand, D. J. (1990). Optical polarization of the crab-like supernova remnant 0540-693 in the Large Magellanic Cloud. *Astrophysical Journal*, 352:167–171.
- Cheng, K. S., Ho, C., and Ruderman, M. (1986). Energetic radiation from rapidly spinning pulsars. I - Outer magnetosphere gaps. II - VELA and Crab. *Astrophysical Journal*, 300:500–539.
- Clarke, D. and Neumayer, D. (2002). Experiments with a novel CCD stellar polarimeter. *Astronomy & Astrophysics*, 383:360–366.
- Cocke, W. J., Disney, M. J., and Muncaster, G. W. (1970). Optical Polarization of the Crab Nebula Pulsar. *Nature*, 227:1327–1329.
- Cocke, W. J., Disney, M. J., and Taylor, D. J. (1969). Discovery of Optical Signals from Pulsar NP 0532. *Nature*, 221:525–527.
- Coll, B. and Tarantola, A. (2009). Using pulsars to define space-time coordinates. *ArXiv e-prints*.
- Collett, E. (1980). Determination of the ellipsometric characteristics of optical surfaces using nanosecond laser pulses. *Surface Science*, 96(13):156 – 167.
- Collett, E. (1993). *Polarized Light - Fundamentals and Applications*. Marcel Dekker, New York.
- Collins, P. (2012). *Development and Implementation of an Ultra High Speed Astronomical Polarimeter: The Galway Astronomical Stokes Polarimeter (GASP)*. PhD thesis, National University of Ireland, Galway.
- Collins, P., Kyne, G., Lara, D., Redfern, M., Shearer, A., and Sheehan, B. (2013). The Galway astronomical Stokes polarimeter: an all-Stokes optical polarimeter with ultra-high time resolution. *Experimental Astronomy*.
- Collins, P., Sheehan, B., Redfern, M., and Shearer, A. (2009). GASP - Galway Astronomical Stokes Polarimeter. *ArXiv e-prints*.

- 
- Compain, E. and Drevillon, B. (1998). Broadband Division-of-Amplitude Polarimeter Based on Uncoated Prisms. *Applied Optics*, 37:5938–5944.
- Compain, E., Poirier, S., and Drevillon, B. (1999). General and Self-Consistent Method for the Calibration of Polarization Modulators, Polarimeters, and Mueller-Matrix Ellipsometers. *Applied Optics*, 38:3490–3502.
- Corbett, E. n. (2009). Polarimetry in Astronomy  
[www.aao.gov.au/local/www/obstech/corbett/ppt](http://www.aao.gov.au/local/www/obstech/corbett/ppt). Technical report.
- Cordes, J. M., Bhat, N. D. R., Hankins, T. H., McLaughlin, M. A., and Kern, J. (2004). The Brightest Pulses in the Universe: Multifrequency Observations of the Crab Pulsar's Giant Pulses. *Astrophysical Journal*, 612:375–388.
- Coroniti, F. V. (1990). Magnetically striped relativistic magnetohydrodynamic winds - The Crab Nebula revisited. *Astrophysical Journal*, 349:538–545.
- Cronin, T. W., Warrant, E. J., and Greiner, B. (2006). Celestial polarization patterns during twilight. *Applied Optics*, 45:5582–5589.
- Cropper, M. (1990). Polarimetry of the recurrent nova RS OPH during its 1985 outburst. *Monthly Notices of the Royal Astronomical Society*, 243:144–150.
- Cumming, A., Zweibel, E., and Bildsten, L. (2001). Magnetic Screening in Accreting Neutron Stars. *Astrophysical Journal*, 557:958–966.
- Daugherty, J. K. and Harding, A. K. (1996). Gamma-Ray Pulsars: Emission from Extended Polar CAP Cascades. *Astrophysical Journal*, 458:278.
- de Martino, A. (2004). General methods for optimized design and calibration of Mueller polarimeters. *Thin Solid Films*, 455:112–119.
- Dean, A. J., Clark, D. J., Stephen, J. B., McBride, V. A., Bassani, L., Bazzano, A., Bird, A. J., Hill, A. B., Shaw, S. E., and Ubertini, P. (2008). Polarized Gamma-Ray Emission from the Crab. *Science*, 321:1183–.
- Delplancke, F. (1997). Automated high-speed mueller matrix scatterometer. *Applied Optics*, 36(22):5388–5395.

- 
- den Hartog, P. R., Kuiper, L., Hermsen, W., Kaspi, V. M., Dib, R., Knöldlseder, J., and Gavriil, F. P. (2008). Detailed high-energy characteristics of AXP 4U 0142+61. Multi-year observations with INTEGRAL, RXTE, XMM-Newton, and ASCA. *Astronomy & Astrophysics*, 489:245–261.
- Deutsch, A. J. (1955). The electromagnetic field of an idealized star in rigid rotation in vacuo. *Annales d'Astrophysique*, 18:1.
- Dhillon, V. S., Marsh, T. R., Littlefair, S. P., Copperwheat, C. M., Kerry, P., Dib, R., Durant, M., Kaspi, V. M., Mignani, R. P., and Shearer, A. (2009). Optical pulsations from the anomalous X-ray pulsar 1E1048.1-5937. *Monthly Notices of the Royal Astronomical Society*, 394:L112–L116.
- Drevillon, B. (1993). Progress in crystal growth and characterization of materials.
- Dyks, J., Harding, A. K., and Rudak, B. (2004a). Relativistic Effects and Polarization in Three High-Energy Pulsar Models. *Astrophysical Journal*, 606:1125–1142.
- Dyks, J., Harding, A. K., and Rudak, B. (2004b). Two-pole Caustic Model for High-energy Radiation from Pulsars - Polarization. In Camilo, F. and Gaensler, B. M., editors, *Young Neutron Stars and Their Environments*, volume 218 of *IAU Symposium*, page 373.
- Dyks, J. and Rudak, B. (2003). Two-Pole Caustic Model for High-Energy Light Curves of Pulsars. *Astrophysical Journal*, 598:1201–1206.
- Eilek, J. A. and Hankins, T. H. (2000). Non-Dipolar Magnetic Fields in Pulsars. In Kramer, M., Wex, N., and Wielebinski, R., editors, *IAU Colloq. 177: Pulsar Astronomy - 2000 and Beyond*, volume 202 of *Astronomical Society of the Pacific Conference Series*, page 377.
- Elmer, P. (2013). Perkin Elmer Technical Data Sheets.
- Forot, M., Laurent, P., Grenier, I. A., Gouiffès, C., and Lebrun, F. (2008). Polarization of the Crab Pulsar and Nebula as Observed by the INTEGRAL/IBIS Telescope. *Astrophysical Journal Letters*, 688:L29–L32.

- 
- Gandorfer, A. M. (1999a). Ferroelectric retarders as an alternative to piezoelastic modulators for use in solar Stokes vector polarimetry. In *Society of Photo-Optical Instrumentation Engineers (SPIE) Conference Series*, volume 38 of *Society of Photo-Optical Instrumentation Engineers (SPIE) Conference Series*.
- Gandorfer, A. M. (1999b). First results from ZIMPOL II. In Nagendra, K. N. and Stenflo, J. O., editors, *Polarization*, volume 243 of *Astrophysics and Space Science Library*, pages 297–304.
- Gandorfer, A. M. and Povel, H. P. (1997). First observations with a new imaging polarimeter. *Astronomy & Astrophysics*, 328:381–389.
- Gandorfer, A. M., Steiner, H. P. P. P., Aebersold, F., Egger, U., Feller, A., Gisler, D., Hagenbuch, S., and Stenflo, J. O. (2004). Solar polarimetry in the near UV with the Zurich Imaging Polarimeter ZIMPOL II. *Astronomy & Astrophysics*, 422:703–708.
- Gangadhara, R. T. and Gupta, Y. (2001). Understanding the Radio Emission Geometry of PSR B0329+54. *Astrophysical Journal*, 555:31–39.
- Gehrels, T. (1962). The wavelength dependence of polarization of the sunlit sky. *Publications of the Goethe Link Observatory*, 47:1165–1173.
- Gold, T. (1968). Rotating Neutron Stars as the Origin of the Pulsating Radio Sources. *Nature*, 218:731–732.
- Golden, A., Shearer, A., Redfern, R. M., Beskin, G. M., Neizvestny, S. I., Neustroev, V. V., Plokhotnichenko, V. L., and Cullum, M. (2000). High speed phase-resolved 2-d UV photometry of the Crab pulsar. *Astronomy & Astrophysics*, 363:617–628.
- Goldoni, P., Musso, C., Caraveo, P. A., and Bignami, G. F. (1995). Multiwavelength phenomenology of isolated neutron stars. *Astronomy & Astrophysics*, 298:535.
- Goldreich, P. and Julian, W. H. (1969). Pulsar Electrodynamics. *Astrophysical Journal*, 157:869.

- 
- Goosmann, R. W., Gaskell, C. M., and Shoji, M. (2007). Modeling the Polarization of Dusty Scattering Cones in Active Galactic Nuclei. In Ho, L. C. and Wang, J.-W., editors, *The Central Engine of Active Galactic Nuclei*, volume 373 of *Astronomical Society of the Pacific Conference Series*, page 485.
- Gould, D. M. and Lyne, A. G. (1998). Multifrequency polarimetry of 300 radio pulsars. *Monthly Notices of the Royal Astronomical Society*, 301:235–260.
- Graham-Smith, F., Dolan, J. F., Boyd, P. T., Biggs, J. D., Lyne, A. G., and Percival, J. W. (1996). The ultraviolet polarization of the Crab pulsar. *Monthly Notices of the Royal Astronomical Society*, 282:1354–1358.
- H., M. E. (1920). On the reciprocal of the general algebraic matrix.
- Halpern, J. P. and Gotthelf, E. V. (2010). Spin-Down Measurement of PSR J1852+0040 in Kesteven 79: Central Compact Objects as Anti-Magnetars. *Astrophysical Journal*, 709:436–446.
- Halpern, J. P. and Ruderman, M. (1993). Soft X-ray properties of the Geminga pulsar. *Astrophysical Journal*, 415:286–297.
- Hankins, T. H., Kern, J. S., Weatherall, J. C., and Eilek, J. A. (2003). Nanosecond radio bursts from strong plasma turbulence in the Crab pulsar. *Nature*, 422:141–143.
- Harding, A. K. (2013). The neutron star zoo. *Frontiers of Physics*, page 3.
- Harding, A. K. and Daugherty, J. K. (1998). Pulse profiles and spectra of gamma ray pulsars in the polar cap model. *Advances in Space Research*, 21:251–254.
- Harding, A. K. and Muslimov, A. G. (2001). Pulsar Polar Cap Heating and Surface Thermal X-Ray Emission. I. Curvature Radiation Pair Fronts. *Astrophysical Journal*, 556:987–1001.
- Harding, A. K., Stern, J. V., Dyks, J., and Frackowiak, M. (2008). High-Altitude Emission from Pulsar Slot Gaps: The Crab Pulsar. *Astrophysical Journal*, 680:1378–1393.

- 
- Hauge, P. S. (1978). Mueller matrix ellipsometry with imperfect compensators. *Journal of the Optical Society of America A*, 68(11):1519–1528.
- Hecht, E. (1987). *Optics 2nd edition*. MA: Addison-Wesley Publishing Company.
- Heiles, C. and Campbell, D. B. (1970). Pulsar NP 0532: Properties and Systematic Polarization of Individual Strong Pulses at 430 MHz. *Nature*, 226:529–531.
- Hewish, A., Bell, S. J., Pilkington, J. D. H., Scott, P. F., and Collins, R. A. (1968). Observation of a Rapidly Pulsating Radio Source. *Nature*, 217:709–713.
- Hirotani, K. (2006). Particle Accelerator in Pulsar Magnetospheres: Super-Goldreich-Julian Current with Ion Emission from the Neutron Star Surface. *Astrophysical Journal*, 652:1475–1493.
- Hobbs, G., Archibald, A., Arzoumanian, Z., Backer, D., Bailes, M., Bhat, N. D. R., Burgay, M., Burke-Spolaor, S., Champion, D., Cognard, I., Coles, W., Cordes, J., Demorest, P., Desvignes, G., Ferdman, R. D., Finn, L., Freire, P., Gonzalez, M., Hessels, J., Hotan, A., Janssen, G., Jenet, F., Jessner, A., Jordan, C., Kaspi, V., Kramer, M., Kondratiev, V., Lazio, J., Lazaridis, K., Lee, K. J., Levin, Y., Lommen, A., Lorimer, D., Lynch, R., Lyne, A., Manchester, R., McLaughlin, M., Nice, D., Oslowski, S., Pilia, M., Possenti, A., Purver, M., Ransom, S., Reynolds, J., Sanidas, S., Sarkissian, J., Sesana, A., Shannon, R., Siemens, X., Stairs, I., Stappers, B., Stinebring, D., Theureau, G., van Haasteren, R., van Straten, W., Verbiest, J. P. W., Yardley, D. R. B., and You, X. P. (2010a). The International Pulsar Timing Array project: using pulsars as a gravitational wave detector. *Classical and Quantum Gravity*, 27(8):084013.
- Hobbs, G., Lyne, A. G., and Kramer, M. (2010b). An analysis of the timing irregularities for 366 pulsars. *Monthly Notices of the Royal Astronomical Society*, 402:1027–1048.
- Hough, J. (2005). Polarimetry Techniques at Optical and Infrared Wavelengths. In A. Adamson, C. Aspin, C. Davis, & T. Fujiyoshi, editor, *Astronomical Polarimetry: Current Status and Future Directions*, volume 343 of *Astronomical Society of the Pacific Conference Series*, pages 3–+.

- 
- Hough, J. (2006). Polarimetry: a powerful diagnostic tool in astronomy. *Astronomy and Geophysics*, 47(3):030000–3.
- Hulleman, F., van Kerkwijk, M. H., and Kulkarni, S. R. (2000). An optical counterpart to the anomalous X-ray pulsar 4U0142+61. *Nature*, 408:689–692.
- Ibez, L., Schroeder, W., Ng, L., Cates, J., the Insight Software Consortium, and Hamming, R. (2003). The ITK Software Guide.
- Jessner, A., Słowińska, A., Klein, B., Lesch, H., Jaroschek, C. H., Kanbach, G., and Hankins, T. H. (2005). Giant radio pulses from the Crab pulsar. *Advances in Space Research*, 35:1166–1171.
- Jones, D. H. P., Smith, F. G., and Wallace, P. T. (1981). Linear polarization of optical radiation from the Crab pulsar. *Monthly Notices of the Royal Astronomical Society*, 196:943–953.
- Jones, P. B. (1980). The source of coherent radio emission in pulsars. *Astrophysical Journal*, 237:590–595.
- Kanbach, G., Arzoumanian, Z., Bertsch, D. L., Brazier, K. T. S., Chiang, J., Fichtel, C. E., Fierro, J. M., Hartman, R. C., Hunter, S. D., Kniffen, D. A., Lin, Y. C., Mattox, J. R., Mayer-Hasselwander, H. A., Michelson, P. F., von Montigny, C., Nel, H. I., Nice, D., Nolan, P. L., Pinkau, K., Rothermel, H., Schneid, E., Sommer, M., Sreekumar, P., Taylor, J. H., and Thompson, D. J. (1994). EGRET observations of the VELA pulsar, PSR0833-45. *Astronomy & Astrophysics*, 289:855–867.
- Kanbach, G., Słowińska, A., Kellner, S., and Steinle, H. (2005). New optical polarization measurements of the Crab pulsar. In Bulik, T., Rudak, B., and Madejski, G., editors, *Astrophysical Sources of High Energy Particles and Radiation*, volume 801 of *American Institute of Physics Conference Series*, pages 306–311.
- Kanbach, G., Stefanescu, A., Duscha, S., Steinle, H., Burwitz, V., and Schwope, A. (2008). High time resolution observations of Cataclysmic Variables with OPTIMA. In Phelan, D., Ryan, O., and Shearer, A., editors, *High Time Resolution*

---

*Astrophysics: The Universe at Sub-Second Timescales*, volume 984 of *American Institute of Physics Conference Series*, pages 32–40.

Karastergiou, A., Jessner, A., and Wielebinski, R. (2004). High-frequency Polarimetric Observations of the Crab Pulsar. In Camilo, F. and Gaensler, B. M., editors, *Young Neutron Stars and Their Environments*, volume 218 of *IAU Symposium*, page 329.

Karastergiou, A. and Johnston, S. (2006). Absolute polarization position angle profiles of southern pulsars at 1.4 and 3.1 GHz. *Monthly Notices of the Royal Astronomical Society*, 365:353–366.

Kargaltsev, O. Y., Pavlov, G. G., Zavlin, V. E., and Romani, R. W. (2005). Ultra-violet, X-Ray, and Optical Radiation from the Geminga Pulsar. *Astrophysical Journal*, 625:307–323.

Kaspi, V. M., Roberts, M. S. E., and Harding, A. K. (2006). *Isolated neutron stars*, pages 279–339.

Katajainen, S., Butters, O. W., Norton, A. J., Lehto, H. J., and Piironen, V. (2007). Discovery of polarized emission from the long period intermediate polar RX J2133.7+5107. *Astronomy & Astrophysics*, 475:1011–1018.

Keller, C. (2002). Instrumentation for astrophysical spectropolarimetry. In J. Trujillo-Bueno, F. Moreno-Insertis, & F. Sánchez, editor, *Astrophysical Spectropolarimetry*, pages 303–354.

Kern, B., Martin, C., Mazin, B., and Halpern, J. P. (2003). Optical phase-resolved polarimetry of PSR B0656+14. In *American Astronomical Society Meeting Abstracts*, volume 35 of *Bulletin of the American Astronomical Society*, page #133.02.

Kirk, J. G. and Skjæraasen, O. (2003). Dissipation in Poynting-Flux-dominated Flows: The  $\sigma$ -Problem of the Crab Pulsar Wind. *Astrophysical Journal*, 591:366–379.

Kirk, J. G., Skjæraasen, O., and Gallant, Y. A. (2002). Pulsed radiation from neutron star winds. *Astronomy & Astrophysics*, 388:L29–L32.

- 
- Knight, H. S., Bailes, M., Manchester, R. N., and Ord, S. M. (2006). A Study of Giant Pulses from PSR J1824-2452A. *Astrophysical Journal*, 653:580–586.
- Kouveliotou, C., Dieters, S., Strohmayer, T., van Paradijs, J., Fishman, G. J., Meegan, C. A., Hurley, K., Kommers, J., Smith, I., Frail, D., and Murakami, T. (1998). An X-ray pulsar with a superstrong magnetic field in the soft  $\gamma$ -ray repeater SGR1806 - 20. *Nature*, 393:235–237.
- Kristian, J., Visvanathan, N., Westphal, J. A., and Snellen, G. H. (1970). Optical Polarization and Intensity of the Pulsar in the Crab Nebula. *Astrophysical Journal*, 162:475.
- Kyne, G., Sheehan, B., Collins, P., Lara, D., Redfern, M., and Shearer, A. (2011). Galway astronomical stokes polarimeter - a high throughput linear and circular polarimeter. In *Frontiers in Optics 2011/Laser Science XXVII*, page FThR4. Optical Society of America.
- Landi Degl'Innocenti, E., Bagnulo, S., and Fossati, L. (2006). Polarimetric Standardization. *The Future of Photometric, Spectrophotometric, and Polarimetric Standardization, ASP Conference Series, C. Sterken (ed.)*, 999:In Preparation.
- Laor, A., Netzer, H., and Piran, T. (1990). Massive thin accretion discs. II - Polarization. *Monthly Notices of the Royal Astronomical Society*, 242:560–569.
- Lara Saucedo, D. (2005). *Three-dimensional Complete Polarisation Sensitive Imaging using a Confocal Mueller Matrix Polarimeter*. PhD thesis, Imperial College London.
- Lommen, A., Donovan, J., Gwinn, C., Arzoumanian, Z., Harding, A., Strickman, M., Dodson, R., McCulloch, P., and Moffett, D. (2007). Correlation between X-Ray Light-Curve Shape and Radio Arrival Time in the Vela Pulsar. *Astrophysical Journal*, 657:436–440.
- Lorimer, D. R. (1998). Binary and Millisecond Pulsars. *Living Reviews in Relativity*, 10.
- Lorimer, D. R. and Kramer, M. (2004). *Handbook of Pulsar Astronomy*.

- 
- Lundgren, S. C., Cordes, J. M., Ulmer, M., Matz, S. M., Lomatch, S., Foster, R. S., and Hankins, T. (1995). Giant Pulses from the Crab Pulsar: A Joint Radio and Gamma-Ray Study. *Astrophysical Journal*, 453:433.
- Lyne, A. G. (1992). Glitches as Probes of Neutron Star Interiors. *Royal Society of London Philosophical Transactions Series A*, 341:29–37.
- Lyne, A. G. and Graham-Smith, F. (2006). *Pulsar Astronomy*.
- Lyubarsky, Y. and Kirk, J. G. (2001). Reconnection in a Striped Pulsar Wind. *Astrophysical Journal*, 547:437–448.
- Mackay, C., Staley, T. D., King, D., Suess, F., and Weller, K. (2010). High-speed, photon-counting CCD cameras for astronomy. In *Society of Photo-Optical Instrumentation Engineers (SPIE) Conference Series*, volume 7742 of *Society of Photo-Optical Instrumentation Engineers (SPIE) Conference Series*.
- Malov, I. F. (2001). Pulsed Optical Emission by Radio Pulsars. *Astronomy Reports*, 45:865–871.
- Malov, I. F. and Machabeli, G. Z. (2001). On Optical Synchrotron Emission of Radio Pulsars. *Astrophysical Journal*, 554:587–592.
- Manchester, R. N., Hobbs, G. B., Teoh, A., and Hobbs, M. (2005). The Australia Telescope National Facility Pulsar Catalogue. *Astrophysical Journal*, 129:1993–2006.
- Manchester, R. N. and Taylor, J. H. (1977). *Pulsars*.
- McConnell, M., Baring, M. G., Bellazzini, R., Bloser, P. F., Costa, E., Dennis, B., Depaola, G., Dovciak, M., Elsner, R., Emslie, A. G., Hartmann, D. H., Hill, J., Hunter, S., Kalemci, E., Kanbach, G., Karas, V., Kaaret, P., Kaspi, V., Kippen, R. M., Kurfess, J., Longo, F., Marshall, H., Matt, G., O'Dell, S., Pavlov, G., Poutanen, J., Produit, N., Sakamoto, T., Toma, K., Weisskopf, M. C., Wunderer, C., and Zhang, B. (2009). X-Ray and Gamma-Ray Polarimetry. In *astro2010: The Astronomy and Astrophysics Decadal Survey*, volume 2010 of *Astronomy*, page 198.

- 
- McConnell, M. and Ryan, J. (2004). Status and prospects for polarimetry in high energy astrophysics. *New Astronomy Review*, 48:215–219.
- McDonald, J., O'Connor, P., de Burca, D., Golden, A., and Shearer, A. (2011). Inverse mapping of polarized optical emission from pulsars: basic formulation and determination of emission altitude. *Monthly Notices of the Royal Astronomical Society*, 417:730–744.
- McLean, I. S., Aspin, C., and Reitsema, H. (1983). High-resolution polarization images of Crab Nebula with a charge-coupled device camera. *Nature*, 304:243–246.
- McMackin, L., Zetocha, P., Sparkman, C., McIntire, H., Fetrow, M., and Bishop, K. (1999). Intelligent Optical Polarimetry Development for Space Surveillance Missions. In M.Perry, editor, *Artificial Intelligence, Robotics and Automation in Space*, volume 440 of *ESA Special Publication*, pages 199–+.
- Melrose, D. B. (1995). The Models for Radio Emission from Pulsars - the Outstanding Issues. *Journal of Astrophysics and Astronomy*, 16:137.
- Michel, F. C. (1994). Magnetic structure of pulsar winds. *Astrophysical Journal*, 431:397–401.
- Middleditch, J., Pennypacker, C. R., and Burns, M. S. (1987). Optical color, polarimetric, and timing measurements of the 50 MS Large Magellanic Cloud pulsar, PSR 0540-69. *Astrophysical Journal*, 315:142–148.
- Mignani, R. P., Bagnulo, S., Dyks, J., Lo Curto, G., and Słowikowska, A. (2007a). The optical polarisation of the Vela pulsar revisited. *Astronomy & Astrophysics*, 467:1157–1162.
- Mignani, R. P., Pulone, L., Iannicola, G., Pavlov, G. G., Townsley, L., and Kar-galtsev, O. Y. (2005). Search for the elusive optical counterpart of PSR J0537-6910 with the HST Advanced Camera for Surveys. *Astronomy & Astrophysics*, 431:659–665.

- 
- Mignani, R. P., Sartori, A., de Luca, A., Rudak, B., Słowikowska, A., Kanbach, G., and Caraveo, P. A. (2010). HST/WFPC2 observations of the LMC pulsar PSR B0540-69. *Astronomy & Astrophysics*, 515:A110.
- Mignani, R. P., Zharikov, S., and Caraveo, P. A. (2007b). The optical spectrum of the Vela pulsar. *Astronomy & Astrophysics*, 473:891–896.
- Moffett, D. A. and Hankins, T. H. (1996). Multifrequency Radio Observations of the Crab Pulsar. *Astrophysical Journal*, 468:779.
- Moran, P., Shearer, A., Mignani, R. P., Słowikowska, A., De Luca, A., Gouiffès, C., and Laurent, P. (2013). Optical polarimetry of the inner Crab nebula and pulsar. *Monthly Notices of the Royal Astronomical Society*, 433:2564–2575.
- Motch, C., Guillout, P., Haberl, F., Krautter, J., Pakull, M. W., Pietsch, W., Reinsch, K., Voges, W., and Zickgraf, F.-J. (1998). Identification of selected sources from the ROSAT Galactic Plane Survey. I. *Astronomy & Astrophysics, Supplement*, 132:341–359.
- Murdin, P. (2001). *Encyclopedia of Astronomy and Astrophysics*. Nature Publishing Group.
- Muslimov, A. G. and Harding, A. K. (2003). Extended Acceleration in Slot Gaps and Pulsar High-Energy Emission. *Astrophysical Journal*, 588:430–440.
- Muslimov, A. G. and Harding, A. K. (2004). High-Altitude Particle Acceleration and Radiation in Pulsar Slot Gaps. *Astrophysical Journal*, 606:1143–1153.
- Nasuti, E. P., Mignani, R., Caraveo, P. A., and Bignami, G. F. (1996). On the optical emission of the Crab pulsar. *The Messenger*, 83:37–40.
- O'Connor, P., Golden, A., and Shearer, A. (2005). Synchrotron Self-Absorption in Pulsar Magnetospheres: Implications for Optical Emission. *Astrophysical Journal*, 631:471–479.
- Oppenheimer, J. R. and Snyder, H. (1939). On Continued Gravitational Contraction. *Physical Review*, 56:455–459.

- 
- Oppenheimer, J. R. and Volkoff, G. M. (1939). On Massive Neutron Cores. *Physical Review*, 55:374–381.
- Pacini, F. (1968). Rotating Neutron Stars, Pulsars and Supernova Remnants. *Nature*, 219:145–146.
- Pacini, F. (1971). The Secular Decrease of Optical and X-Ray Luminosity of Pulsars. *Astrophysical Journal Letters*, 163:L17.
- Pacini, F. and Salvati, M. (1983). The optical luminosity of very fast pulsars. *Astrophysical Journal*, 274:369–371.
- Pacini, F. and Salvati, M. (1987). Optical and X-ray radiation from fast pulsars - Effects of duty cycle and spectral shape. *Astrophysical Journal*, 321:447–449.
- Patat, F. and Romanillo, M. (2006). Error Analysis for Dual-Beam Optical Linear Polarimetry. *Publications of the Astronomical Society of the Pacific*, 118:146–161.
- Patterson, J. (1994). The DQ Herculis stars. *Publications of the Astronomical Society of the Pacific*, 106:209–238.
- Percival, J. W., Biggs, J. D., Dolan, J. F., Robinson, E. L., Taylor, M. J., Bless, R. C., Elliot, J. L., Nelson, M. J., Ramseyer, T. F., van Citters, G. W., and Zhang, E. (1993). The Crab pulsar in the visible and ultraviolet with 20 microsecond effective time resolution. *Astrophysical Journal*, 407:276–283.
- Peterson, B. A., Murdin, P., Wallace, P., Manchester, R. N., Penny, A. J., Jorden, A., Hartley, K. F., and King, D. (1978). Pulsed and unpulsed light from the VELA and Crab pulsars. *Nature*, 276:475–478.
- Pétri, J. and Kirk, J. G. (2005). The Polarization of High-Energy Pulsar Radiation in the Striped Wind Model. *Astrophysical Journal Letters*, 627:L37–L40.
- Podsiadlowski, P., Rappaport, S., and Pfahl, E. D. (2002). Evolutionary Sequences for Low- and Intermediate-Mass X-Ray Binaries. *Astrophysical Journal*, 565:1107–1133.

- 
- Potter, S., Buckley, D., O'Donoghue, D., O'Conner, J., Fourie, P., Evans, G., Sass, C., Crause, L., Butters, O. W., Norton, A., Mukai, K., and Still, M. (2008). A new two channel high-speed photo-polarimeter (HIPPO) for the SAAO. In *Society of Photo-Optical Instrumentation Engineers (SPIE) Conference Series*, volume 7014 of *Society of Photo-Optical Instrumentation Engineers (SPIE) Conference Series*.
- Povel, H., Aebersold, H., and Stenflo, J. O. (1989). *CCD image sensor as a demodulator in a 2-D polarimeter with a piezo-elastic modulator.*
- Povel, H.-P. (1995). Imaging Stokes polarimetry with piezoelastic modulators and charge-coupled-device image sensors. *Optical Engineering*, 34:1870–1878.
- Povel, H. P. (2001). Ground-based Instrumentation for Solar Magnetic Field Studies, with Special Emphasis on the Zurich Imaging Polarimeters ZIMPOL-I and II. In Mathys, G., Solanki, S. K., and Wickramasinghe, D. T., editors, *Magnetic Fields Across the Hertzsprung-Russell Diagram*, volume 248 of *Astronomical Society of the Pacific Conference Series*, page 543.
- Povel, H. P., Keller, C. U., and Yadigaroglu, I.-A. (1994). Two-dimensional polarimeter with a charge-coupled-device image sensor and a piezoelastic modulator. *ao*, 33:4254–4260.
- Radhakrishnan, V. and Cooke, D. J. (1969). Magnetic Poles and the Polarization Structure of Pulsar Radiation. *Astrophysical Journal Letters*, 3:225.
- Robinson, E. A. and Clark, D. (2006). Basic seismology 13 - huygens' principle. *The Leading Edge*, 25(10):1252–1255.
- Romani, R. W. (1993). Magnetic Field Evolution in Isolated and Recycled Pulsars. In van Riper, K. A., Epstein, R. I., and Ho, C., editors, *Isolated Pulsars*, page 75.
- Romani, R. W. (1996). Gamma-Ray Pulsars: Radiation Processes in the Outer Magnetosphere. *Astrophysical Journal*, 470:469.
- Romani, R. W. and Johnston, S. (2001). Giant Pulses from the Millisecond Pulsar B1821-24. *Astrophysical Journal Letters*, 557:L93–L96.

- 
- Romani, R. W. and Yadigaroglu, I.-A. (1995). Gamma-ray pulsars: Emission zones and viewing geometries. *Astrophysical Journal*, 438:314–321.
- Ruderman, M. (2005). A Biography of the Magnetic Field of a Neutron Star. In Baykal, A., Yerli, S. K., Inam, S. C., and Grebenev, S., editors, *NATO ASIB Proc. 210: The Electromagnetic Spectrum of Neutron Stars*, page 47.
- Ruderman, M. A. and Sutherland, P. G. (1975). Theory of pulsars - Polar caps, sparks, and coherent microwave radiation. *Astrophysical Journal*, 196:51–72.
- Ryle, M. and Bailey, J. A. (1968). Optical Identification of the First Neutron Star? *Nature*, 217:907–910.
- Sallmen, S., Backer, D. C., Hankins, T. H., Moffett, D., and Lundgren, S. (1999). Simultaneous Dual-Frequency Observations of Giant Pulses from the Crab Pulsar. *Astrophysical Journal*, 517:460–471.
- Schmidt, G. D., Elston, R., and Lupie, O. L. (1992). The Hubble Space Telescope Northern-Hemisphere grid of stellar polarimetric standards. *The Astronomical Journal*, 104:1563–1567.
- Sen, A., Joshi, U., Deshpande, M., and Prasad, C. (1990). Imaging polarimetry of Comet P/Halley. *Icarus*, 86:248–256.
- Sen, A. and Kakati, M. (1997). Instrumental polarization caused by telescope optics during wide field imaging. *Astronomy & Astrophysics, Supplement*, 126:113–119.
- Serkowski, K. (1974). Polarimeters for Optical Astronomy. In T. Gehrels, editor, *IAU Colloq. 23: Planets, Stars, and Nebulae: Studied with Photopolarimetry*, pages 135–+.
- Shearer, A. (2008). High Time Resolution Astrophysics and Pulsars. In Phelan, D., Ryan, O., and Shearer, A., editors, *Astrophysics and Space Science Library*, volume 351 of *Astrophysics and Space Science Library*, pages 1–4020.
- Shearer, A. and Golden, A. (2001). Implications of the Optical Observations of Isolated Neutron Stars. *Astrophysical Journal*, 547:967–972.

- 
- Shearer, A., Golden, A., Harfst, S., Butler, R., Redfern, R. M., O'Sullivan, C. M. M., Beskin, G. M., Neizvestny, S. I., Neustroev, V. V., Plokhotnichenko, V. L., Cullum, M., and Danks, A. (1998). Possible pulsed optical emission from Geminga. *Astronomy & Astrophysics*, 335:L21–L24.
- Shearer, A., Kanbach, G., Slowikowska, A., Barbieri, C., Marsh, T., Dhillon, V., Mignani, R., Dravins, D., Gouiffes, c., MacKay, C., Bonanno, G., and Collins, S. (2010). High Time Resolution Astrophysics in the Extremely Large Telescope Era : White Paper. In *Proceedings of High Time Resolution Astrophysics - The Era of Extremely Large Telescopes (HTRA-IV). May 5 - 7, 2010. Agios Nikolaos, Crete Greece. Published online at <A href='http://pos.sissa.it/cgi-bin/reader/conf.cgi?confid=108'>http://pos.sissa.it/cgi-bin/reader/conf.cgi?confid=108</A>, id.54.*
- Shearer, A., Redfern, R. M., Gorman, G., Butler, R., Golden, A., O'Kane, P., Beskin, G. M., Neizvestny, S. I., Neustroev, V. V., Plokhotnichenko, V. L., and Cullum, M. (1997). Pulsed Optical Emission from PSR 0656+14. *Astrophysical Journal Letters*, 487:L181.
- Shearer, A., Stappers, B., O'Connor, P., Golden, A., Strom, R., Redfern, M., and Ryan, O. (2003). Enhanced Optical Emission During Crab Giant Radio Pulses. *Science*, 301:493–495.
- Shurcliff, W. and Stanley, S. (1964). *Polarized Light*. D. Van Nostrand Company (Canada), Ltd.
- Silver, E. H., Kestenbaum, H. L., Long, K. S., Novick, R., Wolff, R. S., and Weisskopf, M. C. (1978). Search for X-ray polarization in the Crab pulsar. *Astrophysical Journal*, 225:221–225.
- Slowikowska, A., Jessner, A., Kanbach, G., and Klein, B. (2007). Comparison of giant radio pulses in young pulsars and millisecond pulsars. In Becker, W. and Huang, H. H., editors, *WE-Heraeus Seminar on Neutron Stars and Pulsars 40 years after the Discovery*, page 64.

- 
- Słowińska, A., Kanbach, G., Kramer, M., and Stefanescu, A. (2009). Optical polarization of the Crab pulsar: precision measurements and comparison to the radio emission. *Monthly Notices of the Royal Astronomical Society*, 397:103–123.
- Słowińska, A., Rudak, B., and Kanbach, G. (2008). High energy polarization of pulsars-observations vs. models. In Bassa, C., Wang, Z., Cumming, A., and Kaspi, V. M., editors, *40 Years of Pulsars: Millisecond Pulsars, Magnetars and More*, volume 983 of *American Institute of Physics Conference Series*, pages 142–144.
- Smith, F. G., Jones, D. H. P., Dick, J. S. B., and Pike, C. D. (1988). The optical polarization of the Crab Pulsar. *Monthly Notices of the Royal Astronomical Society*, 233:305–319.
- Smith, M. H., Woodruff, J. B., and Howe, J. D. (1999). Beam wander considerations in imaging polarimetry. In Goldstein, D. H. and Chenault, D. B., editors, *Society of Photo-Optical Instrumentation Engineers (SPIE) Conference Series*, volume 3754 of *Society of Photo-Optical Instrumentation Engineers (SPIE) Conference Series*, pages 50–54.
- Srisailam, A., Dharmia, V., Ramanamurthy, M., and Mondal, P. K. (2001). Encircled energy factor as a point-image quality-assessment parameter. *Advances in Applied Science Research*, 2(6):145–154.
- Staelin, D. H. and Reifenstein, III, E. C. (1968). Pulsating Radio Sources near the Crab Nebula. *Science*, 162:1481–1483.
- Steele, I. A., Bates, S. D., Carter, D., Clarke, D., Gomboc, A., Guidorzi, C., Melandri, A., Monfardini, A., Mottram, C. J., Mundell, C. G., Scott, A. B., Smith, R. J., and Swindlerhurst, J. (2006). RINGO: a novel ring polarimeter for rapid GRB followup. In *Society of Photo-Optical Instrumentation Engineers (SPIE) Conference Series*, volume 6269 of *Society of Photo-Optical Instrumentation Engineers (SPIE) Conference Series*.
- Steele, I. A., Bates, S. D., Guidorzi, C., Mottram, C. J., Mundell, C. G., and Smith, R. J. (2010). RINGO2: an EMCCD-based polarimeter for GRB fol-

---

lowup. In *Society of Photo-Optical Instrumentation Engineers (SPIE) Conference Series*, volume 7735 of *Society of Photo-Optical Instrumentation Engineers (SPIE) Conference Series*.

Stefanescu, A., Kanbach, G., Słowińska, A., Duscha, S., and Mühlegger, M. (2008). OPTIMA-Burst: Observing GRB Afterglows and other Fast Transients with High Time Resolution. In Phelan, D., Ryan, O., and Shearer, A., editors, *High Time Resolution Astrophysics: The Universe at Sub-Second Timescales*, volume 984 of *American Institute of Physics Conference Series*, pages 124–131.

Stenflo, J. O., Keller, C. U., and Povel, H. P. (1992). Demodulation of all four Stokes parameters with a single CCD - ZIMPOL II. Conceptual design. *LEST Foundation, Technical Report*, 54.

Stockman, H. S., Schmidt, G. D., Berriman, G., Liebert, J., Moore, R. L., and Wickramasinghe, D. T. (1992). A search for circular polarization in cataclysmic variables. *Astrophysical Journal*, 401:628–641.

Strader, M. J., Johnson, M. D., Mazin, B. A., Spiro Jaeger, G. V., Gwinn, C. R., Meeker, S. R., Szypryt, P., van Eyken, J. C., Marsden, D., O'Brien, K., Walter, A. B., Ulbricht, G., Stoughton, C., and Bumble, B. (2013). Excess Optical Enhancement Observed with ARCONS for Early Crab Giant Pulses. *Astrophysical Journal Letters*, 779:L12.

Strohmayer, T. E. (2004). Chandra Observations of V407 Vulpeculae: Confirmation of the Spin-up. *Astrophysical Journal*, 610:416–421.

Sturrock, P. A. (1971). A Model of Pulsars. *Astrophysical Journal*, 164:529.

Suhai, B. and Horváth, G. (2004). How well does the rayleigh model describe the e-vector distribution of skylight in clear and cloudy conditions? a full-sky polarimetric study. *Journal of the Optical Society of America A*, 21(9):1669–1676.

Technology, A. (2013). Andor Technology iXon Ultra 897 Technical Data Sheets.

Thompson, R. C., Bottiger, J. R., and Fry, E. S. (1980). Measurement of polarized light interactions via the mueller matrix. *Applied Optics*, 19(8):1323–1332.

- 
- Tinbergen, J. (1996a). *Astronomical Polarimetry*.
- Tinbergen, J. (1996b). *Astronomical Polarimetry*. UK: Cambridge University Press.
- Tinbergen, J. (2003). Circular polarimetry: why and how. *Astrophysics & Space Science*, 288:3–14.
- Tompkins, H. G. and Irene, E. A. (2005). *Handbook of Ellipsometry*. William Andrew publishing, Springer.
- Treanor, P. F. (1968). A new technique for stellar polarimetry. *Monthly Notices of the Royal Astronomical Society*, 138:325.
- Trujillo-Bueno, J., Moreno-Insertis, F., and Sanchez Martinez, F. (2002). *Astrophysical Spectropolarimetry*.
- Turnshek, D. A., Bohlin, R. C., Williamson, II, R. L., Lupie, O. L., Koornneef, J., and Morgan, D. H. (1990). An atlas of Hubble Space Telescope photometric, spectrophotometric, and polarimetric calibration objects. *The Astronomical Journal*, 99:1243–1261.
- Tyo, J. S. (2006). Hybrid division of aperture/division of a focal-plane polarimeter for real-time polarization imagery without an instantaneous field-of-view error. *Opt. Lett.*, 31(20):2984–2986.
- Tyo, J. S., Goldstein, D. L., Chenuault, D. B., and Shaw, J. A. (2006). Review of passive imaging polarimetry for remote sensing applications. *Appl. Opt.*, 45(22):5453–5469.
- Ugolnikov, O. and Maslov, I. (2009). Polarization measurements of twilight sky: Studies of atmospheric aerosol from the troposphere to mesosphere. *Atmospheric and Oceanic Optics*, 22(2):192–197.
- van den Bergh, S. and Kamper, K. W. (1984). The expansion age of the supernova remnant RCW 89 = MSH 15 52 (G320.4 - 1.2). *Astrophysical Journal Letters*, 280:L51–L54.

- 
- Wagner, S. J. and Seifert, W. (2000). Optical Polarization Measurements of Pulsars. In Kramer, M., Wex, N., and Wielebinski, R., editors, *IAU Colloq. 177: Pulsar Astronomy - 2000 and Beyond*, volume 202 of *Astronomical Society of the Pacific Conference Series*, page 315.
- Wallace, P. T., Peterson, B. A., Murdin, P. G., Danziger, I. J., Manchester, R. N., Lyne, A. G., Goss, W. M., Smith, F. G., Disney, M. J., Hartley, K. F., Jones, D. H. P., and Wellgate, G. W. (1977). Detection of optical pulses from the VELA pulsar. *Nature*, 266:692–694.
- Wampler, E. J., Scargle, J. D., and Miller, J. S. (1969). Optical Observations of the Crab Nebula Pulsar. *Astrophysical Journal Letters*, 157:L1.
- Wang, R. C. C., Deen, M. J., Armstrong, D., and Fang, Q. (2011). Development of a catadioptric endoscope objective with forward and side views. *Journal of Biomedical Optics*, 16(6):066015–066015.
- Warner, B., Nather, R. E., and Macfarlane, M. (1969). Further Observations of the Crab Nebula Optical Pulsar. *Nature*, 222:233–238.
- Weisskopf, M. C., Silver, E. H., Kestenbaum, H. L., Long, K. S., and Novick, R. (1978). A precision measurement of the X-ray polarization of the Crab Nebula without pulsar contamination. *Astrophysical Journal Letters*, 220:L117–L121.
- West, S. C. (1989). The optical and near-infrared continuum polarization of five magnetic white dwarf stars - New observations and considerations regarding its origin. *Astrophysical Journal*, 345:511–521.
- Wickramasinghe, D. T. and Meggitt, S. (1986). The electron temperature of AM Herculis type systems. *Astrophysics & Space Science*, 118:287–289.
- Zhang, L. and Cheng, K. S. (1997). Gamma-Ray Production through Inverse Compton Scattering with Anisotropic Photon Field from Accretion Disk in AGNs. *Astrophysical Journal*, 488:94.